



Durham E-Theses

Oligomer/polymer mixtures as model adhesives: Impact of compatibility on surface segregation behaviour

SABATTIE, ELISE,FANNY,DELPHINE

How to cite:

SABATTIE, ELISE,FANNY,DELPHINE (2018) *Oligomer/polymer mixtures as model adhesives: Impact of compatibility on surface segregation behaviour*, Durham theses, Durham University. Available at Durham E-Theses Online: <http://etheses.dur.ac.uk/12459/>

Use policy

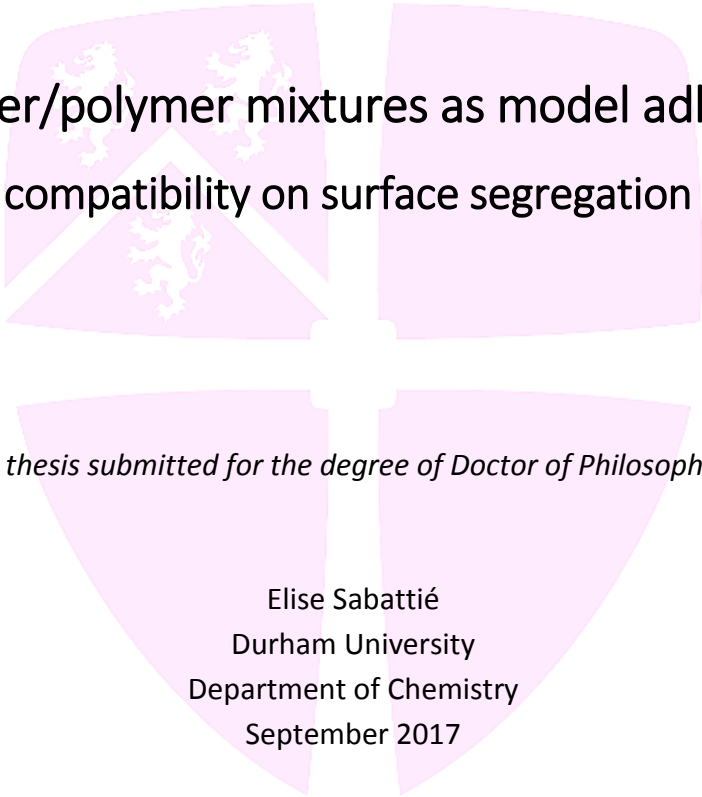
The full-text may be used and/or reproduced, and given to third parties in any format or medium, without prior permission or charge, for personal research or study, educational, or not-for-profit purposes provided that:

- a full bibliographic reference is made to the original source
- a [link](#) is made to the metadata record in Durham E-Theses
- the full-text is not changed in any way

The full-text must not be sold in any format or medium without the formal permission of the copyright holders.

Please consult the [full Durham E-Theses policy](#) for further details.

Academic Support Office, Durham University, University Office, Old Elvet, Durham DH1 3HP
e-mail: e-theses.admin@dur.ac.uk Tel: +44 0191 334 6107
<http://etheses.dur.ac.uk>



Oligomer/polymer mixtures as model adhesives:
Impact of compatibility on surface segregation behaviour

A thesis submitted for the degree of Doctor of Philosophy.

Elise Sabbatié
Durham University
Department of Chemistry
September 2017



*Oligomer/polymer mixtures as model adhesives:
Impact of compatibility on surface segregation behaviour*

Abstract - Elise Sabattié

Molecular migration, segregation and self-organisation in polymers are phenomena that govern the processing, performance and life-time of many materials and formulations. Despite the widespread use of oligomer/polymer mixtures for industrial purposes, such as in paints, coating, packaging and adhesives, relatively little can be found in literature regarding the characterisation of such asymmetric systems. Hence, the aim of this thesis is to determine the causes and consequences of the surface segregation of low molecular weight components in simplified adhesive formulations. In addition, it focuses on producing data for the validation of a new model that bridges the gap evidenced in the existing theories.

First, the key-parameters impacting such surface segregation were hypothesised by extrapolating the conclusions from the research conducted on polymer blends. Then, model systems were defined in order to mimic the molecular migration in hot-melt adhesives. Experimental evidence was generated which showed that the glassy polystyrene domains can be neglected in the model formulations. Hence, binary mixtures of oligomer and rubbery polymer were chosen to evaluate the impact of the oligomer molecular weight and volume fraction, interaction parameter as well as temperature. A systematic evaluation of the compatibility was conducted and correlated with similarity in saturation and solubility parameter. The results were compared with the predictions of the Flory-Huggins theory, for polymer blends. A clear relationship between surface segregation and bulk compatibility was evidenced by comparing the compatibility study with results obtained by ion beam analysis and neutron reflectometry. In some systems, a nearly pure surface wetting layer of well-defined few nm thickness was observed, which was surprisingly independent of sample thickness. In others, lateral segregation on scale of few μm was characterised by atomic force microscopy. While surface segregation is driven by disparity in molecular weight in highly compatible systems, this trend reverses as the critical point is approached. Oligomers of higher molecular weight can phase-separate from the bulk and form a wetting layer at the surface. The impact of surface segregation on mechanical surface and bulk properties was also assessed by atomic force microscopy and oscillatory rheology. It was found that the mechanical bulk properties of the polymer were greatly affected by the presence of oligomer, due to plasticisation effects.

TABLE OF CONTENTS

Table of contents	<i>i</i>
List of abbreviations	<i>vii</i>
Statement of copyrights	<i>xi</i>
Acknowledgements	<i>xii</i>
Introduction	1
Chapter 1: Literature review	4
1.1 Miscibility of polymer blends	4
1.1.1 The Flory-Huggins theory	4
1.1.1.1 Description of the Flory-Huggins solution theory	4
1.1.1.2 Flory-Huggins theory applied to polymer blends	5
1.1.1.3 Phase diagrams from the FH theory	6
1.1.1.4 The FH interaction parameter	8
1.1.1.5 Limitations of the Flory-Huggins theory	10
1.1.2 Case of oligomer/polymer mixtures	11
1.1.2.1 Applying FH to oligomer/polymer mixtures	11
1.1.2.2 Differences with polymer blends	12
1.1.3 Alternatives to the mean-field FH theory	14
1.2 Polymer blends at surfaces	15
1.2.1 Polymer chain properties at surfaces	15
1.2.2 Symmetric polymer blends at surfaces	16
1.2.2.1 Effect of surface energy disparity	16
1.2.2.2 Influence of the substrate	17
1.2.3 Asymmetric polymer blends at surfaces	19
1.2.3.1 Athermal asymmetric blend	19

1.2.3.2	Isotopic asymmetric blend _____	20
1.2.4	Shape of the concentration profiles _____	21
1.2.4.1	Concentration profiles in the one-phase regime _____	23
1.2.4.2	Concentration profiles in the two-phase regime _____	25
1.2.5	Kinetic considerations _____	26
1.2.5.1	Diffusion classes _____	26
1.2.5.2	Oligomer/polymer inter-diffusion _____	26
1.2.5.3	Surface enrichment in polymer blends _____	27
1.2.5.4	Surface enrichment of oligomer/polymer blends _____	28
1.3	Surface partitioning and adhesion properties of polymer blends _____	29
1.3.1	Theories of adhesion _____	29
1.3.1.1	Adhesion via mechanical interlocking _____	29
1.3.1.2	Adsorption and thermodynamic description of adhesion _____	29
1.3.1.3	Other contributions to adhesion _____	33
1.3.2	Hot-melt pressure sensitive adhesives _____	33
1.3.2.1	Pressure sensitive adhesives and tack properties _____	33
1.3.2.2	Styrenic block copolymer-based formulations _____	34
1.3.2.3	Effect of tackifiers on tack properties _____	36
1.3.3	Possible effects of additive segregation on adhesion _____	37
1.3.3.1	Modification of the surface viscoelastic properties _____	38
1.3.3.2	Formation of a weak boundary layer _____	38
1.3.3.3	Modification of the surface roughness _____	39
1.3.3.4	Modification of the work of adhesion _____	39
1.3.3.5	Loss of additive _____	39
1.4	Conclusions of the literature review _____	40
Chapter 2: Experimental	_____	43
2.1	Materials _____	43
2.2	Sample preparation _____	45
2.2.1	Polymer solutions _____	45
2.2.2	Spin coating of thin films _____	45
2.2.3	Solution cast films _____	45

2.2.4	Fractionation of polydisperse polymers	46
2.3	Gel permeation chromatography	46
2.4	Differential scanning calorimetry	47
2.5	Phase diagram through turbidity	47
2.6	Surface energy measurements	48
2.6.1	Surface tension measurement with the pendant drop	48
2.6.2	Surface energy measurements using OWRK method	49
2.7	Ion beam analysis	50
2.7.1	Equipment and measurement principle	50
2.7.1.1	Elastic Recoil Detection Analysis (ERDA)	52
2.7.1.2	Nuclear Reaction Analysis (NRA)	53
2.7.2	Fitting methods	54
2.8	Neutron reflectometry	55
2.9	Atomic force microscopy	60
2.10	Rheology	61
2.10.1	Measurement description	61
2.10.2	Time-temperature superposition principle	62
2.11	Tack tests	63
2.11.1	Loop tack tests	63
2.11.2	Tack tests using the rheometer	63
Chapter 3: Model systems		64
3.1	Determination of the model compounds	64
3.2	Justification of the formulation simplification	65
3.2.1	Diffusion of squalane in deuterated PS	65
3.2.2	Diffusion of industrial tackifiers in deuterated PS	70
3.3	Conclusions on the model systems	74
Chapter 4: Compatibility of oligomer/polymer mixtures		75

4.1	Experimental compatibility study	75
4.1.1	Principles of the compatibility study	75
4.1.1.1	Compatibility study using differential scanning calorimetry	76
4.1.1.2	Compatibility study using the cloud point determination	81
4.1.2	Compatibility study on the model systems	82
4.1.2.1	Effect of the matrix on compatibility	82
4.1.2.2	Effect of the oligomer molecular weight on compatibility	85
4.1.2.3	Effect of the migrant polarisability on compatibility	88
4.2	Discussion of the compatibility results	92
4.2.1	Summary of the results: Compatibility matrix	92
4.2.2	Evaluation of the factors influencing compatibility	93
4.2.2.1	Flory-Huggins theory applied to oligomer/polymer mixtures	93
4.2.2.2	Influence of the oligomer molecular weight on compatibility behaviour	94
4.2.2.3	Influence of the oligomer concentration on compatibility behaviour	95
4.2.2.4	Influence of the interaction parameter on compatibility behaviour	96
4.2.2.5	Influence of temperature on compatibility behaviour	100
4.2.2.6	Influence of matrix crystallinity on compatibility behaviour	105
4.3	Conclusions on compatibility	106
 Chapter 5: Oligomer surface partitioning		108
5.1	Experimental results	109
5.1.1	Surface phenomena for systems in the one-phase regime	109
5.1.1.1	Surface energy investigation	109
5.1.1.2	Evidence for various oligomer depth distributions	112
5.1.1.3	Effect of temperature on oligomer surface segregation	116
5.1.2	Wetting layer formation through the phase boundary	118
5.1.2.1	Effect of oligomer concentration on the wetting layer formation	118
5.1.2.2	Effect of film thickness on the wetting layer	126
5.1.2.3	Effect of polymer molecular weight and polydispersity on the wetting layer	128
5.1.2.4	Effect of time and temperature on the wetting layer formation	130
5.1.3	Wetting layer orientation in phase-separated systems	131
5.1.3.1	Excess directed to the surface	131
5.1.3.2	Excess directed to the interface with the substrate	137

5.1.3.3	Excess directed to both interfaces	140
5.2	Discussion of surface partitioning	146
5.2.1	Impact of surface energy on surface partitioning	146
5.2.2	Impact of film thickness on surface partitioning	148
5.2.2.1	Impact of film thickness on the wetting layer thickness	148
5.2.2.2	Impact of film thickness on interfacial roughness	151
5.2.2.3	Extremely thin films and bulk depletion	151
5.2.3	Impact of polymer molecular weight on surface partitioning	151
5.2.4	Impact of bulk compatibility on surface partitioning	153
5.2.4.1	Surface enrichment in the one-phase regime	153
5.2.4.2	Phase transition and wetting layer	155
5.2.4.3	Concentration profiles for incompatible systems	161
5.2.5	Impact of temperature on surface partitioning	162
5.3	Conclusions on surface partitioning	163

Chapter 6: Adhesion properties of oligomer/polymer mixtures _____ **165**

6.1	Experimental results	165
6.1.1	Surface investigation of oligomer/polymer mixtures	165
6.1.1.1	Adhesion mapping by atomic force microscopy	165
6.1.1.2	Macroscopic adhesion via tack tests	172
6.1.2	Bulk investigation of oligomer/polymer mixtures	174
6.2	Discussion of adhesion properties	179
6.2.1	Surface adhesive properties of phase-separated systems	179
6.2.1.1	Surface lateral composition of oligomer/polymer films	179
6.2.1.2	Underlying lateral composition of oligomer/polymer films	180
6.2.1.3	Surface directed phase separation in oligomer/polymer films	180
6.2.1.4	Mechanisms of phase separation and evolution of the surface features	181
6.2.1.5	Effect of oligomer content on surface topography and adhesion	183
6.2.2	Bulk mechanical properties of oligomer/polymer blends	185
6.2.2.1	Effect of oligomer content on bulk mechanical properties	185
6.2.2.2	Validity of the TTS principle used to build the master curves	189
6.3	Conclusions on adhesion properties	192

Conclusions of the thesis	194
References	198
Annex 1: Fitting error analysis	207
Fitting error with ERDA	207
Fitting error with NR	208
Annex 2: IBA fitting parameters	213
ERDA	213
NRA	219
Annex 3: NR fitting parameters	221

LIST OF ABBREVIATIONS

A: Area occupied by one statistical repetitive unit of a polymer chain	FH: Flory-Huggins
A: Hamaker constant	FRES: Forward recoil spectrometry (equivalent to ERDA)
α: Statistical segment length of a Gaussian chain	F_s: Excess surface free energy per lattice site
α_T: Shifting coefficient in angular frequency, depending on temperature	G': Storage modulus
AFM: Atomic force microscopy	G'': Loss modulus
b_i: Scattering length contribution from the atom i	G^*: Complex modulus
b_T: Shifting coefficient in modulus, depending on temperature	GAE: Gibbs adsorption equation
Ca: Capillary number	G_c: Modulus at the crossover point
d: Film thickness	GPC: Gel permeation chromatography
D: Diffusion coefficient	gsm: $\text{g}\cdot\text{m}^{-2}$
DSC: Differential scanning calorimetry	HMA: Hot-melt adhesive
DP: Degree of polymerisation	hPI: Hydrogenated polyisoprene
dsq: Deuterated squalane	$I(q)$: Coherent small angle neutron scattering intensity
dn/dc: Refractive index increment	IBA: Ion beam analysis
ERDA: Elastic recoil detection analysis	k: Boltzmann constant (= $1.38064852 \times 10^{-23} \text{ m}^2\cdot\text{kg}\cdot\text{s}^{-2}\cdot\text{K}^{-1}$)
erf: Error function	l: Dispersive capillary length
	LCL: Locally correlated lattice

LCST: Lower critical solution temperature

***M*:** Molecular weight

MC: Monte Carlo

***M_e*:** Molecular weight in between entanglements

MICSED: Molecular Interactions in Complex Systems European Doctorate

***M_n*:** Number average molecular weight

***M_w*:** Weight average molecular weight

***N_A*:** Avogadro number
(= $6.022140857 \times 10^{23} \text{ mol}^{-1}$)

***n_i*:** Number of polymer molecules of type *i*

***n_i*:** Refractive index

***N_i*:** Number of repetitive units of a polymer molecules of type *i*

NR: Neutron reflectometry

NRA: Nuclear reaction analysis

oligo d-IB: Deuterated oligoisobutylene

oligo d-S: Deuterated oligostyrene

OWRK: Owens, Wendt, Rabel and Kälble

***p*:** Pressure

PB: Polybutadiene

PDI: Polydispersity

PEP: Poly(ethylenepropylene)

PET: Poly(ethylene terephthalate)

PI: Polyisoprene

***P_i(Q)*:** Single chain form factor for species *i*

PMMA: Poly(methyl methacrylate)

PS: Polystyrene

P&G: Procter and Gamble

Q: Momentum transfer vector

***r*:** Radius of curvature

***R(Q)*:** Reflectivity

***R_{g,i}*:** Radius of gyration of a chain of type *i*

RT: Room temperature

rpm: Rotation per minute

***S(Q)*:** Static structure factors

s.l.d. or *s*: Scattering length density

SAFT-γ Mie: Statistical association fluid theory

SAN: Poly(styrene-ran-acrylonitrile)

SANS: Small angle neutron scattering

SB: Schmidt-Binder

SBC: Styrenic block copolymer

SCFT: Self Consistent Field Theory

SEL: Surface Enriched Layer

SIMS: Secondary ion mass spectrometry

t : Time	z : Lattice coordination number of the Flory-Huggins theory (number of neighbouring sites)
T : Temperature	z : Sample depth
T : Tack property	z₀ : Total polymer film thickness
T_c : Critical temperature	z* : Surface excess
T_g : Glass transition temperature	γ_(i) : Surface tension (of the species <i>i</i>)
T_m : Melting point	γ_i^d : Dispersive component of the surface tension
THF : Tetrahydrofuran	γ_i^p : Polar component of the surface tension
TOF : Time of flight	γ_c : Critical surface tension of the liquid
TTS : Time-temperature superposition	γ_{ij} : Interfacial tension between species <i>i</i> and <i>j</i>
u_i : Adsorption energy of component <i>i</i> to the surface relative to its bulk interaction	Γ_i : Molecular surface excess of species <i>i</i>
UCST : upper critical solution temperature	δ_i : Hildebrand solubility parameter
v : Excluded volume	δ_D : Dispersive Hansen solubility parameter
v₀ : Reference lattice volume of the Flory-Huggins theory, usually fixed at 100 Å ³	ΔC_p : Specific heat capacity
v_i : Reference volume of one repetitive unit of species <i>i</i>	ΔG_m : Gibbs free energy of mixing
V : Velocity of deformation	ΔH_m : Enthalpy of mixing
V_m : Molar volume	ΔS_m : Entropy of mixing
w : Interfacial width	ε_{ij} : Energy (in units of <i>kT</i>) associated with the attractive interaction between two neighbouring sites
w_i : Weight fraction of the component <i>i</i>	η : Intrinsic viscosity
W_A : Work of adhesion	
WBL : Weak boundary layer	
WLF : Williams-Landel-Ferry	

ξ : Decay length of the concentration profile from the SB theory, depending on the FH χ parameter

ϑ : Incident angle

ϑ : Contact angle of the sessile liquid drop on the solid surface

λ : Wave length

μ : Dynamic viscosity

μ_i : Chemical potential of the species i

μ_i^0 : Standard chemical potential of the species i

Π : Osmotic pressure

ρ : Density

φ_i : Volume fraction of species i

φ_c : Volume fraction of species A (later, of the oligomer) at the critical point

φ_s : Volume fraction of oligomer at the surface

φ_∞ : Volume fraction of oligomer in the bulk

φ_{tot} : Total film volume fraction of oligomer

χ : Flory-Huggins interaction parameter

χ_c : Flory-Huggins interaction parameter at the critical point

χ_H : Enthalpic contribution of the Flory-Huggins interaction parameter

χ_S : Entropic contribution of the Flory-Huggins interaction parameter

χ_{sc} : Flory-Huggins parameters measured by neutron scattering

χ_{surf} : Surface adsorption parameter

χ_s^H : Enthalpic contribution from χ_{surf}

ω : Angular frequency

STATEMENT OF COPYRIGHTS

The copyright of this thesis rests with the author. No quotation from it should be published without the author's prior written consent and information derived from it should be acknowledged.

ACKNOWLEDGEMENTS

During these last three years I had the opportunity to work amongst highly qualified professionals from academia and industry, live in two different countries, travel to more than 15 others and meet and receive support from a tremendous amount of individuals who, for some, have become dear friends. This PhD thesis has been an incredible adventure. My biggest worry is now forgetting to acknowledge some contributions.

First, I would like to thank my PhD supervisor, Dr Richard Thompson from Durham University, who is the best supervisor any PhD student could wish to have. I consider myself extremely lucky to have worked with you and am especially thankful for the time you allocated me when I was abroad and for the silly-but-refreshing drawings in my thesis' drafts.

I am grateful to the Marie Skłodowska-Curie Actions for funding my research work and to the European Commission in general. I thank all the members of the MICSED programme from Durham University: Prof John Evans, Dr AnnMarie O'Donoghue, Dr David Hodgson, Prof Andy Beeby and Dr Sharon Cooper with a special mention to my secondary supervisor Dr Buddhapriya Chakrabarti and to our secretary Ms Julie McLoughlin. I thank also the contributors to the MICSED project from the P&G side: Dr Euan Magennis, Dr Jean-Francois Bodet, Dr Stefano Scialla and especially Dr Torsten Lindner, Dr Jan Claußen and Dr Gabriela Schäfer for their collaboration regarding my project. I am grateful to the other MICSED researchers, Anna Stanczak, Niamh Ainsworth, Benjamin Devilliers and especially my theoretical counter-part, Salvatore Croce.

From Durham University, I am also thanking my team: Dr Stephen Boothroyd, Dr Vikki Bird, James Hart, Carl Reynolds, Ben Robertson, Igor Schneider and especially Rebecca Fong, Faye Henri and Arron Briddick for their precious help during the neutron beam times. I am grateful to Jos Tasche and Dr Mark Wilson for the interesting discussions and collaboration. I also thank Doug Carswell for helping me out with the DSC measurements and Jonathan Millican for the GPC analysis.

From Procter and Gamble, the list is also long. I will start by thanking Dr Mattias Schmidt and Dr Todd Mansfield for their interest. I would like to thank the whole Analytical team from

Schwalbach for welcoming me (Matthias, Thomas, Steffen, Lu, Xixi, Cornelia, Uwe, Birgit, Maik, Kristin, Antonio and Luigi), especially their section head, Dr Hans Martin Helbich for funding some of my travel and organising great Christmas events, Behzad Mohebbi for his help on the NMR Mouse, Christian Neu for training me on the rheometers, Ms Heike Krakowiak for letting me use the contact angle equipment and Mr Peter Weyand, from P&G Kronberg, for his help with additional DSC measurements. I also want to thank Dr Ludwig Busam and Dr Holger Beruda for their interest and consideration as well as the whole GMDSO department, for the training sessions, celebrations and team events. Then, I wish to thank my former team, the AGM upstream group, especially Juliane and Arsen for writing recommendations letters when I applied for this PhD, Lisa for helping me out with the microscope and with my German, Natasa for helping with lab paperwork and supplies, Szymon for reading my chapters and for all the data analysis with jmp and Azzurra for giving me shelter for a night when I was homeless. A very special thanks to Alicia for all the support and motherly advice. Many thanks to the P&G NDT team for organising an amazing ski trip to Austria.

From the Rutherford Appleton Laboratory, in Chilton nr Didcot, I want to thank Dr Nina-Juliane Steinke, Dr Maximilian Skoda, Dr Arwel Hughes and Dr Mario Campana, instruments owners (OFFSPEC, INTER and SURF) at ISIS for their help with the neutron reflectivity measurements. From Henkel, in Düsseldorf, I thank Dr Marc Hamm and Dr Andy Swain for allowing me to visit their facilities, present my work and perform tack-test measurements. I also thank Omar, for preparing the samples I needed. I am grateful to Ms Dina Otto, from Data Physics, in Stuttgart, for giving me a training day on surface energy measurements. Finally, I thank Dr Costantino Creton, from ESPCI Paris Tech, for giving me very valuable feedback on the adhesion-related part of my literature review.

From Durham, I am grateful to my friends Roberto Chinchilla for the great mental support, Nuria Polo-Perez for the Spanish-French tandems and Natasha Boulding for sweating the stress out together with me. I want to thank the volleyball team from Team Durham, the Durham climbing centre and the Tempest dance and fitness studio for keeping me strong and healthy. I also thank my French community, for reminding me what home is: first, my roommate, the amazing Sébastien Gilment but also Côme, Fiona (and Charles) Ponterubeo as well as the French-speaking Andrea Carletto and Katie Smart. A special mention to the delicious Lebanese restaurant, The Library and Vennels café for the most amazing chocolate fudge cake in town. Kept me going.

From Frankfurt, I am grateful to my 16-month-roommates Björn and Nadine without whom my German would never have progressed (from inexistent to pitiful). I thank the Eintracht Frankfurt Damen IV Volleyball Mannschaft, especially Dani, for being such a good friend, the Boulderwelt climbing centre and the coaches at the P&G Wellbeing centre. I thank my friends from P&G/Coty for the fun in Waxy's, Yours and other places in Frankfurt or around: Taryn, Amit, Christel, Konrad, Ksenija, Otto, Patrick, Ricardo, Deniz, Brian and many others. I also thank the young Benjamin Ruff, for reminding me of my university years and scarring me (almost) for life. Special thanks to Arsen, my bro' in law, for the BS Sitzungen at work and the evenings spent swearing on the balcony. Finally, I must thank my sun and stars, moon-of-my-life, overwhelming me by his *joie de vivre* and his delicious pizzas: Jean Philippe Couturier (should I say Dr?) for hearing (and echoing) the complaints of a poor PhD student.

A very special gratitude goes to all of my friends from home, who were with me for so many years: my 10-year old friends Cyril and Alice, and to the others, Pierre, Justine, Elena, Germain, Amélie and Thomas. I also wish to thank Arnaud (and Bernard) who supported me when I moved to England.

I thank my family, starting from my parents, Jocelyne and Marc Sabattié who tried their best to be supportive of my choices. I am grateful for the encouragements from my siblings, Aurélie and Clément, their respective partners, Yann and Aurélie and my aunt, Odile. I want to thank my grandparents Serge and Jacqueline for being so inspiring. I hope that Monique and Guy would be proud of me. Last but not least, thank you so much Szymon for having supported me in so many ways. I truly believe that I may not have managed all of that without you. I am immensely grateful for having met you and Laura on the way.

*“Das Volumen des Festkörpers wurde von Gott geschaffen,
seine Oberfläche aber wurde vom Teufel gemacht.”*

Wolfgang Pauli

A mes parents.

INTRODUCTION

This project is an Industrial European Doctorate funded by the Marie Curie Actions. It is part of the *Molecular Interaction in Complex Systems European Doctorate* (MICSED) programme, which is a partnership between Durham University and the Procter and Gamble Company (P&G). This particular funding gives the PhD candidate the opportunity to spend half of his/her time at the industrial partner's facilities. The work focused on the study of additive migration in complex polymer formulations relevant to P&G business areas, such as hot-melt adhesives for Baby and Feminine Care. Migration and stability issues are of fundamental interest to ensure appropriate shelf-life, performance and reducing costs.

Polymers are often mixed with other components in a formulation in order to achieve the desired properties for a specific application. Components of a polymer formulation are numerous and can be roughly classified as: a host polymer, solvents, inorganic particles – e.g. pigments, fillers – and organic additives – i.e. plasticisers and specialty additives (e.g. antimicrobial agents, antioxidants, fragrances). Understanding the mixing and stability behaviour of complex polymer formulations at surfaces and interfaces is of crucial importance in a wide range of technologies and applications such as coatings, membranes, adhesives, free films, composites or colloidal dispersions.

Even in the case of a simple mixture, for example, a binary polymer blend, the surface or interface composition is known to differ from the bulk. When smaller molecules are mixed with polymers, they tend to migrate and settle preferentially at the surface. A common illustration of this migration can be found in chocolate: when stored at too high a temperature, fatty acids separate from the bulk and form white spots at the surface.¹ At a microscopic scale, these spots present a fine flake structure, similar to flower petals which inspired the name of fat blooming.

The blooming phenomenon observed in chocolate can be more generally related to the surface segregation of organic additives in polymer formulations – i.e. preferential partitioning of additives at the surface. Such segregation is irreversible and can have a disastrous effect on the

Introduction

formulation due to a modification of its surface properties and/or structure. On the other hand, by controlling additive surface migration, designed surface functionalisation of materials could be achieved – e.g. lubrication, hydrophobicity, hydrophilicity, softness agents.

The aims of this work are therefore to understand which parameters are driving the surface segregation of additives and to quantify the extent of the additive partitioning in model formulations in order to predict and eventually control this phenomenon. Additionally, it is intended to evaluate the impact of the surface segregation on adhesion properties, as bulk and surface properties. The experimental data generated is also expected to support the validation of a segregation model, developed in parallel in the frame of two other PhDs, that use theoretical calculations based on the self-consistent field theory (SCFT) and statistical association fluid theory (SAFT- γ Mie) as well as molecular dynamics simulations.

To achieve these goals, this thesis is divided into 5 chapters.

In *Chapter 1: Literature review*, the project is situated among the published research. The main parameters influencing surface segregation of additives are hypothesised, based on the existing theories and literature. An important outcome of this review is that oligomer/polymer melts were rarely studied in the past which consolidates the relevance of this thesis.

In *Chapter 2: Experimental*, the materials and experimental techniques are introduced, including the analysis methods used in the frame of this project.

In *Chapter 3: Model systems*, simple model formulations are selected in order to experimentally evaluate the impact of the identified key-parameters. These model systems are based on oligomer/polymer binary blends. Initial experimental results are also presented to support the relevance of such a simplified formulation.

The *Chapters 4, 5 and 6* present the main results of this work, in light of the literature. To challenge the hypothesis regarding the parameters affecting surface segregation and gain insight on the phenomenon, several measurements were performed on the selected model formulations. *Chapter 4: Compatibility of oligomer/polymer mixtures* focuses on the impact of the identified parameters on blend compatibility. The compatibility between oligomer and polymer was systematically assessed by differential scanning calorimetry and completed, for some systems, by optical assessment of turbidity. *Chapter 5: Oligomer surface partitioning* is devoted to understanding the relationship between blend compatibility and partitioning of the

Introduction

oligomer at the surface and interface. One dimensional concentration profiles were measured by ion beam analysis and neutron reflectometry. These profiles were compared to the compatibility results to evaluate the relationship between bulk compatibility and surface segregation. These measurements also allowed the quantification of the thickness of the segregated layer. In *Chapter 6: Adhesive properties of oligomer/polymer mixtures*, the link between surface segregation at the nanoscale and adhesion properties at the macroscale was investigated. Surface energies were evaluated by contact angle measurements and the organisation of the oligomer at the surface was also characterised by optical microscopy and atomic force microscopy. Oscillatory rheology helped determine the effect of oligomer content on the bulk mechanical properties, which also impacts adhesion. The data obtained as part of this investigation are archived in the electronic archive DOI number [10.15128/r11544bp095](https://doi.org/10.15128/r11544bp095).

Finally, the *Conclusions of the thesis* are shared, followed by recommended areas of focus for future work. For example, this thesis is mainly focused on mixtures of amorphous polymers and apolar migrants but the results could be extended to polymers presenting low oligomer solubility regions such as glassy or crystalline domains.

Chapter 1: LITERATURE REVIEW

1.1 MISCIBILITY OF POLYMER BLENDS

1.1.1 THE FLORY-HUGGINS THEORY

1.1.1.1 Description of the Flory-Huggins solution theory

For many decades, polymers and their blends have been widely investigated in order to comprehend their structural and physical properties. In the early 40s, Kurt H. Meyer² studied the polymers in solution via a statistical approach. His work inspired Maurice L. Huggins and Paul J. Flory to develop what is now known as the Flory-Huggins (FH) theory.^{3,4,5,6} This theory, originally designed to describe the statistical thermodynamics of a polymer / solvent mixture, uses a lattice model (Figure 1-1) and assumes random mixing.

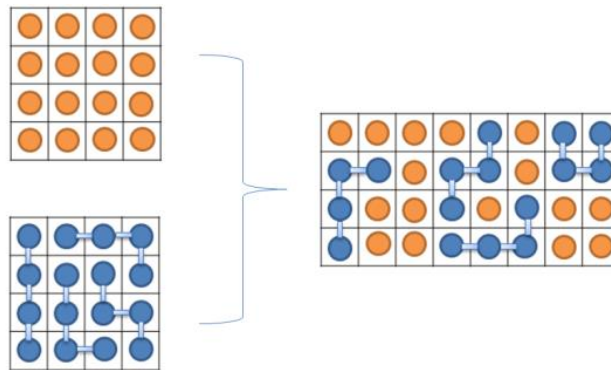


Figure 1-1: Illustration of the lattice model: molecules of solvent (orange) are mixed with polymer chains (blue).

The model accounts for the difference in molecular weight between the solvent and polymer molecules by setting a reference lattice volume v_0 (usually the molecular volume of one solvent molecule), and assuming that a polymer chain consists of connected segment of volume v_0 . In a first approximation the lattice volumes are equal for both repeat units. The repulsive interactions between the repeat units are described by the impossibility to have more than one polymer chain segment or solvent molecule per site and all the lattice sites are filled, implying that the materials and their mixtures are incompressible.

1.1.1.2 Flory-Huggins theory applied to polymer blends

The FH description can be generalised to the case of polymer blends, considering a mean-field approach. In the case of a binary polymer mixture, one can consider n_A molecules of polymer A with a degree of polymerisation N_A , mixed with n_B molecules of polymer B with a degree of polymerisation N_B . The volume fraction of A is $\varphi_A = \frac{n_A N_A}{n_A N_A + n_B N_B}$ and similarly, $\varphi_B = \frac{n_B N_B}{n_A N_A + n_B N_B}$.

The entropy of mixing ΔS_m is then given by equation (1.1). The entropy is assumed to be purely combinatorial and is calculated by enumerating the number of arrangements of the molecules on the lattice.⁷

$$\Delta S_m = -k \left(\frac{\varphi_A}{N_A} \ln \varphi_A + \frac{\varphi_B}{N_B} \ln \varphi_B \right) \quad (1.1)$$

with k the Boltzmann constant.

The enthalpy of mixing ΔH_m is the difference between the initial energy of the pure components E_0 and the energy of the mixed blend E_m . It is expressed at a given temperature T , assuming the mixture to be a regular solution.⁷

$$\begin{aligned} \Delta H_m &= E_m - E_0 \\ &= z \left(\frac{1}{2} \varepsilon_{AA} \varphi_A^2 + \frac{1}{2} \varepsilon_{BB} \varphi_B^2 + \frac{1}{2} \varepsilon_{AB} \varphi_A \varphi_B \right) - z \left(\frac{1}{2} \varepsilon_{AA} \varphi_A + \frac{1}{2} \varepsilon_{BB} \varphi_B \right) \\ &= kT \chi \varphi_A \varphi_B \quad (1.2) \end{aligned}$$

with ε_{ij} being the energy (in units of kT) associated with the attractive interaction between two neighbouring sites – polymer A/polymer A, polymer B/polymer B and polymer A/polymer B interactions –, z the lattice coordination number and χ the dimensionless Flory-Huggins interaction parameter. χ is function of the interaction energy characteristics of a given solvent-solute pair and is defined as follows.⁷

$$\chi = \frac{z \Delta \varepsilon_{AB}}{kT} \quad (1.3)$$

with $\Delta \varepsilon_{AB} = \varepsilon_{AB} - \frac{1}{2}(\varepsilon_{AA} + \varepsilon_{BB})$. This parameter typically gives the energy difference between two adjacent lattice sites when, in one site, a molecule of solvent A is exchanged with a segment of polymer B.

Assuming equal lattice volume v_0 , which is often fixed at 100 \AA^3 ,⁷ the Gibbs free energy of mixing per lattice site $\Delta G_{m,site}$ for a mixture of a polymer A with a polymer B can be deduced from the previous equations.⁸

$$\Delta G_{m,site} = \Delta H_m - T\Delta S_m = kT \left(\frac{\varphi_A}{N_A} \ln \varphi_A + \frac{\varphi_B}{N_B} \ln \varphi_B + \chi \varphi_A \varphi_B \right) \quad (1.4)$$

with k the Boltzmann constant, T the temperature, N_i is the number of repeat units of volume v_0 on a single chain of the polymer i , and χ the FH interaction parameter.

A more general expression for the free energy density of mixing per unit volume is:⁷

$$\Delta G_{m,volume} = kT \left(\frac{\varphi_A}{v_A N_A} \ln \varphi_A + \frac{\varphi_B}{v_B N_B} \ln \varphi_B + \frac{\chi \varphi_A \varphi_B}{\sqrt{v_A v_B}} \right) \quad (1.4')$$

for which v_A and v_B are the volumes of a repetitive unit of polymer A and B respectively and $v_0 = \sqrt{v_A v_B}$.

In the first instance, a negative value of ΔG_m implies that the polymers interact favourably and are therefore miscible. These favourable interactions can be for instance hydrogen bonding. A positive value of ΔG_m suggests that the polymers are rather incompatible.

It is notable in equation (1.4) that the degree of solubility of a binary polymer-polymer mixture depends on the temperature, concentration and molecular weights of the polymers. If the molecular weight of the polymers increases, the entropic term, driving mixing, is lowered – inversely proportional to the number of repeat units. Thus the chains become less likely to mix.

1.1.1.3 Phase diagrams from the FH theory

Phase diagrams can be obtained using classical thermodynamics. Assuming that χ is only dependent on the temperature T , the spinodal (limits of metastability) and binodal (equilibrium phase boundary between single phase and phase-separated region) curves can be calculated (Figure 1-2).

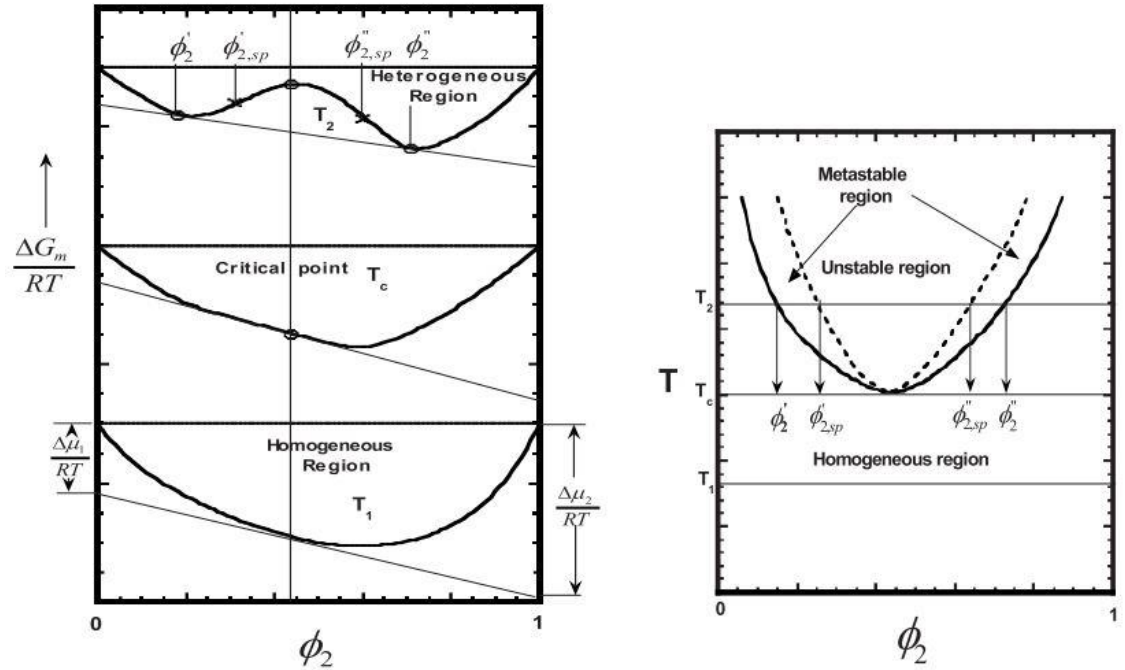


Figure 1-2: Left. Schematic showing the Gibbs free energy of mixing as a function of composition temperatures T_1 (1 phase region), T_c (critical point) and T_2 (2 phases region). Right. Corresponding phase diagram showing the binodal (outer, solid line) and spinodal (inner, dashed line) curves. Reprinted with permission from Lloyd M. Robeson, *Polymer blends: a comprehensive review*, Carl Hanser Verlag Munich, 2007.⁷

In a binary system, the binodal is the equilibrium state where the chemical potentials of each component in the two phases are equal. The chemical potential of species i is defined as:

$$\mu_i = \left[\frac{\partial G}{\partial n_i} \right]_{T,p,N_{j \neq i}} \quad (1.5)$$

with n_i the number of molecules of species i , T the absolute temperature, p the pressure and n_j the number of molecules of species j .

The binodal is therefore defined as⁷

$$\Delta\mu_1^a = \Delta\mu_1^b \quad \text{and} \quad \Delta\mu_2^a = \Delta\mu_2^b \quad (1.6)$$

where 1,2 are the two polymers and a,b the two phases.

Moreover, from (1.5),

$$\Delta\mu_i = \left[\frac{\partial \Delta G_m}{\partial n_i} \right]_{T,p} \quad (1.7)$$

and since

$$\left[\frac{\partial \Delta G_m}{\partial n_i} \right] = \left[\frac{\partial \Delta G_m}{\partial \varphi_i} \right] \left[\frac{\partial \varphi_i}{\partial n_i} \right] \quad (1.7')$$

the binodal curve is given by finding the common tangent to the $\Delta G_m(\varphi_i)$ curves at each different temperature T .

The spinodal curve is built by finding the inflection points of the same curves, when⁷

$$\left[\frac{\partial^2 \Delta G_m}{\partial \varphi_i^2} \right] = 0 \quad (1.8)$$

The critical value of the FH parameter χ_c at the critical composition φ_c is a value below which the polymers are miscible in all proportions. It corresponds to the point where the spinodal and the binodal curves meet, i.e. when

$$\left[\frac{\partial^2 \Delta G_m}{\partial \varphi_i^2} \right] = 0 \quad \text{and} \quad \left[\frac{\partial^3 \Delta G_m}{\partial \varphi_i^3} \right] = 0 \quad (1.9)$$

For a polymer/polymer asymmetric blend⁸

$$\chi_c = \frac{\sqrt{v_A v_B}}{2} \left(\frac{1}{\sqrt{v_A N_A}} + \frac{1}{\sqrt{v_B N_B}} \right)^2 \quad \text{and} \quad \varphi_c = \left(1 + \sqrt{\frac{v_A N_A}{v_B N_B}} \right)^{-1} \quad (1.10)$$

To predict the phase diagrams of various polymer blends, it is therefore crucial to know the evolution of the energy of mixing with composition. The attractive feature of the FH theory is that one needs knowledge of only a single parameter to describe the thermodynamics of any polymer blend, regardless the blend composition or the molecular weight of the components. However χ is difficult to measure experimentally and the hypotheses regarding its non-dependency are often challenged.⁹

1.1.1.4 The FH interaction parameter

The χ parameter depicts the chemical interactions between the repeat units of polymer A and B. Through a simple analysis of equation (1.4) and knowing the value of χ , one can easily calculate the miscibility behaviour of a polymer blend.

The first two terms of the equation (1.4) are related to the entropy of mixing ($-\Delta S_m$). These terms always favour mixing as ΔS_m is always positive, and therefore $-\Delta S_m$ is always negative. In the case of polymers, they are also small, due to the large degree of polymerisations N encountered.

Thus, a negative value of ΔG_m can be obtained only if χ is a negative or is a small positive number. A large and positive value of χ suggests that the system is rather immiscible.¹⁰

1.1.1.4.1 FH interaction parameter for polymer solutions

Semi-empirical techniques have been developed to calculate χ for polymer solutions, based on the Hildebrand-Schatchard theory of solutions and on the theory of intermolecular forces.¹¹ In this approach, the interaction parameter χ is divided into entropic and enthalpic contributions (χ_s and χ_H , respectively).

$$\chi = \chi_s + \chi_H \quad (1.11)$$

Or, alternatively^{12,13}

$$\chi = \chi_s + \frac{\chi_H}{T} \quad (1.11')$$

Huggins' derivation⁴ for the free energy of mixing predicts that the entropy parameter is $\chi_s = 1/z$, z being the number of neighbouring sites (or coordination number). However, the value of χ_s has been empirically found to have a value of approximately 0.3 to 0.4¹⁴ (0.34 is often used). The enthalpic parameter χ_H (as in equation (1.11)) is defined as

$$\chi_H = \frac{V_m}{kT} (\delta_A - \delta_B)^2 \quad (1.12)$$

where δ_A and δ_B are the Hildebrand solubility parameters of the pure components – these parameters can be divided into dispersive, polar and hydrogen bonding contributions¹⁵ – and V_m is the solvent molar volume. Sources of data for the solubility parameters are numerous and are tabulated for most of the industrially relevant polymers.¹⁶

1.1.1.4.2 The FH interaction parameter for polymer blends

The Hildebrand-Schatchard approach can also be applied to binary polymer melts. The solubility parameters are then defined for each type of polymer repeat unit. However, there is very little solubility parameter data reported in the literature for asymmetric blends and the results vary greatly.¹⁷

Experimentally, χ_{sc} can be defined as the interaction parameter measured for polymer blends by means of small-angle neutron scattering. The measured scattering profiles of single phase

polymer blends, which reflect the magnitude of concentration fluctuations are fit to theoretical predictions based on the random phase approximation introduced by De Gennes.¹⁸

The coherent small angle neutron scattering (SANS) intensity is linked to χ_{sc} through the following equation:

$$I(Q) = \left(\frac{b_1}{v_1} - \frac{b_2}{v_2}\right)^2 \frac{1}{v} \left[\frac{1}{N_1 \phi_1 P_1(Q)} + \frac{1}{N_2 \phi_2 P_2(Q)} - 2\chi_{sc} \right]^{-1} \quad (1.13)$$

with \mathbf{Q} the momentum transfer vector ($Q = 4\pi \sin(\vartheta)/\lambda$, with ϑ and λ the angle and wavelength of the incident neutron beam, as shown later in section 2.8), b_i the neutron scattering length contribution of the monomer i , v_i the volume of the monomer used to determine b_i , and $P_i(Q)$ the single chain form factor for species i , given by the Debye function

$$P_i(Q) = \frac{2}{(Q^2 R_{g,i}^2)^2} \left\{ \exp \left[-(QR_{g,i})^2 \right] + (QR_{g,i})^2 - 1 \right\} \quad (1.14)$$

where $R_{g,i}$ is the radius of gyration of a chain of species i and is related to the statistical segment length a_i of a Gaussian chain of type i by $R_{g,i} = a_i(N_i/6)^{1/2}$.

With this method, χ_{sc} can be approximated with an error less than 15 %.¹⁹ However when χ_{sc} depends on composition, χ_{sc} can be significantly different from the thermodynamic χ parameter. Additionally, characterising a unique binary polymer system requires investigation of a large range of compositions and temperatures, which represents a significant amount of experimental work. Developing predictive models to evaluate the interaction parameter is therefore of crucial interest for understanding the mixing behaviour of polymer blends in a more systematic way. It is also important to note that the random phase approximation accounts for the perturbations around Gaussian chains in a polymer melt. Oligomers do not behave like Gaussian chains, hence, this approach cannot be transferred to oligomer/polymer blends. Alternatively, one will prefer calculating the energy of mixing through Mie potential optimisations, which leads to a prediction of the compatibility behaviour.²⁰

1.1.1.5 Limitations of the Flory-Huggins theory

The FH theory, adopted in 1953, provides the basic understanding of the thermodynamic processes involved for polymer blends. Because of the simplicity of the equations, it has been widely applied by the scientific community. However, it has been found unable to predict and

describe accurately real systems. Equation (1.4) does not take into account the effects of the structure, degree of branching and interactions between the chains on the solubility.

This model is based on four assumptions (and therefore limitations): (i) the lattice is fully occupied, i.e. the volume before and after mixing is equal, no free space is gained due to mixing even if strong unfavourable interactions are formed, (ii) the long-range statistics of a polymer chain are ideal random walks, (iii) interaction between polymers are short-ranged and isotropic, (iv) local structure and packing do not restrict configurations, and entropy is not affected by the behaviour of local structures.

The χ parameter being inversely proportional to the temperature in this description, the theory can only describe upper critical solution temperature (UCST) systems – i.e. systems for which the phase separation happens on cooling – and not lower critical solution temperature (LCST) systems – i.e. phase separation happens on heating. This issue arises mainly because the FH theory ignores any volume change on mixing and considers only one enthalpic parameter.

Shibayama *et al.* also found in their case that χ was dependent on composition, again due to the lack of description of the compressibility and thermal expansion of the system.²¹ The composition dependence has been observed by others since,^{22,23} and more recently a component molecular weight dependence was experimentally evidenced.¹⁹ Such dependencies could largely undermine the predictive power of the theory in the case of oligomer/polymer blends.

1.1.2 CASE OF OLIGOMER/POLYMER MIXTURES

1.1.2.1 Applying FH to oligomer/polymer mixtures

Applying the Flory-Huggins theory to oligomer/polymer mixture is not trivial. One might expect the assumptions (i) and (iv) of the theory to be less valid due to the larger number of chain-ends introduced to the system by the oligomer. Indeed, the compressibility of the mixed system is increased with respect to a purely polymeric blend.²⁴

It has been shown experimentally that mixtures of oligomers and polymers have various miscibility behaviours that are not predictable with FH. For example, Fujita *et al.* led a comprehensive study on the miscibility between natural rubber (mainly cis-polyisoprene) with several types of industrial additive, called tackifiers, of molecular weight 700-4000 g.mol⁻¹: 17

prepared from rosin and terpenes²⁵ and 12 prepared from petroleum resins²⁶ – i.e. oligomers of aliphatic and aromatic hydrocarbons. Four types of phase diagrams were obtained between 20 and 120 °C: fully miscible, LCST, UCST and fully immiscible.

However, they noted that the miscible range of a blend tends to become smaller as the molecular weight of the additive is increased,^{25,26} which is expected from equation (1.4). As a first hypothesis, one can also infer from equation (1.10) that the critical concentration φ_c should be shifted towards the higher oligomer concentration as the ratio N_A/N_B tends to 0.

Hence, the FH theory is less well established in the case of relatively small molecules dispersed in host polymer matrices than for polymer blends.

1.1.2.2 Differences with polymer blends

1.1.2.2.1 Fluctuation effects

In binary mixtures of simple fluids, it is empirically known that the mean-field descriptions are not adequate close to the critical point, due to local concentration fluctuations. For polymer blends, the mean-field approach generates a good description of the system, even close to the critical point, because, for long chains, the average field experienced by a coil is generated by a large number of *A* and *B* polymer chains present in the coil volume. However, those effects should be kept in mind for the case of a mixture of components of large molecular weight disparity.

1.1.2.2.2 Excluded volume effects

In the case of a polymer chain in a good solvent, it is considered that the chain is best described by a self-avoiding walk, in which the segments cannot overlap (volume exclusion), leading to chain expansion. Theory has shown that for such a structure the radius of gyration R_g of the polymer chain is proportional to $N^{3/5}$ (Flory radius).^{5,27}

Consider a polymer solution *P* in osmotic pressure with a pure solvent *P'* on both sides of a semi-permeable membrane. One can write that the chemical potential of the polymer solution $\mu_A(P, T)$ equals the standard chemical potential of the pure solvent $\mu_A^0(P', T)$. From equation (1.7), and knowing the definition of the osmotic pressure Π , it follows that

$$\frac{\partial \Delta G_m}{\partial n_A} = \mu_A(P, T) - \mu_A^0(P, T) = \mu_A^0(P', T) - \mu_A^0(P, T) = -\Pi V_m \quad (1.15)$$

with V_m the molar volume and $\mu_1^0(P, T)$ the standard chemical potential of the polymer solution.

In the case of a polymer solution, one can consider a polymer presenting $N_B = N$ repetitive units in a solvent ($N_A = 1$) and note $\varphi = \varphi_B$. The partial differentiation of ΔG_m with respect to n_A at constant T gives the equation (1.15'). Details about the calculation can be found elsewhere.²⁸

$$\frac{\partial \Delta G_m}{\partial n_A} = kT \left[\ln(1 - \varphi) + \left(1 - \frac{1}{N}\right) \varphi + \chi \varphi^2 \right] \quad (1.15')$$

Combining equation (1.15) and (1.15'), with the volume of one lattice site is $V_m = a^3$ one obtains:

$$a^3 \frac{\Pi}{kT} = \frac{\varphi}{N} - \ln(1 - \varphi) - \varphi - \chi \varphi^2 \quad (1.16)$$

For a dilute solution ($\varphi \ll 1$) the logarithm can be expanded in Taylor series which leads to the virial expansion of the osmotic pressure, usually cut-off after the second term:

$$\frac{\Pi}{kT} = \frac{c}{N} + \frac{1}{2} a^3 (1 - 2\chi) c^2 \quad (1.16')$$

with $c = \varphi/a^3 = \varphi/v_0$.

Hence, as reported by several workers^{29,30}, the second coefficient of equation (1.16') is the half of the excluded volume parameter, v , which in this case is expressed as

$$v = a^3 (1 - 2\chi) \quad (1.17)$$

For a mixture where $N_A > 1$ the appropriate expression of v is

$$v = a^3 \left(\frac{1}{N_A} - 2\chi \right) \quad (1.17')$$

In polymer melts, the chain expansion is compensated by the forces exerted by neighbouring chains. Therefore, in such systems, the chains are well described by Gaussian coil models with a radius of gyration proportional to $N^{1/2}$ (random walk). The effect of the excluded volume is to swell the polymer chain from the random walk to the self-avoiding walk behaviour.³¹ The mean-field theory, which supposes that all polymer chain segments experience, on average, the same force field, is expected to be valid only when the excluded parameter v is small.

For simplicity, one can consider the case of an athermal blend where $\chi = 0$. Then $v = a^3/N_A$. The excluded volume contribution to the free energy for a Gaussian polymer coil at equilibrium scales as³¹

$$kTv \frac{N_B^2}{2R_g^3} \sim kT \frac{1}{2} \frac{vN_B^{1/2}}{a^3} = kT \frac{1}{2} \frac{N_B^{1/2}}{N_A} \quad (1.18)$$

Comparing the magnitude of this term for various values of N_A , one can conclude that

- for $N_A \sim N_B$ the contribution is proportional to $1/N_B^{1/2}$ and is therefore negligible
- for $N_A < N_B^{1/2}$ the contribution of the excluded volume is however significant

Thus, excluded volume effect can be significant and should be considered for mixtures with large molecular weight disparities such as the oligomer / polymer blends of interest in this thesis. As the consequence, the mean-field theory might not properly describe them.

1.1.3 ALTERNATIVES TO THE MEAN-FIELD FH THEORY

Several solutions have been suggested to deal with the lack of predictive capability of the FH theory. An early adaptation was made by Flory, who allowed χ to take complex temperature dependence.¹⁰ In the original theory, the entropy of mixing was assumed to be purely combinatorial, but it has been proved that non-combinatorial contributions are also significant in polymer systems. These are known as free volume effects, equation of state effects, and packing effects. The two main alternative models developed are the hole-filling^{15, 32} and the lattice fluid³³ theories which try to take into account the volume modification due to mixing by including holes in the lattice and modifying the equations of state formalism. However these models are more often used for polymers in solution. The Born-Green-Yvon theory has been successfully used by Lipson *et al.* to model polymer blends.³⁴⁻³⁶ This model is a more sophisticated lattice theory which allows sites to be vacant and is more applicable to oligomer/polymer binary mixtures.

Higgins *et al.* suggested that there is a temperature and concentration independent parameter that should be a more characteristic indicator of blend behaviour than χ .³⁶ This team later developed an interesting theory which shows a better predictive capability than the FH theory: the locally correlated lattice (LCL) theory.⁹ This approach is designed to describe polymer blends but might be extended to oligomer/polymer mixtures. It includes the effects of compressibility

and non-random mixing and presents the general ability to model both the mixture properties and the corresponding properties of the pure components. The theory is based on an integral equation approach wherein segment-segment (pair) distributions are formulated in terms of their corresponding derivatives (with respect to separation distance) and thus are related to the average force between the segments. The solutions for these site-site distributions allow calculation of the system's internal energy U and from this result, obtain all the equations of state. It has been demonstrated that this theory is able to predict quite precisely thermodynamic quantities – phase diagrams, evolution of compressibility with temperature, pressure and molecular weight dependence of the UCST, etc.— and to probe the nature of the shift in phase boundaries caused by deuteration of one component in the blend.

1.2 POLYMER BLENDS AT SURFACES

1.2.1 POLYMER CHAIN PROPERTIES AT SURFACES

The presence of a surface (or hard wall) can perturb the bulk properties of a polymer melt. These perturbations are of three forms: the chain conformation is altered from the bulk Gaussian chain (i), the chain-ends are partitioned at the surface (ii) and the density is decreased in the transition region (iii).

- (i) The conformation of polymer chains in the vicinity of a hard wall was investigated by Monte Carlo simulations in order to find deviation from the chain conformation in the bulk³⁷ – i.e isotropic Gaussian chain of radius of gyration R_g . The structure of the polymer close to the wall is driven by the competition between loss in conformational entropy and the packing constraints exerted by the chains further away in the bulk. This leads to an increase of the monomer (and chain-end monomer) density at the hard wall. The chains segments are preferentially orientated parallel to the wall and the polymer molecule is altered in its spherical conformation into an ellipsoidal shape. When located near a surface or a non-interacting wall, the bulk chain dimension of $2R_g$ is distributed over a distance of about one radius of gyration R_g of the chain, which is the largest length scale characterising the extent of the interfacial region.³⁷ However this phenomenon was found to happen experimentally only for ultrathin films (thinner than $6R_g$).³⁸

- (ii) It has been well established through theoretical considerations,^{39, 40} simulations^{41, 42} and neutron reflectivity (NR) experiments⁴³ that chain-ends from a region of about two polymer segment lengths a will be preferentially enriched at the surface or non-interacting wall, in a layer of thickness d (~ 1 -2 nm). This phenomenon can be explained by the higher conformational entropy of chain-ends at surfaces which minimises the system energy – i.e. a chain-end is connected only at one side, therefore it can explore the surface more freely. The chain-end segregation effect is widely utilised for surface functionalisation using bottlebrush polymers.^{44,45}
- (iii) The modification of the chain symmetry and the orientation of the chain-ends at the surface reduces the number of entanglements locally.⁴⁶ Therefore, the chain mobility is increased and the polymer density is reduced at the surface.⁴⁷

The presence of a surface disrupts the chain bulk properties even in the case of a single component polymer melt. In the next part, the effect of a surface on a binary mixture of two polymers is investigated.

1.2.2 SYMMETRIC POLYMER BLENDS AT SURFACES

1.2.2.1 Effect of surface energy disparity

In the case of a two-component symmetric polymer blend – i.e. similar molecular weight – the surface is expected to be enriched in the component of lower surface energy. The concentration profile of a d-PS / h-PS blend was studied experimentally by Jones *et al.* by NR⁴⁸ and then by Zhao *et al.* by secondary ion mass spectrometry (SIMS) and time of flight forward recoil spectrometry (TOF-FRES).⁴⁹ In both cases, the small difference in polarisability between the C-H and C-D bond is shown to lower the surface energy of the deuterated PS and causes the appearance of a surface excess with a length scale for the decay set by the size of the polymer Gaussian chain (100s of Å).

Surface segregation phenomena are often monitored via deuterium labelling of one of the species. The effect of deuteration on χ was assumed to be negligible prior to 1980. However, Buckingham and Hentschel⁵⁰ calculated that there exist a small change in molar specific volume between deuterated and protonated polymer molecules which corresponds to an estimated weakly unfavourable (positive) χ with a value of about 10^{-3} for $v_0 = 100 \text{ \AA}^3$. They concluded that isotopic blends should phase separate at modest degrees of polymerisation ($N \sim 10^3$).

Experimental proof of this phenomenon was performed by Bates *et al.*⁵¹ Graessley *et al.* found similar values (up to 6×10^{-4})⁵² which are sufficient to induce surface segregation of the deuterated component for the case of a symmetric blend but is usually considered as a negligible variation if either component is of low molecular weight.⁵³

Hariharan *et al.*⁵⁴ modelled the influence of energetic factors on the surface segregation of polymer blends. They studied a binary polymer mixture in contact with a hard surface. They modelled this system on a quasi-crystalline lattice in the mean-field approximation of Scheutjens and Fleer.⁵⁵ An adsorption energy parameter χ_{surf} , based on the principle of the Flory-Huggins interaction parameter can be defined. It corresponds to the adsorption energy difference between the segments of the two polymers and defines which type of chain has a preference for the surface.

$$\chi_{surf} = -\frac{u_A - u_B}{kT} = \frac{1}{kT} \left[(\varepsilon_{AS} - \varepsilon_{BS}) - \frac{1}{2}(\varepsilon_{AA} - \varepsilon_{BB}) \right] \quad (1.19)$$

with u_i the adsorption energy of component i to the surface relative to its bulk interaction and ε_{ij} the interaction energy of a segment of the polymer i with the surface s or the polymer j .

From this study they concluded that the surface segregation is driven mainly by the surface energy difference χ_{surf} when systems are far from their bulk critical points. In this situation, the surface behaviour is almost unaffected by the value of the bulk compatibility. However, the bulk compatibility plays a significant role in determining the interfacial composition when the systems are close to their critical point. Kokkinos and Kosmas also showed that surface enrichment of one of the components is enhanced when χ_{surf} increases and reaches its largest value near the coexistence curve of the corresponding phase diagram of the blend.⁵⁶

Interestingly, at small values of χ_{surf} , the polymer segments were found lying mainly parallel to the surface. However, at high values of χ_{surf} , the depleted compound had the tendency to be oriented perpendicular to the surface. In addition, these polymer chains showed a stronger partitioning of their end-segments to the surface than its middle ones,⁵⁴ which is consistent with the behaviour of a polymer chain close to a surface.

1.2.2.2 Influence of the substrate

Krausch *et al.*⁵⁷ monitored the phase separation of thin films of poly(ethylene propylene) (PEP). Mixtures of hPEP and dPEP ($N_h = N_d = 2286$) were studied after quenching, in the two-phase

region. The films were spun cast on a silicon wafer from a toluene solution and annealed under vacuum at 48 °C. The glass transition temperature (T_g) of the PEP being -56 °C, the samples were analysed immediately after annealing or stored into liquid nitrogen to stop the phase separation. Figure 1-3 illustrates the difference in composition profiles, obtained by ion beam analysis, when the silicon wafer is covered with an organic monolayer prior to film deposition.

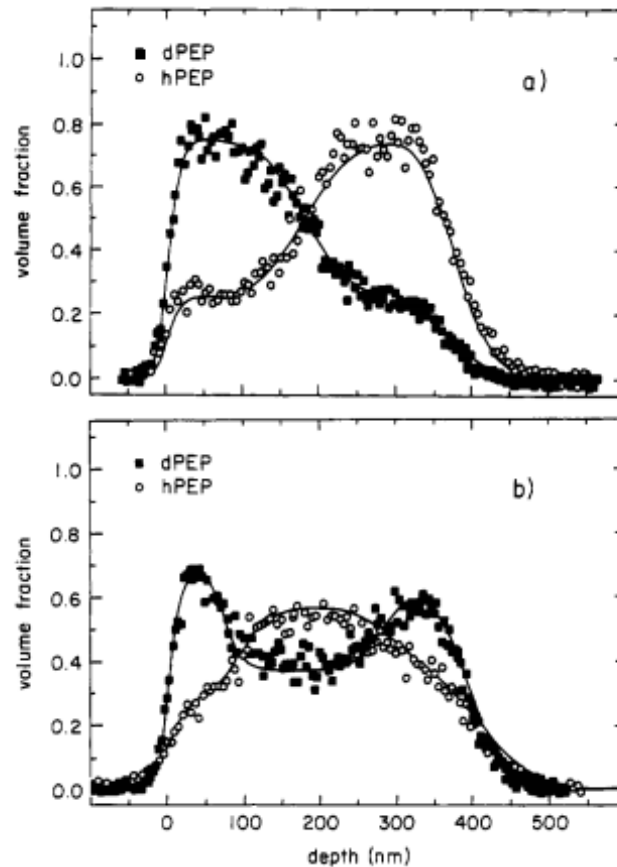


Figure 1-3: Volume fraction vs depth profiles for dPEP (squares) and hPEP (open circles) as determined by FRES. The films were annealed for 116 h at 321 K. a) Si substrate b) Si substrate covered with an organic layer. Reprinted with permission from Krausch et al., *Macromolecules*, 26 (21), 5566–5571. Copyright 1993 American Chemical Society.

In the case of the non-treated substrate, the deuterated compound is surface segregated and positioned at the air surface, due to its lower surface energy. In the case of the treated silica, the compound is positioned at both the air surface and the interface with the substrate. This leads to the conclusion that hPEP interacts more favourably with the silica interface than dPEP. One can here note that PEP is equivalent to hydrogenated polyisopene (hPI), described in 2.1 and used in the compatibility study in Chapter 4.

1.2.3 ASYMMETRIC POLYMER BLENDS AT SURFACES

In the frame of this project, the interest focuses mainly on mixtures of organic additives with host polymers. The degree of polymerisation (DP) ratio between polymer and oligomer is generally of about a thousand. Very few research groups looked into the segregation behaviour of such disparate systems.

1.2.3.1 Athermal asymmetric blend

Hariharan *et al.*⁵⁸ developed a lattice model for the surface segregation of polymer chains due to molecular weight effects. They considered an athermal polymer blend with a bimodal distribution in the vicinity of a neutral surface – i.e. the surface has the same energetic interaction with any segment of the two different chain length species comprising the bimodal melt. Therefore there is no difference in surface energy between the two chain distributions: only the entropic contribution is investigated.

From Hariharan *et al.*'s purely entropic model, the shorter chains in the system were found to partition preferentially to a neutral “hard” surface. This effect is enhanced when the disparity between the two distributions is increased. The suggested surface enhancement of the smaller chains due to entropic effects is small (approximately 1 vol%). The one dimensional concentration profile for the short chains was described by a hyperbolic tangent functional form with a single variable: the correlation length τ in the system that represents the width of the interface. From their results, the lower the amount of short chains, the lower the correlation length. This correlation length depends on the radii of gyration $R_{g,i}$ of the two chain length polymers and on their compositions in the bulk $\varphi_{\infty,j}$.⁵⁸

$$\tau^{-2} = \varphi_{\infty,2}R_{g,1}^{-2} + \varphi_{\infty,1}R_{g,2}^{-2} \quad (1.20)$$

Relation (1.20) also suggests that for a system with infinitesimal amounts of short (alternatively, long) chains in the melt, the interfacial decay is described by a correlation length of the order of the radius of gyration of the shorter (alternatively, longer) chains.⁵⁸

This work spanned only DP ratios between 16 and 100 and suggested that the segregation is enhanced when the disparity is increased. One might then expect that for a DP ratio of 500-1000 (typical of an oligomer/polymer blend) the entropic contribution would be more significant.

Surface segregation can be measured only if one of the components of the blend is differentiated from the other. This is generally done by deuterium labelling. The modification of the C-H bonds into C-D bonds induces a change in the interactions between the species and therefore the addition of an energetic factor in the system which usually implies the surface segregation of the deuterated chains (as discussed previously). Hence, the sole contribution of the pure entropic factors cannot be readily measured experimentally.

1.2.3.2 Isotopic asymmetric blend

In a more recent study Hariharan *et al.*⁵³ studied asymmetric blends by NR, where one of the polymer was deuterated. The surface segregation of hPS/dPS blends was proved to be controlled by the disparity in molecular weights: if the deuterated PS chains were approximately 10 times longer than the hydrogenated PS chains, the low molecular weight polymer will surface segregate (even if the deuteration should give to the high molecular weight PS segments a surface preference). For different polymers (different H/D to C ratio), this number can be different but the same partitioning behaviour is observed.⁵⁹

The original mean-field lattice theory for polymer blends near a “hard neutral surface” predicts that the component with the lowest surface energy will always partition to the surface, independently from the DP of the two polymers. The apparent chain length dependence of χ_{surf} can be explained considering that modelling the air surface as a hard, impenetrable barrier is equivalent to assuming a Heaviside step density gradient at the surface. Hence in the case of a mixture of molecules of different sizes, one has to consider the difference in surface tension between the two components caused by the differences in density gradients. χ_{surf} , defined in equation (1.19), can be re-written for an asymmetric blend:

$$\chi_{surf} = \chi_S^H + \Delta\left(\frac{\gamma A}{kT}\right) \quad (1.19')$$

with γ the surface tension, A the area occupied by one statistical segment of the polymer chain and χ_S^H the enthalpic contribution obtained from equation (1.19).

This second term can be expanded (see ref ⁵³) to give the expression (1.21), with C_2 the system specific constant and r_1 and r_2 the chain lengths of the blend components.

$$\Delta\frac{\gamma A}{kT} = C_2 \times \left(\frac{1}{r_1} - \frac{1}{r_2}\right) \quad (1.21)$$

From equations (1.19') and (1.21), one can see that for symmetric, high molecular weight polymer blends, χ_{surf} is purely enthalpic. However, for an asymmetric blend, the presence of short chains creates a density gradient at the surface; this entropic effect balances the enthalpic contribution. Those results show that the free-volume effect has to be taken into account in determining the behaviour near the free surface by adding non interacting lattice sites in the model. Moreover, modelling these systems as an incompressible blend near a hard surface might lead to incorrect predictions of surface segregation.

Therefore, in light of these results, one can expect the oligomer to surface segregate, as the molecular weight difference between polymer and oligomer is large enough. It seems however difficult to predict which of the enthalpic or entropic contribution will be predominant for a specific polymer/oligomer mixture. Walton and Mayes⁶⁰ and more recently Minnikanti and Archer⁶¹ showed that there exists a critical molecular weight at which an energetically unfavourable branched polymer is always enriched at the surface of a linear host. This critical molecular weight depends on characteristics of the branched molecule (number of chain-ends, number of branch points, integrated force of attraction of branched and end segments towards the surface) and on characteristics of the linear host polymer (degree of polymerisation, integrated strength of attraction of the ends towards the surface). It is also influenced by the difference in potentials acting on the midsections of branched species and the linear polymer host due to loss of coordination number at the surface.⁶¹ However, most of these parameters – i.e. strengths of attraction – are not directly accessible experimentally and need to be estimated theoretically.

1.2.4 SHAPE OF THE CONCENTRATION PROFILES

The surface composition of a mixed condensed phase at the surface differs from the composition observed in the bulk. In the presence of a difference in surface energy, the system will automatically reorganise to lower its total free energy by placing at the surface the component of lower surface energy.⁶² In the absence of any discernible difference in surface energy, the lower molecular weight component is enriched at the surface. It is not easy to assess which of those two contributions will be predominant and, in certain cases, they could compensate each other. The extent of surface segregation is further augmented by reducing the compatibility of the components.^{63,64}

- In the one-phase regime, a surface excess (or enrichment) layer (SEL) is formed, grows and stabilises to an equilibrium value (proportional to the critical adsorption).^{62, 65} The decay length can persist to depths of hundreds of Ångstroms as suggested by equation (1.20).
- In the two-phase regime, the SEL initially formed is unstable: it breaks into droplets of finite contact angle for partial wetting or grows indefinitely for total wetting.⁶⁴

These conclusions are mainly based on the classical work from Cahn, who suggested in 1977 that in a two-phase mixture of fluids near their critical point and in contact with a third phase, two critical points should be considered: a surface critical point and a bulk critical point.⁶⁶ A first order transition between perfect (or total) wetting and partial wetting exists in the two-phase region of the phase diagram and extends into the single phase region, separating SELs of low and high adsorption, as shown in Figure 1-4. Cahn evidenced that for *any* binary mixture exposed to a surface and close to its critical point, perfect wetting occurs and that the wetting layer should be infinitely thick in an infinite system.⁶⁶ In light of this work, it appears of crucial interest to know the bulk mixing behaviour of the blend.

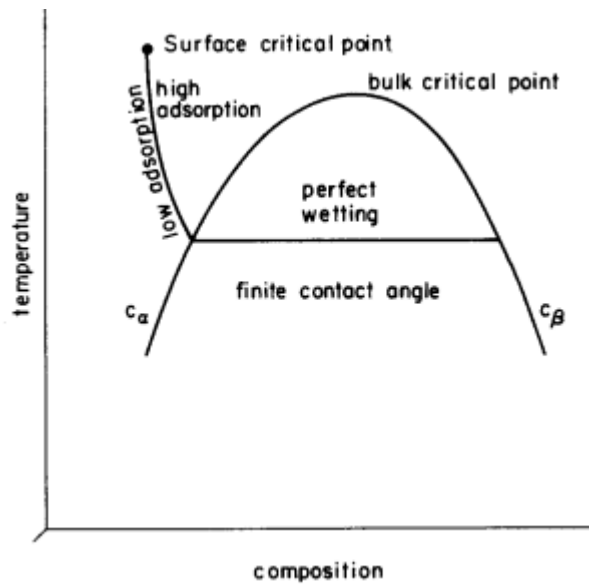


Figure 1-4: The properties of the surface of a binary mixture as a function of the temperature and the concentration can be mapped on a phase diagram. Reprinted with permission from, Cahn, J. W., *The Journal of Chemical Physics*, 66, 3667. Copyright 1977 American Institute of Physics.

1.2.4.1 Concentration profiles in the one-phase regime

Two main theories have been developed to describe the shape of the SEL with depth z in the one-phase regime.⁵⁹

The Schmidt-Binder (SB) theory⁶⁷ is based on the mean-field theory and relies on the minimisation of the excess surface free energy per lattice site, F_s . From equation (1.22), one can extract the whole composition profile of the component of interest, $\varphi = f(z)$, expressed as an exponential decay (equation (1.23)).

$$\frac{F_s(\varphi(z))}{kT} = f_s + \int_0^\infty dz \left[\Delta G(\varphi) - \Delta\mu\varphi + \frac{a^2}{36\varphi(1-\varphi)} \left(\frac{d\varphi}{dz} \right)^2 \right] \quad (1.22)$$

with ΔG the Gibbs free energy expressed in equation (1.4), a the statistical segment length of the polymer chain, $\Delta\mu = \frac{\delta G}{\delta\varphi}$, f_s the bare surface energy depending on the concentration at the surface φ_1 and given by $f_s = -\mu_1\varphi_1 - \frac{1}{2}g\varphi_1^2$, μ_1 describing the chemical potential favouring one component at the surface and g accounting for the missing interactions of segments at the surface.

$$\varphi(z) = \varphi_\infty + (\varphi_1 - \varphi_\infty) \exp\left(\frac{-z}{\xi}\right) \quad (1.23)$$

$$\xi = \frac{a}{6} \left[\frac{\varphi_\infty}{2N_A} + \frac{1 - \varphi_\infty}{2N_B} - \chi\varphi_\infty(1 - \varphi_\infty) \right]^{-1/2} \quad (1.24)$$

where φ_∞ is the concentration far away from the surface – i.e. in the bulk – and ξ is the decay length depending on the FH χ parameter as according to equation (1.24).

The Gibbs adsorption equation (GAE) (1.25) is the surface equivalence of the Gibbs-Duhem equation:

$$d\gamma = -\sum_i \Gamma_i d\mu_i \quad (1.25)$$

where γ is the surface energy, Γ_i is the molecular surface excess of species i and μ_i is the chemical potential per molecule i . Combining this expression with NR data, one can extrapolate a value for the surface energy difference between the pure components without requiring a detailed description of the segregation profiles, such as for SB. For the full description of the method see ref.⁵⁹

Norton *et al.* used the above theories to characterise the segregation to a free surface of hydrogenated and deuterated poly(ethylenepropylene) (PEP) symmetric blends.⁵⁹ The profiles predicted by SB theory decay exponentially with depth whereas the experimental composition profiles showed a layer of nearly constant dPEP concentration, over a distance about half the correlation length ξ , before approaching the SB mean-field theory shape (Figure 1-5). Hence, Norton *et al.* decided to place more reliance on the GAE method since it is less model dependent. It was extracted from this method that the surface enrichment is driven by a small surface energy difference between hydrogenated and deuterated PEP ($\sim 0.21 \text{ mJ.m}^{-2}$).

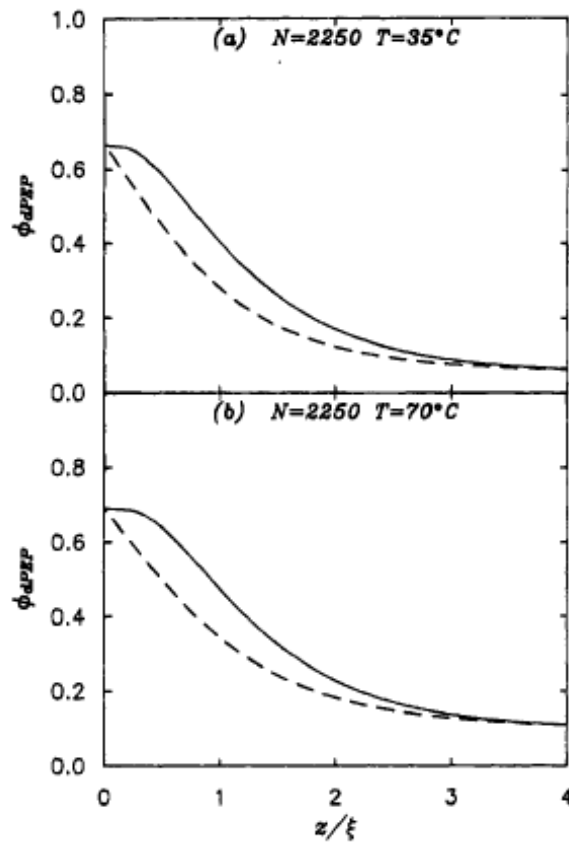


Figure 1-5: Measured composition profiles (solid lines) by NR scaled by the bulk correlation length ξ . Dashed lines are computed with the SB theory. Reprinted with permission from Norton *et al.*, *Macromolecules*, 28, 8621-8628. Copyright 1995 American Chemical Society.

Models dependent on the FH mean-field theory such as SB are based on assumptions including incompressibility, ideal random walk and isotropy (see 1.1.1.5). As discussed in 1.1.2 and 1.2.1, the discrepancy between theory and experiment for the description of polymer blends in the vicinity of hard walls might be explained by fluctuations in concentration, density and polymer chain conformation which are directly challenging these assumptions.

1.2.4.2 Concentration profiles in the two-phase regime

In the two-phase regime, the SEL is not stable and a phase separation of the blend into two phases of different concentration is expected.

Wang *et al.*⁶⁸ investigated the early-stage surface compositional enrichment in a two-phase regime polymer blend, constituted of deuterated poly(methyl methacrylate) (PMMA) ($M_w = 90 \text{ kg}\cdot\text{mol}^{-1}$, PD = 1.06, $T_g \sim 120 \text{ }^\circ\text{C}$) and hydrogenated poly(styrene-ran-acrylonitrile) (SAN) (33 % (w.w) acrylonitrile, $M_w = 124 \text{ kg}\cdot\text{mol}^{-1}$, PD = 2.24, $T_g \sim 114 \text{ }^\circ\text{C}$). Films of dPMMA-SAN 50-50 by mass were characterised by forward recoil spectrometry (FRES or also called ERDA) and atomic force microscopy (AFM).

Three stages of phase evolution were identified. During the early stage, dPMMA rich wetting layers grow rapidly at the air/polymer and polymer/substrate interfaces. An increase in the surface roughness is observed as well as a layering. During the intermediate stage, the wetting layer spreads, thins and dPMMA rich domains grow in the SAN rich middle layer of the film. During the late stage, capillary fluctuation cause spontaneous rupturing of the middle layer resulting in an interconnected 2D network which eventually coarsens into isolated SAN rich droplets encapsulated by thick dPMMA rich wetting layer. From the interpretation of the AFM pictures they suggested a three-stage model for thin film phase separation and symmetric wetting (Figure 1-6).

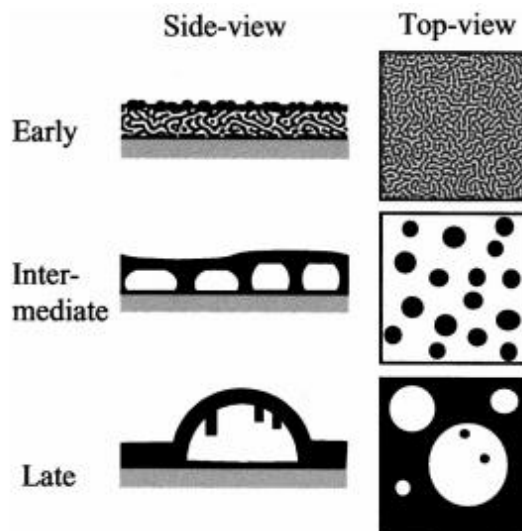


Figure 1-6: Three-stage model. The dark and light regions represent the dPMMA rich and SAN rich phases, respectively. Reprinted with permission from Wang *et al.*, *Journal of Chemical Physics*, 113, 10386-10397. Copyright 2000 AIP Publishing LLC.

1.2.5 KINETIC CONSIDERATIONS

Neutron reflectivity (NR) has been widely used to characterise polymer thin films and is an ideal technique for studying polymer surfaces and interfaces. The measurement time of a whole NR data set takes typically 1-2 hours, depending on the instrument and the neutron source. Therefore, the question of the diffusion speed of small molecules in polymers has to be raised to justify assumptions made about the equilibrium state of the samples.

1.2.5.1 Diffusion classes

Diffusion processes are usually split into three classes: Case I or “Fickian” diffusion, Case II diffusion and “non-Fickian” or anomalous diffusion. Experimentally, the Fickian systems (Case I) are characterised by a dependence of the relative rate of diffusion on $t^{1/2}$, Case II systems by a dependence on t and non-Fickian ones by a dependence on t^n with n comprised between $\frac{1}{2}$ and 1.⁶⁹ Fickian behaviour is often observed for compatible polymers above their T_g and is common for rubbers. For glassy amorphous polymers, Case II behaviour is often observed.⁶⁹ However, some other diffusion characteristics have been encountered in the literature such as a double Fickian diffusion for the case of erucamide diffusion in a matrix of i-PP (semi-crystalline polymer).⁷⁰

1.2.5.2 Oligomer/polymer inter-diffusion

Bucknall *et al.* have developed a very interesting real-time measurement to measure front velocities using NR.^{71,72,69,73} Because of the very long NR measurement time, it can be very difficult to measure any kinetic effect for polymers blends where one or more of the components has a T_g close to room temperature (RT). This includes of course the case of the oligomers/polymer blends. The technique allows collecting a limited reflectivity profile within a few minutes. They used the fact that at each fixed angle, a full reflectivity profile is registered over a limited momentum transfer Q range. By moving the Q window towards lower angles with increasing time, the full diffusion process can be followed.

With this technique, they studied the penetrant behaviour of phthalates plasticisers into thin films of dPMMA: DINP ($M = 418.6 \text{ g}\cdot\text{mol}^{-1}$) and DOP ($M = 390.5 \text{ g}\cdot\text{mol}^{-1}$).⁷¹ In the case of DINP and DOP, they were able to demonstrate the presence of three penetration phases: an induction period of several minutes, followed by a linear growth rate of the dPMMA layer thickness, which is characteristic from Case II diffusion behaviour and finally a much slower linear diffusion rate.

During the induction period, the thickness of the dPMMA layer remains constant, but the interfacial width changes. It is assumed that this corresponds to the establishment of a gel layer (approximately 10-12 nm) between the bulk dPMMA and the plasticiser. In this layer, the plasticiser concentration is high enough to plasticise the polymer matrix and so, the diffusion of plasticiser is very fast. In the initial diffusion phase the diffusion front velocities were $(6.6 \pm 0.8) \times 10^{-12}$ and $(2.8 \pm 0.2) \times 10^{-11}$ m/s for the DINP and DOP respectively. In the second phase, the diffusion front velocities were $(1.7 \pm 0.4) \times 10^{-12}$ and $(8 \pm 5) \times 10^{-13}$ m/s for the DINP and DOP systems respectively. Calculated velocities of diffusion front are positive values, indicating that the dPMMA/plasticiser interface is moving towards the plasticiser and therefore that the polymer matrix is plasticised and swelled. A smaller rate of ingress into the polymer film was observed for the larger, less mobile DINP. These diffusion front velocities are however small due to the glassy nature of the polymer matrix at the temperature considered.

1.2.5.3 Surface enrichment in polymer blends

In another study, Wang *et al.*⁶³ focused on the early-stage surface compositional enrichment in a two-phase regime polymer blend, constituted of a slightly lower molecular weight deuterated PMMA ($M_w = 51 \text{ kg.mol}^{-1}$, $PD = 1.04$, $T_g \sim 120 \text{ }^\circ\text{C}$) and hydrogenated poly(styrene-ran-acrylonitrile) (SAN) (33 % (w.w) acrylonitrile, $M_w = 124 \text{ kg.mol}^{-1}$, $PD = 2.24$, $T_g \sim 114 \text{ }^\circ\text{C}$). LCST of the blend was proved via small angle neutron scattering (SANS), as the static structure factors $S(Q)$ increased with temperature, implying phase separation upon heating. The spinodal temperature of the blend was estimated at 115 °C.

NR was used to monitor the phase separation of the blend after annealing at 130 °C for 0, 65, 215 and 1200 s. The best dPMMA compositional depth profiles giving the best fit for the NR data are shown in Figure 1-7. Two stages of surface enrichment layer growth were observed in the early stage segregation: a rapid local surface enrichment at the chain segmental level and then, a slower growth of a diffuse layer having a scale on the order of the bulk correlation length and the radius of gyration of the surface preferred component. This late-stage evolution of the SEL exhibits “non-universal” growth laws, dependent on the phase stability, wetting characteristics of the film, confinement and on the details of the polymer-surface interaction potential.⁶³

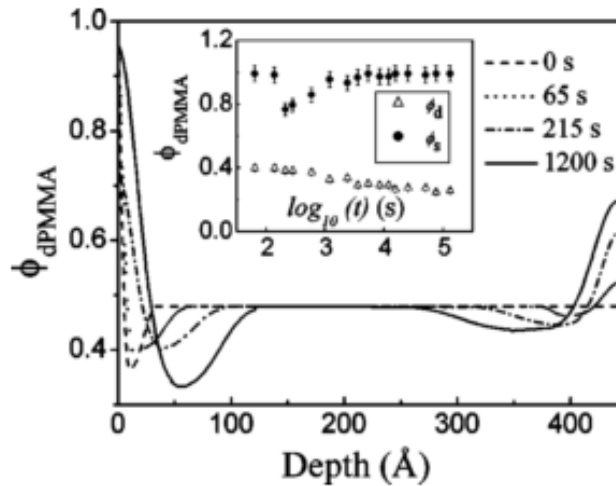


Figure 1-7: Evolution of dPMMA compositional depth profiles with time. The inset shows the evolution of surface composition ϕ_s and depletion layer ϕ_d . Reprinted with permission from Wang et al., *Physical Review E*, 67, 061801. Copyright 2003 American Physical Society.

It is also interesting to notice the presence of a depletion layer: the depletion zone broadens with time while the amount of wetting component increases. Moreover the depletion layer composition ϕ_d decreases monotonically, suggesting that the equilibrium state is not reached, and that the diffusion is a relatively slow phenomenon. However, the uniqueness of the derived profiles should be treated with caution. Other studies⁷⁴ show that NR is very insensitive to the small concentration gradients associated with depletion.

1.2.5.4 Surface enrichment of oligomer/polymer blends

In oligomer/polymer blends, diffusion of the oligomers can result in their segregation to the exposed surface. The diffusion flux of oligomers in polymer matrices is dependent on the compatibility between the two components. Therefore, it is determined by the free volume of the polymer and its structure, the size and shape of the oligomer and the polymer-polymer as well as polymer-oligomer thermodynamic interactions.⁷⁵

Depending on the components, the equilibrium composition can be reached almost instantaneously or in a few weeks. The diffusion coefficient usually decreases with increasing size of the polymer chains (the scaling law for large molecular weights is $D \sim M_w^{-2}$), and depends on the local structure of the films (glassy, amorphous, semi-crystalline). In the first instance, because of the low molecular weight of the oligomers and the amorphous, rubbery character of the polymer matrix used in this project, the equilibrium was expected to be reached in relatively short times.

1.3 SURFACE PARTITIONING AND ADHESION PROPERTIES OF POLYMER BLENDS

1.3.1 THEORIES OF ADHESION

Adhesion is a complex and multi-disciplinary topic. It involves mainly polymer and surface science, ranging from surface chemistry to polymer rheology and fracture analysis. To properly understand the adhesion between an adhesive and a substrate, various phenomena are described in the literature. Several physical and chemical theories have been developed to describe the work of adhesion.^{76,77,78}

1.3.1.1 Adhesion via mechanical interlocking

A first approach to adhesion was to consider the concept of mechanical interlocking. This concept suggests that adhesion is attributed to interlocking between the adhesive and the irregularities of a rough substrate, as in a “hook and eye” system. This is particularly valid when adhering to textile or wood, where the penetration of adhesive into the fibres has proven significance on peel test strength. The importance of this contribution on the total adhesion strength is governed by the roughness of the substrate and the extent of penetration of the adhesive into the irregularities. However, strong adhesive bonds can also be achieved between very smooth surfaces. Therefore, this contribution cannot explain all the adhesion phenomena.

1.3.1.2 Adsorption and thermodynamic description of adhesion

The molecular bonding between the adhesive and substrate layers is believed to be sufficient to give a high bond strength through a simple adsorption phenomenon. These attraction forces include ionic attraction, hydrogen bonds and van der Waals forces. This is the most widely accepted mechanism of adhesion in the literature.

Such adsorption requires close contact at molecular levels. Therefore the presence of bubbles or defects can greatly impact this adhesion contribution. Huntsberger^{79, 80} reported that the beneficial effect of roughening the substrate is not due to mechanical interlocking but to the increased amount of adsorption forces (increased surface area).

1.3.1.2.1 Work of adhesion and surface energies

The thermodynamic work of adhesion W_A is a fundamental measure of adhesion. It represents the forces of attraction between the fundamental particles comprising a material, or in other terms, the reversible and minimum work that must be done to separate two adjacent phases. It is defined as the free energy change required to separate two phases 1 and 2.

$$W_A = \gamma_1 + \gamma_2 - \gamma_{12} \quad (1.26)$$

with γ_i the surface energy of the phase i and γ_{12} the interfacial tension between the two phases. It is commonly accepted that the optimum adhesion occurs at the minimum interfacial tension (W_A maximum).

Young described 200 years ago the case of a liquid phase in contact with a solid phase for “dry wetting” – i.e. the surface pressure of the liquid vapour on the solid is negligible. His work led later to Young’s equation (1.27), defining γ_S the solid surface energy. The Young-Dupré equation (1.27’) based on equations (1.26) and (1.27), defines the work of adhesion of a liquid drop on a solid surface:⁸¹

$$\gamma_S = \gamma_{SL} + \gamma_L \cos(\theta) \quad (1.27)$$

$$W_A = \gamma_L [1 + \cos(\theta)] \quad (1.27')$$

where ϑ is the contact angle of the sessile liquid drop on the solid surface, γ_S the solid surface energy, γ_L the liquid surface energy and γ_{SL} the interfacial tension between the solid and the liquid. One can note that “wetting” can be determined from Young’s equation when the relation $\gamma_S - \gamma_{SL} \leq \gamma_L$ is found valid at equilibrium – equality being for total wetting ($\vartheta = 0$) and inequality for partial wetting.⁶⁵

Hence, the work of adhesion can be directly calculated from the contact angle and surface tension of the liquid phase. In practice, roughness of the substrate can introduce hysteresis between the advancing and receding drops which makes the contact angle difficult to determine.

1.3.1.2.2 Critical surface tension and surface energy

By measuring the contact angle of several reference liquids of known γ_L on the same surface, Zisman⁸² discovered in the 50s an empirical quasi linear connection between $\cos(\vartheta)$ and γ_L . Extrapolating this linear trend to $\cos(\vartheta) = 1$, he introduced the critical surface tension of the liquid γ_C , given from Young’s equation (1.27) as:

$$\gamma_C = \gamma_S - \gamma_{SL}^* \quad (1.28)$$

with γ_{SL}^* , defined as γ_{SL} when $\cos(\vartheta) = 1$ and dependent on the chosen combination of solid and liquid. γ_C is therefore different from γ_S and varies with the chemical nature of the reference liquids, which can be seen as a big disadvantage of the approach. Yet, a small polarity difference between the solid and liquid is believed to give a small value of γ_{SL}^* and therefore yield a critical surface tension approaching the value of the solid surface energy.

An interesting outcome of the Zisman plot approach is that a criterion for optimum adhesion can be defined; as from equation (1.26), $\gamma_{SL} = 0$ also corresponds to the maximum work of adhesion, Kitazaki *et al.* suggested that the optimum adhesion can be achieved when $\gamma_L = \gamma_S$.⁸³

1.3.1.2.3 Fowkes' theory and extensions to determine the surface energy

To overcome the limitations of the Zisman approach, Fowkes introduced an equation in 1962⁷⁶, separating the total surface tension γ_i^{tot} into two parts: the dispersive component (van der Waals forces) γ_i^d and the polar component (hydrogen bonding) γ_i^p .

$$\gamma_i^{tot} = \gamma_i^d + \gamma_i^p \quad (1.29)$$

Considering a liquid that interacts with the surface only by dispersive forces and expressing the dispersive work of adhesion W_A^d as the geometric mean of the dispersive forces at the solid/liquid interface one can write:

$$W_A^d = \gamma_S + \gamma_L - \gamma_{SL} = 2\sqrt{\gamma_S^d \gamma_L^d} \quad (1.30)$$

$$\gamma_{SL} = \gamma_S + \gamma_L - 2\sqrt{\gamma_S^d \gamma_L^d} \quad (1.30')$$

From the additivity of the dispersive and polar surfaces forces (1.29), one obtains the extended Fowkes' theory (or OWRK after its originators Owens, Wendt, Rabel and Kaeble):⁸⁴

$$\gamma_{SL} = \gamma_S + \gamma_L - 2\sqrt{\gamma_S^d \gamma_L^d} - 2\sqrt{\gamma_S^p \gamma_L^p} \quad (1.31)$$

Replacing γ_S as in equation (1.27) one can develop equation (1.31) as

$$Y = \sqrt{\gamma_S^p} \times X + \sqrt{\gamma_S^d} \quad (1.32)$$

$$\text{with } Y = \frac{\frac{1}{2}(1 + \cos(\theta)) \times \gamma_L}{\sqrt{\gamma_L^d}} \text{ and } X = \sqrt{\frac{\gamma_L^p}{\gamma_L^d}}$$

Using two different liquids of known surface energy (dispersive and polar components) on the same surface, one can solve the equation (1.31) and by plotting Y as a function of X , directly obtain the dispersive and polar parts of the solid surface free energy. Usually a polar and non-polar liquids are used to maximise the difference in the X term.

An extension of the previous “optimum bonding” criteria is that not only the surface energies of the liquid and solid should be equalised to obtain the maximum work of adhesion. It is also advised to try matching the polar and dispersive parts of the two phases. Usually, polar tackifiers are added in industrial formulations so as to help the adhesive bond to polar surfaces.⁸⁵

Kwok and Neumann,⁸⁶ proposed another approach, based on an equation of state for interfacial tensions. The equation of state for a solid/liquid interface is written

$$\gamma_{SL} = \gamma_S + \gamma_L - 2\sqrt{\gamma_S\gamma_L}e^{\beta(\gamma_S-\gamma_L)^2} \quad (1.33)$$

where β is a constant of the interface.

Combining this equation with Young’s equation (1.27a) one may obtain

$$\cos(\theta) = -1 + 2\sqrt{\frac{\gamma_S}{\gamma_L}}e^{\beta(\gamma_S-\gamma_L)^2} \quad (1.34)$$

In a more recent publication Kwok and Neumann suggested an alternative equation⁸⁷

$$\cos(\theta) = -1 + 2\sqrt{\frac{\gamma_S}{\gamma_L}}[1 - \beta'(\gamma_S-\gamma_L)^2] \quad (1.35)$$

Equations (1.34) or (1.35) enable calculating the solid surface free energy knowing only the surface tension of a reference liquid and the contact angle. As β is usually unknown, at least two reference liquids must be used. In contrast to the OWRK approach, there is no need to know the values of the dispersive and polar contributions to the surface free energy of the liquid with this method.

1.3.1.3 Other contributions to adhesion

Other contributions to adhesion were reported in literature. For instance, it is common to create covalent bonds between the substrate and the adhesive, by means of chemical reactions, in order to increase the interfacial adhesion.⁸⁸

Deryaguin *et al.* were the first to suggest that electrostatic forces can be created if the substrate and adhesive have different electronic band structures.⁸⁹ A double layer formed at a boundary is similar to a parallel plate condenser: Coulombic attraction exists between the layers. This contribution is mainly seen for substrates presenting high charge density (metals, polyelectrolytes etc.)

Voyutskii *et al.* introduced the diffusion theory of adhesion between polymers in 1963.⁹⁰ The adhesion is thought to be attributed to molecular entanglements. The idea supporting this theory is that if two polymers are brought in contact at temperatures above their T_g , the chains (or at least some segments) will interdiffuse across the interface and become entangled.

1.3.2 HOT-MELT PRESSURE SENSITIVE ADHESIVES

1.3.2.1 Pressure sensitive adhesives and tack properties

One of the industrial systems of interest for this project is the family of pressure sensitive adhesives (PSAs) obtained by hot-melt. PSAs are adhesives that are able to form a bond under very light pressure – i.e. establish molecular contact to enable van der Waals forces – and sustain a minimum level of stress upon debonding. This very unique property is achieved from the hysteresis of the thermodynamic work of adhesion; there is a difference between the energy gained in forming the interactions and the energy dissipated during the fracture of these bonds.⁹¹ Applications of PSAs usually set three important requirements: (i) show some degree of stickiness and form a good bond on various surfaces, (ii) be easily peeled off at a controlled peeled force vs velocity and leave no or very little residue on the surface – i.e. possess strain-hardening properties –, (iii) be able to resist to a certain degree of stress over long times, hence exhibit minimum creep.

The “tackiness” or stickiness of a PSA is mainly related to its ability to form bridging fibrils during a debonding event. When pulling the adhesive away from the substrate, cavities are formed at the interface. If these cavities coalesce, it leads to interfacial failure. In the opposite case, the

bulk material is deformed, allowing energy dissipation, and the walls of these cavities correspond to the observed fibrils. In other words, tackiness is obtained for materials that demonstrate high resistance to the interfacial propagation of a crack.^{91,92} An empirical criterion was established by Dahlquist⁹³ that states that a good “tack” is obtained for a storage modulus G' less than 0.3 MPa. To be representative of pressure sensitive adhesive applications, with timescales that are typically of the order of 1 s, the measurements are usually performed at 1 Hz and 25 °C. However, this criterion does not seem to be sufficient to fully describe tackiness, since the debonding process is determined by the coupling of bulk and interfacial properties of the material.

1.3.2.2 Styrenic block copolymer-based formulations

Hot-melt PSAs, also called “hot glue”, are a form of thermoplastic adhesive. Their bonding process do not involve any chemical reaction and they are solvent-free, which eliminates the curing step and the issue of the volatile organic compounds noxiousness. Their formulation typically includes, as schematised in Figure 1-8:^{94,88}

- Backbone polymer (~ 20-40 %): traditionally a styrenic block copolymer (SBC) of structure “styrene-elastomer-styrene”, with ~ 30 % styrene and the elastomer block being polyisoprene (PI) or polybutadiene (PB).
- “Tackifier” (~ 40-60 %): generally resins of molecular weight 300-2000 g.mol⁻¹ which are solid at RT – e.g. rosins and derivatives, terpenes and modified terpenes, oligomers from aliphatic (C5) and aliphatic/aromatic (C5/C9) monomers, hydrogenated hydrocarbon resins, terpene-phenol resins.^{94,95,96}
- Plasticisers (~ 0-15 %): mineral oils (paraffinic or naphthenic) of molecular weight 200-300 g.mol⁻¹, added to modify viscosity.
- Other specialty additives such as antioxidants (< 0.5 %).

It has been shown that the compatibility of these ingredients is directly related to the adhesive performance, since it affects a large range of mechanical properties – e.g. tack, cohesive strength, softening point and melt viscosity.⁹⁷

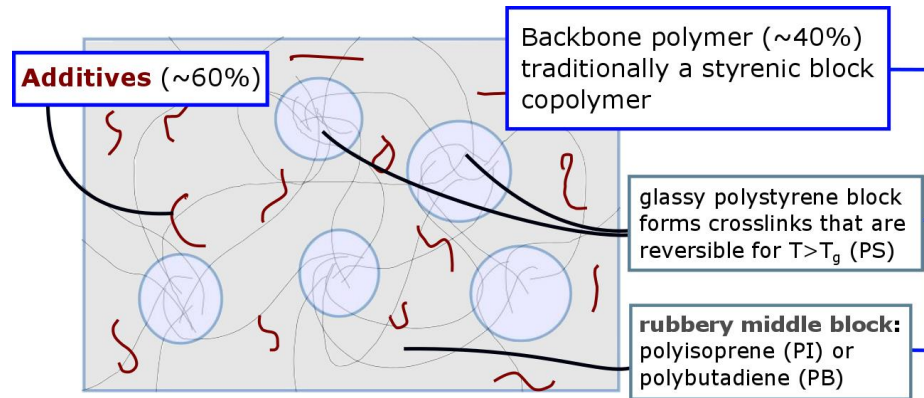


Figure 1-8: Simplified schematic of a SBC based PSA formulation.

SBCs represent the largest-volume market of thermoplastic elastomers and are primarily used in PSA applications such as disposable products, stamps and envelopes. They undergo microphase separation at room temperature: the polystyrene chain-ends form glassy domains that act as physical crosslinks and restrict the mobility of the central block, while the central elastomer segment brings rubberlike properties. The extent and length of the bridges between the styrene blocks controls the strain-hardening properties. Because of this particular nanostructure, SBCs' mechanical properties are similar to vulcanised elastomers but they can be processed like thermoplastics – SBCs melt at temperatures above the glass transition temperature of the PS block (T_g PS ~ 90 °C).⁹⁸ SBC based PSAs are therefore supplied in solid form, applied as melts at $T \sim 120$ °C and very high speed (order of a few m/s), by means of electric hot glue “guns”, to maximise contact with the substrate and solidified quickly upon cooling to room temperature.⁹⁹

Tackifiers are primarily added to PSAs to increase the debonding energy. They are usually chosen to be soluble in the rubbery domains of the SBCs (PI or PB) at all compositions and insoluble in the glassy domains, in order to improve the tack properties.^{100,91} They act like plasticisers and decrease the elastic modulus of the rubbery block by disrupting chain entanglements, which renders the polymer more compliant to substrate roughness and helps the fibrils formation. However, contrary to common plasticisers, tackifiers are solid at room temperature and exhibit a high T_g . They are also added to the formulation to increase the T_g of the rubbery domains – which is originally ~ -80 °C – because, to be “tacky”, the T_g of the adhesive must be 25 to 45 °C below the usage temperature.¹⁰¹ It is also desired for the adhesive to exhibit a broad T_g – i.e. a broad peak of the loss modulus, G'' – in order to maximise the viscoelastic dissipation.⁹¹ This result can be achieved for example, by the use of several types of tackifiers of various T_g s. Some

tackifiers also introduce polarisable groups in the formulation and help bond to more polar surfaces by matching their polarity (see 1.3.1.2.3). Because of their high T_g and their particular chemical structure they are considered as specialty chemicals. Hence, tackifiers are very critical components of the PSA formulations as they are more expensive than usual plasticisers and needed in large proportion.

SBC based formulations meet PSA's material requirements: at room temperature, they exhibit solid-like properties at low frequencies – hence fairly good resistance to creep – and at the same time, viscoelastic properties at high frequencies – hence high peel force, thanks to the formation of fibrils at the interface.⁹¹

1.3.2.3 Effect of tackifiers on tack properties

Fujita *et al.* used their comprehensive miscibility study between natural rubber ($M_w = 299\ 000\ \text{g}\cdot\text{mol}^{-1}$) and industrial tackifiers ($M_w = 240\text{-}4200\ \text{g}\cdot\text{mol}^{-1}$)^{25,26} to investigate the effect of miscibility on three mechanical properties: shear creep,¹⁰² probe tack¹⁰³ and peel strength.¹⁰⁴

The shear creep experiment measures the holding time – i.e. time to failure – of an adhesive on an adherent against a shear load pulling parallel to the interface. The probe tack experiment determines the orthogonal force needed to separate the adhesive from its substrate as a function of pulling rate, after a specified load is applied to the sample. Finally, in a peel strength test, the average load required to separate bonded materials with an angle of 180 degrees is recorded as a function of pulling rate.

A first effect of the blending of a polymer with a miscible, shorter molecule is the decrease in its plateau modulus. This plasticisation is due to the disruption of the molecular entanglements in the polymer melt. The chains have fewer entanglements per unit volume, hence are less constrained and can relax more easily, their relaxation time being also shortened. Fujita *et al.* observed this effect during shear creep experiment on miscible tackifier/natural rubber mixtures.¹⁰² The holding time of the natural rubber decreased as the tackifier content was increased. They attributed this result to the plasticisation – i.e. decrease in plateau modulus.

A second effect is that the T_g of a tackifier/polymer miscible mixture is expected to be higher than the T_g of the pure polymer, because of the tackifier's relatively high T_g ($\sim 45\text{-}75\ ^\circ\text{C}$). With an increased amount of tackifier, Fujita *et al.* observed a shift in peel strength and probe tack maximum peaks to lower velocities (or higher temperature). This dynamic phenomenon is

believed to be linked to the elevation of the T_g as it is not observed in the case of immiscible systems.¹⁰⁵

In the case of an incompatible tackifier/polymer mixture, peel strength and probe tack maximum peaks exhibit lower values,^{103,104} however holding times vary from mixtures to mixtures, depending on the level of incompatibility.¹⁰² It could be hypothesised that for extremely immiscible mixtures, the tackifier acts like a solid filler and increases the plateau modulus compared to the pure natural rubber.¹⁰⁵ Nonetheless the tack properties are lower, as shown by the probe tack and peel strength tests, as the T_g of the natural rubber is not increased.

In both cases, miscible and immiscible mixtures, peel strength tests showed that the velocity range of interfacial failure (between the adhesive and the adherent) decreases as the amount of tackifier increases.¹⁰⁴ This result shows that the presence of the tackifier, be it miscible or immiscible, is reducing interfacial failure. Therefore, one could suggest that the tackifier also has an effect on the interfacial properties of the formulation. However, it is also known that a strong coupling between geometry and mechanical properties exists which influence greatly the results of such peel tests.⁹¹

The reason why tackifiers improve the tack properties is not yet fully understood. Sasaki *et al.* believe that the miscible tackifiers develop “wettability” of the adherent interface while phase-separated tackifier agglomerates increase cohesive strength – i.e the theoretical stress that causes fracture in tensile test when no plastic deformation is involved.¹⁰⁰ Yet, they define “wettability” as “flowability” – i.e. a bulk mechanical property of spreading and fit closely the roughness of a substrate – and do not discuss any thermodynamic wettability. Considering the great difference between surface and bulk properties expected in this type of asymmetric system, it seems sensible to also hypothesise a surface effect as responsible for the increase in tack.

1.3.3 POSSIBLE EFFECTS OF ADDITIVE SEGREGATION ON ADHESION

From their relatively low molecular weight (200-2000 g.mol⁻¹), the additives – i.e plasticisers (liquids) and tackifiers (solids) – have a relatively high diffusive mobility and may spontaneously segregate to surfaces or interfaces. Yet, the first requirement for a successful bond is to establish contact at molecular level.⁷⁸ It is therefore of crucial importance to understand the surface characteristics of the adhesive to obtain a high quality seal.

1.3.3.1 Modification of the surface viscoelastic properties

The effect of the presence of the tackifier on adhesion has been mainly explained in the literature by assessing bulk properties – e.g. miscibility, T_g , elastic modulus. This additive is indeed modifying the polymer mechanical properties by a plasticisation effect and its high T_g . These effects are extremely important for a good application of the adhesive on the adherent and compliance to its roughness.

However, it has been evidenced in 1.2.3 that small molecules have the tendency to segregate at the surface of a polymer film. One could argue that the viscoelastic properties in the first tens of nm of the film might be different from those of the bulk which could be critical for creating a good contact between the adhesive and the adherent and avoid the formation of air pockets at the interface. Yet, this argument might be valid for improving adhesion of substrates of relatively low roughness ($< 0.1 \mu\text{m}$).

Alternatively, Newby *et al.* evidenced that interfacial slippage – i.e. low resistance to shear stresses – can affect the maximum peel force needed to separate an adhesive tape from a substrate.¹⁰⁶ In the case of slip, the adhesive strength is dominated by the friction between the adhesive and the substrate. The adhesion is hence weaker because there is no large viscoelastic dissipation in the bulk.⁹² It is suggested that substrates presenting higher surface mobility – i.e. liquid-like monolayers vs equivalent crystalline state – should allow more slippage and hence exhibit poorer adhesion.¹⁰⁶

1.3.3.2 Formation of a weak boundary layer

Some authors, like Bikerman,¹⁰⁷ consider that “failures in adhesion” – i.e. a separation that takes place at the interface between the substrate and the adhesive – are low probability phenomena, as opposed to a “failure in cohesion” that happens within the adhesive joint. *Apparent* failures in adhesion – i.e. which happens within a few μm within the adhesive joint – would be more common. The only failure that may happen at the interface would be due to the presence of a *weak boundary layer* (WBL); a third material present between the adhesive and the adherent. This case should not be considered as a “failure in adhesion” as no interface exists between the adherent and the adhesive. The WBL keeps the adhesive and adherent apart from each other and has weaker mechanical properties. Thus, the presence of a WBL would lead to rupture with forces which might be a fifteenth of what would be required to break a joint free of WBL.¹⁰⁷

The formation of a WBL can be due to air (caused by the application process or the formulation's viscosity), to a reaction product between the adhesive and the adherent (depending on the nature of the adherent) or to migrating impurities (related to the adhesive formulation), the latest being the area of interest of this work as migrating additives separating from the bulk formulation can be considered as impurities.

1.3.3.3 Modification of the surface roughness

Additives in PSA formulations are either solid (tackifiers) or liquid (plasticisers). Their segregation at the surface can induce a modification of the surface roughness, especially in the case of crystalline materials. If fractal structures are formed at the surface, the roughness would increase dramatically and alter wettability, tending to superhydrophobic effects due to the presence of air pockets, such as for chocolate blooming.¹ It might be more difficult to achieve a contact at molecular level in this eventuality.

1.3.3.4 Modification of the work of adhesion

As discussed in 1.2.2.1, the surface free energy of the pure polymer will also be affected by the surface segregation of smaller chains. An adsorbed monolayer of additives can be sufficient to change the adhesive's surface energy. In addition, if immiscible additives segregate at the interface between the adhesive and the adherent forming a so called WBL, the work of adhesion between the adherent and the WBL and/or between the WBL and the adhesive might be smaller than the work of adhesion between the adherent and the adhesive.

As it is important to match the surface energies of the two phases in contact (and, optimally, their polar and dispersive components), the surface migration of the additives might lower the work of adhesion.

1.3.3.5 Loss of additive

Small organic molecules are added in PSA formulations to act as plasticisers and/or modify the backbone polymer's T_g . Losing additive from the polymer bulk might increase the formulation's storage modulus – i.e. make it less spreadable and more brittle – and decrease its tack properties.

Smith *et al.*,¹⁰⁸ evidenced a loss of plasticiser by evaporation from a polyester-polyurethane film by NR. They observed segregation of the plasticiser at both interfaces with air and silica substrate

and proved that the loss of plasticiser from the polymer film was only limited by its rate of evaporation from the surface and not by its mobility in the film. Similarly a cause of additive loss from the bulk could be attributed to the presence of a “sink” material in contact with the formulation – i.e. a material in which the additive is less concentrated and/or more compatible. In such a case, the additive might diffuse and partition into the more compatible phase in order to reach a thermodynamic equilibrium.

1.4 CONCLUSIONS OF THE LITERATURE REVIEW

Oligomer/polymer blends are widely applied in industry. Understanding the phenomenon of surface segregation of small additive molecules can be of great interest to reduce the cost and/or improve the performance of formulations related to P&G businesses. However, this extensive literature search showed that very little experimental data has been published about the surface behaviour of such greatly asymmetric blends. Moreover only few theoretical models can fully describe these systems across their critical point.

The main characteristic of oligomer/polymer blends is the significant disparity in molecular weights between the two species. From the published research, it appears that several entropic and enthalpic factors could be in balance to describe their surface behaviour.

Firstly, chain-ends (therefore, mainly the oligomers) are preferentially positioned at the surface/interface to minimise the loss in conformational entropy. Secondly, the species of lower surface energy should be positioned at the surface to minimise the system’s enthalpy. Therefore, the difference in surface energy between the oligomer and the polymer is expected to direct the orientation of the oligomer segregation, towards the surface or the interface with another material.

From the trends observed for polymer mixtures, one can suggest that the thermodynamics of these systems favour:

- in the one-phase regime: a surface segregation of the low molecular weight species – i.e. one phase is present everywhere but a surface/interface excess can be observed on a length scale of $\sim R_g = 100\text{s of \AA}$ (Figure 1-9, blue curves). Theories suggest that the correlation length could be expressed as in equation (1.20) or (1.24). This surface

segregation might be desirable in adhesives where the presence of the additive could help match the surface energy of the substrate. Moreover it could be used to provide surface functionality to materials in other types of formulations– e.g. softness, hydrophobicity or hydrophilicity.

- in the two-phase regime: one would expect from equation (1.10) to obtain a critical concentration $\varphi_c \sim 1$ when $N_A \ll N_B$. This corresponds to a complete phase separation of the oligomer from the host polymer, leading to the appearance of a macroscopically thick, almost pure oligomer phase – the “wetting layer” – spreading at the surface of a polymer-rich phase (Figure 1-9, pink curve). This phenomenon is unwanted in adhesives as it can produce a weak boundary layer in the system and affect the mechanical adhesion.

Hence, the behaviour of oligomer/polymer blends at the surface might also largely depend on their compatibility.

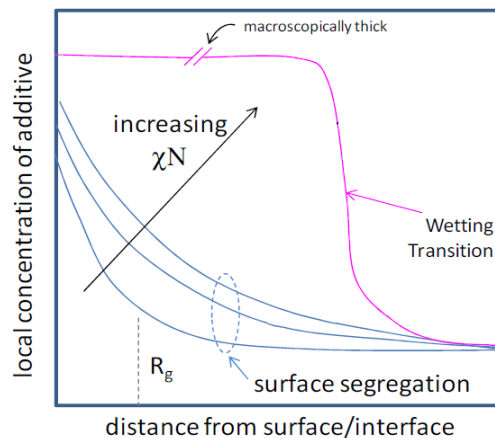


Figure 1-9: Schematic diagram of the expected evolution of a concentration profile of an additive in a polymer blend near a surface as the critical point is approached.

Several theoretical models have been developed to characterise the mixing behaviour of polymer blends, most of them starting from the Flory-Huggins mean-field theory. However, their effectiveness is limited, especially for describing the oligomer/polymer mixtures, mainly due to fluctuation and excluded volume effects. Despite these shortcomings, Flory-Huggins provides a base to hypothesise what key-parameters govern phase separation.

The kinetic aspect of the oligomer diffusion will not be taken into account in detail in this thesis, as the polymers of interest are in their rubbery amorphous state and the oligomers are small enough to have a relatively fast diffusion compared to the time scale of the experiments. Thus,

in a first instance, it is considered in this thesis that the samples are in their equilibrium state (or at least a local energy minimum), keeping in mind the sample preparation as a potential source of metastability.

When trying to model concentration profiles vs depth profiles and quantify the surface excess, the Schmidt-Binder theory provides a good prediction in the one-phase regime even though the description is one of an exponential decay. However, because it is also based on the mean-field approach of FH, it fails when approaching phase separation.

To tackle this gap in the literature, a three-angle-approach was chosen to create a relevant model describing the behaviour of oligomer/polymer mixtures around the critical point:

- An experimental investigation was led, as described in this thesis. It studies the oligomer partitioning in model binary formulations.
- A theoretical study was developed by the PhD candidate Salvatore Croce using the Schmidt-Binder and the Self-Consistent Field theory.
- A computational model was built by the PhD candidate Jos Tasche that uses a coarse graining technique combining statistical associating fluid theory (SAFT- γ Mie) and molecular dynamics.

The objectives of this model are to predict the concentration profile of the oligomer in the polymer and to understand what governs the formation of wetting layers.

Chapter 2: EXPERIMENTAL

2.1 MATERIALS

A selection of polymers and oligomer were used in this project. The compounds names, suppliers, product numbers and structure (when applicable) are listed below. The justification of the model systems definition is given in *Chapter 3*.

Polymers:

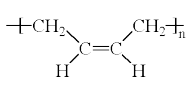
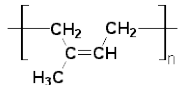
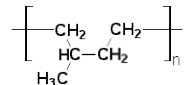
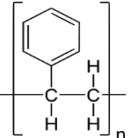
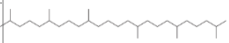
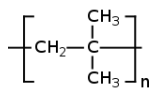
- Polybutadiene (PB): Sigma-Aldrich Inc., product number 181382, 36 % cis 1,4 addition, 56 % trans 1,4 addition, 8 % 1,2 addition (vinyl)
- Polybutadiene, cis (PBcis): Sigma-Aldrich Inc., product number 181374, 98 % cis 1,4 addition
- Polyisoprene (PI): synthesized¹⁰⁹ and provided by Dr Todd Mansfield (P&G Cincinnati), 80 % cis-1,4 addition, 13 % trans-1,4 addition, 7 % 1,2 addition (vinyl)
- Hydrogenated polyisoprene (hPI): synthesized¹⁰⁹ and provided by Dr Todd Mansfield (P&G Cincinnati), made by saturation of the PI sample
- Deuterated Polystyrene (d-PS): Polymer source Inc., product ID P3088

Oligomers:

- d-squalane (dsq): Qmx Laboratories, U.K., product code D-0958/0.5, 99 % deuterated
- squalane (sq): Sigma-Aldrich Inc., product number 234311
- oligomeric d-styrene (oligo-dS): Polymer source Inc., product ID Tetramer-d33
- oligomeric d-isobutylene (oligo-dIB 900): Polymer source Inc., product ID P18618-d8PIb
- oligomeric d-isobutylene (oligo-dIB 2200): Polymer source Inc., product ID P18651-d8PIb

The key characteristics of the polymers and oligomers relevant to this study are summarised in Table 2-1.

Table 2-1: Physical properties for key components of the model HMA films.

component	Structure (hydrogenated analogues)	M_w /g mol ⁻¹	$PDI = M_w/M_n$	ρ / g.cm ³ (at 25 °C)	n_i	s.l.d. × 10 ⁶ / Å ²	δ / (MPa) ^{1/2}
polymers							
PB [C ₄ H ₆] _n		280 000	2.1	0.913 ₁₇	1.5173 (1.516 ¹⁷)	0.416	16.6-17.6 ¹⁷
PBcis [C ₄ H ₆] _n		567 000	4.4	0.915 ₁₇	1.5230 (1.526 ¹⁷)	0.416	16.6-17.6 ¹⁷
PI [C ₅ H ₈] _n		160 000	1.1	0.913 ₁₇	1.5188 (1.519 ¹⁷)	0.264	15.18-17.09 ¹⁷
hPI [C ₅ H ₁₀] _n		165 000	1.1	0.90	1.4749 (1.475-1.480 ¹¹⁰)	-0.32	
dPS [C ₆ H ₈] _n		340 000	/	1.04	1.590-1.592 ¹⁷	6.47	17.4-19.09 ¹⁷
oligomers							
dsq C ₃₀ D ₆₂		484	-	0.93	1.4474 ¹¹¹	6.75	18.8 ¹¹²
sq C ₃₀ H ₆₂		423	-	0.81	1.4501 (1.4474 ¹¹¹)	-0.37	18.8 ¹¹²
oligo-dS D[C ₈ D ₈] _n	<i>idem</i> PS	448	-	0.9	1.590-1.592 ¹⁷	5.72	17.4-19.09 ¹⁷
oligo-dIB C ₈ H ₁₇ [C ₄ D ₈] _n H		1260	1.4	1	1.505-1.510 ¹⁷	6.57	15.76-17.0 ¹⁷
oligo-dIB C ₈ H ₁₇ [C ₄ D ₈] _n H		2970	1.35	1	1.505-1.510 ¹⁷	6.57	15.76-17.0 ¹⁷

The deuterium labelling of some of the compounds enabled their composition versus depth profiles to be resolved by ion beam analysis or neutron reflectometry. Molecular weight M_w and polydispersity M_w/M_n were determined by gel permeation chromatography for the hydrogenated polymers. The small amount of available deuterated materials did not allow running GPC. Therefore for dPS and oligo-dIBs the PDI and M_w given in the table are the values provided by the supplier. The densities ρ , refractive indices n_i and Hildebrand solubility

parameters δ are values from the literature for the materials or in the case of deuterated components, their hydrogenous analogues. Values of refractive indices in *italics* were measured at 25 °C using a refractometer RFM 390 from Bellingham & Stanley Ltd. The scattering length densities (s.l.d.) were calculated from the compounds' formula and density (see 2.8).

2.2 SAMPLE PREPARATION

2.2.1 POLYMER SOLUTIONS

Oligomers and host polymers were dissolved in toluene to create 2-10 vol% stock solutions. These solutions were usable after 1 to 2 days dissolution. They were combined in different proportions to obtain 2-10 vol% solutions in toluene containing the required oligomer and polymer ratio (typically 30 to 70 % (w.w)).

2.2.2 SPIN COATING OF THIN FILMS

Spin coating of the films was performed from the prepared toluene solutions using a Laurell spin coater model WS-650MZ-23NPP. Silicon wafers were cut to approximately 3 × 3 cm in dimension for IBA or 1 × 1 cm for AFM usage and washed with acetone to remove any hydrophobic impurities and ensure consistent film production. Approximately 5 mL of solution was pipetted onto the centre of the wafers and spun onto them for about 30 s using an electric spin coater at a speed ranging from 2000 to 4000 rpm for the desired thickness (~ 100-150 nm) until dry. Alternatively, 5 mm thick silicon blocks were used for neutron reflectometry instead of thin wafers.

2.2.3 SOLUTION CAST FILMS

30 g of the prepared solutions were poured into a 4 cm diameter Teflon dish. After a week of solvent evaporation at room temperature and pressure in a fume cupboard, a film of ~ 1 mm containing the desired oligomer/polymer ratio was obtained, cut and peeled off for turbidity assessment, rheology and contact angle measurements.

2.2.4 FRACTIONATION OF POLYDISPERSE POLYMERS

PBCis was dissolved at 4 % (w.w) in toluene. Using a separating funnel placed in a thermostated bath at 22 °C, methanol was slowly added until white rings formed at the surface of the solution, along the glass. The separating funnel was then shaken to redissolve the precipitated polymer fraction of high M_w . These steps were repeated until the solution becomes cloudy. The bath was then heated up to 26 °C (until the solution is transparent again). Subsequently, the separating funnel was removed from the bath and left on a support stand at room temperature overnight. The bottom toluene phase was retrieved and washed with cold methanol to reprecipitate the polymer. Finally the polymer toluene solution was dried at 45 °C under light vacuum for 14 hours. The molecular weight distributions achieved by fractionation were then characterised by GPC.

2.3 GEL PERMEATION CHROMATOGRAPHY

The molecular weight of the polymers was determined by gel permeation chromatography (GPC). This technique separates the molecules based on their effective radius of gyration in solution. A GPC column is filled with a stationary phase: a gel and microporous polymer beads. The polymer sample is dissolved (here, at 1 mg/mL in THF) and ~ 100 μ L of solution are injected in the column. An eluent (also THF) flows through the column at a controlled rate (1 mL/min) at 35 °C. Smaller molecules are entering the pores of the beads more easily which increases their retention time. Comparing the retention times of the sample with some reference polystyrenes of low polydispersity allows calculating its molecular weights (in number average $M_n = \frac{\sum M_i N_i}{\sum N_i}$ and weight average $M_w = \frac{\sum M_i^2 N_i}{\sum M_i N_i}$) and polydispersity ($PDI = M_w / M_n$).

Triple detection GPC was used with refractive index, right angle light scattering and viscosity detectors. The instrument used for GPC measurements was a Viscotek TDA 302 from Malvern equipped with two PLgel 5 μ m mixed C columns (300 \times 75 mm) as a stationary phase. A value of 0.124 mL.g⁻¹, obtained from the Viscotek analysis software, was used as the refractive index increment (dn/dc) of polystyrene for both the calibration and the analysis of the polybutadiene samples. An example of GPC data is given in 5.1.2.3.

The determination of the molecular weights and polydispersity of PI and hPI was performed by P&G Cincinnati, using their own GPC equipment.

2.4 DIFFERENTIAL SCANNING CALORIMETRY

Differential scanning calorimetry (DSC) analyses the thermal characteristics linked to the physical (glass transition T_g , melting point T_m) or chemical (cross-linking, oxidation...) change of state of polymers. It was used in this project to determine the glass transition temperature, T_g , of oligomer/polymer mixtures and assess their compatibility as a function of oligomer content.

The DSC samples were prepared by solution casting. They were weighed into standard aluminium pans as mixed solutions, then dried at RT overnight to obtain ~ 1 mg product. Measurements were performed using a Perkin Elmer DSC 8000 between -130 °C and 120 °C at a 100 °C/min rate. This unusually high scanning rate was used to ensure that the T_g s were clearly observable. The cycle was repeated three times to ensure consistency of results. To perform a DSC measurement, two pans are simultaneously heated: an empty reference pan and a matched pan containing the sample. The difference in heat between the two pans needed to increase the temperature at a defined rate is recorded as a function of the temperature. The experimental error in ΔC_p associated with the instrument is ± 2 % over the full range. The T_g s were determined as the mid-point in step in specific heat capacity ΔC_p . Typical data and analysis are presented in 4.1.1.1.3.

2.5 PHASE DIAGRAM THROUGH TURBIDITY

Change in turbidity of pieces of polymer/oligomer films obtained by solution casting, as described in 2.2.3, was observed with naked eye over temperatures ranging from 0 to 60 °C to determine the cloud point of the mixture – i.e. temperature of phase separation. The temperature was increased at a rate of 2 °C/min and the cooling/heating cycle was repeated 2 times to ensure consistency of results.

2.6 SURFACE ENERGY MEASUREMENTS

Contact angle and pendant drop measurements were carried out with optical contact angle measuring and contour analysis system from Data Physics. The equipment was an OCA 230 with electronic dosing. A drop (sessile or hanging) is placed between a light source and a camera that captures images such as shown in Figure 2-1. Greyscale analyses of the images were performed with the SCA software with a SCA 21 module for surface free energy and SCA 22 module for surface and interfacial tension.

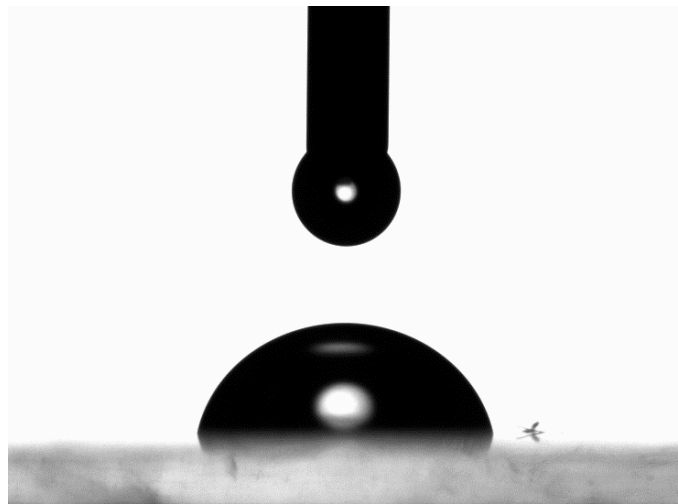


Figure 2-1: Example of sessile drop image for a drop of diiodomethane on PB.

2.6.1 SURFACE TENSION MEASUREMENT WITH THE PENDANT DROP

The Laplace pressure Δp – i.e. pressure difference between the inside and the outside of the drop – is linked to the surface tension γ and the radii of curvature r_1 and r_2 of the drop by the Young-Laplace equation.

$$\Delta p = \gamma \times \left(\frac{1}{r_1} + \frac{1}{r_2} \right) \quad (2.1)$$

Pendant drops are deformed from their spherical shape under the effect of gravity. Hence, while surface tension seeks to minimise the drop's surface area, gravitation stretches it into a pear-like shape. The hydrostatic pressure created by gravity is dependent on the height and weight of the drop. The radii of curvature at the drop vertex is used as a starting point for a parameterisation using the arc length of the drop shape. A theoretical drop shape is obtained by

solving a set of three first-order differential equations with three boundary conditions. A numerical fit of the theoretical drop shape to the recorded image eventually yields the surface tension using equation (2.1). For this calculation, it is necessary to know the shape and volume of the droplet as well as the density of the liquid phase (and the air phase). For the pendant drop measurements, a drop of liquid was vertically dispensed in air from 1.36 mm inner diameter Nordson precision tip at a rate of 2 $\mu\text{L/s}$. The volume of liquid was adjusted so as to obtain a pear-shaped hanging droplet. The outer diameter of the tip (1.65 mm) was used as a reference length to calculate the exact volume of the droplet.

2.6.2 SURFACE ENERGY MEASUREMENTS USING OWRK METHOD

The surface energy of polymer films was calculated from the OWRK method (described in 1.3.1.2) using sessile drop contact angle measurements. Pieces of polymer were cut from the bulk material as supplied and set as flat as possible on the sample stage. A 2 μL hanging droplet of reference liquid was dispensed vertically from a 0.51 inner diameter Nordson precision tip at a rate of 2 $\mu\text{L/s}$. The sample stage was slowly elevated to put the sample surface in contact with the hanging drop and gently lowered. The sequence was recorded by a camera at 1220 frames/s which allowed selecting the very first contact angle between the drop and the sample surface (see Figure 2-1). For each sample, the contact angle between the surface and three reference liquids was measured, with at least five drops per reference liquid. The characteristics of the chosen reference liquids are given in Table 2-2.

Table 2-2: Reference liquids for the contact angle measurements. Characteristics are reproduced from the liquid database of the SCA software.

	Surface tension $\gamma / \text{mN.m}^{-1}$	Dispersive component $\gamma^d / \text{mN.m}^{-1}$	Polar component $\gamma^p / \text{mN.m}^{-1}$
Water (deionised)¹¹³	72.80	21.80	51.00
Diiodomethane¹¹⁴	50.00	47.40	2.60
Thiodiglycol¹¹⁵	54.00	39.20	14.80

2.7 ION BEAM ANALYSIS

2.7.1 EQUIPMENT AND MEASUREMENT PRINCIPLE

Ion beam analysis (IBA) is a family of techniques that enables rapid quantitative analysis of elemental composition versus depth profiles of a labelled component within a material. Its use in polymer physics dramatically increased in the early 1990s to understand the behaviour of polymer blends and their surfaces. The techniques and their applications were discussed in details by Composto *et al.*¹¹⁶ and Thompson.¹¹⁷

Briefly, a beam of positive ions is created from a plasma, induced by feeding Helium-3 or Helium-4 gas into a radio frequency (RF) source chamber. The positive ions are forced out of the RF source by applying a 6 kV potential and are injected into a rubidium charge exchange cell (alkali vapour) to yield negative ions (Figure 2-2).

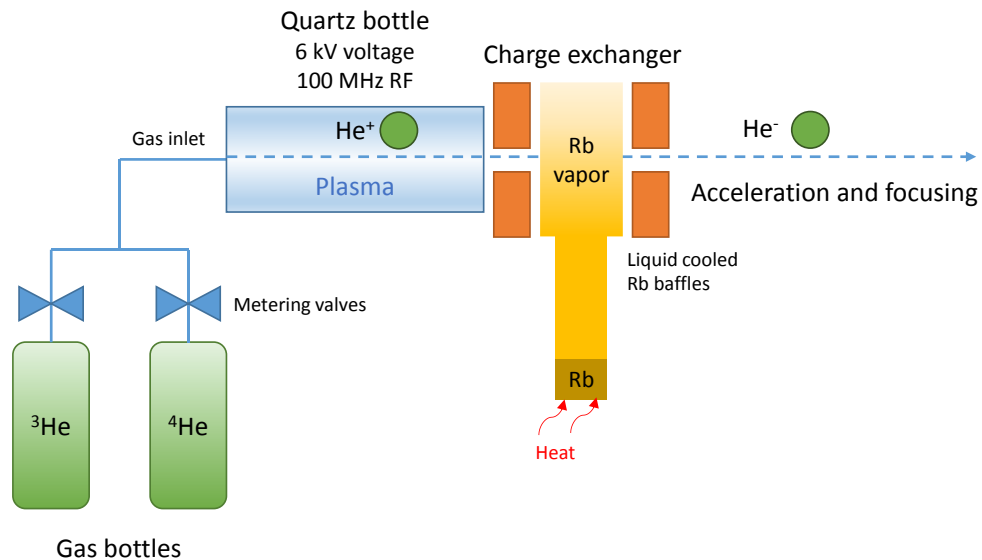


Figure 2-2: Schematic of a RF charge exchange ion source.

The negative ions go through a velocity selector and are focused, by means of a magnet, into the accelerator (Figure 2-3). The 1.7 MeV 5SDH pelletron accelerator tube (National Electrostatics Corp., Wisconsin, USA) is protected with x-ray shielding to ensure low radiation levels. It is worth mentioning that the radiation was monitored and well below $2 \mu\text{Sv/h}$ and that the exposure was within the dose limit for a classified worker (20 mSv/year).

The negative ions accelerated into the accelerator are converted back into positive ions and accelerated out. They form a 2 mm diameter beam which is then scattered by electrostatic and nuclear interactions with the sample situated in the RC43 end station (Figure 2-3). The end station is brought under high vacuum for analysis and is cooled down to approximately -80 °C using liquid nitrogen to avoid evaporation of volatile components. For the same reason, samples were also vitrified (by plunging them into liquid nitrogen) within a few minutes after spin coating onto a silica wafer. The resulting scattered ions, ejected ions, nuclear decay products and photons are detected by a passivated implanted planar silicon detector and their energy spectra analysed to obtain elemental or isotopic depth distributions.

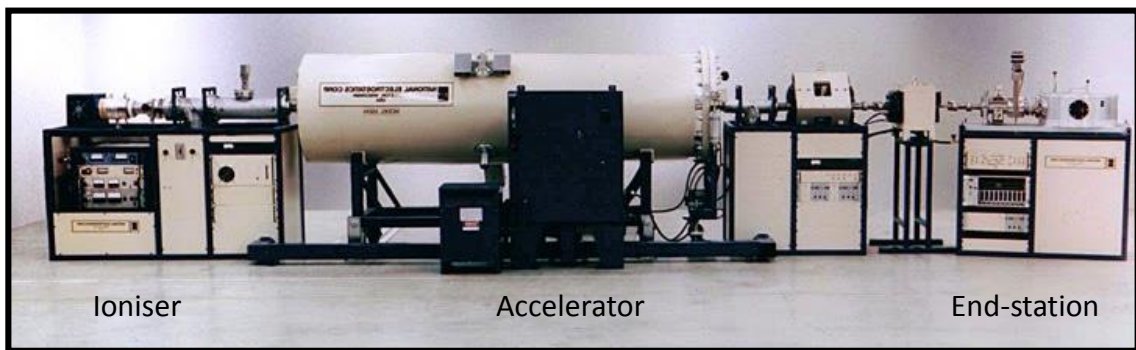


Figure 2-3: Picture of an Ion Beam accelerator.

The elemental depth distribution is obtained by knowing the relationship between the detected beam energy and the thickness of the sample. Indeed, the beam loses kinetic energy as it interacts with electrons in the sample. The stopping power S is the energy loss as the beam travels through a material:

$$S = -\frac{dE}{dz} \quad (2.2)$$

where E is the ion energy and z the distance traversed by the beam. S varies with the type of material considered, but for most polymers the stopping power for 1 MeV hydrogen and helium ions are of the order of 20 and 200 keV. μm^{-1} respectively.¹¹⁷

This technique can present at its best an elemental sensitivity of the order of parts per million and a depth resolution of 10s of nanometres. However, the beam of ions irreversibly damages the sample. It is then necessary to control the beam charge and to change the location of the beam print at each measurement to collect reliable data. To obtain statistically significant data

while controlling beam damage, multiple measurements can be taken at different points on the sample and data added together.

The elastic recoil detection analysis (ERDA) was mainly used in this project. Nuclear reaction analysis (NRA) has been used to confirm and reinforce ERDA data when necessary.

2.7.1.1 Elastic Recoil Detection Analysis (ERDA)

ERDA has had the greater impact on fundamental polymer science as it can quantify hydrogen isotopes depth distribution and does not require the use of costly ^3He .¹¹⁷ Combined with deuterium labelling, it enables the differentiation between labelled and non-labelled components.

Most commonly, 1 to 3 MeV Helium-4 ion beam is directed at the sample of interest¹¹⁶. For this project the samples consist in thin polymer films of about 150 nm thickness containing variable amounts of deuterated model additives. Some of the incident beam is forward scattered towards the detector. A suitable range foil thickness needs to be chosen so bigger ^4He ions are stopped by the foil while hydrogen H^+ and deuterium D^+ can pass through and be detected as shown in Figure 2-4. Deuterium ions are heavier than the hydrogen ions and therefore closer in mass to the incident ^4He ion beam. The kinematics of elastic scattering dictate that the maximum energy transfer between incident and scattered ions occurs when they are of similar mass. Hence, deuterium ions are detected at a higher energy range since they take a greater proportion of the kinetic energy in the collision. By choosing the right incident angle, it is possible to obtain H^+ and D^+ signals resolved from each other.

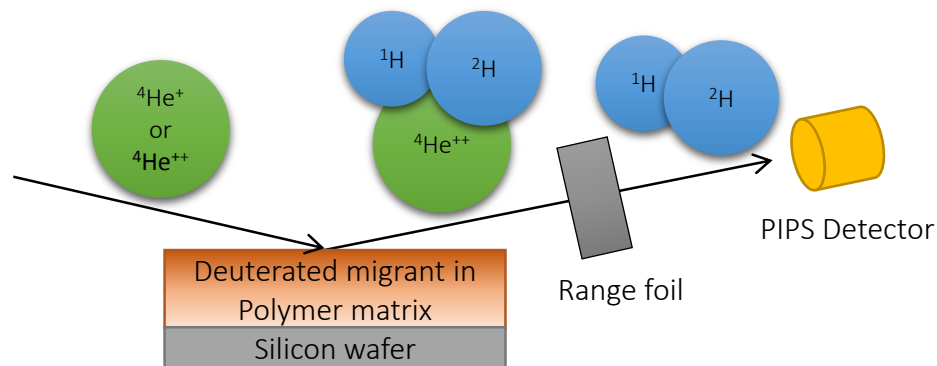


Figure 2-4: Schematic representation of ERDA.

In general, the beam was hitting the sample at an angle of 66° and the charge per sample spot was $1\ \mu\text{C}$. Up to 5 spots per spin coated sample could be measured. The data recorded at a specific angle was added for better statistics. The detector solid angle for ERDA is 1.43 msr. ERDA is considered as an accurate technique with an error of less than 10 % in counts per channel is usually achieved with a depth resolution of approximately 15 nm.¹¹⁶

2.7.1.2 Nuclear Reaction Analysis (NRA)

Unlike in ERDA, where the sample is submitted to elastic scattering (billiard ball-like collision where the total kinetic energy of the system is conserved, the atoms remain chemically the same and only the direction of propagation is changed), in the NRA experiments the incident ion penetrates into the target nucleus to excite a nuclear cascade. The most common reaction for detecting deuterium in the sample uses a Helium-3 incident ion. The probability of this reaction occurring being maximum around 0.65-0.7 MeV, a beam of 700 keV is generally used. This reaction is exothermic ($Q = 18.352\ \text{MeV}$) and can be written in the form ${}^2\text{H}({}^3\text{He}, {}^1\text{H}){}^4\text{He}$, where ${}^2\text{H}$ is the targeted nucleus, ${}^3\text{He}^+$ is the beam ion, ${}^1\text{H}^+$ is the detected element, and ${}^4\text{He}$ is a by-product.¹¹⁶

The high energy proton can be detected in backscattering geometry which eliminates the need of a range foil and improves the depth resolution. Moreover, the protons suffer less from energy loss as they exit the sample: a wider depth range can thus be profiled.¹¹⁷ The energy of the detected proton gives information on the depth of the reaction that has occurred and the quantity of atoms reacted. Deuterium concentration profiles can thus be obtained.

An incident beam angle of 80 or 83° was preferred for these experiments. The beam charge per spot was $1\ \mu\text{C}$. Generally, up to 5 beam spots could be recorded per spin-coated film. Data collected at one particular incident beam angle could be added to obtain more accurate results. The detector solid angle for NRA experiments was 2 msr. With an error of measurement of less than 10 % in counts per channel and a depth resolution of 8 nm this technique is considered more accurate than ERDA.¹¹⁶ However, using the isotope ${}^3\text{He}$ as an incident ion increases significantly the cost of the analysis. Hence, NRA was used in this project only to validate and precise ERDA concentration profiles.

2.7.2 FITTING METHODS

All IBA data were analysed with the Surrey University DataFurnace¹¹⁸⁻¹²⁰ software (WiNDF v9.3.68 running NDF v9.6a) to determine the concentration versus depth profile, where the densities of PI, PB and hPI were assumed to be ~ 0.9 and those of squalane, oligo-dS and oligo-dIB 0.81, ~ 0.9 and ~ 1 respectively.

Datafurnace can fit multiple spectra simultaneously, by iterating from an estimated layer profile to the best fit it can find, defined by the statistical parameter χ^2 (chi squared, not the Flory-Huggins parameter), based on the calculated difference between the data and fit at each data point. From this optimised fit, a compositional layer profile (of the deuterated oligomer in this case) is given. In order to avoid over-parameterisation, model composition profiles were restricted to a few layers, for which the composition and thickness was allowed to vary to obtain the best possible fit to the experimental data.

Alternatively, Datafurnace can fit data analytically, optimising equation parameters to gain the best fit. The profile output from an analytical fit is of the form of the given function, with the found parameters, and is more realistic. However, it can be difficult to find the optimal equation to fit the data. When the shape of the concentration profiles was simple enough (unique surface excess), the following fitting equation was used, with a_0 and a_1 the fitting parameters:

$$\phi(z) = 0.5 + 0.5 \times \operatorname{erf}\left(\frac{a_0 - z}{a_1}\right), \quad \text{with} \quad \operatorname{erf}(x) = \frac{2}{\pi} \int_0^x e^{-t^2} dt \quad (2.3)$$

The fitting procedures used for DataFurnace are described in more detail elsewhere.¹²⁰⁻¹²²

The Datafurnace profiles outputs (layered and analytical), have a depth scale expressed in atoms/cm² because this unit does not require information on density. Typically, for polymers with a density of $\sim 1 \text{ g.cm}^{-3}$, a surface excess of $1 \times 10^{15} \text{ atoms.cm}^{-2}$ corresponds to a thickness of 1 Å.ⁱ Converting the depth scale in length unit, one can calculate the surface excess concentration z^* of the oligomer by using the area under the curve.⁵⁹

ⁱ Conversion of depth scale between atoms per unit area and length:

For example, PB has a density of 0.9 g.cm^{-3} . Hence, 1 cm^3 of PB has a mass of 0.9 g . 1 repeat unit (C_4H_6) has 10 atoms and a mass of $\frac{54}{6.02 \times 10^{23}} = 9.0 \times 10^{-23} \text{ g}$. Therefore, 1 cm^3 of PB has $10 \times \frac{0.9}{9.0 \times 10^{-23}} = 1.0 \times 10^{23}$ atoms. This cube may be viewed as a 1 cm^2 square that is 1 cm deep. Thus, $1 \text{ Å} = 10^{-8} \text{ cm}$ depth of PB = $1 \times 10^{15} \text{ atoms.cm}^{-2}$.

$$z^* = \int_0^{z_0} \phi(z) - \phi_\infty dz \quad (2.4)$$

where $\phi(z)$, ϕ_∞ are the total and bulk volume fraction of the component respectively, z being the depth variable.

2.8 NEUTRON REFLECTOMETRY

Neutron reflectometry (NR) is a reflectivity technique which also yields depth distribution profiles of deuterated components. However, its depth resolution is about 0.5 nm which is superior to what can be achieved by IBA (~ 10 nm).¹²³ This high depth resolution is necessary to test theoretical predictions of the composition profile, which are typically of the order of polymer or molecular dimensions. It also provides a direct measure of film surface structure and layer thickness, density and roughness and can be performed under atmospheric conditions. However it is less sensitive to gradual changes in composition over ranges of > 10 nm and specular reflectometry can only be applied to very smooth materials (roughness < 10 nm) without lateral inhomogeneity to get a proper beam reflection.

NR involves the use of a highly collimated beam of neutrons that is directed onto an extremely flat surface (in this case, a ~ 50 -100 nm thick spin coated sample) with an incident angle ϑ_i , reflected at an angle ϑ_f and detected (Figure 2-5).

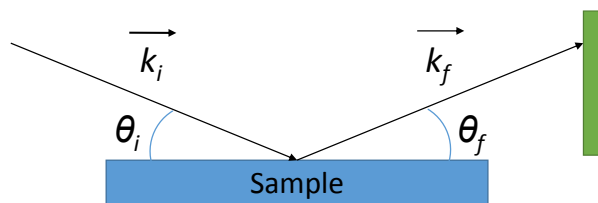


Figure 2-5: Schematic of a NR experiment.

The momentum transfer vector \mathbf{Q} is defined as the difference between the momentum of the incident wave \mathbf{k}_i and the momentum of the reflected wave \mathbf{k}_f .

$$\vec{Q} = \vec{k}_i - \vec{k}_f \quad (2.5)$$

Chapter 2: Experimental

In the case of a specular reflection ($\theta_i = \theta_f = \theta$), the moduli of the incident and reflected momenta are the same because the reflection of the beam is elastic. Hence, for a beam of wavelength λ (typically 2-10 Å),¹²³

$$\|\vec{k}_i\| = \|\vec{k}_f\| = \frac{2\pi}{\lambda} \quad (2.6)$$

and from combining equations (2.5) and (2.6), one can express the modulus Q of the momentum transfer vector, which depends only on the angle ϑ and the neutron wavelength λ .¹²³

$$Q = \|\vec{k}_i - \vec{k}_f\| = \sqrt{\|\vec{k}_i\|^2 + \|\vec{k}_f\|^2 - 2\|\vec{k}_i\| \times \|\vec{k}_f\| \times \cos(2 \times \overrightarrow{k_i, k_f})} = \frac{4\pi \sin\theta}{\lambda} \quad (2.7)$$

Within Born approximation which consists in ignoring the generally weak multiple reflection processes, the specular reflectivity defined as¹²⁴

$$R(Q) = \frac{16\pi^2}{Q^4} \left| \int s'(z) e^{-iQz} dz \right|^2 \quad (2.8)$$

is calculated as a function of the momentum Q , with z the depth of the film and s is the scattering length density (s.l.d.) – dependent on the density and on the atomic percentage of the components of the sample. Hence, for organic hydrocarbon systems, NR also requires deuterium labelling to obtain the contrast in s.l.d.. The s.l.d. is calculated according to equation (2.9) from the scattering length contributions b_i of each atom in a unit cell of volume $V_m = M / \rho N_A$. The b_i corresponding to the atoms of interest in this thesis are reported in Table 2-3.¹²³

$$s = \frac{\sum_{i=1}^N b_i}{V_m} \quad (2.9)$$

Table 2-3: Scattering length contributions of the elements and isotopes of interest.¹²⁵

Element / Isotope	Scattering length contribution, $b_i / 10^{-15} \text{ m}$
H	-3.7406
D	6.671
C	6.6460
O	5.803
Si	4.107

In the case of a single interface between a medium of refractive index n_0 and a medium of refractive index n_1 the reflectivity at high Q becomes simply:

$$R(Q) = \frac{16\pi^2}{Q^4} \Delta s^2 \quad (2.8')$$

And the reflectivity profile is following a Q^4 decay, such as in Figure 2-6.

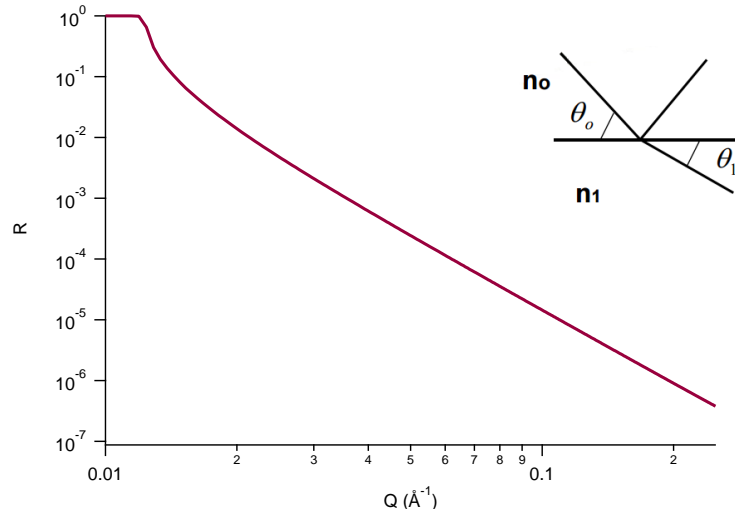


Figure 2-6: Theoretical reflectivity profile of a perfectly flat interface between air (s.l.d=0) and a phase of s.l.d.= $3 \times 10^{-6} \text{ \AA}^{-2}$, obtained with Igor pro software and Motofit package.

In the case of a single film of refractive index n_1 and thickness z_1 on a substrate of refractive index n_2 – i.e. two interfaces between 3 media – the reflectivity $R(Q)$ is written as:¹²⁴

$$R(Q) = \left| \frac{r_{01} + r_{12}e^{-2i\beta}}{1 + r_{01}r_{12}e^{-2i\beta}} \right|^2 \quad (2.8'')$$

where $r_{ij} = \frac{(p_i - p_j)}{(p_i + p_j)}$ is the Fresnel coefficient at the ij interface, defined with $p_i = n_i \sin\theta$, and

the coefficient $\beta = \frac{2\pi}{\lambda} n_1 z_1 \sin\theta_1$ is the optical path length in the film.¹²⁴ In this case the reflectivity profile presents “Kiessig fringes”, due to constructive and destructive interferences between the reflected beams on the 2 interfaces, as shown in Figure 2-7.

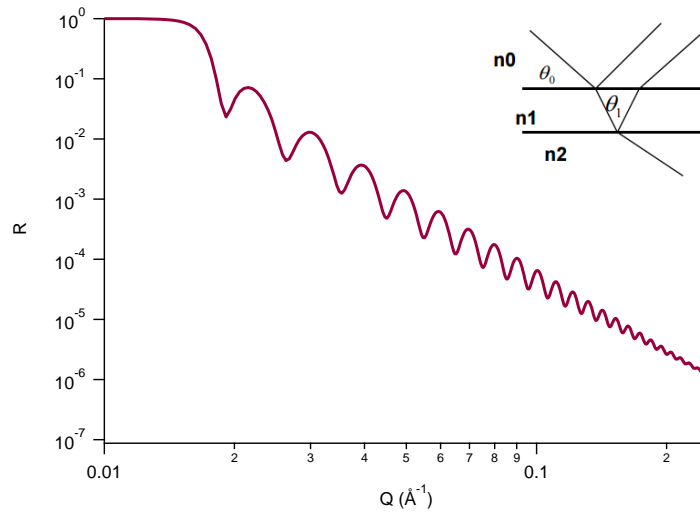


Figure 2-7: Modified theoretical reflectivity profile from Figure 2-6 when adding a 60.0 nm thick film of s.l.d=5 between the two original phases, obtained with Igor pro software and Motofit package.

The spacing in between the Kiessig fringes, ΔQ , depends on the thickness of the film z_0 , following the equation:¹²³

$$\Delta Q = \frac{2\pi}{z_0} \quad (2.10)$$

The above equations describe theoretically flat surfaces. Experimentally, surfaces and interfaces might exhibit local imperfections and roughness. Alternatively, the interface between two materials can be diffuse. For a simple interface, it is then possible to apply a Debye-Waller-like factor to the Fresnel coefficient that will result in a larger Q^{-4} dependence in the specular reflectivity as:¹²⁴

$$R(Q) = R_0 \exp(-q_i q_j \langle \sigma \rangle^2) \quad (2.8''')$$

where $\langle \sigma \rangle$ is the root mean square Gaussian roughness, $q_0 = 2k \sin \theta_0$ and $q_1 = 2k \sin \theta_1$. Alternatively, for thin films, the Debye-Waller-like factor can also be directly applied to the Fresnel coefficient r_{ij} defined in equation (2.8''). It is also important to note that it is impossible to distinguish surface roughness from a diffuse interface by specular neutron reflectometry.¹²⁴

When the neutron beam is reflected by more than 2 interfaces, the reflectivity profile becomes more complex. Its shape and number of fringes will depend on the thicknesses and s.l.d.s of the different layers, and the s.l.d. gradient at the interface between each layer.

The reflectivity is ideally measured from before the critical edge – i.e. total reflection – ($Q_c = \sqrt{16\pi\Delta\rho} \sim 0.01 \text{ \AA}^{-1}$ for silicon/air) to the point at which the signal is indistinguishable from the background ($Q \sim 0.25 \text{ \AA}^{-1}$). These measurements required two to three angles of incidence and approximately 1.5-2 hours of acquisition time per sample on the SURF, INTER or OFFSPEC reflectometers at ISIS pulsed neutron and Muon source, UK. This latter factor imposed a requirement that films must be stable for several hours: alteration in film thickness during measurement would make accurate interpretation of the data impossible. The three instruments generated largely equivalent data over this range of Q for these samples. Data acquisition on INTER was somewhat more rapid than the other reflectometers due to the large flux and simultaneous Q range. Measurements were carried out according to established protocols, which are outlined in earlier works on SURF¹²¹ and INTER.¹²⁶ Typical running conditions are reported in Table 2-4.

Table 2-4: Typical running conditions on the three neutron reflectometers.

Instrument	1 st angle, Beam fluence / $\mu\text{A.h}$	2 nd angle, Beam fluence / $\mu\text{A.s}$	3 rd angle, Beam fluence / $\mu\text{A.h}$
SURF	0.3°, 30	0.65°, 60	1.5°, 90
OFFSPEC	0.35°, 15	0.7°, 30	1.6°, 35
INTER	0.5°, 8	2.3°, 25	/

The software MantidPlot¹²⁷ version 3.6.0 or the Open Genie¹²⁸ script window (available from ISIS) was used to stitch the data at the different angles and subtract the incoherent background, measured as the signal detected through air (or through the Silica block, in the case of an inverted sample). Fitting of the NR data was performed with the analysis software IGOR Pro, using the Motofit package.¹²⁹ This fitting method usually consists in a layer fit, in which each layer is defined by its thickness and s.l.d.. The roughness in between layers – i.e. gradient – has the shape of an error function and is therefore symmetric. Once the s.l.d. depth profiles were obtained from the fitting of the reflectivity data, a simple proportional scaling was applied, knowing the s.l.d.s of the pure components, in order to plot concentration depth profiles. The scattering length densities of the organic components in the film are shown in Table 2-1. The s.l.d. value for the silicon ($2.07 \times 10^{-6} \text{ \AA}^{-2}$) and the native oxide layer ($\sim 3.45 \pm 0.4 \times 10^{-6} \text{ \AA}^{-2}$) was

consistent with results that have been inferred from previous experiments on silicon substrates.^{126, 130, 131}

2.9 ATOMIC FORCE MICROSCOPY

Atomic force microscopy (AFM) – or scanning probe microscopy (SPM) – uses the deflection of a cantilever, caused by the interaction between the tip of the cantilever and the sample, to measure the sample's surface topology at micro and nanometre lengths scales. The position of the cantilever is achieved with high resolution thanks to the use of a piezo-ceramic element that expand or contract when a voltage gradient is applied. The cantilever angular deflections are measured by light reflection onto a sensitive photodiode that prompts a voltage output. This voltage is compared to a reference value corresponding to the rest position. Any difference with the reference gives information on the surface atomic forces and topology.

Samples were prepared by spin coating or solvent casting onto $\sim 1 \times 1 \text{ cm}^2$ substrates. Double sided tape was then applied to the bottom of the substrate so a small steel disk could be attached to the sample. This would then be held in place inside the AFM sample housing by a magnet. A Bruker MM8 Multimode AFM was used to characterise lateral variations in the sample's surface properties. Analysis was made with a least 256 line resolution in Peakforce quantitative nanoscale mechanical characterisation (QNM) mode at 2 kHz in the vertical direction and Nanoworld Arrow™ NCR probes with a nominal force constant of 42 N.m^{-1} . Images were analysed using Bruker NanoScope Analysis v1.1 software. 3D topographic mappings presented in this thesis use the adhesion channel as a colour-coded skin. The adhesion channel measures the pull-off force, as schematised on Figure 2-8. The adhesion maps obtained are only qualitative because of the uncertain area of contact between the tip and the sample for the considered samples.

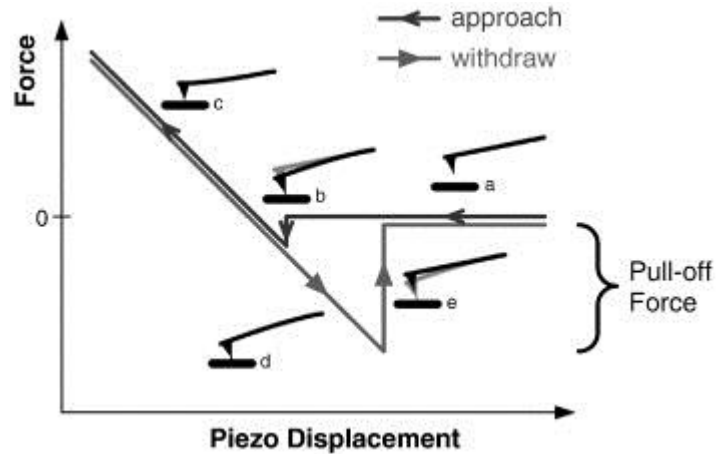


Figure 2-8: Sketch of a typical AFM force versus displacement curve. The pull-off force corresponds to the measured adhesion force. Reprinted from *Cement and Concrete Research*, 41, Lomboy et al., A test method for determining adhesion forces and Hamaker constants of cementitious materials using atomic force microscopy, 1157-1166, Copyright (2011), with permission from Elsevier.¹³²

2.10 RHEOLOGY

2.10.1 MEASUREMENT DESCRIPTION

A rheometer AR2000ex from TA instruments Trios was used to perform oscillating rheology measurements of oligomer/polymer mixtures. A 2.5 cm diameter parallel plate was used to measure the storage and loss moduli – respectively G' and G'' – of a ~ 1 mm thick solution cast sample at temperatures ranging from 10 to 125 °C. A 1 % strain was used and the angular frequency was varied from 0.01 to 100 rad/s with 5 points per decade. Two repetitions per sample were measured, leading to similar results.

To make sure that the sample was presenting a linear viscoelastic behaviour over this range of temperature and angular frequencies, control experiments were performed at 125 °C and 10 °C, at a frequency of 1 Hz and varying the strain from 0.01 to 10 %. A deviation of the complex modulus G^* by more than 10 % from a constant (plateau) value would indicate deviation from the linear viscoelastic behaviour. This has not been evidenced for any of the samples in this thesis over the chosen range of parameters.

2.10.2 TIME-TEMPERATURE SUPERPOSITION PRINCIPLE

A time-temperature superposition (TTS) construction was performed from the data collected at the different temperatures. The origin of this method is empirical.¹³³ The curves of G' and G'' as a function of frequency at several temperatures can be superposed. This construction yields G' and G'' curves called *master curves* at a certain reference temperature T_0 , over a wider range of frequencies. The master curve G_R at the reference temperature T_0 is therefore defined independently from T as follows

$$G_R(a_T\omega) = b_T G(a_T\omega, T) \quad (2.11)$$

with ω the angular frequency and a_T and b_T the shifting coefficients dependent on temperature, corresponding to the shifts in angular frequency and modulus, respectively.

As explained previously, the master curve G_R does not depend on the temperature; it regroups the response from the system at different temperatures. The viscoelastic answer is constant for the same ωa_T values. The polymer has an identical behaviour at (ω_0, T_0) and in the state at $(\omega_0/a_T, T)$: this is the theorem of corresponding states.¹³⁴ The determination of the shift coefficients a_T and b_T is mainly empirical.¹³³ The shift coefficients can be brought in relation with the intrinsic viscosity in the case of low molecular weight polymers such as

$a_T = \frac{\eta_0(T)}{\eta_0(T_0)} \cdot \frac{\rho(T_0)T_0}{\rho(T)T}$ and $b_T = \frac{\rho(T_0)T_0}{\rho(T)T}$ where ρ is the density and η_0 the viscosity during continuous flow. More generally, the WLF (Williams, Landel, Ferry) equation can be used as below:

$$\ln(a_T) = \frac{-A(T - T_0)}{B + (T - T_0)} \quad (2.12)$$

with A and B two constants dependent on the polymer's nature (independent from its molecular weight). When T_g is used as T_0 , A and B are called C_1 and C_2 respectively and are tabulated in the literature for most polymers, with, generally, $6 < C_1 < 34$ and $20 < C_2 < 130$ Kelvin. Typically, the WLF equation is employed in the range of temperatures between T_g and $T_g + 100$ °C. It has been observed experimentally that most of the time a_T follows the WLF equation. Thus, this equation became a validity test for TTS constructions.¹³³

2.11 TACK TESTS

For the tack tests, the sample preparation was performed by Henkel in Düsseldorf. 10 vol% solutions of PBcis in toluene were prepared. Squalane was added in the necessary proportions to obtain new solutions containing 0, 10, 20, 40 and 60 % (w.w) squalane in PBcis. The solution was spread at 3 m/min onto a PET film using a surgical blade. The coating was left to dry at room temperature for 30 min, then at 120 °C for 5 min in order to obtain a 20 gsm thick film (about 20 μm).

2.11.1 LOOP TACK TESTS

The loop tack test was performed following the ASTM D6195 test method description.¹³⁵ A strip of coated PET of 175 mm long and 25 mm large was attached to the clamps of a tensile testing machine, forming a loop with the coating on the outside. The loop was brought into contact with the entire face of a clean steel plate of area 25 × 25 mm² at a rate of 300 mm/s. The only force applied is the weight of the adhesive strip itself. It was then left in contact for 2 s and withdrawn at the same rate. The peak in normal force required to remove the loop from the steel plate was recorded. The procedure was repeated 3 times for each sample.

2.11.2 TACK TESTS USING THE RHEOMETER

The tack performance was alternatively evaluated using an AR2000ex rheometer from TA instruments Trios. The coated PET films were fixed onto the sample stage using double sided tape. A normal force of 5 N was applied with a 4 cm diameter parallel plate for 10 s, before pulling the geometry up at a rate of 500 $\mu\text{m/s}$. The peak in normal force was recorded following this procedure at 23 °C, for 3 sample repetitions on samples issued from the same solution cast film.

Chapter 3: MODEL SYSTEMS

3.1 DETERMINATION OF THE MODEL COMPOUNDS

Based on the discussions in *Chapter 1*, the main parameters impacting segregation in oligomer/polymer mixtures were identified:

- the difference in surface energies between the oligomer and the polymer
- the difference in molecular weight between the oligomer and the polymer
- the interaction parameter between the oligomer and the polymer
- the concentration of oligomer
- temperature

One can note that some of these parameters are coupled to each other such as the surface energies and the interaction parameter. It is also suggested, from FH, that the molecular weight of the polymer does not affect the bulk compatibility if it is big enough compared to the oligomer molecular weight.

From these parameters, knowing the main components of an SBC-based adhesive formulation and trying to keep the system as simple as possible, bi-component mixtures were hence established as model formulations. Polymers representative of the middle rubbery block were selected: two polybutadienes of distinct chemical structures as well as a polyisoprene and its hydrogenated analogue – i.e poly(ethylene-alt-propylene). Squalane was chosen as the main oligomer of the study. It is a molecule largely used and well-characterised in the cosmetic industry and commercially available in its deuterated form for IBA and NR purposes. In order to test the effect of the oligomer molecular weight, two deuterated oligomers of isobutylene of M_w 1260 and 2970 g.mol⁻¹ were also selected – i.e. respectively $\sim 3 \times$ and $\sim 7 \times$ bigger than squalane, but with a similar saturated structure. A deuterated tetramer of styrene, of comparable molecular weight as squalane but of higher polarisability, was used to study the effect of the interaction parameter and surface energy on the segregation. The proportions of polymer/oligomer were kept as close as possible to the industrial formulation, with weight ratios

ranging from 30/70 to 70/30. Additionally, the impact of temperature on the surface segregation was studied by NR. The detailed list of components and their physical properties of interest for the study were given earlier in *Chapter 2* (see 2.1).

3.2 JUSTIFICATION OF THE FORMULATION SIMPLIFICATION

3.2.1 DIFFUSION OF SQUALANE IN DEUTERATED PS

Tackifiers, such as aliphatic C5 resins, have a high compatibility with the rubbery mid-block of SBCs and are considered insoluble in its PS glassy domains.^{136,101} Hence, in order to keep the model systems as simple as possible while obtaining a reliable first-level understanding of the phenomenon of additive surface segregation in polymer melts, binary model formulations were chosen, prepared as blends of oligomer with rubbery polymer but neglecting the presence of the glassy domains. To justify the elimination of the PS blocks from the model formulation, neutron reflectometry experiments were performed to quantify the interdiffusion of hydrogenated squalane in deuterated polystyrene (d-PS). As discussed in 1.2.5.2, similar NR investigations were performed, studying the interdiffusion of oligo-styrene ($M_w = 1.11 \text{ kg.mol}^{-1}$) in deuterated polystyrene films⁷² or phthalates additives in deuterated poly(methyl methacrylate) films.^{69,73,71} Here, the focus was however on the equilibrium state of the samples and the affinity of the oligomer with the polymer rather than on the kinetic aspect of the oligomer diffusion. The equilibrium state was assumed to be reached within the 2-3 hours needed to measure the neutron reflectivity data at 3 incident angles as described in 2.8.

A film of d-PS was spin coated onto a silicon block. After subtraction of the off-specular background, the reflectivity data was fitted to obtain a real-space profile of the scattering length density (s.l.d.) as a function of depth, using a 4-layer fit: an infinite backing media corresponding to the silicon block with a s.l.d. equal to $2.07 \times 10^{-6} \text{ \AA}^{-2}$, a 2 nm thick silicon oxide layer of s.l.d. $3.45 \times 10^{-6} \text{ \AA}^{-2}$, a layer of d-PS of unknown thickness nor s.l.d. and an infinite fronting media of s.l.d. 0 \AA^{-2} corresponding to air. The fitting parameters used are reported in Table 3-1 for this sample (for the next samples, the fitting parameters are reported in *Annex 3*). Assuming that the film was purely composed of d-PS, the related concentration profile was obtained using a simple

scaling of the s.l.d. profile, and suppressing the part of the profile describing the substrate. The stitched reflectivity data, fitting and resulting s.l.d. and concentration depth profiles are shown in Figure 3-1.

Table 3-1: Fitting parameters related to the fit shown in Figure 3-1.

Layer	Thickness / Å	s.l.d. / 10^{-6}Å^{-2}	Roughness / Å
fronting	INF	0	
1	617.98	6.3001	5
2	20	3.45	5
backing	INF	2.07	5

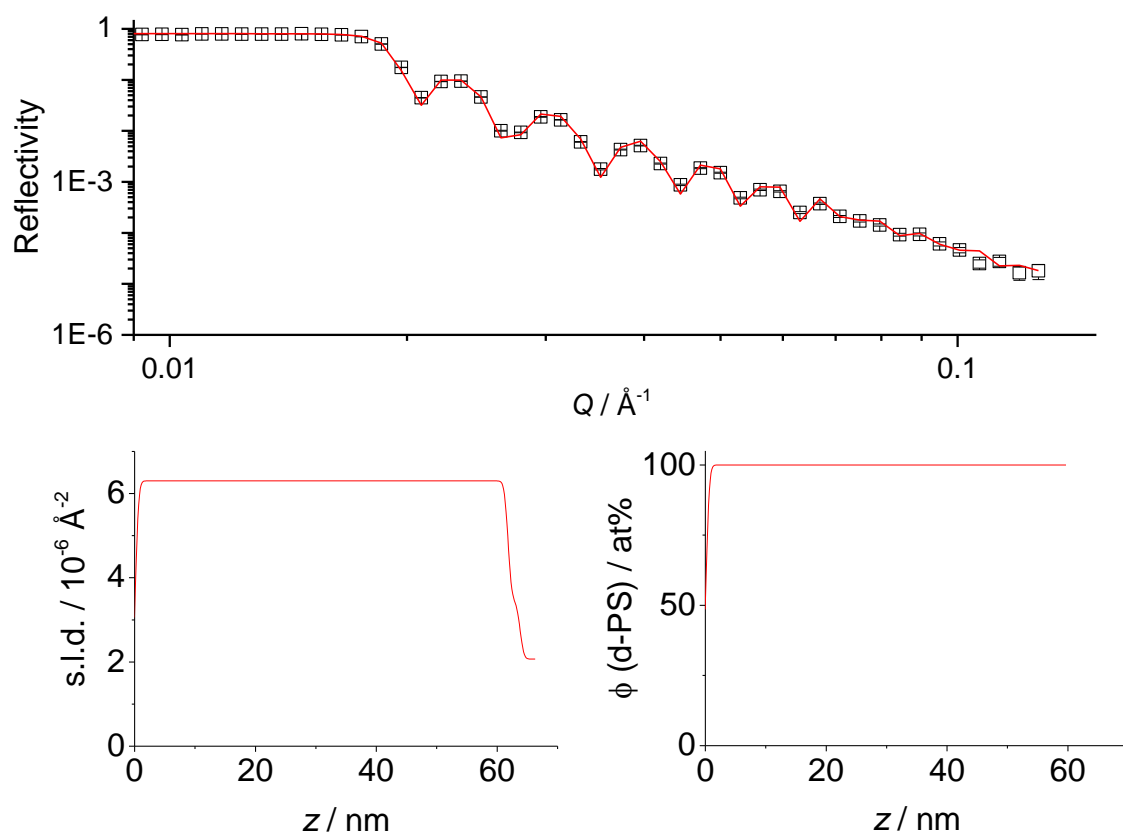


Figure 3-1: (top) Neutron reflectivity data measured with OFFSPEC (open squares) and fit to the data (red line) as a function of the momentum transfer Q and (bottom left) s.l.d. and (bottom right) concentration depth profiles corresponding to the fit.

The original thickness and s.l.d. of the d-PS film were obtained from the fit to the reflectivity data as being 61.7 nm and $6.30 \times 10^{-6} \text{Å}^{-2}$ respectively (see Table 3-1). One can note that the s.l.d. is slightly lower than what can be commonly found in literature.¹³⁷ This is not surprising since the

film was not annealed after spin coating and therefore could have a slightly lower density than expected for bulk polystyrene.

Following this first measurement, a drop of squalane was set onto a non-reflective etched Si block and the d-PS film was inverted and put in contact with the pure squalane (as shown schematically in Figure 3-2) in a similar set-up used by Bucknall *et al.* for real-time measurement of polymer diffusion front velocities.⁷² Specular reflectivity was then measured against the momentum transfer Q at 25, 35, 45, 55 and 65 °C.

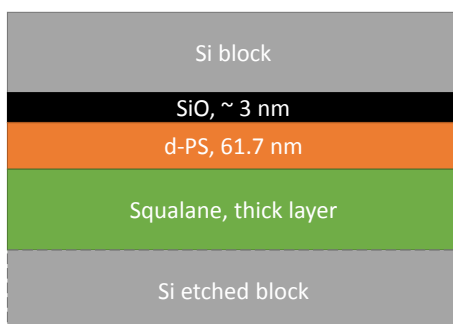


Figure 3-2: Schematic of the sample set up for the interdiffusion of squalane in d-PS.

Raw reflectivity data and their fits are given in the inset of Figure 3-3 with the composition profiles obtained from the fits in the main figure. The evolution of the s.l.d. and thickness of the d-PS layer as well as the interfacial width between the d-PS and squalane layer are given as a function of temperature in Table 3-2. For compatible additives, it is expected to measure a swelling of the film thickness and a broadening of the interfacial width w due to the oligomer diffusion into the polymer film, even at temperatures lower than the polymer's T_g .⁷¹ The variation in the data is insufficient to conclude on any effect of the contact with squalane on the d-PS film in this range of temperature, when compared to the method resolution of ~ 0.5 nm and accuracy of the fits. Therefore, in the case of a glassy d-PS (for $T < T_g \sim 100$ °C), the hypothesis of insolubility of the model additive in the PS blocks is validated.

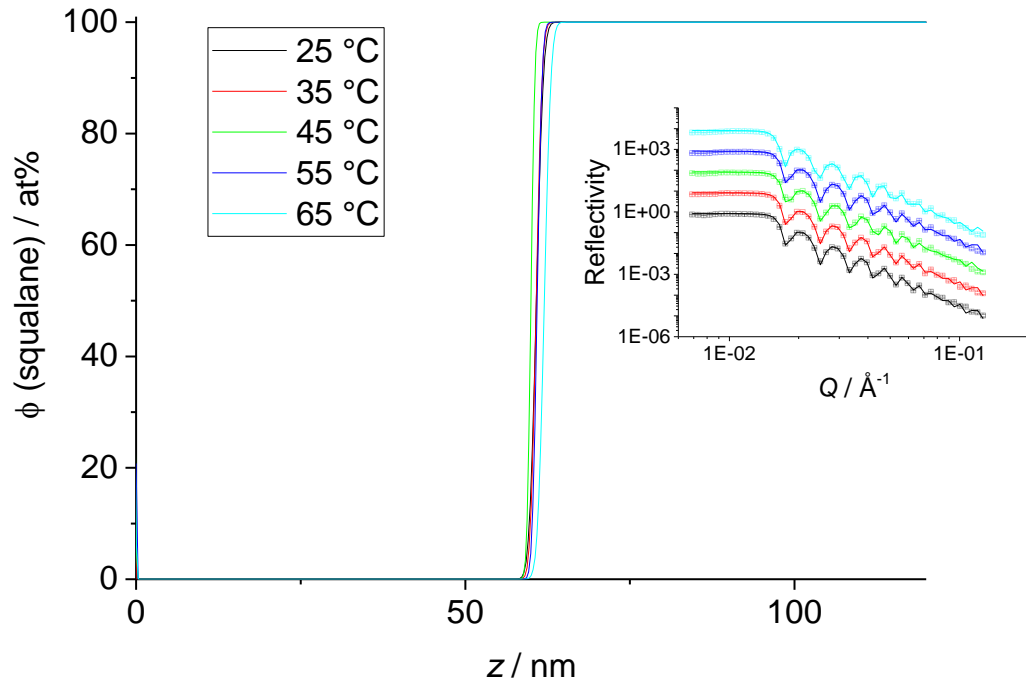


Figure 3-3: Squalane ingress into a d-PS film with increasing T .
The raw data measured with OFFSPEC and corresponding fits are in the inset.

Table 3-2: Main characteristics of the d-PS layer as the squalane is put in contact at various temperatures.

Temperature / °C	s.l.d. d-PS layer / 10^{-6}\AA^{-2}	Thickness d-PS / nm	Interfacial width / nm
original	6.29	61.7	
25	6.19	61.7	1.3
35	6.21	61.6	1.3
45	6.39	61.5	1.2
55	6.26	61.9	1.2
65	6.02	62.8	1.1

A second d-PS film in contact with squalane was produced. In this experiment, the sample was measured at room temperature, heated to 120 °C to overcome the glass transition and expose a rubbery d-PS, with more mobile chains, to the model additive. Then, it was cooled down to room temperature to evidence any irreversibility in the behaviour. Raw reflectivity data and their fits are given in the inset of Figure 3-4 with the composition profiles issued from the reflectivity fits presented in the main figure. The evolution of the s.l.d. and thickness of the d-PS layer as well as the roughness between the d-PS and squalane layer are given as a function of

temperature in Table 3-3. Drawing conclusions from the previous result, showing that the d-PS layer in contact with squalane remains pure at 25 °C, the fitted s.l.d. of the polymer layer at 25 °C was chosen as the one representative of the pure d-PS spin coated film ($6.17 \times 10^{-6} \text{ \AA}^{-2}$). Due to the significant difference in temperature and to the change of state of the d-PS, the s.l.d.s at 120 °C were recalculated according to modified densities.^{138,139} the s.l.d. for d-PS was adjusted to $6.13 \times 10^{-6} \text{ \AA}^{-2}$ (instead of $6.17 \times 10^{-6} \text{ \AA}^{-2}$ at 25 °C) and for squalane to $-0.34 \times 10^{-6} \text{ \AA}^{-2}$ (instead of $-0.37 \times 10^{-6} \text{ \AA}^{-2}$ at 25 °C). The concentration profile at 120 °C was scaled from these adjusted values.

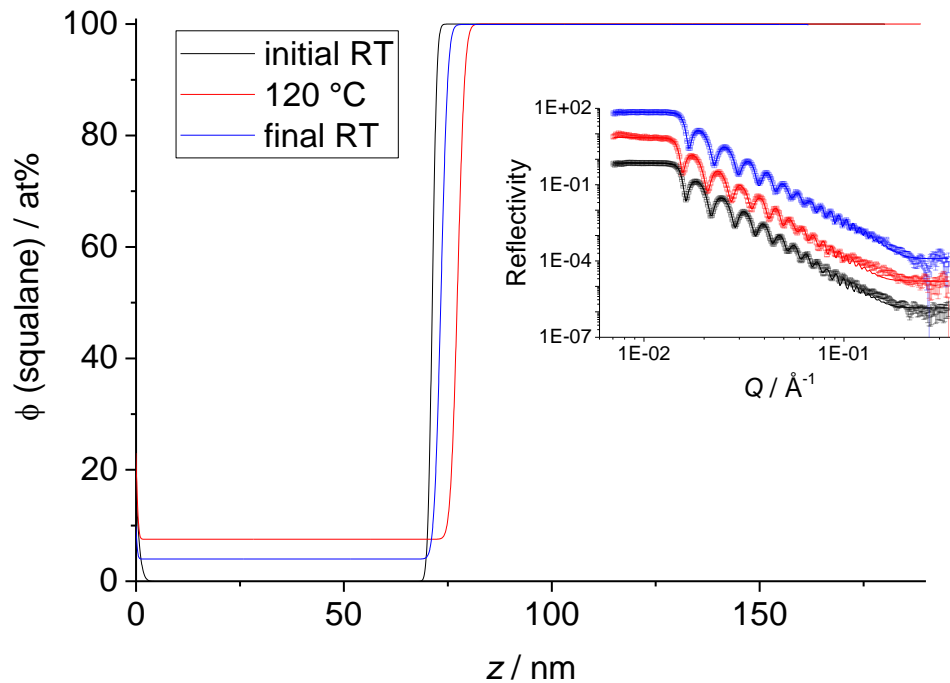


Figure 3-4: Squalane ingress into a d-PS film for $T > T_g$. The raw data measured with INTER and corresponding fits are presented in the inset.

Table 3-3: Main characteristics of the d-PS layer as squalane is put in contact before, during and after heating to $T > T_g$.

Temperature / °C	s.l.d. d-PS layer / 10^{-6} \AA^{-2}	Thickness d-PS / nm	Interfacial width / nm
25	6.17	71.0	0.8
120	5.64	77.5	1.4
25	5.90	73.9	1.3

Interestingly, as the polymer is heated above T_g , some squalane ingresses into the film. A reduction of the s.l.d. is observed – which is translated after a linear calculation into an increase in concentration from 0 to 8 at% – and corresponds well to the observed increase in thickness from 71 to 77.5 nm (+ 9 %). Over the time of measurement (2-3 hours), this value can be considered as the equilibrium saturation value of squalane in the d-PS film. Upon cooling, the squalane is not fully removed from the film: about 4 at% remains, which also corresponds to an increase in thickness of 4 % relative to the initial thickness. Additionally, one can note that the best fit obtained for these samples implies the use of relatively large thicknesses for the silicon oxide layer (4.5 to 5 nm, as reported in *Annex 3*). Since such oxide layers are expected to be no more than 4 nm, this data might suggest the presence of a thin layer of hydrogenated squalane at the interface with the substrate.

3.2.2 DIFFUSION OF INDUSTRIAL TACKIFIERS IN DEUTERATED PS

The effect of two industrial adhesive tackifiers on PS blocks was investigated. The two tackifiers are produced by the Eastman Chemical Company: Picco 6100, a partially unsaturated hydrocarbon resin produced from petroleum derived aromatic monomers and Regalite S1100, a fully hydrogenated resin, also derived from petrochemical feedstock. More properties of these components can be found in Table 3-4, as available from the technical data sheets.^{140,141} For convenience, Picco 6100 and Regalite S1100 will henceforth be called Picco and Regalite.

Table 3-4: Typical properties of Picco and Regalite, industrial tackifiers.

	Picco 6100 (unsaturated)	Regalite S1100 (saturated)
Softening point / °C	104	100
Colour	amber	water-white
Density at 25 °C / g.cm³	1.02	0.99
M_w / g.mol⁻¹	1800	900
M_n / g.mol⁻¹	550	600
M_z / g.mol⁻¹	5300	1300

The same experimental setup was used as described in Figure 3-2. The s.l.d.s of the hydrogenated Picco and Regalite were calculated from their density and likely C to H ratio: $0.20 \times 10^{-6} \text{ \AA}^{-2}$ was chosen for Picco (C_3H_5 , partially unsaturated) and $-0.35 \times 10^{-6} \text{ \AA}^{-2}$ for Regalite (C_1H_2 ,

fully saturated). For both sets of experiments, the s.l.d. and thickness of the d-PS film was measured at 80 °C and used as a “pure” reference for further calculations. The film was then reversed and put in contact with a Si etched block onto which the tackifier was melted and then spread, and specular reflectivity was measured at 80, 90, 100, 110, 120 °C and one more time after cooling down the sample well below the T_g of the d-PS.

In Figure 3-5 are gathered the reflectometry data and fits (inset) as well as the corresponding concentration profiles related to the Picco samples (main figure). In this case, the fitting to the raw data seems of inferior quality compared to the squalane samples. The fitting resolution used in the software was fixed at a 5 % dQ/Q , but it seems that the fitting quality improves by increasing the resolution to 8 %. Since the fitting resolution is not a fitting parameter, this improvement could suggest that the film is quite rough or wavy, or that it poorly covers the substrate. The Picco layer might also not be very homogeneous since the tackifier is a hard solid up to 100 °C and that it was difficult to spread it onto the etched silica block even at high temperature. The quality of the data also worsens with increasing temperature (critical edge becomes wobbly) which could be due to film dewetting. However, from the position of the fringes and critical edge it is still possible to fairly fit the thickness and s.l.d. of the d-PS film, once it is in contact with Picco.

The s.l.d. and thickness of the pure polymer film were determined as $5.89 \times 10^{-6} \text{ \AA}^{-2}$ and 90.2 nm. Again, the s.l.d. determined is somewhat lower to values commonly reported in literature¹³⁷ but still corresponds to reasonable density values for dPS,¹³⁸ considering the absence of annealing step and the slightly higher temperature in the SURF instrument room versus OFFSPEC. The evolution of s.l.d. and thickness with temperature is given in Table 3-5. From the data, it is evident that the s.l.d. of the pure d-PS layer is decreased by about 15 % and that its thickness increases by about 19 %. Considering the loose accuracy of the fitting, this data is pointing to the direction of a fairly good compatibility between the Picco and the d-PS layer (~ 15 % Picco dissolved in the d-PS film), even at temperatures lower than the T_g of d-PS (~ 100 °C), which led to film swelling and eventually dewetting. At temperatures above the T_g of d-PS, there is no evidence of a further modification of the film. Upon cooling, it seems that no extensive phase separation or shrinkage of the film with loss of Picco occurs.

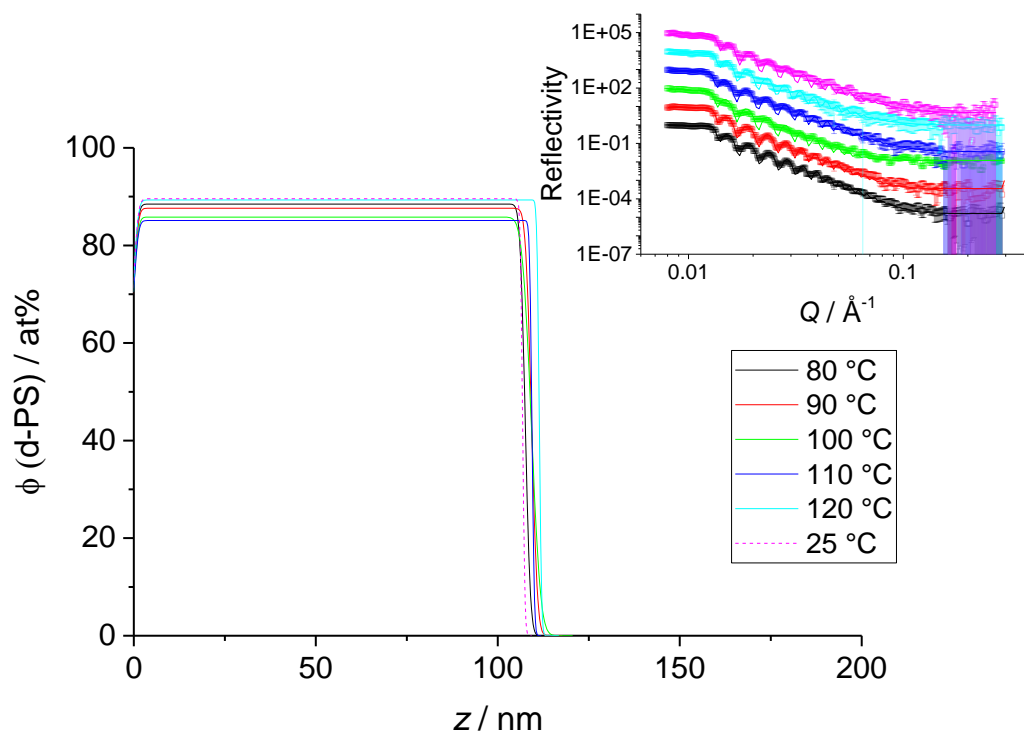


Figure 3-5: Picco ingress into a d-PS film with T .
The raw data measured with SURF and corresponding fits are presented in the inset.

Table 3-5: Main characteristics of the d-PS layer as the Picco is put in contact at various temperatures.

Temperature / °C	s.l.d. d-PS layer / 10^{-6} \AA^{-2}	Thickness d-PS / nm	Roughness / nm
Reference	5.89	90.2	/
80	5.23	107.5	1.1
90	5.17	109.3	1.3
100	5.07	109.3	2.0
110	5.03	109.4	0.5
120	5.27	111.4	0.5
25	5.28	106.7	0.5

Again, similar experiments were performed with Regalite, a saturated hydrocarbon of low molecular weight (Figure 3-6). The reflectivity data seem here more reliable than the Picco data since the critical edge remains consistent at each temperature. The quality of the fits was improved at high Q s by adding a thin layer of Regalite at the interface with the substrate. It is difficult to determine if this interfacial Regalite layer truly exists or if it corresponds to an unusually thick silicon oxide layer (as it was treated in the case of squalane). It might be due to

some faults in the d-PS film, through which the Regalite could flow and then spread at the interface, or to density differences at the temperature considered here, since the s.l.d.s were not adjusted in this case. From the 80 °C data, showing no Regalite in the d-PS film, it seems difficult to believe that the Regalite, (hypothetically less polar than the d-PS, from the information available from the supplier) would migrate through the incompatible d-PS film and segregate at the interface. More generally, the results are comparable to what happened with squalane. The d-PS film remains unchanged at temperatures lower than 100 °C. At temperatures higher than 100 °C, it starts swelling with an uptake of Regalite up to ~ 20 % at 120 °C. Upon cooling, the film shrank but most of the Regalite remained trapped in the film. The behaviour of Regalite is very different from the behaviour of Picco, which seems more compatible with the d-PS. It was expected from their molecular structure, since Picco is derived from aromatic resins and is therefore more alike with the PS repeating units.

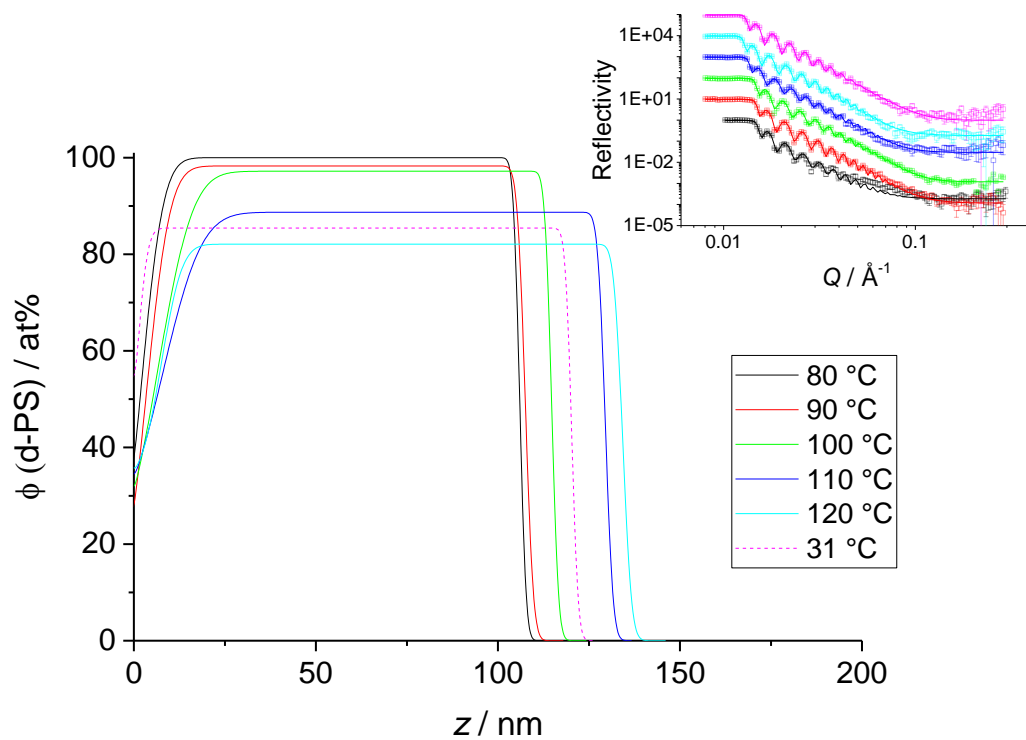


Figure 3-6: Regalite ingress into a d-PS film with temperature. The raw data measured with SURF and corresponding fits are presented in the inset.

3.3 CONCLUSIONS ON THE MODEL SYSTEMS

In this short results chapter binary oligomer/polymer mixtures were defined to model middle-block tackifiers, such as aliphatic C5 resins, used in SBC-based adhesive formulations. These tackifiers have a limited compatibility with the polystyrene end-blocks.¹³⁶ Polybutadiene and polyisoprene of various structure and degree of saturations were selected to represent the middle-block of a SBC. Squalane was chosen as model aliphatic resin because it is a well-defined molecule and is commercially available in its hydrogenated and deuterated form. Other oligomers (of isobutylene and styrene) were also selected to assess the impact of the key-parameters influencing surface segregation, identified in 3.1.

Experimental evidence was generated to justify that, in the first instance, the glassy domains of the SBC-based formulation can be neglected. Squalane was proven to be immiscible with the glassy PS domains at room temperature and slightly compatible (up to 9 %) with the rubbery d-PS at 120 °C. Upon cooling, some additive might remain kinetically trapped in the glassy d-PS but this state is likely metastable. A similar behaviour was found for the industrial saturated tackifier Regalite. This is an important element to know about, as the process of application of such adhesives requires heating the material to temperatures above the T_g of the PS blocks and a rapid cooling. Considering the small saturation value recorded for the solubility of squalane in d-PS, even in the rubbery state, it is sensible to model the behaviour of squalane (and aliphatic tackifiers such as Regalite) in an SBC matrix by omitting the presence of the PS block. However, some tackifiers exist which are mainly end-block tackifiers, such as rosins and rosin esters.¹³⁶ The industrial tackifier Picco also showed rather good compatibility with polystyrene at RT. Hence, one must keep in mind that the work presented in the next chapters was restricted to homopolymer matrices. The surface segregation behaviour of a molecule compatible with both microphase-separated domains might not be entirely captured here.

Chapter 4: COMPATIBILITY OF OLIGOMER/POLYMER MIXTURES

In *Chapter 1*, it has been shown that the compatibility of oligomer/polymer mixtures might affect the surface composition and structure of the blend, as well as its mechanical bulk properties. These two characteristics are key in the adhesion process. Therefore, in this second results chapter, it has been chosen to evaluate the bulk compatibility behaviour of the model formulations, first by DSC and then by cloud point measurement. The trends in compatibility are then discussed in terms of Hansen solubility parameters, polarisability and surface energies. They were then compared with the predictions from the Flory-Huggins theory. This work underpins the interpretation of the surface composition profiles in *Chapter 5*. Some of the results presented in the following sections have been published in *Soft Matter*.¹⁴²

4.1 EXPERIMENTAL COMPATIBILITY STUDY

4.1.1 PRINCIPLES OF THE COMPATIBILITY STUDY

In this chapter, the efforts are focused on assessing systematically the compatibility of an oligomer/polymer model system pair, by varying parameters suspected to affect compatibility. The aim is to understand which parameters are key in oligomer/polymer systems and to compare the effects of these parameters with the FH and SAFT- γ Mie predictions. The mixtures are considered compatible when the pair is miscible at the molecular scale in the solid amorphous state (rubbery or glassy). Semi crystalline polymers will be assessed as compatible with the oligomer if the oligomer is compatible with its amorphous portions.

Here, the miscibility analysis has been carried out with the hydrogenated squalane and the same deuterium labelled oligomers used for the surface segregation analysis that is presented in *Chapter 5*. It was decided to use the less expensive hydrogenated squalane since the artefacts that might arise as a result of deuterium labelling – which slightly reduces the cohesive energy

density and surface energy of materials when compared to their hydrogenous counterparts⁵³ – are considered to be small relative to the measurement accuracy and would not alter the conclusions drawn from the DSC data analysis.

4.1.1.1 Compatibility study using differential scanning calorimetry

4.1.1.1.1 Glass transition temperature (T_g)

The T_g is the temperature at which amorphous – i.e. non crystalline – polymers change from the glassy state to the rubbery state. It is a second order transition which means that there is an increase of the polymer's thermal expansion coefficient and specific heat capacity from the glass to the rubbery state but no enthalpy or *latent heat* is associated with the transition.

The T_g is a very important characteristic of a polymer material as it greatly impacts the mechanical properties. It can be thought of as a critical value of free volume at which cooperative chain motion becomes possible. The T_g of a polymer depends mainly on the local environment of the chains that affect their mobility. In the glassy state, segmental motions of the chains are hindered by the interaction with neighbouring chains and the polymer material is brittle. In the rubbery state, the polymer chains are comparatively less hindered. Torsion angles along the polymer backbone can be changed and the relaxation times related to the long-range chain motion are shorter. The polymer material is more flexible.

4.1.1.1.2 Using the T_g as a measure of compatibility

The compatibility of polymers is commonly determined by observing the T_g of their mixtures. When a mixture of polymers is compatible, a single T_g at an intermediate temperature is usually expected to be seen. The Fox equation (4.1) predicts the compositional dependence of the mixture's T_g where w_i is the weight fraction of the component i .¹⁴³

$$\frac{1}{T_{g,mix}} = \sum_i \frac{w_i}{T_{g,i}} \quad (4.1)$$

The founding principles of the Fox equation are discussable as it can seem odd to take an average of temperatures which are intensive variables – i.e. variables that are not dependent on the amount of material in the system and should not be added. However, it has proven its relatively good predictive power when applied to “very well behaving” miscible systems.^{144,145}

In contrast, in an incompatible system, the T_g of the pure components should not change upon mixing since the polymers remain segregated and their local environment is independent of bulk composition. Hence, two separate T_g s should be present in the blend.

This principle was applied to the oligomer/polymer mixtures of interest in this thesis. In this case, the predictive power of the Fox equation is not of immediate interest. Having in mind its limitations, the equation is only used to assess if the mixture behaves as a fully compatible system, by following the theoretical prediction, or as an incompatible system, by keeping the T_g of the pure components. Any behaviour in between will be considered as a partially compatible system. The shifts in T_g of oligomer/polymer blends were observed by DSC. The DSC measurements were performed as explained in 2.4. An example of T_g and T_m determination is given in Figure 4-1. This permitted 13 model systems with samples of concentrations between 20 and 80 % oligomer (w.w) to be measured in a quick and reproducible way.

As a first step, the T_g s of the pure components were measured. The results are reported in Table 4-1. These values are used for the data analysis in 4.1.2.

Table 4-1: Measured T_g s and T_m (when applicable) of the pure oligomers and polymers by DSC.

Oligomer	$T_g / ^\circ\text{C}$	Polymer	$T_g / ^\circ\text{C}$	$T_m / ^\circ\text{C}$
sq	-96.8	PB	-87.9	/
oligo-dIB 900	-67.2	PBcis	-95.5	-17.1
oligo-dIB 2200	-63.9	PI	-55.3	80
oligo-dS	-13.3	hPI	-52.4	/

One can note that the T_g s of the oligomers that have similar structures increase as the molecular weight is increased from squalane to oligo-dIB 900 and to oligo-dIB 2200. This trend is expected from the Flory-Fox equation (4.2). This equation predicts that the T_g of a polymer of number-average molecular weight M_n will be smaller than the one of the theoretical infinite molecular weight polymer $T_{g,\infty}$.

$$T_g = T_{g,\infty} - \frac{K}{M_n} \quad (4.2)$$

where K an empirical parameter, related to the free volume of the polymer. Interestingly, a melting temperature of -38°C can be found in literature for squalane.¹⁴⁶ A melting transition of

-22.1 °C was measured in one of the preliminary projects involving squalane,¹⁴⁷ however, such a melting transition was not observed in the Master's project.¹⁴⁸ Once again, it is absent in these DSC scans. Hence, if such a melting transition exists, it is probably quite small.

4.1.1.1.3 Detailed example: the case of sq/PBcis

The raw DSC data for the model system sq/PBcis was chosen as an example as it illustrates the problem encountered when the T_g of the pure compounds are close to each other. Moreover, the endothermic melting peak at temperature T_m measured for the pure PBcis gives another level of freedom on the interpretation of the result.

DSC signals for mixtures of 10 to 90 % (w.w) of squalane in PBcis were compared to those of the pure components (Figure 4-1). The T_g of the mixtures was determined by extrapolating the half difference in heat capacity on the DSC signal. The melting point onset was obtained from the endothermic peak as shown on Figure 4-1. Determination of the T_g and T_m was done with an accuracy of approximately ± 3 °C, since the transitions were quite broad. The T_g for squalane is different from what is reported in Table 4-1. The measurement was repeated to ensure reproducibility, accounting for changes such as DSC equipment calibration.

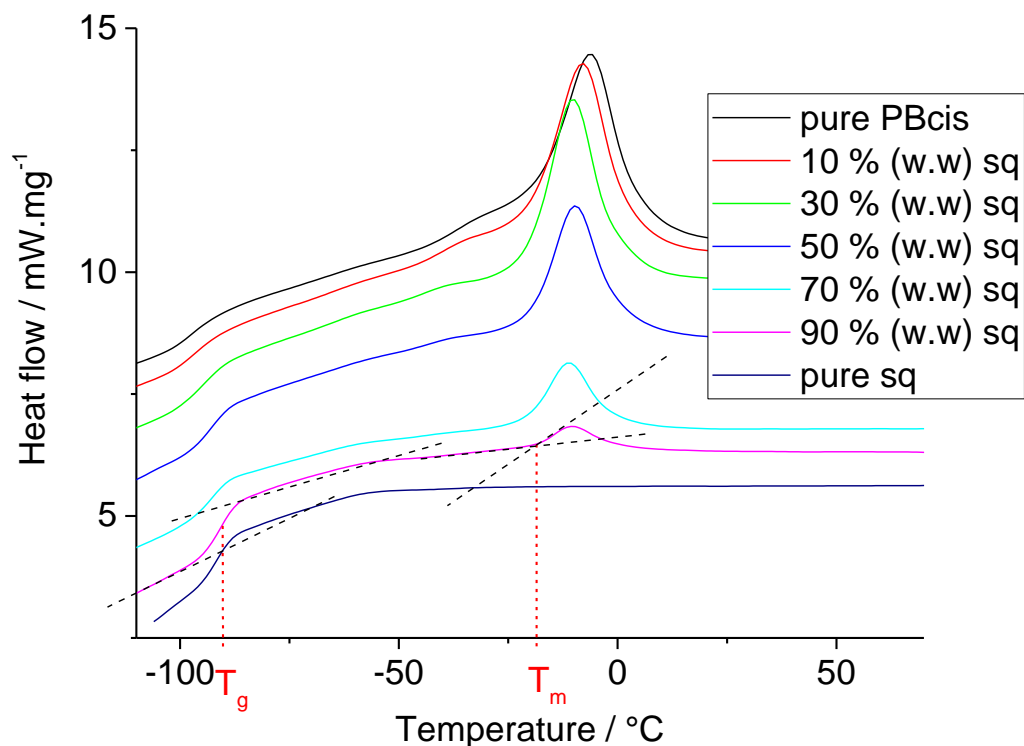


Figure 4-1: Raw DSC data for sq/PBcis mixtures at diverse compositions (2nd heating cycle, endo up, heating rate was 100 °C/min). On the 90 % (w.w) sample, the determination method of the T_g and T_m is shown.

The change of state of the material at the T_g is also associated to a sharp modification of the specific heat, thermal expansion, free volume and mechanical properties. In the DSC experiment, the increase of heat capacity is recorded and manifests itself as a sudden shift in the baseline at temperatures in the region of -90 °C in Figure 4-1. The second feature on the DSC scans is a large endothermic peak, associated with the melting of the crystalline domains of the PBcis. No exothermic crystalline peak is resolved on the scans as the crystallites were formed during the cooling step. A small shift in heat flow is also recorded at ~ -30 °C. It is suggested that this shift be related to the melting of crystallites of lesser quality formed during the previous cooling step.

The melting peak areas were calculated from each DSC thermogram and converted into enthalpies of melting, assuming a heating rate of 100 °C/min. The obtained enthalpies of melting values were then normalised with respect to the amount of PBcis in the sample in % (w.w): $normalised\ enthalpy = \frac{enthalpy\ of\ melting}{1-squalane\ fraction}$. Finally, these values were compared with the enthalpy of melting of the pure polymer (PBcis) by calculating the following ratio: $\frac{normalised\ enthalpy - normalised\ enthalpy\ of\ pure\ PBcis}{normalised\ enthalpy\ of\ pure\ PBcis} \times 100$. This ratio represents the impact of squalane on the crystallisation of PBcis. The experimental data extracted from Figure 4-1 is presented in Table 4-2 including the results of post-processing the data. The evolution of T_g and T_m with the squalane content is presented in Figure 4-2.

Table 4-2: Data interpretation of the DSC raw data presented in Figure 4-1.

Squalane content / % (w.w)	$T_g / ^\circ\text{C}$	$T_m / ^\circ\text{C}$	Area melting peak / $^\circ\text{C.W.g}^{-1}$	Enthalpy of melting / J.g^{-1}	Enthalpy of melting normalised with respect of PBcis content / J.g^{-1}	Enthalpy modification in regards to pure PBcis / %
0	-95.5	-17.1	54.4	32.6	32.6	0
10	-95.4	-19.6	54.8	32.9	36.6	+12
30	-94.1	-21.0	50.2	30.1	43.0	+32
50	-92.5	-19.43	37.2	22.3	44.6	+37
70	-92.5	-20.3	16.9	10.1	33.8	+3.6
90	-90.7	-18.6	6.2	3.7	37.2	+14
100	-91.5	/	/	/	/	/

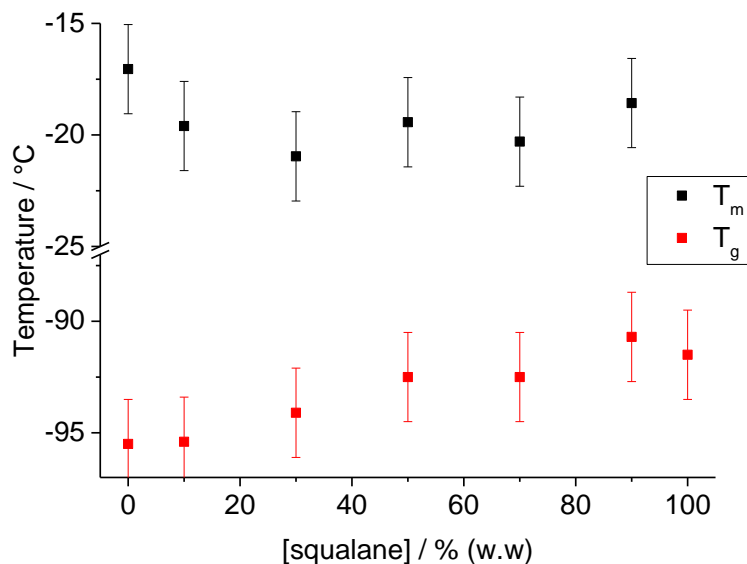


Figure 4-2: Evolution of T_g and T_m as a function of squalane content in mixtures of sq/PBcis.

As expected for a miscible blend, the T_g of the mixture increases with increasing squalane content, as shown in Figure 4-2. However, the trend is not statistically significant as the error on the measurements is relatively high in comparison with the span of T_g values (from -91.5 °C for pure squalane to -95.5 °C for pure PBcis). A plausible explanation is that the two T_g s overlap, forming only one resolvable shift in the heat capacity baseline.

In the case of a miscible blend, one might expect an effect on the crystalline domains of the polymer. Within the given experimental error, Figure 4-2 illustrates that the T_m change with increasing oligomer content is inconclusive. The enthalpy of melting, normalised with respect to the content of PBcis in the sample, seems to increase when squalane is added into the sample (see Table 4-2). This result is not expected as a consequence of a miscible system: if squalane molecules disturb the packing of the chains, crystallisation of the polymer would be less favourable and therefore the melting peak would decrease in intensity. As the percentage of crystallinity is mainly dependent on the polymer molecular structure, this increase in enthalpy of melting does not only correspond to a thermodynamic effect. However, this result may be due to kinetic considerations. It has been shown that the number and size of many polymer crystallites tend to increase when a small quantity of plasticiser is added to the blend.¹⁴⁹ Indeed, the plasticisation of the polymer is accompanied by a small increase in free volume, which allows a new redistribution of the chain configurations and induces a lower viscosity, as expressed in the empirical Doolittle equation.¹⁵⁰ Hence, the presence of squalane, even if only partially

soluble, in the amorphous regions of the PBcis, eases the movement of the polymer chains and their rearrangement into crystals upon cooling. Considering the very rapid cooling rate used for these experiments (100 °C/min) the reduction in viscosity can increase the degree of crystallisation.

As the presence of squalane does not seem to have a significant thermodynamic influence on the melting peak of the mixture, and the observed shift in T_g might simply come from the difficulty in resolving two very close T_g s, it not possible to confirm on the miscibility of the pair from this set of data. Nonetheless, at higher concentrations of squalane > 70 % (w.w), solution cast samples appeared slightly cloudy (visually) at room temperature, which is indicative of an incompatible mixture. This system was therefore expected to have a critical point close enough to room temperature to be measured experimentally. For this system, a phase diagram was constructed using the cloud point determination (see 4.1.2.1).

4.1.1.2 Compatibility study using the cloud point determination

If two pure compounds have similar T_g s, it may not be possible to resolve the two T_g s even in the case of an incompatible, phase-separated system. To overcome this issue, solution cast films of the mixtures were created to assess the film clarity as a function of temperature. Perfect miscibility would result in a completely transparent sample. In contrast, in an immiscible blend, phase-separated microdroplets are formed that scatter light and hence clouds the sample.

Yet, this method is applicable only if the refractive indices of the pure compounds are different enough from each other. It would, for example, be difficult to apply it to a mixture of oligo-dIB ($n_i = \sim 1.51$) and PB or PI ($n_i = \sim 1.52$). It can also be hard to assess the turbidity of the film in the case of a semi crystalline polymer, whose crystallites would have a different refractive index from the amorphous regions and impact the turbidity of the sample (even in the case of a compatible mixture).¹⁷

Phase diagrams were established using the cloud point method for mixtures of squalane with PB and PBcis. As seen in Table 4-1 the T_g s of these compounds were very similar (~ -90 °C) which made it difficult to distinguish the difference between miscible and immiscible mixtures by DSC. The lower refractive index of squalane ($n_i = 1.45$) enables one to see clearly when a system was phase-separated. The cloud point for PBcis was also easy to determine, as the melting

temperature of the crystals was lower than the temperature of measurement ($T_m = -17.1$ °C as determined by DSC).

4.1.2 COMPATIBILITY STUDY ON THE MODEL SYSTEMS

For the next set of model systems, the compositional dependence of T_g was chosen to be presented as:

$$\frac{T_{g,x} - T_{g,0}}{T_{g,100} - T_{g,0}} = \frac{\Delta T_g}{\Delta T_{g,max}} \quad (4.3)$$

where $T_{g,x}$ is the T_g of an oligomer/polymer mixture containing x % (w.w) of oligomer. This representation enables direct comparison of different mixtures by normalising with respect to the T_g 's of their pure components.

4.1.2.1 Effect of the matrix on compatibility

The reference oligomer, squalane (sq), was mixed in various proportions with three polymer matrices: hPI, PI and PB. These matrices are apolar and from the DSC scans, entirely amorphous on the range of measured temperature (-130 to 130 °C). For these systems, the T_g variation with increasing squalane content has been plotted in Figure 4-3.

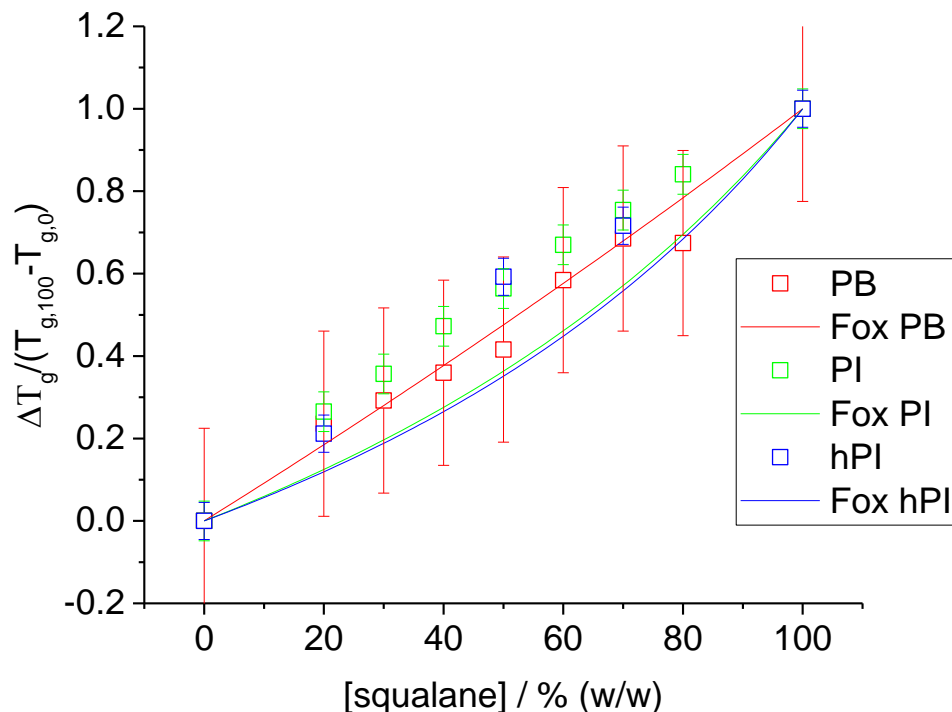


Figure 4-3: Effect of squalane content on the T_g of the hPI (blue), PI (green) and PB (red) matrices. Solid lines show the predictions from the Fox equation for each mixture.

The observed trend is quite similar in each matrix: a steady T_g shift with increasing squalane content. The predictions from the Fox equation, represented by solid lines, are different for each mixture since their shape depend on the T_g of the pure components. Comparing the experimental data to the Fox equation, it seems that these systems are compatible as the experimental results follow the prediction. In the case of squalane in PI and hPI, the T_g shift is even bigger than that predicted by the Fox equation. However, the shift measured for PB samples presents large error bars due to the fact that the T_g of squalane and PB are quite close (-95.5 and -87.9 °C, respectively). Considering the unclear DSC results obtained for squalane in PBcis (discussed in 4.1.1.1.3) and the fact that these two matrices are very similar, a phase diagram was also constructed for the sq/PB model system.

Samples of squalane in PB and PBcis were prepared by solution casting. The samples were placed on a Peltier stage and their state (transparent or cloudy) assessed with the naked eye or with an optical microscope, as presented in Figure 4-4. This visual method is very efficient to determine phase separation in a polymer mixture. However, to determine the cloud point accurately, it is necessary to heat the sample at a very low rate to reach the equilibrium state. In this case, the characterisation was limited by the temperature range accessible with the stage (-2 to 200 °C).

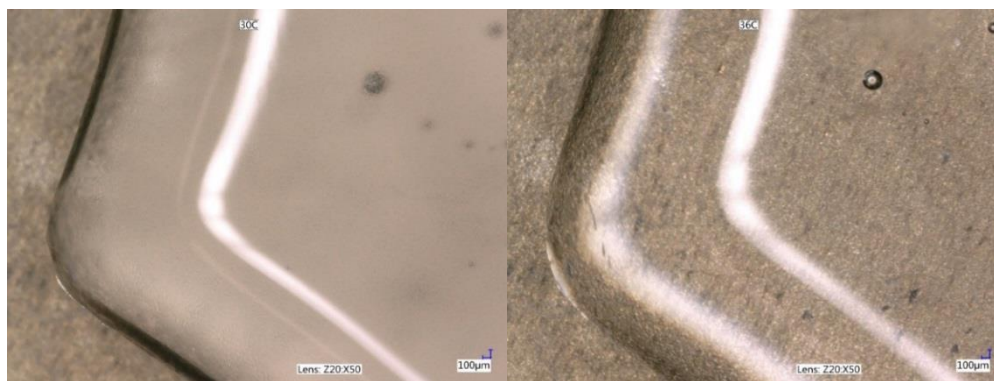


Figure 4-4: Visual assessment of the cloud point of a sample of 70 % (w.w) sq/PB using an optical microscope, 100x magnification. Left: cloudy sample at 30 °C. Right: transparent sample at 36 °C.

Cloud points of samples comprising of 30, 40, 50, 60, 70 and 80 % (w.w) sq/PB and sq/PBcis were determined. The cloud points of the 30 % (w.w) sq/PBcis sample and the 30 and 40 % (w.w) sq/PB samples were not accessible with this setup as temperatures lower than -2 °C could not be reached. The behaviour for concentrations above 80 % (w.w) could not be explored because the sample was too liquid to be measurable as a solid film on a Peltier stage. The two phase diagrams obtained with the cloud point method are presented in Figure 4-5. A guide to the eye for the binodal curve is also drawn.

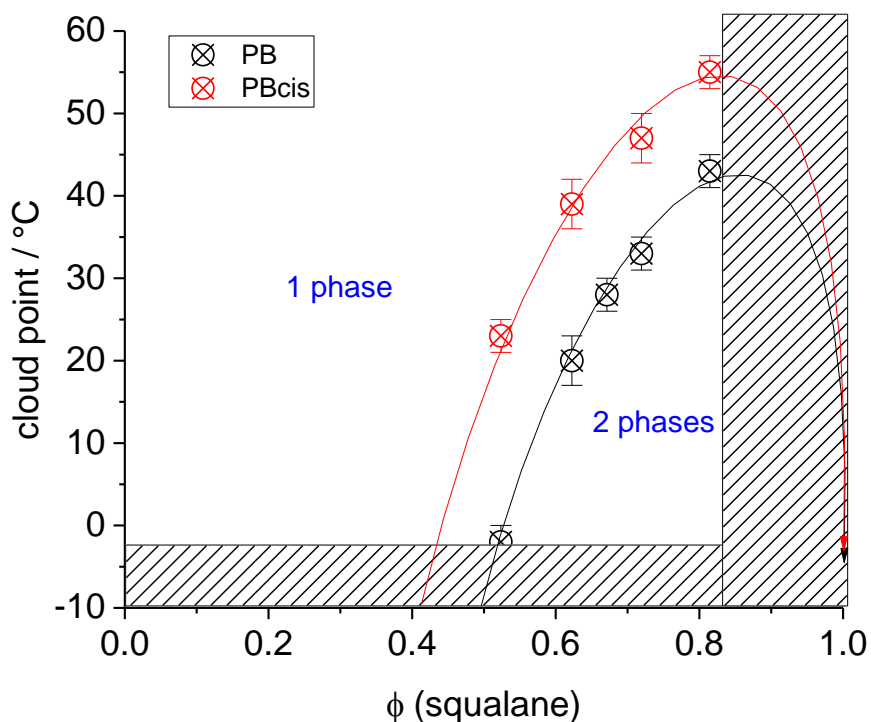


Figure 4-5: Measured cloud points of squalane in PB (black) and in PBcis (red). The solid lines are guides to the eye for the binodal curves. Experimentally unachievable measurements are represented by the dashed surfaces.

Squalane in PB and PBcis are UCST systems – i.e. phase separating upon cooling. As expected from the Flory-Huggins theory, in a high molecular weight polymer, the critical point is very close to a concentration of squalane equalling to 1. For the same volume fraction, the determined cloud point temperature is higher for PBcis than for PB. In other terms, squalane is more compatible with PB because the phase separation for their mixture happens at lower temperatures than for PBcis. Putting this result in parallel with the previous conclusions from the DSC measurements, it seems that squalane in PB and PBcis is only partially compatible at temperatures close to the T_g of the polymers (probably up to ~ 40 % (w.w) for PB and ~ 30 % (w.w) for PBcis at ~ -90 °C, by rough visual extrapolation of the drawn phase diagram). This behaviour could not be assessed by DSC as the T_g of the oligomer and polymer were too close to each other and could not be resolved from the T_g of the pure compounds. From the DSC data in Figure 4-3, complemented by the phase diagrams, squalane seems to be very compatible with hPI and PI and less compatible with PB and finally least compatible with PBcis.

From the FH theory, it is expected that the phase behaviour be nearly independent from the polymer molecular weight. Therefore, the slight changes in chemistry and/or structure of the matrix are responsible for a big difference in compatibility behaviour. Squalane, itself fully saturated, is more compatible with the saturated polymer matrices than with the unsaturated matrices. This is the intuitively expected result based on “like dissolves like” arguments. The two phase diagrams presented in Figure 4-5 will be used to validate the SAFT- γ Mie model, by adjusting beads interactions to obtain the right diagram shape.²⁰

4.1.2.2 Effect of the oligomer molecular weight on compatibility

In the previous section, it was shown that squalane is fully compatible with hPI and PI at all concentrations and partially compatible with PB. To investigate the effect of increasing molecular weight on compatibility, DSC experiments were led on mixtures of the matrices with model oligomer of similar structure but higher molecular weight than squalane – i.e. oligo-dIB 900 and oligo-dIB 2200. Oligomers of isobutylene have more pendant methyl groups along the chain than squalane but are also saturated molecules.

The compatibility of squalane and oligo-dIB 900 in the hPI matrix was evaluated by DSC. The results in Figure 4-6 show a similar outcome for both oligomers: the T_g s are varying with oligomer content, consistently following the predictions from the Fox equation. In this case, the molecular

weight does not have an impact on the compatibility behaviour around the T_g s of the pure compounds. The fully saturated hPI matrix is fully compatible with the two saturated oligomers.

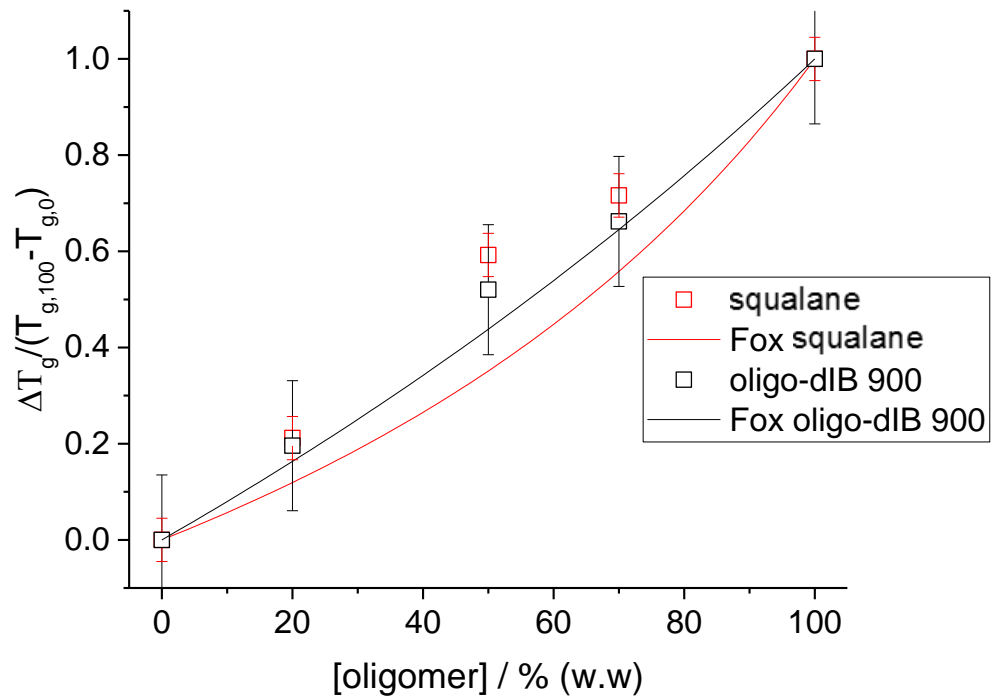


Figure 4-6: T_g variation by blending hPI with squalane (red) and oligo-dIB 900 (black). Solid lines show the predictions from the Fox equation for each mixture.

Blending PI with squalane alters the T_g consistently with increasing squalane amount, as expected from a compatible system (Figure 4-7, red). The shift in T_g is even bigger than the shift predicted by the Fox equation. When blending PI with oligo-dIB 900, shifts in T_g are still recorded, but to extents that are slightly lower than the predictions from the Fox equation (Figure 4-7, black). For the higher molecular weight oligomer, two T_g s were measured, which is characteristic of a clearly phase-separated system (Figure 4-7, green).

From Figure 4-7, it seems that the increase in molecular weight from squalane to oligo-dIB 900 and oligo-dIB 2200 is decreasing the compatibility of the oligomer with the PI matrix, going from fully compatible, to partially compatible and finally to highly incompatible.

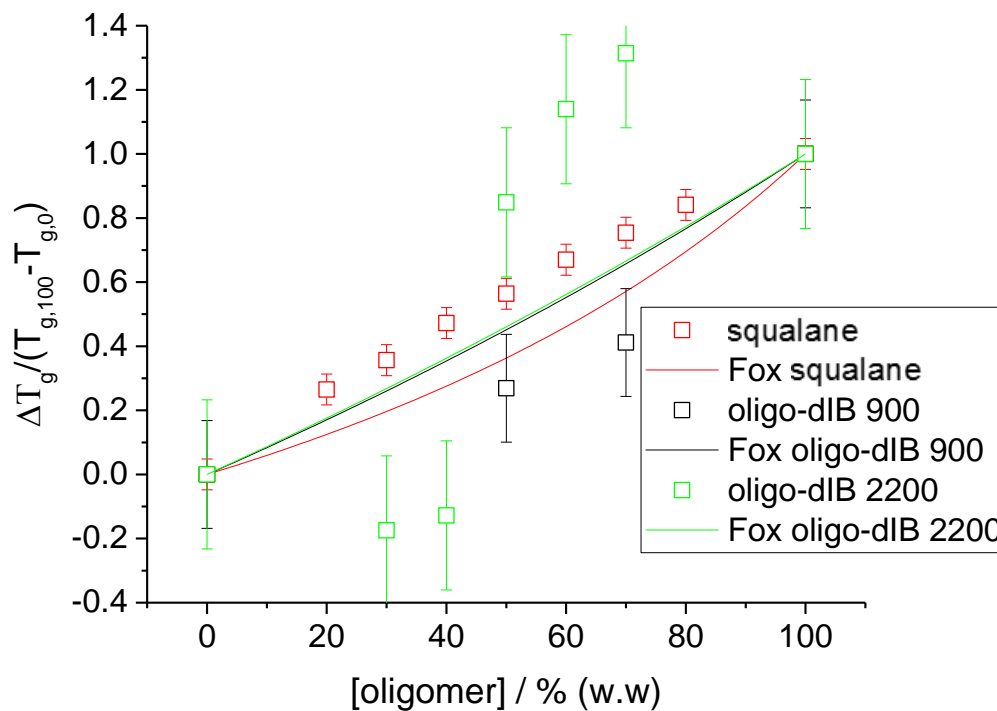


Figure 4-7: T_g variation by blending PI with squalane (red), oligo-dIB 900 (black) and oligo-dIB 2200 (green). Solid lines show the predictions from the Fox equation for each mixture.

Figure 4-8 also reveals different levels of compatibility for each model oligomer in PB. The T_g variation for squalane seems to vary steadily between the extreme values as a function of overall composition. This may be due, by comparison with the phase diagram, to a system fairly compatible below $\sim 40\%$ (w.w). Moreover, as discussed, the relatively large error bars on the data come from the fact that the T_g s of the pure components are similar. In contrast, the T_g s for oligomers of higher molecular weight are well resolved and clearly characteristic of incompatible systems: there is almost no effect on the T_g of PB when blending with 30-70% (w.w) oligo-dIB 900 and oligo-dIB 2200. It was even possible to distinguish 2 separate T_g s in the PB mixtures via DSC. The more pronounced scatter in the data for the oligo-dIB 2200 is most likely due to sample aging – the solutions used to perform the DSC measurements were generally prepared and measured within a few days; however, for these samples, repeat measurements were required from the original stock solutions which were a few months old, which raises the possibility of oxidation over time.

In summary, an increase in molecular weight is again responsible for a lower compatibility with the PB matrix. The matrix is partially compatible with squalane, and highly incompatible with the two oligo-dIB's.

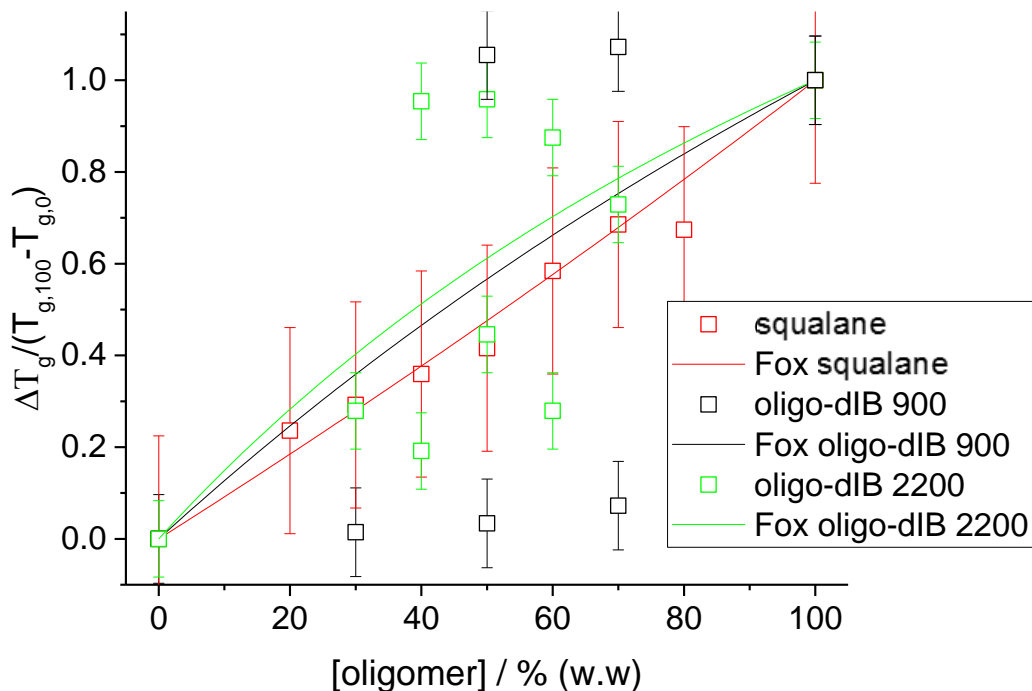


Figure 4-8: T_g variation by blending PB with squalane (red), oligo-dIB 900 (black) and oligo-dIB 2200 (green). Solid lines show the predictions from the Fox equation for each mixture.

From the behaviour of apolar, saturated oligomers of various molecular weight in hPI, PI and PB, it was shown that the effect of increasing the molecular weight of these oligomers on compatibility was not noticeable in the fully saturated matrix (hPI). When blended with an unsaturated matrix (PI and PB) an increase in oligomer size was decreasing the compatibility of the oligomer/polymer pair. Taking into account that squalane was more compatible with the less polarisable matrices (hPI and PI), one can conclude that the more favourable interactions between hPI and the saturated oligomers compensate the destabilisation coming from the increase in molecular weight (in the range of molecular weights studied).

4.1.2.3 Effect of the migrant polarisability on compatibility

In this section, the effect of modifying the migrant polarisability on the compatibility behaviour of the mixture is investigated. To do so, a deuterated styrene tetramer, oligo-dS, of approximately same molecular weight as squalane was mixed in several proportions with hPI, PI and PB.

In hPI, the T_g shows no variation at all (Figure 4-9) with increasing oligo-dS content. This result suggests that the hPI is phase-separated from the oligo-dS. This conclusion was expected as oligo-dS and hPI are the components that are represented by a big polarisability difference.

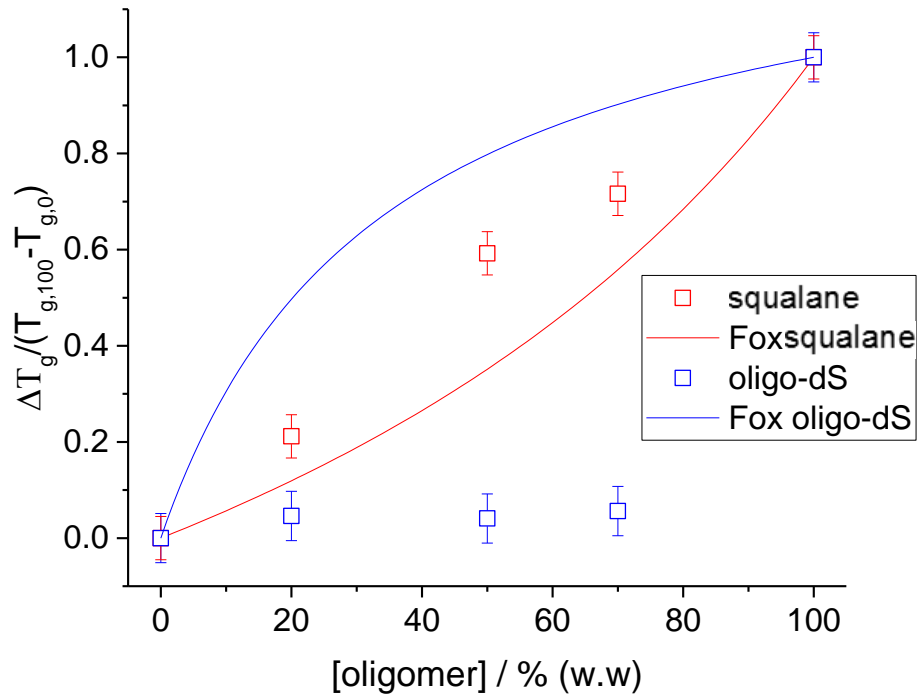


Figure 4-9: T_g variation by blending hPI with squalane (red), oligo-dS (blue). Solid lines show the predictions from the Fox equation for each mixture.

In contrast, as shown in Figure 4-10, the effect of blending PI with oligo-dS on the T_g shift is less than predicted by the Fox equation but is still significant compared to the experimental uncertainty, with regards to the low error bars on the data points. The system exhibits partial compatibility, with eventually a saturation at about 20 % (w.w) of oligo-dS.

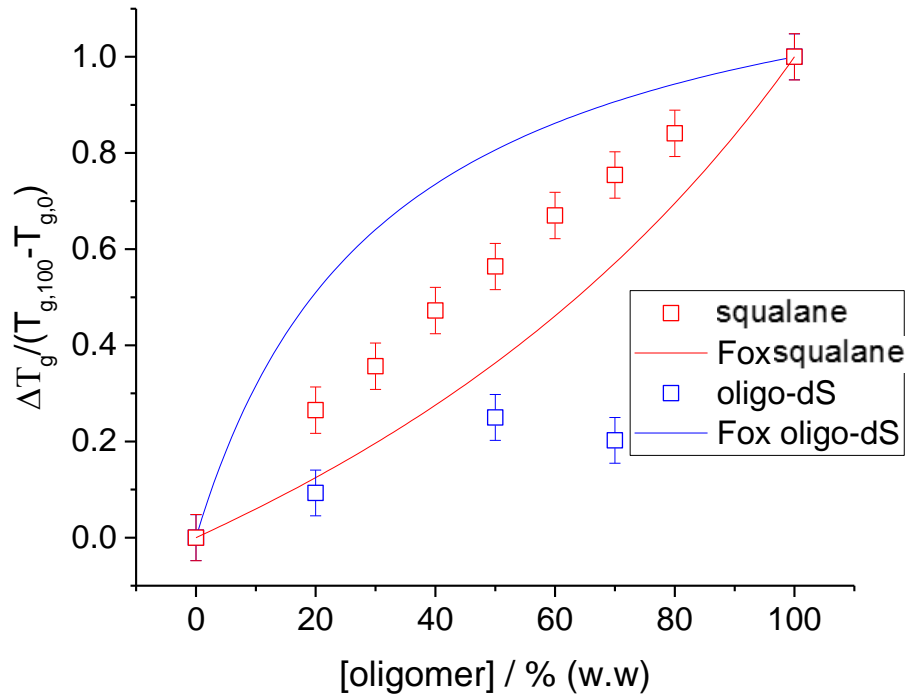


Figure 4-10: T_g variation by blending PI with squalane (red) and oligo-dS (blue). Solid lines show the predictions from the Fox equation for each mixture.

From Figure 4-9 and Figure 4-10, it is evident that the more polarisable oligo-dS is less compatible with hPI and PI compared with squalane. Squalane exhibited a compatible system behaviour, as already discussed above.

It is more difficult to compare the data of squalane and oligo-dS in PB (Figure 4-11) because of the poorer signal to noise ratio on the squalane data (due to the close T_g s of the pure components). From the previous conclusions, squalane is only partially compatible with PB. The oligo-dS is consistently affecting the T_g of the PB matrix with increasing oligomer content. However the T_g variation is lower than expected from the Fox prediction. Therefore the system shows some evidence for compatibility. There is no conclusive data showing different compatibility behaviour when PB is blended with squalane or with oligo-dS.

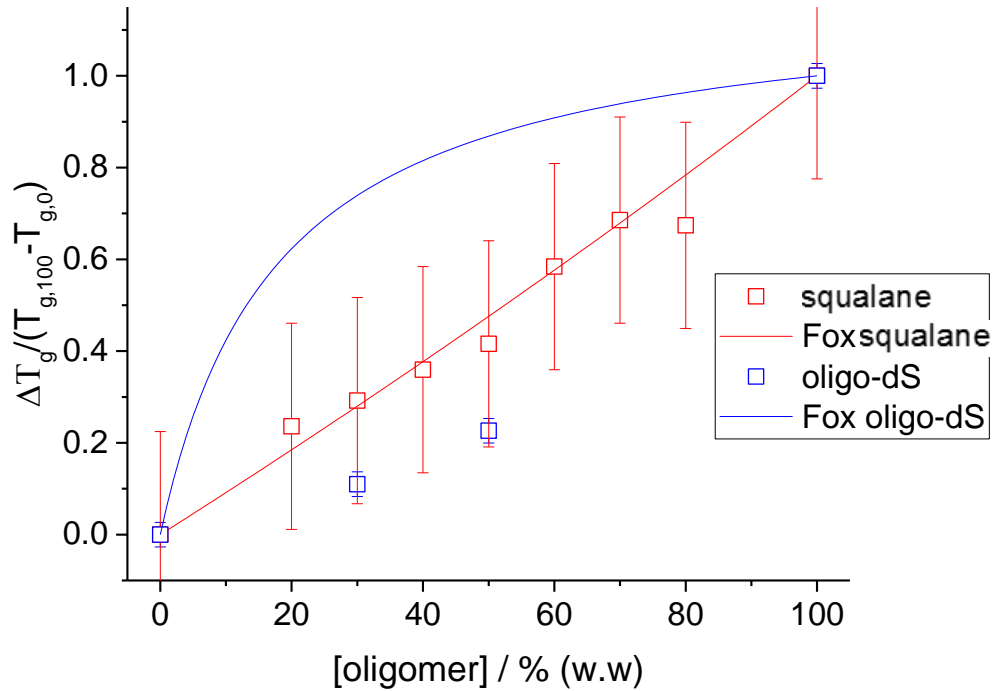


Figure 4-11: T_g variation by blending PB with squalane (red), oligo-dS (blue). Solid lines show the predictions from the Fox equation for each mixture.

Using oligo-dS in the model binary mixture instead of the saturated squalane shows a different effect, which also depends on the matrix. The hPI polymer, which was fully compatible with squalane, is highly incompatible with oligo-dS. When blending with PI, the reduction of compatibility is less pronounced but is still clearly measurable as a deviation from the Fox equation prediction. In the case of PB, it is more difficult to conclude: squalane is partially compatible with PB and the oligo-dS seems to also show some compatibility. Therefore, when comparing the effect in the three matrices, one can conclude that the more polarisable oligomer is more compatible with the more polarisable matrices. This result agrees and completes the conclusions drawn from the section 4.1.2.1, showing that the saturated squalane was more compatible with the saturated matrix.

4.2 DISCUSSION OF THE COMPATIBILITY RESULTS

4.2.1 SUMMARY OF THE RESULTS: COMPATIBILITY MATRIX

Discussing the published work in *Chapter 1* resulted in the hypothesis that the bulk compatibility of the model oligomer/polymer systems is closely related to the extent of surface segregation and to the bulk mechanical properties. While differences in surface energy of the pure components are expected to direct surface or interfacial segregation of oligomers, it is anticipated that incompatibility will be a significant factor responsible for the formation of a pure oligomer wetting layer at the surface of a polymer film.

The DSC analysis provides a direct guide to compatibility behaviour, utilising sufficiently small quantities of material to be practical with the small quantities of deuterated components available. Table 4-3 summarises the overall results obtained by comparing the Fox equation's predictions with the T_g values measured by DSC. When the polymer T_g is independent of the oligomer concentration in the mixture, the blend is incompatible (red). If the T_g approaches that of the pure oligomer more rapidly than predicted by the Fox equation (light green) or following the Fox equation (dark green), the system is compatible. In intermediate cases where the T_g changes with blend composition, but by less than is predicted by the Fox equation, the system is considered to be partially compatible (amber).

Table 4-3: Compatibility matrix obtained by comparing DSC data with results expected from the Fox equation. In red are the incompatible mixtures, in yellow the partially compatible mixtures and in green the compatible mixtures.

	Squalane	Oligo-dIB 900	Oligo-dIB 2200	Oligo-dS
hPI				
PI				
PB				
PBcis	Less than PB			

Assessing the shift in T_g is a good quantitative method to determine compatibility behaviour of a polymer mixture. However, it is representative of the system's behaviour close to its T_g (here, ~ -90 °C). One must keep in mind that the compatibility behaviour observed via DSC might not be valid at RT. Besides, this method is not applicable to systems where the T_g s of the pure components are too close to each other to be resolved by DSC. This is the case of the sq/PB and

sq/PBcis mixtures, for which phase diagrams were determined and proved that there was only partial compatibility and that squalane was more compatible in PB than in PBcis. These two systems also presented further benefits, as their critical points were close to room temperature, which was experimentally convenient to assess the effect of compatibility on the oligomer concentration profiles in thin polymer films.

4.2.2 EVALUATION OF THE FACTORS INFLUENCING COMPATIBILITY

4.2.2.1 Flory-Huggins theory applied to oligomer/polymer mixtures

From 1.1.1, it has been shown that the most widely used theory for describing the compatibility of a polymer mixture is the Flory-Huggins theory. With this theory, the Gibbs free energy of mixing per unit volume ΔG_m for a mixture of a polymer A with a polymer B can be defined as in equation (1.4'). In the case of an oligomer A blended with a polymer B, it has been shown that the Flory-Huggins theory encounters limitations due to the violation of the assumptions established for a mean-field description (notably density fluctuations and excluded volume effect). However, as a first approximation, one can re-write equation (1.4') when N_B is very large compared to N_A , with φ the volume fraction of oligomer, as:

$$\Delta G_m = kT \left(\frac{\varphi}{v_A N_A} \ln \varphi + \frac{\chi \varphi (1 - \varphi)}{\sqrt{v_A v_B}} \right) \quad (4.4)$$

In the investigated model systems, this is justified due to the order of magnitude of the N_B/N_A ratio ($> 10^3$). Hence, the contribution of the polymer molecular weight to the Gibbs free energy of mixing is insignificant in this range.

A negative value of ΔG_m would correspond to a relatively miscible mixture. However, the mixture's stability depends on the sign of $\frac{\partial^2 \Delta G_m}{\partial \varphi^2}$, the second derivative of $\Delta G_m(\varphi)$.

- When $\frac{\partial^2 \Delta G_m}{\partial \varphi^2} > 0$, the mixture is stable and forms only one phase.
- When $\frac{\partial^2 \Delta G_m}{\partial \varphi^2} < 0$, the mixture is unstable and separates into two phases. The composition of the phases is given by the rule of the tangent, as described in 1.1.1.3.

In this framework and considering the model systems chosen, one can, as a first approximation, define the reference volumes as $v_A = v_B = 100 \text{ \AA}^3$ – i.e. approximately one repeat unit of PB as the

volume of a PB unit is $\frac{M}{\rho \times N_A} = \frac{54}{0.913 \times 6.02 \cdot 10^{23}} = 98 \text{ \AA}^3$. Given this assumption, and a molecular weight of $54 \text{ g} \cdot \text{mol}^{-1}$ for one repetitive unit of PB, N_A would be ~ 8 , ~ 17 and 41 for squalane (and oligo-dS), oligo-dIB 900 and oligo-dIB 2200, respectively.

The remaining parameters influencing compatibility are then N_A , φ , χ and T . The following sections will investigate and visualise the enthalpy of mixing ΔG_m when considering a fixed temperature T_0 .

4.2.2.2 Influence of the oligomer molecular weight on compatibility behaviour

When χ and φ are constant, an increase in the oligomer molecular weight, represented by an increase in N_A , decreases the entropy of mixing – i.e. the first term in equation (4.4a), which is negative (φ is comprised between 0 and 1 and therefore $\ln(\varphi)$ is always negative). Thus, the overall free energy of mixing increases. In other terms, oligomers of higher molecular weight are expected to be less compatible with the polymer.

This effect is shown in Figure 4-12 in which ΔG_m was calculated as a function of φ for $\chi = -0.1$ (favourable interactions) and 0.1 (unfavourable interactions) at several values of N_A , based on equation (4.4a). The second derivative of ΔG_m is becoming less negative as N_A increases which is a sign of decreasing stability.

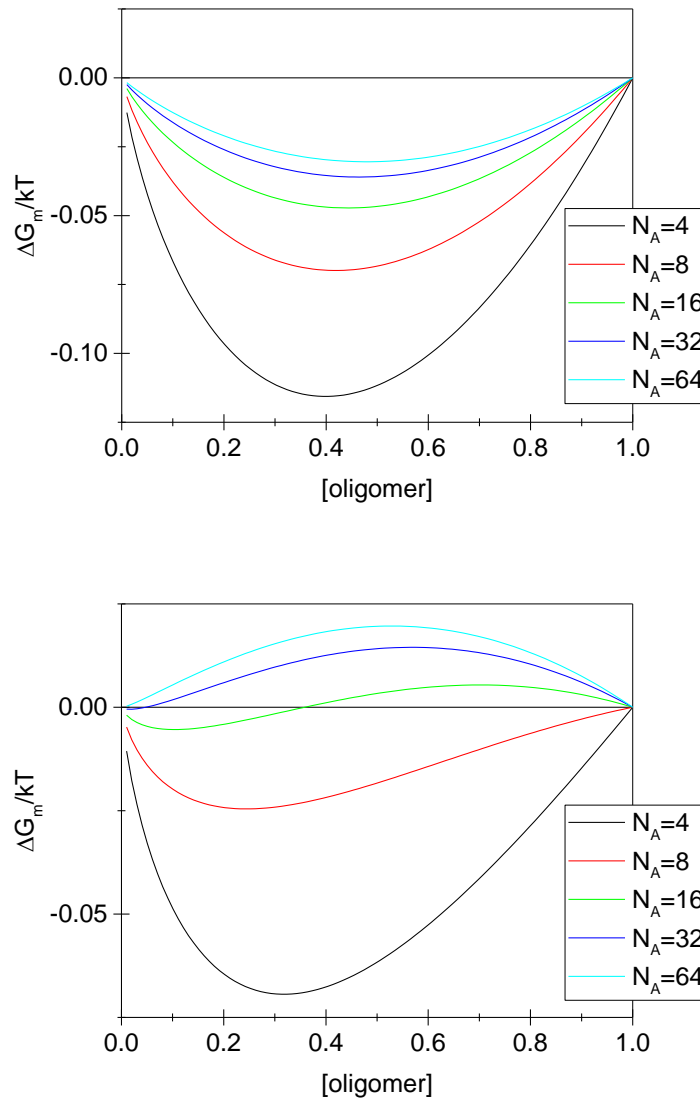


Figure 4-12: Variation of the Gibbs enthalpy of mixing at various values of N_A with $\chi = -0.1$ (top) and 0.1 (bottom).

This prediction from equation (4.4a) is consistent with the data in the first three columns in Table 4-3. As the oligomer goes from squalane to oligo-dIB 900 to oligo-dIB 2200, the compatibility is decreased. It is important to note that squalane does not have the same structure than the oligomers of isobutylene – i.e. there are fewer pendant methyl groups on the squalane chain. However it is still reasonable to conclude that for the saturated oligomers in every matrix, the higher molecular mass oligomer was also experimentally the least compatible.

4.2.2.3 Influence of the oligomer concentration on compatibility behaviour

It is interesting to note from Figure 4-12 that the lower the oligomer molecular weight, the more asymmetric the diagram is: the system tends to be more incompatible at higher oligomer

concentrations – i.e. ΔG_m is less negative. The critical composition, φ_c , predicted by the Flory-Huggins theory, contains a high proportion of the oligomer when $N_A \ll N_B$ according to equation (1.10). In other terms, it is entropically more favourable to dissolve a small amount of oligomer molecules in the polymer than to dissolve the equivalent volume fraction of polymer in a large proportion of oligomer.

One can note that for some cases – e.g. both oligo-dIBs in PB – there appears to be a transition from a single phase mixture (one T_g) to a two-phase mixture (two T_g s) at high oligomer concentrations. This result is also evident from the phase diagrams of sq in PB and PBCis. Clearly, this indicates that some mixtures are highly incompatible and that there is a tendency to phase separate at high oligomer concentration. This result is qualitatively consistent with the Flory-Huggins theory, according to the equation (4.5).

4.2.2.4 Influence of the interaction parameter on compatibility behaviour

4.2.2.4.1 Prediction from the FH theory

Figure 4-13 shows the predicted curves from equation (4.4a) for the values of N_A of the oligomers stated above, when varying the interaction parameter χ from very favourable oligomer/polymer interactions ($\chi = -0.4$) to very unfavourable oligomer/polymer interactions ($\chi = 0.3$). It is clear that an increase in χ renders the mixture less compatible – i.e. the second derivative of $\Delta G_m(\varphi)$ becomes negative – for the values of N_A considered. Again, the lower N_A , the more asymmetric the free energy of mixing, tending to less compatible behaviour close when φ tends to 1.

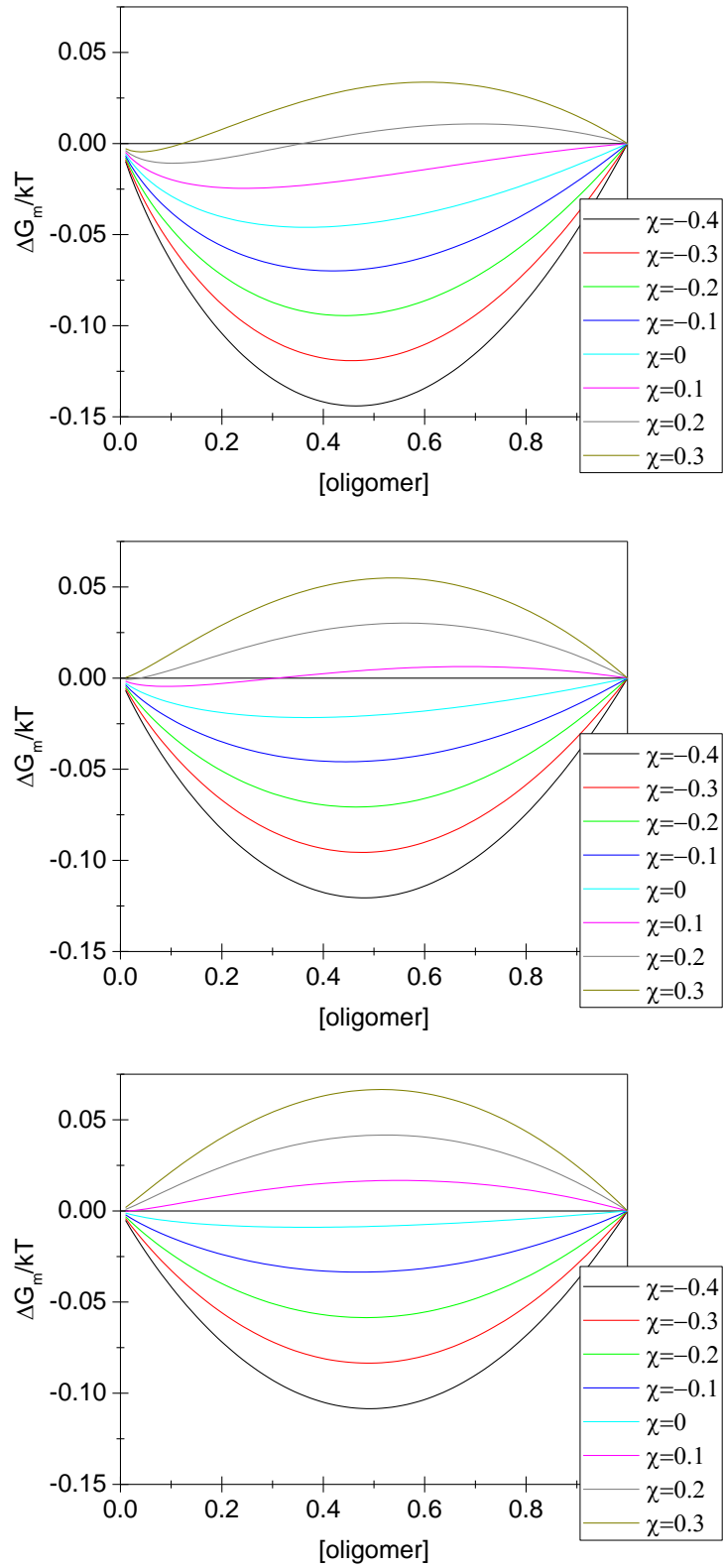


Figure 4-13: Effect of the value of χ on the Gibbs energy of mixing of the system for $N_A=8$ (top), $N_A=17$ (centre) and $N_A=41$ (bottom).

4.2.2.4.2 Solubility parameter considerations to estimate the interaction parameter

As χ is increased, the compatibility of the system is reduced, as shown in Figure 4-13. χ is in theory a very convenient parameter to describe compatibility but it is not easily accessible experimentally. One way to provide some insight into the observed miscibility behaviour of the nonpolar materials under consideration in this work is to apply the Hildebrand-Schatchard theory of solutions and the theory of intermolecular forces¹¹ introduced in 1.1.1.4. This approach calculates χ , generally for a polymer solution, as:

$$\chi = \chi_s + \frac{V_m}{kT} (\delta_A - \delta_B)^2 \quad (4.5)$$

where δ_A and δ_B are the Hildebrand solubility parameters of the pure components and V_m is the solvent molar volume (from combining equations (1.11) and (1.12)).

The Hildebrand solubility parameter can be divided into three Hansen solubility parameters related to dispersive, polar and hydrogen bonding forces. The chosen model systems are mixtures of apolar oligomers and polymers. Hence, the interactions between the two species are mainly dispersive – i.e. London type of van der Waals forces, between temporary dipoles. The dispersive Hansen solubility parameter δ_D would be most dominant and is related to refractive index, n_i , by:¹⁵¹

$$\delta_D(\text{MPa})^{1/2} = 9.55 n_i - 5.55 \quad (4.6)$$

The measured refractive index of squalane was 1.4501. The matrices of interest in this project are hPI, PI, PB and PBcis. The refractive indices discussed here were measured from the pure components. Having the closest refractive index to squalane, hPI should show the best compatibility ($n_i = 1.4749$) – i.e. lowest χ according to equations (4.5) and (4.6). PBcis ($n_i = 1.5230$) should show the lowest compatibility – i.e. highest χ – as its refractive index is the furthest away from squalane. The similarity in refractive index values for PB ($n_i = 1.5173$) and PI ($n_i = 1.5188$) results in almost identical dispersive Hansen solubility parameters but would suggest a lower compatibility of dsq with PI than with PB.

To compare the compatibility of squalane in PI and in PB, one may use directly the Hildebrand solubility parameters found in literature. The Hildebrand solubility parameter of PI (15.18-17.09 MPa^{1/2}) is slightly lower from the solubility parameter of squalane (18.8 MPa^{1/2})¹¹² than the one of PB (16.6-17.6 MPa^{1/2}).¹⁷ This would again imply a higher χ in the case of sq/PI than for sq/PB

according to equation (4.5) – therefore a lower compatibility. However, a full compatibility of dsq in PI by DSC was observed while the phase diagram showed a partial compatibility of dsq with PB.

This reasoning can also be applied to the oligo-dS samples which literature values for the refractive index is $n_i = 1.590-1.592$ and Hildebrand solubility parameter are in the range of $\sim 17.4-19.09$.¹⁷ The refractive index and solubility parameters of PBcis are most similar to oligo-dS, which should result in the most compatible system. In contrast, hPI has refractive index and solubility parameters that are the most different from oligo-dS which should result in the least compatible system. However, it is again difficult to conclude on the compatibility behaviour of oligo-dS with PI and PB because their solubility parameters and refractive indices are so similar. From the experimental data, the compatibility trend observed for oligo-dS is totally opposite from the trend observed for squalane which agrees with the solubility parameter predictions for the two extreme polymers (hPI and PBcis).

The accuracy of these interpretations is limited by the accuracy of solubility parameters or refractive index data for these materials. For example, only one solubility parameter value was found for squalane in the published research.¹¹² Moreover it has been noted in literature that these methods do not apply very well to polymer mixtures.¹⁵² Therefore, relying on the Hildebrand or dispersive Hansen solubility parameters does not prove to be appropriate to predict compatibility of the model systems.

4.2.2.4.3 Influence of polarisability on the interaction parameter

Following the argument of the effect of molecular interactions, the strength of London dispersive forces usually increases with the molecule size and polarisability and is affected by molecular shape. As the polarisability of a polymer increases with its degree of unsaturation, the chemical structure of the repetitive units of these polymers suggests that the least polarisable matrix is hPI, as it is fully saturated. As such, PI would be of lower polarisability than PB due to the lower unsaturation based on atomic percentage. The polarisability, as well as the shape of the PB and PBcis chains, is expected to be different due to the presence of pendant vinyl groups in the PB, which should consequently modify the strength of the dispersive forces. The molar polarisability (α) of PB is slightly lower than the one of PBcis (respectively $70.4 \times 10^{-25} \text{ cm}^3$ and $71.4 \times 10^{-25} \text{ cm}^3$).¹⁷ PB and PBcis have very similar densities (0.913 and 0.915 g.cm^3 respectively), it is therefore expected that PBcis is slightly more polarisable than PB.

Comparing this analysis with the results in Table 4-3, it is shown that the saturated oligomers compatibility's decreases as the polymer's polarisability increases. This trend is reversed when looking at the more polarisable oligomer (oligo-dS, column 4). Therefore, as a first approximation one can conclude that χ increases as the polarisability difference between the oligomer and polymer is increased.

4.2.2.4.4 *Balanced effect of χ and N_A on compatibility behaviour*

The curves from Figure 4-13 also show that for a higher N_A , $\Delta G_m(\varphi)$ becomes positive (and its second derivative negative) at lower values of χ . For $N_A = 8$, the second derivative is positive (stable miscible mixture) until $\chi = 0.2$ while for $N_A = 41$, it is only until $\chi = 0.1$. In other terms, the interactions do not need to be as unfavourable for phase separation to happen.

One should hence expect the existence of a compensative effect between χ and N_A for these asymmetric model systems. This effect is indeed visible in the experimental data from Table 4-3.

One can classify the oligomer/polymer pair by increasing value of χ when blended with the saturated oligomers: hPI, PI, PB and PBcis. Squalane (the lower molecular weight oligomer) is miscible in PI and is only partially compatible with PB. When increasing the molecular weight slightly – i.e. for oligo-dIB 900 – the mixture with PI becomes only partially compatible while the one with PB is fully incompatible. Therefore, this supports the argument that on increase of molecular weight the phase separation happens at lower values of χ .

4.2.2.5 *Influence of temperature on compatibility behaviour*

Understanding the impact of temperature on compatibility is of importance, especially close to the critical point of the mixture. In such oligomer/polymer blends the phase diagrams are highly asymmetric, hence, the effect of temperature has to be jointly considered with the oligomer content.

The effect of the temperature on ΔG_m , as described by FH, is difficult to evaluate, as χ is not purely enthalpic – i.e. it is usually dependent on T . In the case of an UCST system, the mixture becomes more compatible as the temperature is increased: in other terms, χ varies with $1/T$. In contrast, in a LCST system, the mixture becomes less compatible when the temperature is increased. This is generally due to the destruction of favourable polar or hydrogen bonds with increasing T or because a large expansion factor difference exists between the two species. Therefore, χ should increase with T . LCST behaviour cannot be predicted using the original Flory-

Huggins description because it does not take into account any volume changes of mixing. Although not formally within FH theory, χ can be treated as a fitting parameter and is generally allowed to follow a complex temperature dependence to account for these effects.⁹

The FH theory itself cannot predict the UCST or LCST behaviour of a certain mixture. This information is however accessible via experimentation or with some appropriate modelling tools. Through the experimental construction of phase diagrams (Figure 4-5) it was shown that the sq/PB and sq/PBcis model mixtures are of UCST type – i.e. phase separation occurs upon cooling. Therefore, for these model systems, an elevation of temperature results in an increase in compatibility.

For such UCST systems the interaction parameter dependency on temperature is usually expressed as equation (1.11'). Using this expression of χ one can proceed in fitting the experimental phase diagram cloud points. The output parameters χ_S and χ_H can then be used to estimate a range of values for χ . The spinodal points (limit of metastability) are calculated from equation (1.8). By differentiation of equation (1.4'), one obtains:

$$\frac{\partial \Delta G_m}{\partial \varphi} = kT \left(\frac{\ln \varphi + 1}{v_A N_A} - \frac{\ln(1 - \varphi) + 1}{v_B N_B} + \frac{\chi(1 - 2\varphi)}{\sqrt{v_A v_B}} \right) \quad (4.7)$$

and

$$\frac{\partial^2 \Delta G_m}{\partial \varphi^2} = kT \left(\frac{1}{v_A N_A \varphi} + \frac{1}{v_B N_B (1 - \varphi)} - \frac{2\chi}{\sqrt{v_A v_B}} \right) \quad (4.8)$$

Therefore, according to (1.8) the spinodal points are defined as

$$\frac{\partial^2 \Delta G_m}{\partial \varphi^2} = kT \left(\frac{1}{v_A N_A \varphi} + \frac{1}{v_B N_B (1 - \varphi)} - \frac{2\chi}{\sqrt{v_A v_B}} \right) = 0 \quad (4.9)$$

With a few more steps, one can also obtain the values of φ_c and of the critical χ parameter χ_c given in expression (1.10) by solving equation (4.9) when the third derivative of the free energy of mixing equals 0.

From equation (1.11'), equation (4.9) also implies that

$$\chi = \frac{\sqrt{v_A v_B}}{2} \left(\frac{1}{v_A N_A \varphi} + \frac{1}{v_B N_B (1 - \varphi)} \right) = \chi_S + \frac{\chi_H}{T} \quad (4.9')$$

And therefore

$$T = \frac{2\chi_H N_A \varphi}{\sqrt{\frac{v_B}{v_A}} + \sqrt{\frac{v_A}{v_B}} \frac{N_A \varphi}{N_B(1-\varphi)} - 2\chi_S N_A \varphi} \quad (4.10)$$

Consequently, from equation (4.10) and knowing the expression of φ_c (see equation (1.10)) it is possible to determine the critical temperature T_c . Additionally, if $N_B > 10^3 N_A$, the quotient $\frac{N_A \varphi}{N_B(1-\varphi)}$ can be considered negligible for $\varphi < 0.9$ and the equation (4.10) becomes in such a case:

$$T = \frac{2\chi_H N_A \varphi}{\sqrt{\frac{v_B}{v_A}} - 2\chi_S N_A \varphi} \quad (4.10')$$

As a first approximation equation (4.10') was fitted to the experimental cloud points of the phase diagrams of squalane in PB and PBcis (Figure 4-5). Again, it was assumed that the reference volumes of the two components are identical and approximately equal to one repetitive unit of PB of molecular weight 54 g.mol⁻¹ ($v_A = v_B = 100 \text{ \AA}^3$) and that N_B is so large versus N_A that its value does not affect the compatibility behaviour.

The values for χ_S and χ_H are gathered in Table 4-4 for several values of N_A . The row for $N_A = 8$ is highlighted as it represents the approximated number of repetitive units of squalane assuming a reference volume of one repeat unit of PB of $M=54 \text{ g.mol}^{-1}$.

Table 4-4: Fitted values of χ_S , χ_H from equation (4.10') when $v_A = v_B = 100 \text{ \AA}^3$ to the experimental cloud point data for a mixture of squalane with PB and PBcis.

N_A	PB		PBcis	
	χ_S	χ_H / K^{-1}	χ_S	χ_H / K
1	-1.5	661	-2.6	1058
2	-0.73	331	-1.3	529
4	-0.37	165	-0.65	265
8	-0.18	83	-0.33	132
16	-0.092	41	-0.16	66
32	-0.046	21	-0.081	33

Equation (4.10') and the related calculation of χ in equation (4.9') are heavily dependent on the value of N_A – when N_B is large and $v_A = v_B$, χ is directly proportional to $1/N_A$. The entropic and enthalpic contributions to χ , respectively χ_S and χ_H/T , are of the same order of magnitude, which illustrates the high sensitivity of these systems to small variations of polarisability and molecular weight. To determine the value of χ as accurately as possible, and test the validity of the approximations stated above, the parameters χ_S and χ_H were refitted using the original equation (4.10) with $v_B = 98 \text{ \AA}^3$, the volume of one repetition unit of PB. N_B was chosen equal to 5185 for PB and to 11074 for PBcis, according to their weight average molecular weights. A squalane molecule was determined as a succession of $N_A = 6$ repetitive units of C_5H_{10} of molecular weight 70 g.mol^{-1} and of density 0.81 g.cm^{-3} . Therefore, the volume of one repetitive unit of squalane is $v_A = \frac{M}{\rho \times N_A} = \frac{70}{0.81 \times 6.02 \cdot 10^{23}} = 144 \text{ \AA}^3$. The results of the new fits are shown in Figure 4-14 and the corresponding fitted parameters are in Table 4-5.

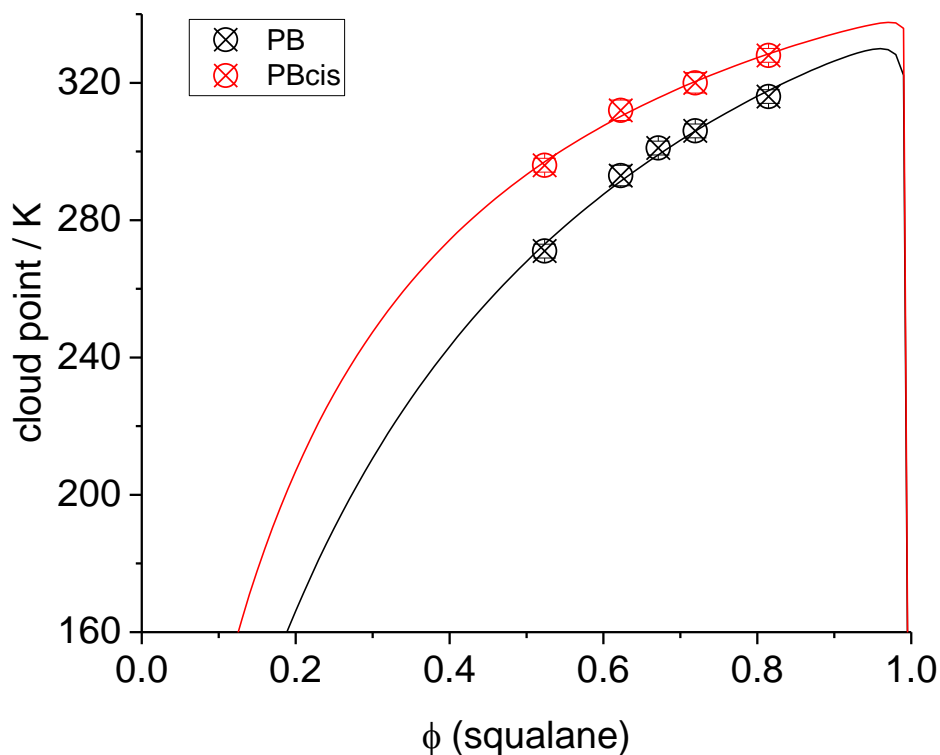


Figure 4-14: Left: experimental cloud points and fits according to equation (4.10) for PB (black) and PBcis (red) for $N_A=6$, $v_A = 144 \text{ \AA}^3$ and $v_B = 98 \text{ \AA}^3$. The fitting region below 273 K is an extrapolation.

Table 4-5: Fitted values of χ_s , χ_H from equation (4.10) corresponding to the results in Figure 4-14.

PB		PBcis	
χ_s	χ_H / K	χ_s	χ_H / K
-0.20	90	-0.36	145

The results are similar to the ones obtained when choosing the simplified equation (4.10') (to an accuracy of 1-2 %). Therefore, the hypotheses established earlier – i.e. $v_A = v_B = 100 \text{ \AA}^3$ and no effect of N_B on the compatibility behaviour – seem reasonable enough to describe these two systems of interest. Calculating χ from equation (1.11') and the fitting results in Table 4-5. It is evident in Figure 4-15 that $\chi(\text{sq/PB})$ is always smaller than $\chi(\text{sq/PBcis})$ for temperatures between 0 and 50 °C – i.e. temperature of the experimental cloud points. It was also chosen to extrapolate the fits to a temperature of 180 K which corresponds to the polymers' T_g s (~ -90 °C according to 4.1.1.1.2). The fitting to the data suggests a partial miscibility at this temperature with ~ 15 and ~ 23 vol% sq in the PBcis and PB rich phase respectively. Thus, the position of the polymers' T_g s measured by DSC might have been slightly affected by the presence of some sq in the polymer-rich phase. Unfortunately this effect was not distinguishable since the T_g of sq was too close to resolve the two shifts in the heat capacity baseline (see 4.1.1.1.3).

The critical interaction parameters calculated from equation (1.10) are 0.075 and 0.073 for PB and PBcis respectively. The corresponding critical temperatures obtained from equation (4.10) are 329 K (57 °C) for PB and 337 K (65 °C) for PBcis. From Figure 4-15, it is shown that for temperatures between 0 and 50 °C, χ is in the range of 0.080 to 0.13 for a sq/PB mixture and of 0.092 to 0.17 for sq/PBcis. These χ values are higher than χ_c which indicates a phase separation for both systems in this range of temperatures.

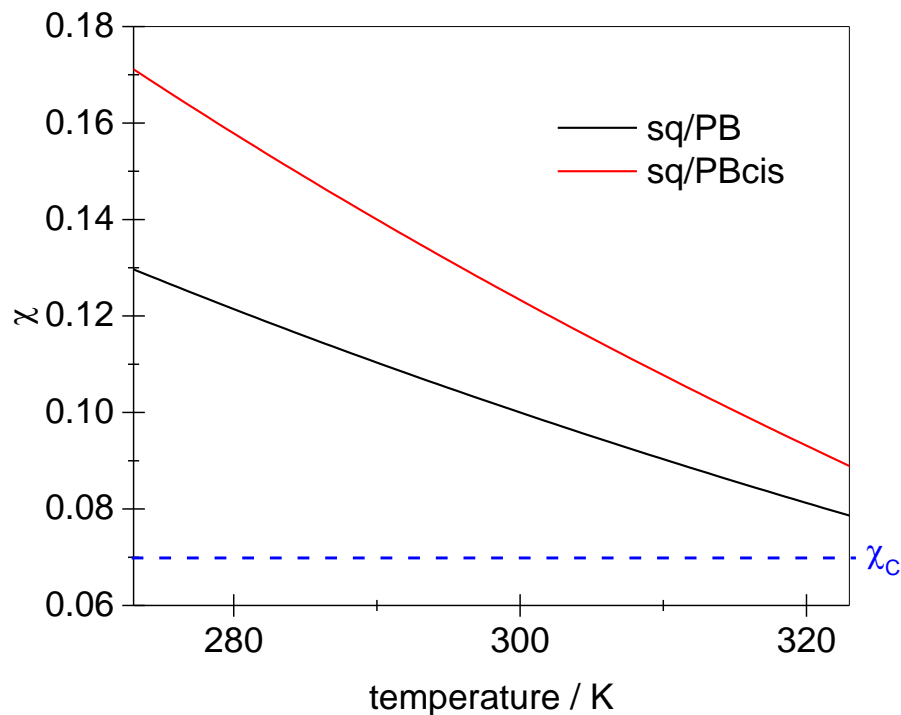


Figure 4-15: χ parameter as a function of T , using equation (4.8) and results in Table 4-5.

4.2.2.6 Influence of matrix crystallinity on compatibility behaviour

The effect of the crystallinity of the mixture on compatibility is not included in the FH theory. PB and PBcis are matrices of very comparable molecular structure. They differ by the ratio of structural cis and trans conformations, the percentage of 1,2 addition, and by their degree of crystallinity. As crystallites should be pure and not contain any squalane, one could argue that (below T_m) the difference in phase diagrams, evidenced in Figure 4-5, could be due to the presence of “forbidden” volume in the PBcis sample, which increases the concentration of squalane in the amorphous regions of the polymer and therefore shifts the binodal towards lower volume fractions of squalane. This kind of effect is not taken into account in the Flory-Huggins description. However, in this case, the melting peak of the crystallites is ~ -17 °C (256 K) (from Figure 4-1). Thus, the PBcis samples used for the determination of the cloud points are totally amorphous and the compatibility difference is not due to the crystalline domains.

In the absence of crystalline domains to explain the lower compatibility of squalane in PBcis, the molecular structure of the matrices must be the main factor affecting compatibility. Interestingly, squalane is more compatible with PB, which present more 1,2 additions (8 %) – therefore some pendant vinyl groups – and 1,4 trans conformations (36 %).

4.3 CONCLUSIONS ON COMPATIBILITY

In this chapter, the compatibility of oligomer/polymer pairs was systematically determined via two experimental approaches. In order to compare compatibility behaviour and concentration profiles as fairly as possible, the same deuterated components as used in NR and IBA were used for the compatibility study. The DSC method is very efficient in capturing a shift in T_g which would suggest compatibility of an oligomer/polymer pair (even with the low amount of deuterated material available). However, when the T_g of the pure components are too similar, the method of cloud point determination must be used in order to assess compatibility of the hydrogenated analogues.

The main contribution to the interaction between oligomer and polymer is concluded to be the dispersive forces between temporary dipoles. These forces are mainly dependent on the polarisability of the molecules, their shape and size. Using DSC and cloud point techniques, it has been shown that the compatibility of the oligomer is reduced when increasing the molecular weight and the difference in polarisability between the components. Clear evidence was presented of the effect of the polarisability by comparing oligomer compatibility in saturated (hPI) and unsaturated (PI, PB and PBcis) matrices. When the polymers were more similar in structure (PI, PB, PBcis) the difference in compatibility behaviour was evident experimentally but was difficult to justify using the existing solubility parameter theories. It is evident that very significant changes in compatibility can be found with polymer matrices that have nearly identical solubility parameters. Close to the critical point, an increase in oligomer concentration and a decrease in temperature are shown to also reduce compatibility.

A simplified Gibbs free energy equation was applied, adapted from the FH theory to these systems. This equation highlights the main parameters affecting compatibility and identifies their main trends. Additionally, it was shown that through the fitting of experimental UCST phase diagrams, it is possible to evaluate the values of the temperature-dependent χ parameter, using N_A as the only input parameter. However, these values must be treated with caution as the assumptions from the mean-field description are not respected in the case of an oligomer/polymer blend due to density fluctuations and excluded volume effects, described previously. Moreover, the χ parameter might show dependency on the oligomer content ϕ and on the molecular weight. Hence, it cannot be expected that the FH theory predicts precisely and

quantitatively the mixing behaviour of such oligomer/polymer mixtures (for example by producing a phase diagram without any experimental data). However, the simplified equation is still a satisfactory qualitative tool to estimate compatibility trends and obtain a range of values for the χ parameter by fitting experimental phase diagrams. The compatibility data generated is nonetheless relevant to test and validate predictions from other models and computational simulation such as a SAFT- γ Mie approach.¹⁴²

Chapter 5: OLIGOMER SURFACE PARTITIONING

From *Chapter 1* it has been shown that, due to the disparity of molecular weights between the oligomer and the polymer in the chosen model formulations, a surface segregation of the oligomer is expected – i.e. the oligomer is more concentrated at the surface than in the bulk. Other factors impact the oligomer depth profile: the difference in surface energy and the incompatibility between components. The effect of temperature and sample thickness have also been reported. Elasticity,¹⁵³ crystallisation¹²⁶ or deformation may be relevant to more complex matrices, but are not considered here since all of the components are amorphous and have shorter relaxation times than the timescale of observation.

In this chapter, the vertical concentration profiles of selected model systems were measured by ion beam analysis (IBA) and by neutron reflectometry (NR), as a function of z , the distance from the air surface. Several oligomer partitioning behaviours have been observed showing the preference of the migrant for the surface with air and/or the interface with the substrate. The presence of a surface excess was correlated to the compatibility between the oligomer and the polymer as presented in *Chapter 4* and to the difference in their surface energies. ERDA and NR experiments were performed on thin films (~ 100 nm) which were mixtures of deuterated oligomers with polymer matrices for oligomer contents from 2 to 70 % (w.w). Assuming that the surface migration by diffusion for such thin films should occur within the time frame of the sample preparation, the following measured concentration profiles are suggested to be representative of the equilibrium state of the samples (or at least a metastable state).

5.1 EXPERIMENTAL RESULTS

5.1.1 SURFACE PHENOMENA FOR SYSTEMS IN THE ONE-PHASE REGIME

5.1.1.1 Surface energy investigation

As discussed in 1.2.2.1, a binary polymer blend will minimise its free energy by partitioning the lower surface energy component onto the surface. Similarly polar, high energy components tend to segregate to high energy surfaces such as silica.^{154, 155} Unfortunately, most of the oligomers of interest (oligo-dS and both oligo-dIBs) fall between the extremes of liquid or solid material. Additionally, no reliable technique exists to measure surface energies for mixtures of highly mobile and highly immobile components;

- the pendant drop method or the use of a micro-Wilhelmy plate¹⁵⁶ would not be appropriate as these materials will not flow to an equilibrium shape on an experimentally realisable time,
- the sessile drop contact angle method would not be applicable as the some components can dewet, undertake local reorganisation and/or contaminate the reference liquids in an experimentally realistic time-frame.

Surface energy measurements of oligomer/polymer mixtures were also not manageable due to inhomogeneity and solvent contamination (for solution cast samples) or film dewetting (for spin coated films). Hence, a surface energy investigation was performed but focused on squalane (liquid model oligomer) and on two polymers which were provided in sufficient quantity to perform contact angle measurement on the bulk material (PB and PBcis).

The surface tension of squalane (liquid oligomer) was measured using the pendant drop measurement method, described in 2.6.1. A value of $\gamma = 28.4 \pm 0.5 \text{ mN.m}^{-1}$ was obtained (averaged on measurements for 5 droplets) at 23.7 °C which is in agreement with literature values (27.8-29.4 mN.m⁻¹ between 20 and 25 °C, with a null or very low polar contribution < 1 mN.m⁻¹).¹⁵⁷⁻¹⁵⁹

Surface free energy measurements of PB and PBcis were performed, according to the OWRK approach (see 1.3.1.2). The contact angles of 5-7 sessile drops of reference liquids (deionised water, thiodiglycol and diiodomethane) were measured at $23.5 \pm 0.5 \text{ °C}$ as described in 2.6.2. By

plotting the OWRK linear construction (expressed in equation (1.32)), one can obtain the polar and dispersive parts of the surface energy of the polymer (square of the slope and intercept respectively) as well as its total surface free energy (sum of the two components). Figure 5-1 shows the OWRK construction from which the surface free energy of PB and PBcis were calculated. The total surface energy of the polymers as well as its dispersive and polar components are summarised in Table 5-1.

The results obtained (for PB, $28.0 \pm 2.6 \text{ mN.m}^{-1}$ and for PBcis, $28.6 \pm 2.2 \text{ mN.m}^{-1}$) are lower than typical literature values¹⁷ for the surface energy of PB (43.1 and 48.6 mN.m^{-1} at 20 °C for carboxyl acid end groups and methyl ester end groups, respectively). Unfortunately, in this reference, neither the structure of the polymer nor the measurement method are specified. Other sources¹⁶⁰ quote critical surface energies, determined by contact angle and Zisman plots, for PB with 1,2 addition (25 mN.m^{-1}) but also for trans-1,4 PB (31 mN.m^{-1}) and cis-1,4 PB (32 mN.m^{-1}). These values are closer to the experimental results but do not include any error analysis and are not obtained using the OWRK method. Surface energy data should be treated with some caution since these values are sensitive to factors such as microstructure, end-groups and temperature. Moreover, from the scatter in the data in Figure 5-1, one can see that the determination of the surface energy is subject to a significant experimental error, that can be associated with the sample preparation (purity of the polymer film, traces of solvent, roughness of the polymer film's surface) or even with the purity of the reference liquids.

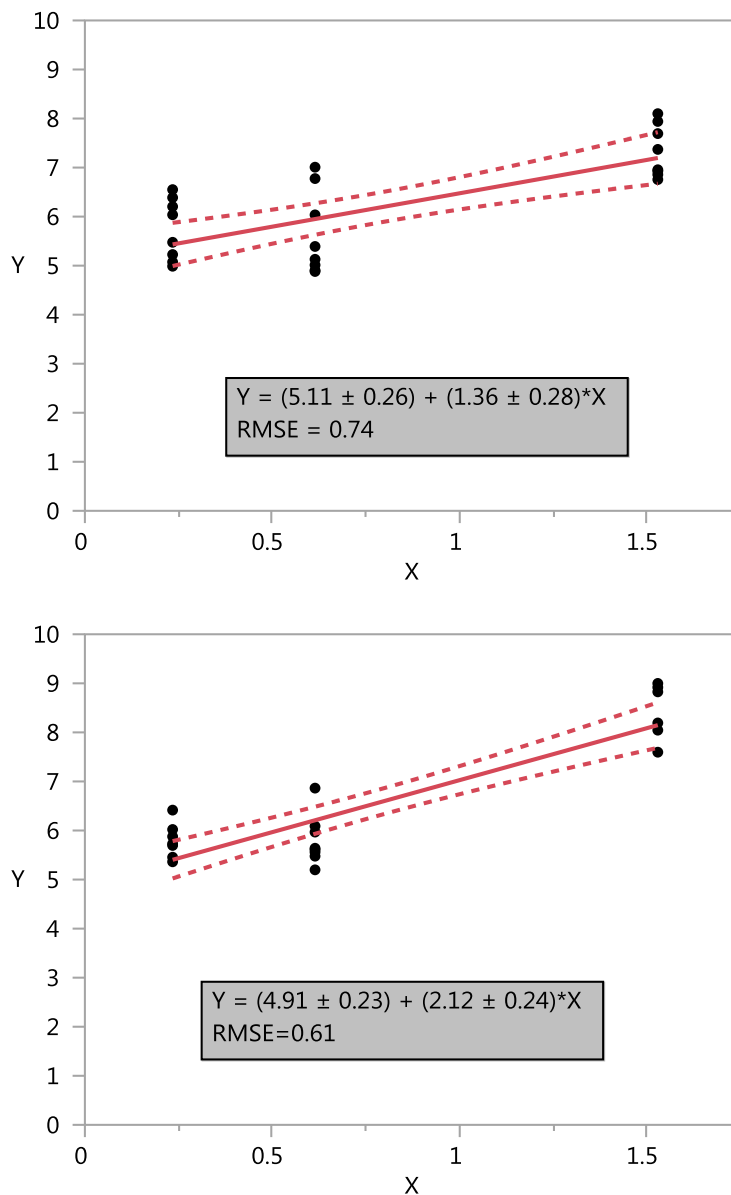


Figure 5-1: OWRK constructions for PB (top) and PBcis (bottom).

Table 5-1: Values for the total surface free energy as well as its dispersive and polar parts for PB and PBcis as calculated from the fit to the OWRK construction in Figure 5-1.

	Surface tension $\gamma / \text{mN.m}^{-1}$	Dispersive component $\gamma^d / \text{mN.m}^{-1}$	Polar component $\gamma^p / \text{mN.m}^{-1}$
PB	28.0 ± 2.6	26.1 ± 2.6	1.9 ± 0.8
PBcis	28.6 ± 2.2	24.1 ± 2.2	4.5 ± 1.0

5.1.1.2 Evidence for various oligomer depth distributions

5.1.1.2.1 Absence of oligomer surface enrichment

A first behaviour was observed, for the model mixture of oligo-dS/PB. From the DSC compatibility analysis, it was evident that this system showed some compatibility but the T_g shift was less than predicted by the Fox equation. The depth distribution of oligo-dS in a spin coated thin film composed of 15 % (w.w) of oligo-dS in PB was measured by fitting NR data. Due to the difference in scattering length density (s.l.d.) between oligo-dS (s.l.d. = $5.72 \times 10^{-6} \text{ \AA}^{-2}$) and the hydrogenated PB matrix (s.l.d. = $0.416 \times 10^{-6} \text{ \AA}^{-2}$), reflectivity fringes are detected corresponding to constructive and destructive interferences of neutrons reflected by the different interfaces (Figure 5-2, inset). One can note from the concentration profile resulting from the fit to the NR data (Figure 5-2, main figure) that a slight oligomer depletion occurs at the very surface, within the first nanometre. This apparent enrichment of non-deuterated material is implausible since the layer thickness is very small in comparison to the R_g of the polymer. Hence, it is more likely to be due to the surface roughness and will not be discussed further for the interpretation of the results.

Interestingly, the oligo-dS/PB system did not present any measurable oligomer excess which would suggest a complete miscibility with the polymer at the temperature of the measurement (around room temperature). This result is surprising as one might expect the presence of a small excess, due to the difference in molecular weight between the oligomer and the polymer or to the disparity in their surface energies.

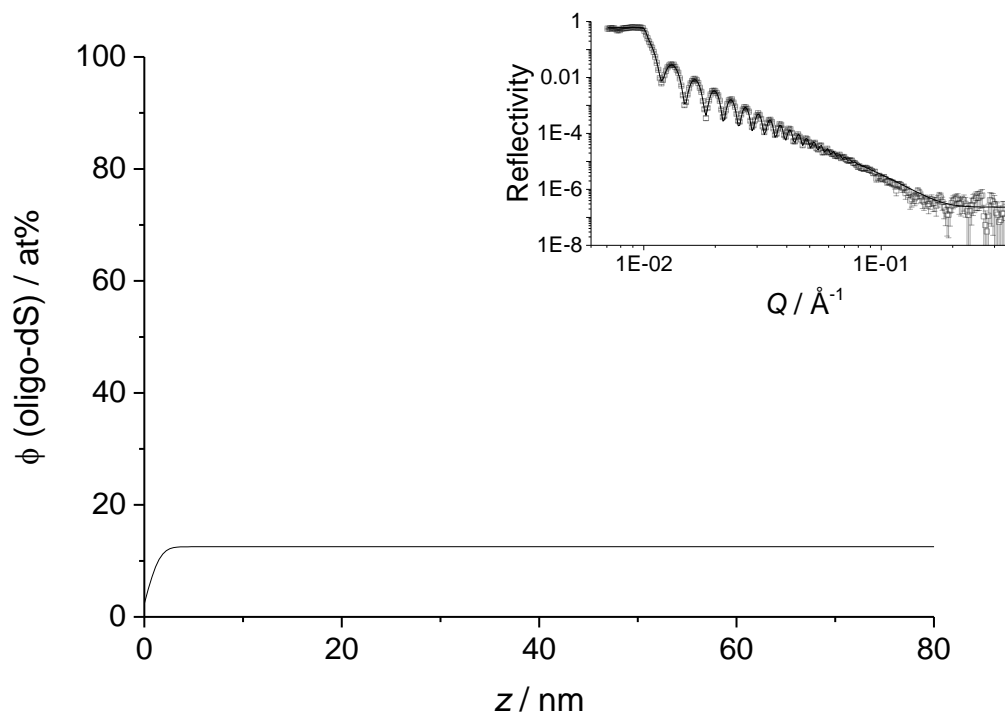


Figure 5-2: 15 % (w.w) oligo-dS in a thin PB film.

Inset: NR data measured with INTER and fits. Main figure: Profile corresponding to the fit in the inset.

5.1.1.2.2 Presence of oligomer surface enrichment

Mixtures of deuterated squalane (dsq) with PI or PB were spin coated from toluene solutions onto silicon wafers and the resulting thin films measured by ERDA. The measurements were performed at ~ -80 °C to avoid evaporation of the low molecular weight components under high vacuum. From the compatibility study, dsq/PI has been assessed as fully compatible while dsq/PB is a partially compatible system whose phase diagram was clearly determined in 4.1.2.1.

Typically, during an ERDA experiment, two signals are detected: one D signal which in this case corresponds to the deuterated species – i.e. the oligomer – and one H signal which corresponds to the hydrogenous species – i.e. the host polymer. As explained in 2.7.1.1, the D signal is recorded at higher energies than H, as D^+ is heavier than H^+ . Moreover, as the beam of ions is going deeper into the film, energy is lost. Thus, going from high to low detected energies is equivalent to going deeper into the film. One should also expect that the D and H signals have a similar energy spread as they are characteristic of the same film thickness and the energy loss through this thickness is identical for both scattered particles (dominated by the incident ^4He beam).

One can then fit the two signals to obtain concentration profiles. The ERDA results have high inherent accuracy because they are constrained by known factors such as scattering cross section and stopping power. However, the finite resolution of ERDA means that while the surface excess z^* , defined in equation (2.4), is well defined by the area of the peak in the raw data, the absolute surface concentration is imprecisely measured because the technique cannot distinguish between a very thin, pure surface layer and a thicker, less pure one. For this reason, the ERDA analysis was restricted to simple layer models.

The inset of Figure 5-3 presents an example of raw ERDA data for 40 % (w.w) dsq. The main graph in Figure 5-3, corresponds to the concentration profile for the ERDA data presented in the inset. Some example of fitting parameters for the ERDA data are given in Annex 2.

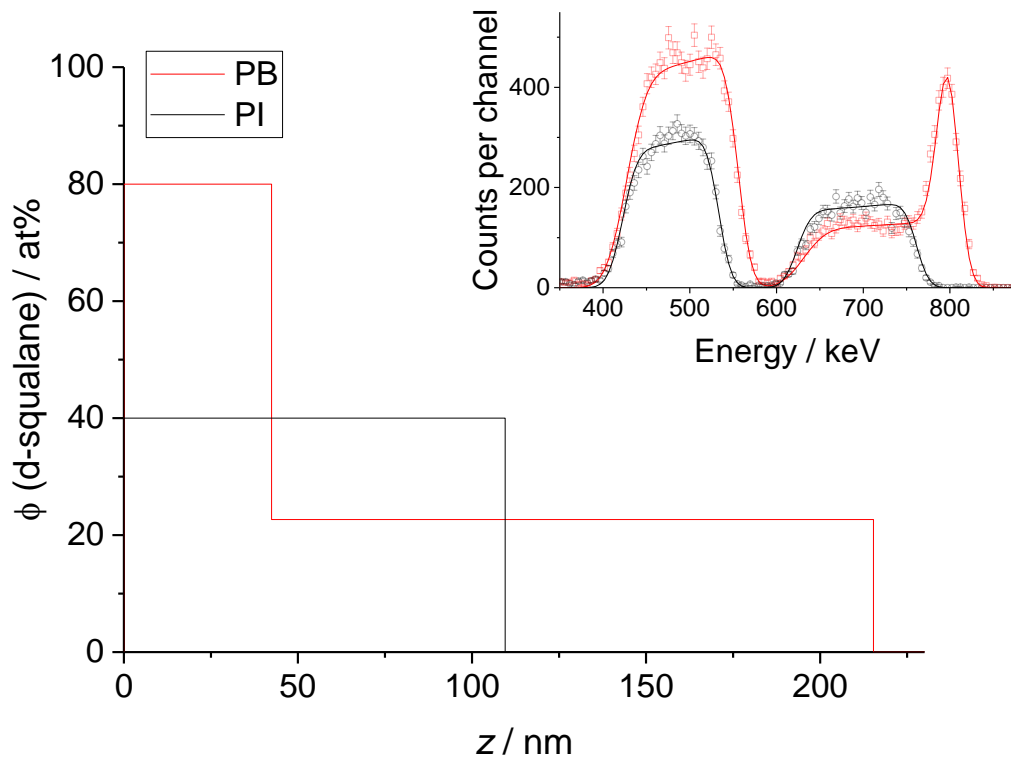


Figure 5-3: Raw ERDA data (inset): number of counts (detected particles) as a function of the energy range for 40 % (w.w) of dsq in PI (black, incident angle 63° , charge = $1 \mu\text{C}$) and in PB (red, incident angle 66° , charge = $1 \mu\text{C}$). The concentration profiles corresponding to the layer fit of the raw data are presented in the main figure.

It is possible to infer by inspection of the ERDA data, even prior to fitting, that dsq shows very different behaviour in the two rubbery polymer matrices: the H and D peaks (400-600 keV and 600-900 keV respectively) are similarly shaped for the PI film (black), whereas they are of very

different shapes for PB (red), which clearly indicates that the oligomer and matrix have different depth distributions. As is apparent from the shape of the raw data, the vertical composition profile of dsq (main figure) is strikingly sensitive to the polymer matrix in which it is dispersed: dsq is evenly distributed in PI but shows segregation at the surface of the PB film.

NR experiments were performed at room temperature (RT) on similarly prepared thin PB and PI films, containing 40 % (w.w) dsq. With NR's higher resolution it was possible to detect small surface excesses and obtain concentration profiles with a properly defined gradient, as needed for theoretical development. Also, NR is capable of distinguishing surface segregation in a single phase film from surface directed spinodal decomposition more directly, by the shape of the profiles obtained.¹⁵³ Fitting of the reflectivity data yielded concentration profiles, as shown in Figure 5-4.

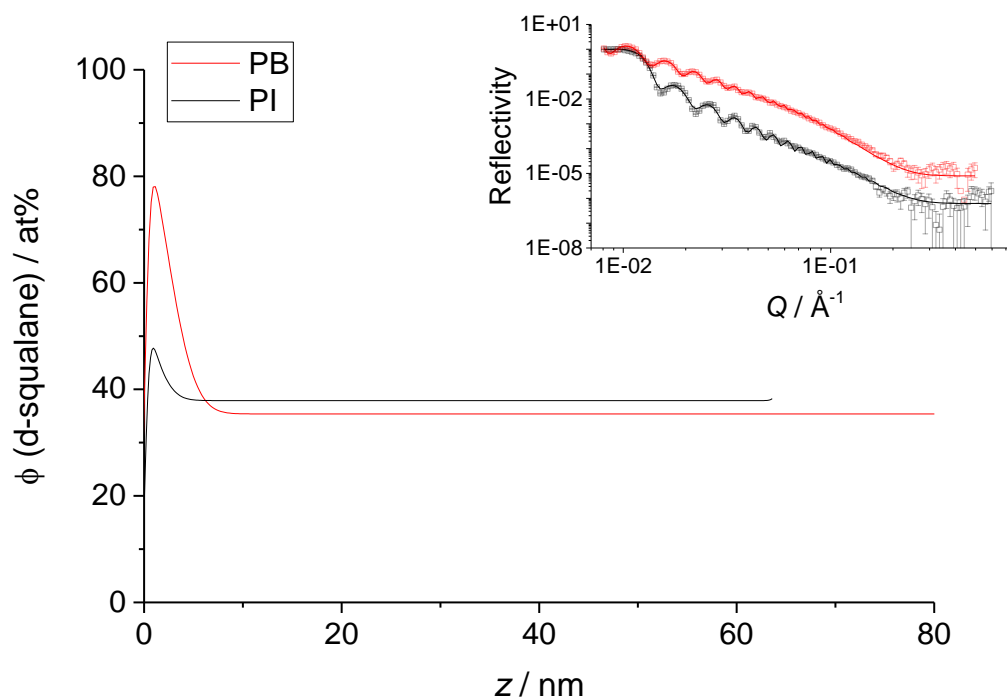


Figure 5-4: 40 % (w.w) dsq in a thin PI (black) and PB (red) film.
 Inset: NR data measured with SURF and fits. Main figure: Profiles corresponding to the fits in the inset.

The better resolution of the NR measurements (~ 0.5 nm versus 15 nm for ERDA) resolved a slight surface enrichment of dsq at the surface of the PI film for an oligomer content of 40 % (w.w) (Figure 5-4, main graph, black), which was not detectable by ERDA (Figure 5-3, main graph, black). Besides, the surface excess z^* of dsq in PB (Figure 5-4, main graph, red), defined as the amount of material from the bulk that is segregated at the surface, in excess of what the

concentration would be if the bulk concentration persisted all the way to the interface, seems smaller than the one detected by ERDA. A calculation of z^* will be presented in section 5.1.2.1.2, as a function of the oligomer content.

5.1.1.3 Effect of temperature on oligomer surface segregation

The concentration profiles of a ~ 100 nm thick film of 40 % (w.w) dsq in PB were measured with increasing temperature. The raw NR data and corresponding concentration profiles issued from the fit to the raw data are presented in Figure 5-5. It was shown in 4.1.2.1, from the phase diagram, that dsq/PB is fully compatible at this concentration and temperatures above 0 °C. However, one might expect a diminution of the interaction parameter with increasing temperature for this UCST system.

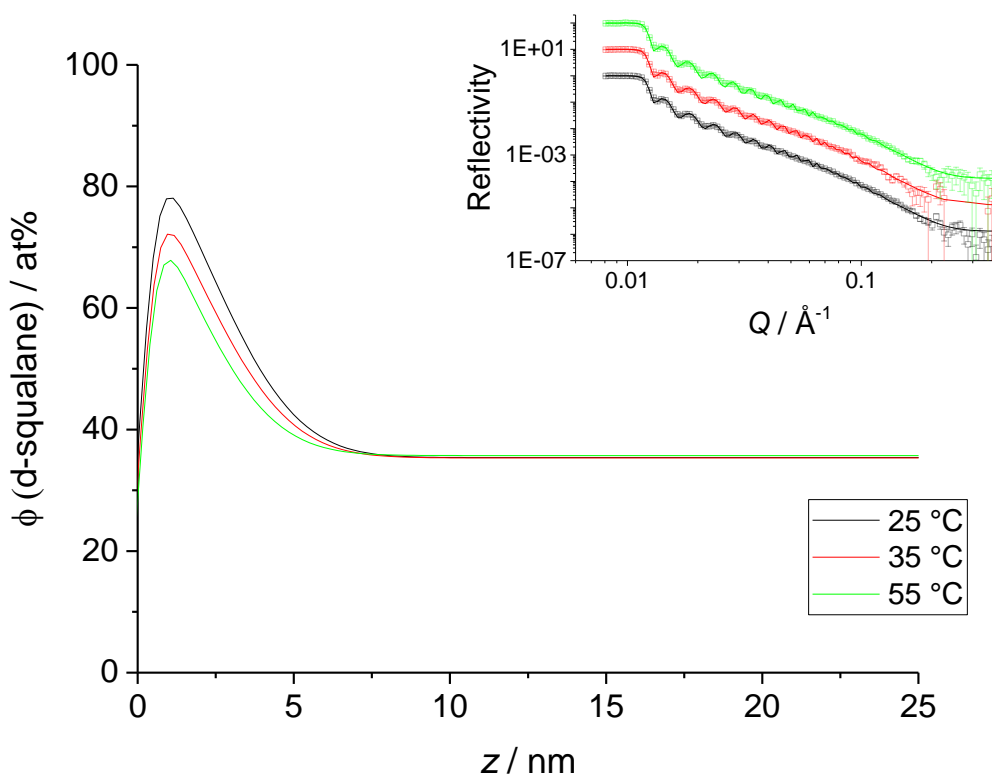


Figure 5-5: 40 % (w.w) dsq in thin PB film sample, with increasing temperature.
Inset: NR data measured with SURF and fits. Main figure: Profiles corresponding to the fits in the inset.

From the inset of Figure 5-5 one can note that an increase of temperature has a direct impact on the reflectivity curves: at medium Q values ($\sim 0.02 \text{ \AA}^{-1}$), the fringes are slightly shifted towards lower Q and the bulge in the data at high Q values ($\sim 0.04\text{-}0.2 \text{ \AA}^{-1}$) becomes less pronounced. This reflectivity behaviour, fitted into concentration profiles, indicates that the surface

concentration and the thickness of the excess layer decrease slightly but consistently with increasing temperature and is accompanied by a 5 % increase in film thickness (from 97.8 nm at 25 °C to 102.6 nm at 55 °C). The bulk concentration remains around 40 vol% and is not affected by the temperature since the mixture is in the one-phase regime.

Similar conclusions were obtained from the temperature dependency of a 50 % (w.w) blend of dsq with PB, which is still in the one-phase part of the sq/PB phase diagram in this range of concentration and temperature. This sample being thicker, the reflectivity fringes cannot be resolved in the raw data (Figure 5-6, inset) and the total thickness of the film does not affect greatly the determination of the surface excess. This is because these samples are so thick that the fringes are too narrow to resolve with a dQ/Q of 3 % resolution, which corresponds to the nominal resolution defined by the slit settings for beam collimation. Additionally, thicker films have the tendency to exhibit larger variation in film thickness across the sample which renders the absolute thickness more difficult to determine on an absolute scale. However, the shape of the R vs Q curve and the position of the critical edge enable to determine accurately the concentration and thickness of the surface layer.

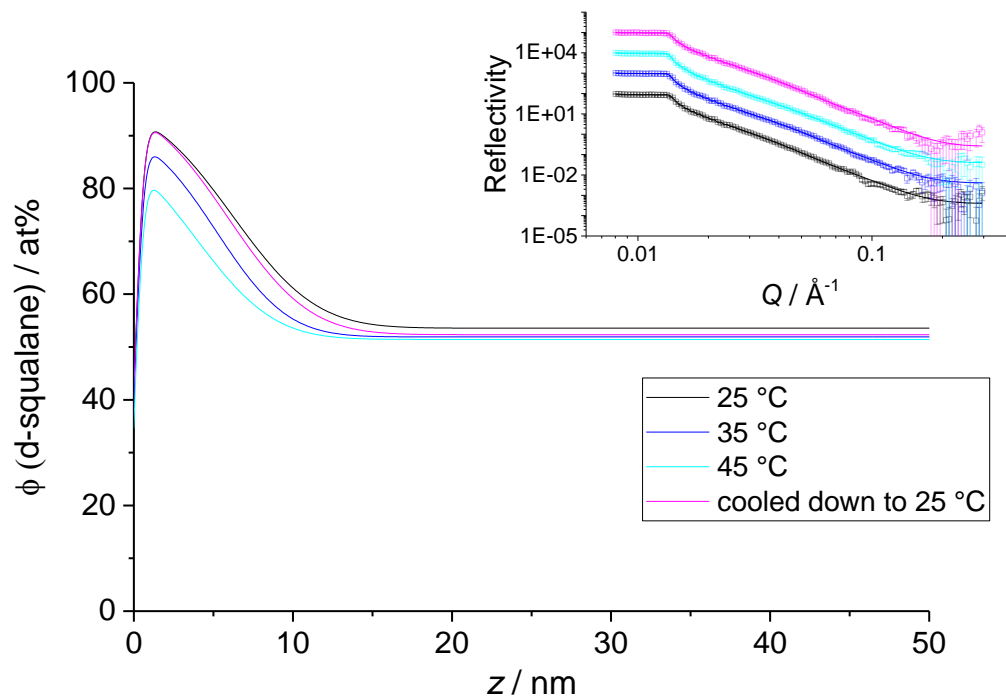


Figure 5-6: 50 % (w.w) dsq in thin PB film sample, with increasing temperature, followed by cooling back to 25 °C. Inset: NR data measured with SURF and fits. Main figure: Profiles corresponding to the fits in the inset.

Again, it is shown that an increase of temperature leads to a diminution of the surface segregation, without affecting the bulk concentration. Additionally, in this set of measurements, the sample was subsequently cooled down to room temperature, to determine whether this phenomenon was due to a simple evaporation of dsq at the surface. The concentration profile after cooling (Figure 5-6, main figure, pink curve) overlaps almost perfectly with the one of the sample before heating (Figure 5-6, main figure, black curve). Hence, this surface segregation behaviour is reversible and appears to be in equilibrium.

5.1.2 WETTING LAYER FORMATION THROUGH THE PHASE BOUNDARY

5.1.2.1 Effect of oligomer concentration on the wetting layer formation

In 4.1.2.1, it was determined that the order of preferential compatibility for sq in the host polymers was: PI, PB and then PBcis. In this section, the effect of the oligomer concentration on the surface excess of these three model systems of various compatibilities is assessed.

5.1.2.1.1 Deuterated squalane in polyisoprene

When blending the PI films with dsq at concentrations from 30 to 70 % (w.w), the concentration profiles obtained by ERDA showed an even distribution of dsq in PI (Figure 5-7). One could also notice the reduction of the film thickness with increased dsq content, as the viscosity of the spin coated solution decreases with increasing dsq content. This result is consistent with preliminary work¹⁴⁸ showing that for a given spinning speed, there is a linear trend between the spin-coated-film thickness and oligomer content.

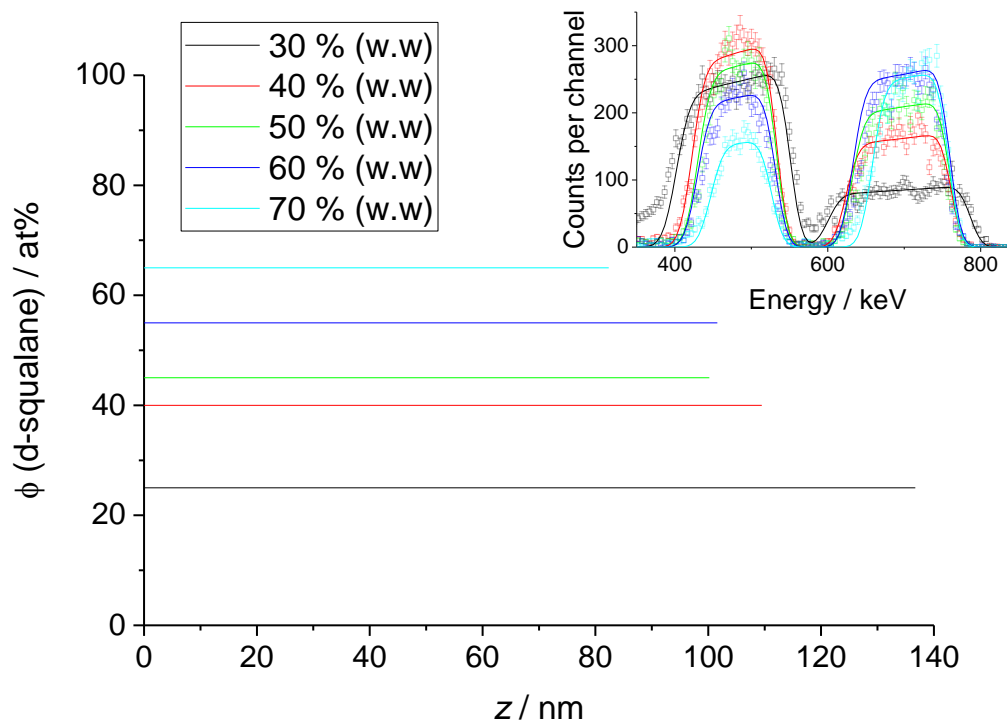


Figure 5-7: Raw ERDA data (inset) of dsq in PI.

The concentration profiles corresponding to the layer fit of the raw data are presented in the main figure.

Neutron reflectometry (NR) measurements were also performed on thin films (~ 70 nm) of PI containing various dsq contents. Vertical concentration profiles for dsq in the PI matrix are presented in Figure 5-8. At 30 and 40 % (w.w) of dsq, a small surface excess is measured by NR. However, when increasing dsq concentration (for contents of 60 and 70 % (w.w)), it seems that the concentration of dsq at the surface of the PI film is depleted, with a surface saturation at around 50 at%. The depletion in oligomer concentration observed at the surface actually corresponds to a measured decrease in s.l.d.. Hence, more realistically, this measured depletion might simply come from a roughening of the film's surface. One can also notice the depletion of oligomer at the interface with the silicon substrate for the higher concentrations. Again, this interfacial depletion does not seem very realistic, as there is no obvious physical explanation for such an occurrence – e.g. surface treatment to reduce the substrate's surface energy. These phenomena could be indicative of a partial film dewetting for the 60 and 70 % (w.w) samples.

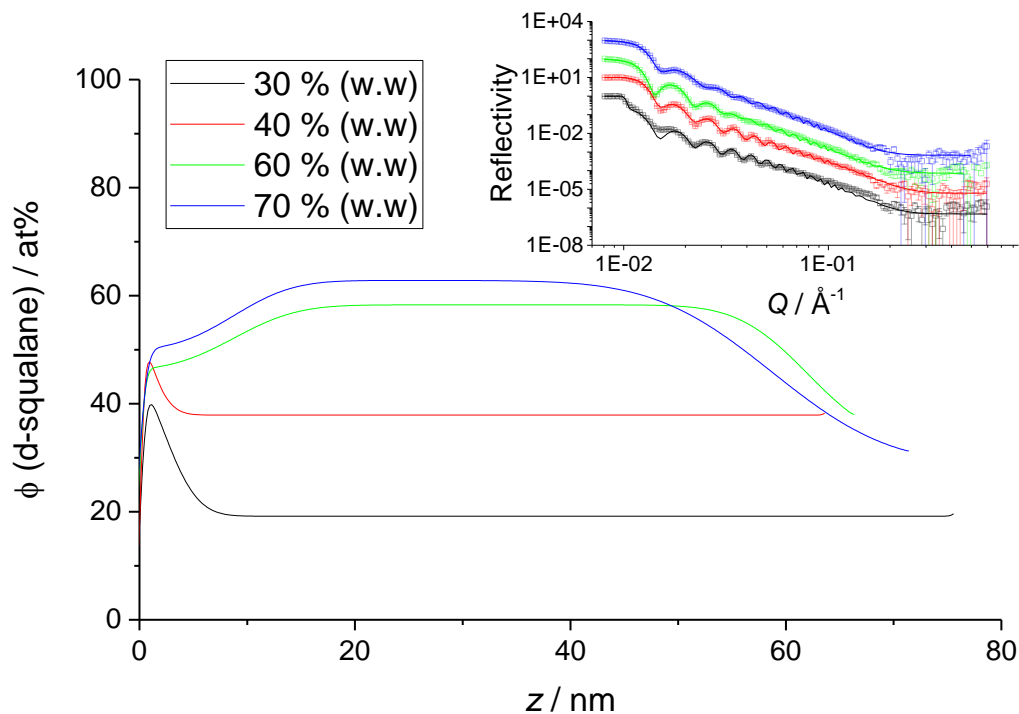


Figure 5-8: dsq in a thin PI films at various concentrations of dsq.
 Inset: NR data measured with SURF and fits. Main figure: Profiles corresponding to the fits in the inset.

As the ERDA experiment is performed at ~ -80 °C (vs NR at RT), and assuming an UCST type mixture, one would expect a higher incompatibility, and therefore, an accentuation of the surface excess in the ERDA experiment. Nonetheless, the surface excess was again not detectable by ERDA, suggesting that the amount of depleted / excess material is relatively low, even at lower temperature, or that the film is vitrified before interfacial segregation can occur.

5.1.2.1.2 Deuterated squalane in polybutadiene

In the case of dsq in PB (Figure 5-9), a surface excess was recorded by ERDA, increasing with the total oligomer content.

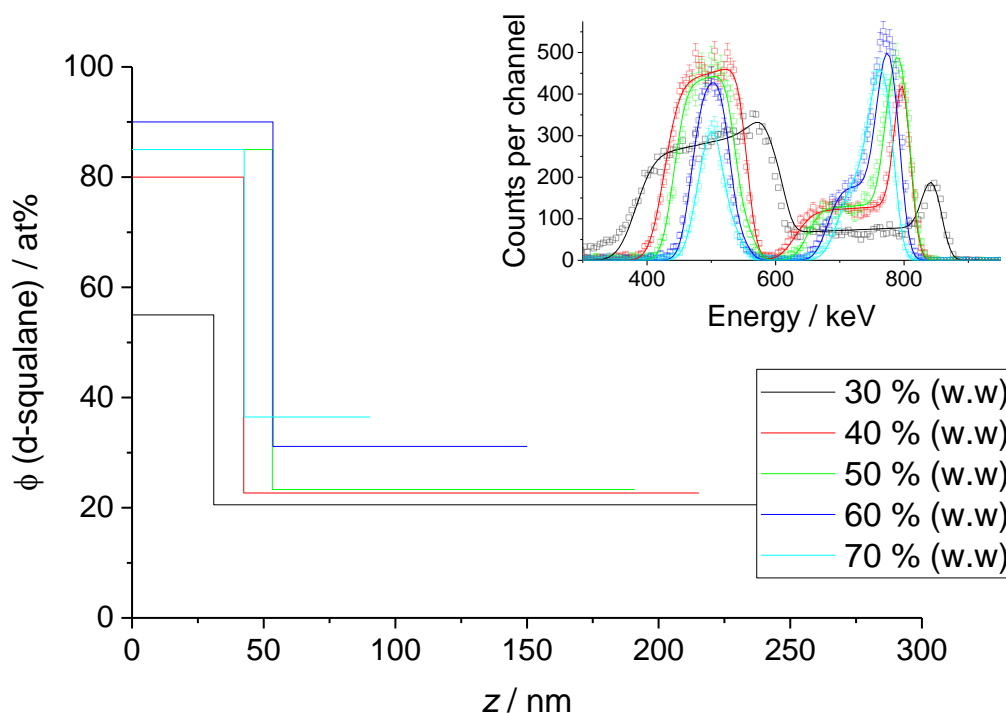


Figure 5-9: Raw ERDA data (inset) of dsq in PB.

The concentration profiles corresponding to the layer fit of the raw data are presented in the main figure.

From the concentration profiles in Figure 5-9, one can calculate, for dsq/PB the surface excess z^* from equation (2.4) — i.e. equivalent thickness of a pure layer of deuterated squalane. Although the precise thickness of this excess layer is difficult to determine with ERDA due to the limited resolution, the product of concentration and depth is well characterised; therefore surface excess values are normally accurate within the experimental error, which will be of the order of $\pm 10\%$ (range of error on the scattering cross section value used to fit the profiles). A more complete example of error analysis is given in *Annex 1*.

Considering that the maximum size of one molecule of dsq is the all-trans configuration length, and taking a carbon bond length and angle for an sp-sp bond of 1.38 \AA and 109.5° respectively,¹⁶¹ one can estimate that if the surface excess is larger than $23 \times 1.38 \times \sin(109.5/2) = 26 \text{ \AA}$ or 2.6 nm the surface layer is more than 1 dsq molecule thick. In other terms, one can infer phase separation — i.e. formation of a wetting layer — from the calculation of z^* .

One can also calculate, by integration of the concentration profiles over the whole thickness of the film, the total oligomer content φ_{tot} and verify that this amount matches the concentration of the solution used to spin coat the film. The values of φ_{tot} and z^* calculated for each concentration of dsq from the concentration profiles in Figure 5-9 are presented in Table 5-2.

Relative errors of 11 % and 14 % were calculated on the values of z^* and φ_{tot} respectively, from the error on the ERDA fits in the case of the 30 % (w.w) sample (more details are available in Annex 1). φ_{tot} is expressed in at% (direct result of the integration) and in % (w.w) which was calculated from the percentage of C, D and H in the oligomer and polymer.

Table 5-2: φ_{tot} and z^* calculated for each dsq content in PB from the concentration profiles in Figure 5-9.

Sample dsq content / % (w.w)	φ_{tot} / at%	φ_{tot} / % (w.w)	z^* / nm
30	25	24.5	10.7
40	34	33.4	24.3
50	41	40.3	32.9
60	52	51.3	31.5
70	59	58.3	20.7

The values of z^* suggest that for each dsq content, a phase-separated oligomer wetting layer is formed at the surface of the film as they are all in excess of 2.6 nm. The value of φ_{tot} obtained from the integration of the profiles is slightly but consistently lower than the experimental relative error of 14 % and might be indicative of a slight dsq evaporation due to the high vacuum in the end station or/and some surface segregation occurring in the early stages of the spin-coating.

In the PB matrices, surface segregation of dsq is also observed by NR using SURF and INTER (Figure 5-10), in agreement with ERDA. All measurements were performed at room temperature, which can vary depending on the time of the year and on the instrument: target station 1, in which is located SURF is usually warmer than target station 2, in which one can find OFFSPEC and INTER. It is important to bare this in mind since, from 5.1.1.3, one might expect temperature to affect the composition profiles.

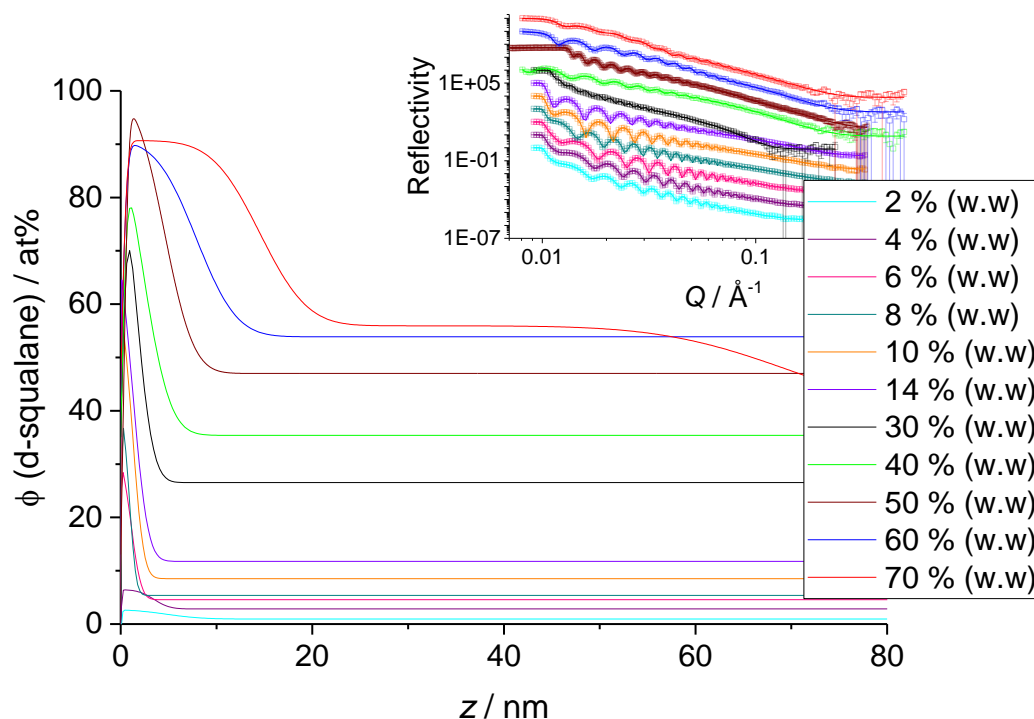


Figure 5-10: dsq in thin PB films at various concentrations of dsq.

Inset: NR data measured with SURF and INTER and fits. Main figure: Profiles corresponding to the fits in the inset.ⁱⁱ

Segregation is detected in PB for concentrations as low as 4 % (w.w) dsq. The surface excess z^* increases with overall migrant content. At 50 % (w.w) the surface appears to be saturated with oligomer at 94 %, based on the assumption that the mass density of the surface enriched layer is the same as it would be in the bulk. For the 70 % (w.w) sample a ~ 17 nm thick wetting layer is recorded, composed of 90 % d-squalane. For this last sample, a better fit was obtained when adding a diffuse layer at the interface with the substrate. This could indicate a roughening of the film and/or a slight dewetting, similar to what was obtained for the dsq/PI film of higher concentration. The results of the calculations for φ_{tot} and z^* from Figure 5-10 are summarised in Table 5-3.

The relative errors of φ_{tot} and z^* were estimated at 6 % from the error on the NR fits (see Annex 1). The values of φ_{tot} correspond to the expected content in the bulk, well within an experimental error of 6 %. In the case of the 70 % (w.w) sample, the rather low value of φ_{tot} might be a sign of

ⁱⁱ Samples from 2 to 14 % (w.w) were measured on the INTER reflectometer by Miss Rosie Davey & Arron Briddick, as part of preliminary experiments,¹³⁷ and refitted in the frame of this work. The SURF reflectometer was used to investigate samples at 30, 40, 60 and 70 % (w.w). The 60 and 70 % (w.w) dsq samples were measured inverted, in an early attempt to avoid squalane evaporation. The 50 % (w.w) sample was measured using the INTER instrument.

film dewetting. Very little squalane evaporation is expected here since the measurements are performed at room temperature and pressure. From the calculated values of z^* and the shape of the concentration profiles, it appears that a wetting layer is formed for concentrations of dsq superior to 50 % (w.w), which is in agreement with the bulk saturation value observed directly from the profiles.

Table 5-3: φ_{tot} and z^* calculated for each dsq content in PB from the concentration profiles in Figure 5-10.

Sample dsq content / % (w.w)	φ_{tot} / at%	φ_{tot} / % (w.w)	z^* / nm
2	1	1.0	0.1
4	3	2.9	0.1
6	5	4.9	0.3
8	6	5.8	0.3
10	9	8.8	0.7
14	13	12.7	0.9
30	27	26.5	0.9
40	37	36.4	1.3
50	49	48.3	2.3
60	57	56.3	2.8
70	58	57.3	5.0

5.1.2.1.3 Deuterated squalane in cis-polybutadiene

Similar NR results were obtained for dsq in PBcis (Figure 5-11). The values of φ_{tot} and z^* calculated for each concentration of dsq from the concentration profiles in Figure 5-11 are presented in Table 5-4.

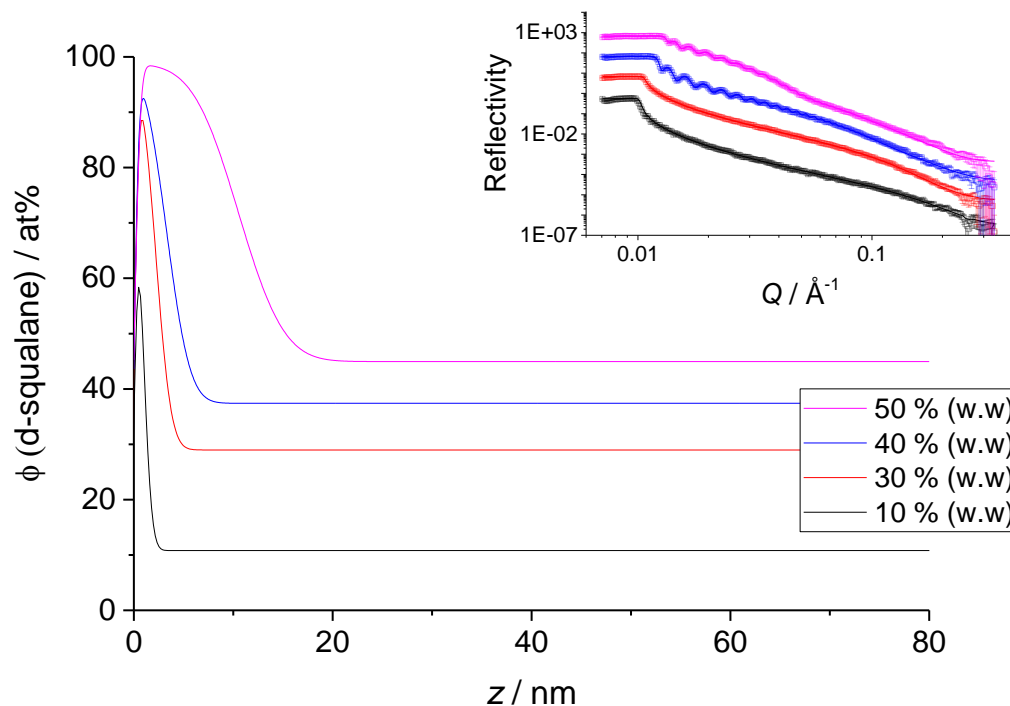


Figure 5-11: dsq in thin PBcis films at various concentrations of dsq.

Inset: NR data measured with INTER and fits. Main figure: Profiles corresponding to the fits in the inset.

Table 5-4: φ_{tot} and z^* calculated for each dsq content from the concentration profiles in Figure 5-11.

Sample dsq content / % (w.w)	φ_{tot} / at%	φ_{tot} / % (w.w)	z^* / nm
10	11	10.6	1.6
30	29	28.1	1.9
40	39	37.9	2.6
50	49	47.9	5.7

Again, the values of φ_{tot} correspond to the expected content in the bulk, within 6 % relative error. One can note from Table 5-4, that z^* becomes greater than the maximum monolayer value (2.6 nm) when the dsq content in the PBcis film is higher than 40 % (w.w). This value also corresponds to the point at which the surface gets saturated in dsq (> 95 % concentration is reached at the surface). Hence, in PBcis, the saturation of the surface is obtained at lower dsq concentration than in PB. The higher purity of the wetting layer in this system and its formation at lower concentration correlate well with a lower compatibility than for dsq/PB, evidenced earlier by the construction of the phase diagrams – i.e. a phase separation at 20 °C around 50 vol% dsq.

5.1.2.2 Effect of film thickness on the wetting layer

NR measurements were performed on films of 40 and 50 % (w.w) dsq/PBcis of various thicknesses, as illustrated in Figure 5-12 and Figure 5-13, respectively. Again, one can note that for the thickest films, almost no fringes are resolved in the raw data. Therefore, no interferences are formed and the total thickness of the sample is difficult to determine from the fit. Unfortunately, there was no equipment on-site to measure precisely the film thickness (ellipsometer or AFM) and the films were destroyed after NR measurement, which did not permit to perform the characterisation back in Durham. Nonetheless, the knowledge of the spinning speed and concentration of the toluene solutions should allow one achieving similar film thicknesses and hence concentration profiles; the 40 and 50 % (w.w) sq/PBcis samples labelled “thick” in the caption of Figure 5-12 and Figure 5-13 were obtained from spin coating a 5 % (w.w) toluene solution at 2000 rpm. These films are considered to have thicknesses greater than 300 nm (above this thickness there is no more effect on the quality of the fit to the NR data) but inferior to 1 μm (from the colour and coverage quality of the spin coated film on the substrate).

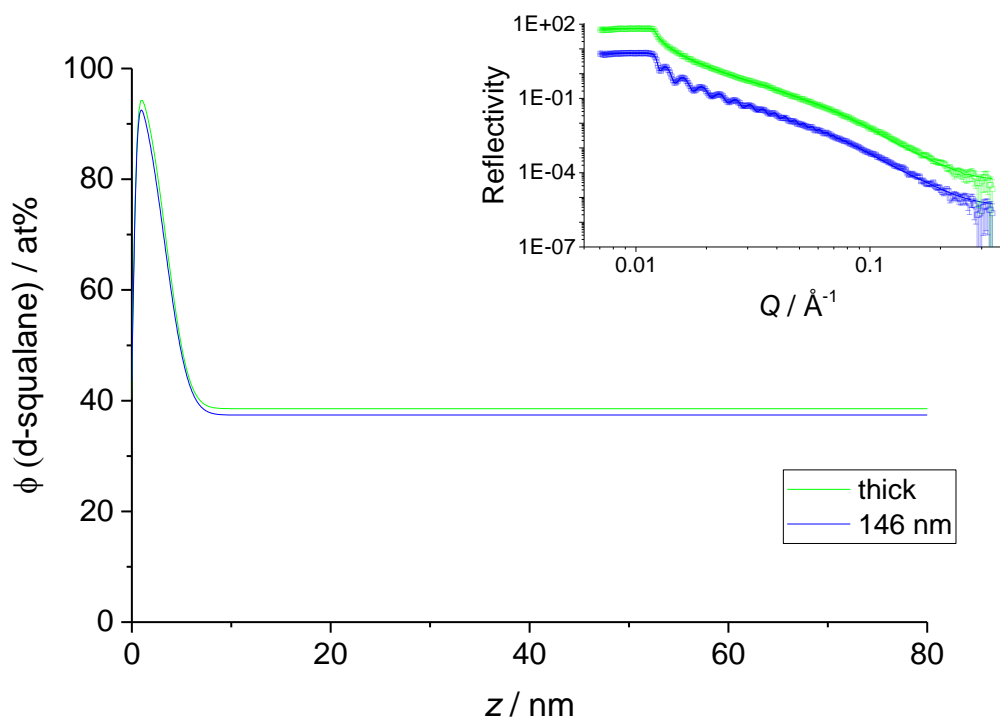


Figure 5-12: 40% (w.w) dsq in PBcis films of various thicknesses. Inset: NR data measured with INTER and fits. Main figure: Profiles corresponding to the fits in the inset.

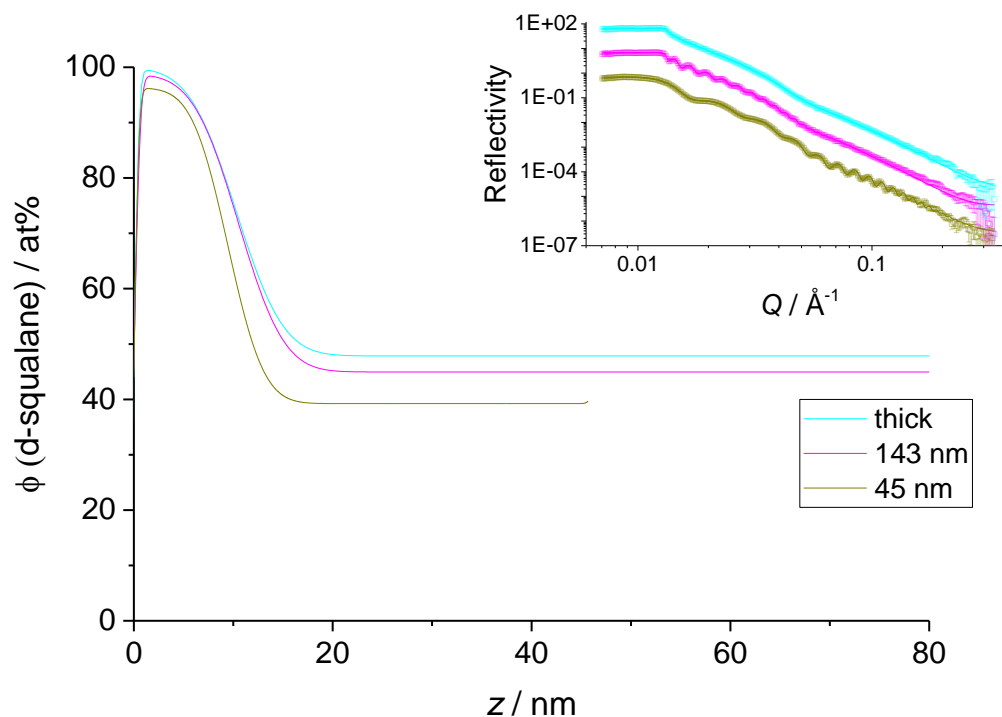


Figure 5-13: 50 % (w.w) dsq in PBcis films of various thicknesses.
 Inset: NR data measured with INTER and fits. Main figure: Profiles corresponding to the fits in the inset.

Interestingly, the thickness of the segregated layer of almost pure dsq is independent of the total film thickness (about 3 nm for the 40 % (w.w) sample and 10 nm for the 50 % (w.w) one). In the thinnest film of the 50 % (w.w) dsq content (45 nm), the bulk concentration is slightly depleted, when compared to the 2 thicker films, which seems to show that for very thin films, the affinity of the molecules for the surface is sufficient to alter the bulk equilibrium concentration.

NR measurements were performed on films composed of a 50 % (w.w) mixture of dsq and PB. According to the phase diagram of the sq/PB system, this concentration is very close to the phase boundary. Samples were spin coated at various thicknesses and measured on SURF (for the 200, 375 nm and “thick” sample, as determined from the fits to the NR data) and INTER (for the 125 nm sample) reflectometers. The “thick” sample was obtained from spin coating a 6 % (w.w) toluene solution at 2000 rpm. Apart from this thick film, all samples produced large surface excesses. Yet, the concentration profiles exhibit a rather large variability for the 4 samples considered (Figure 5-14) and show no real consistency with the film thickness. The 4 films were spin coated from 2 main solutions, one of the solution being diluted to produce the three thicknesses for the films measured on SURF (6, 4 and 2 % (w.w)). The lack of consistency in the data might come from different concentrations of the main solutions. Additionally various

temperature and relative humidity conditions during the measurements as well as the presence of residue on the substrates might have affected the sample preparation and equilibration.

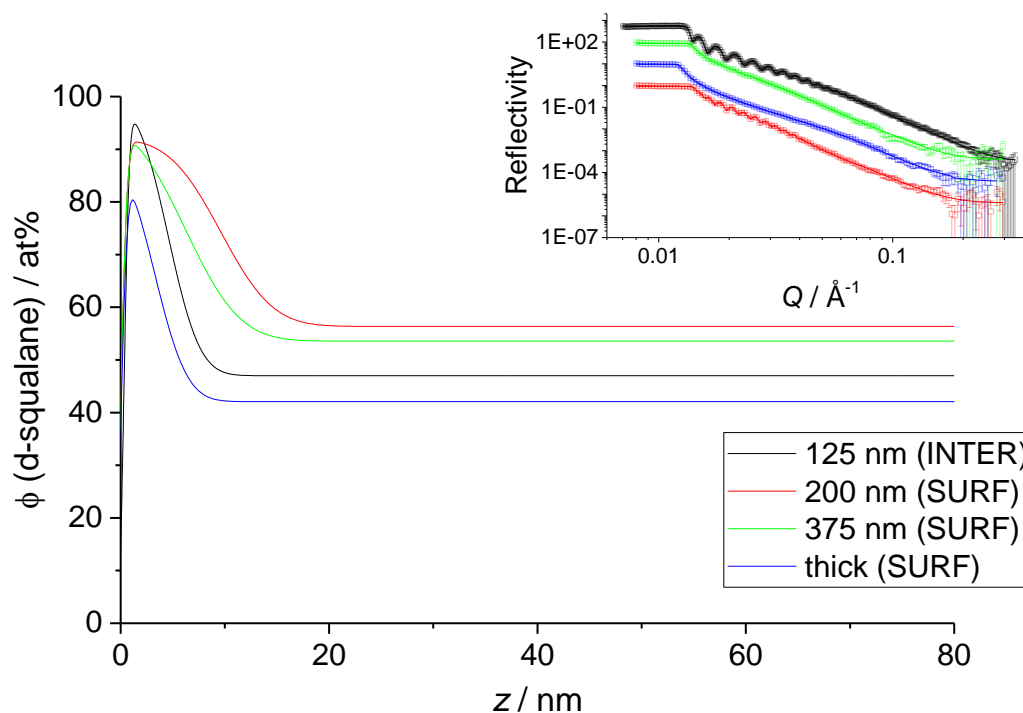


Figure 5-14: 50 % (w.w) dsq in thin PB films of various thicknesses.
Inset: NR data measured with INTER and SURF and fits. Main figure: Profiles corresponding to the fits in the inset.

5.1.2.3 Effect of polymer molecular weight and polydispersity on the wetting layer

A fractionation of the PBcis was performed by dissolving PBcis at 4 % (w.w) in toluene and, with the use of a thermostated fractionation flask, adding slowly methanol to precipitate the low M_w end of the polydisperse polymer. The full method description is given in 2.2.4. After removal of the methanol phase, the toluene was evaporated and a GPC was run on the remaining PBcis indicating a M_w of 844 kg.mol⁻¹ and a PDI of 3.51 (vs M_w of 567 kg.mol⁻¹ and a PDI of 4.45 for the original PBcis). The raw GPC data is given in Figure 5-15. From this figure, one can see that, at longer retention times, the signals for the 3 detectors are weaker in the case of the fractionated PBcis in comparison with the original PBcis. This means that the smaller molecules, retained for longer times in the GPC column, have indeed been removed from the sample as a result of the fractionation.

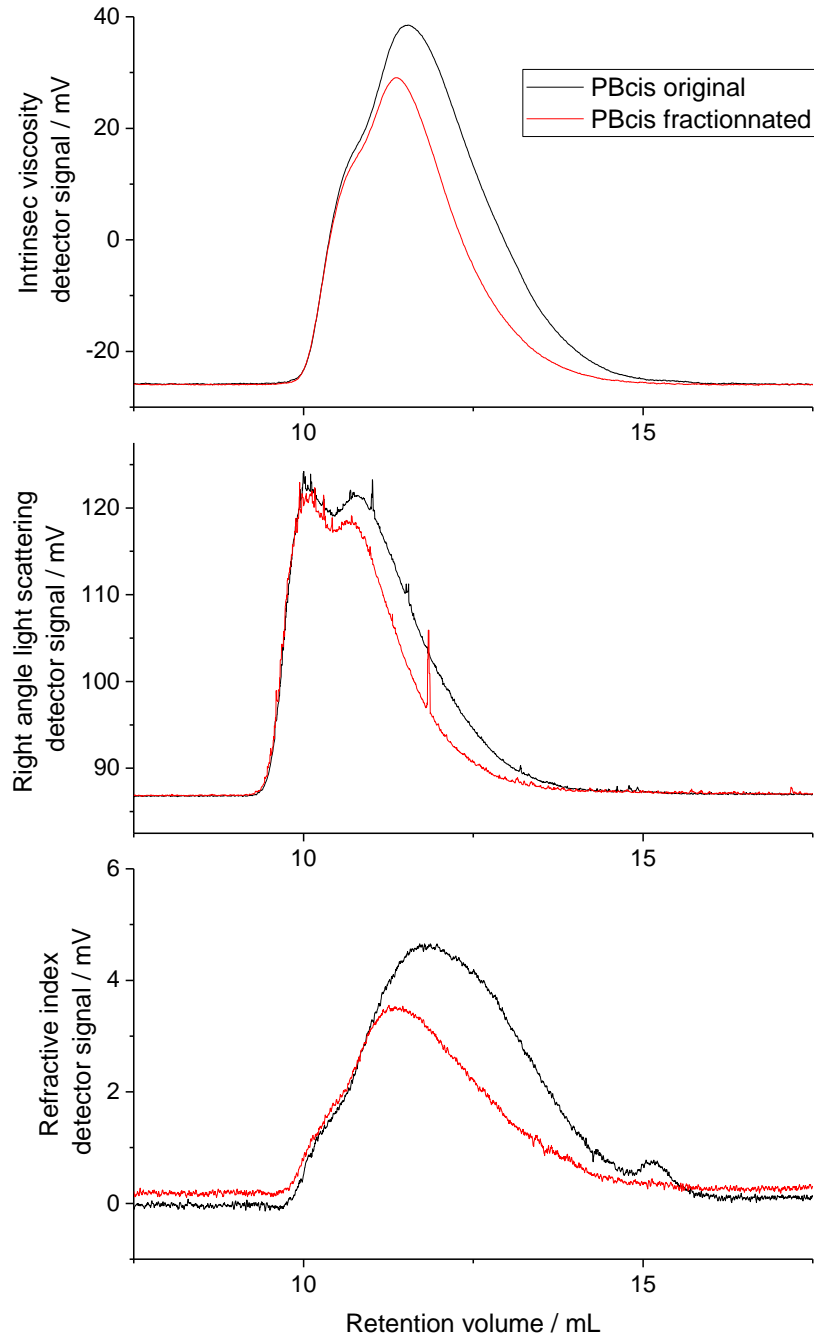


Figure 5-15: Raw triple detection GPC data for the original PBcis and after fractionation.

Two films containing 50 % (w.w) dsq and fractionated PBcis were spin coated and measured by NR. Both films were rather thick (300 nm to 1 μ m), as suggested from their colour and the absence of fringes on the NR data. The film coated from the lower concentration solution is labelled “thin” while the other one is labelled “thick”. They were obtained from spin coating at 2000 rpm of a 4 and 2 % (w.w) toluene solution, respectively.

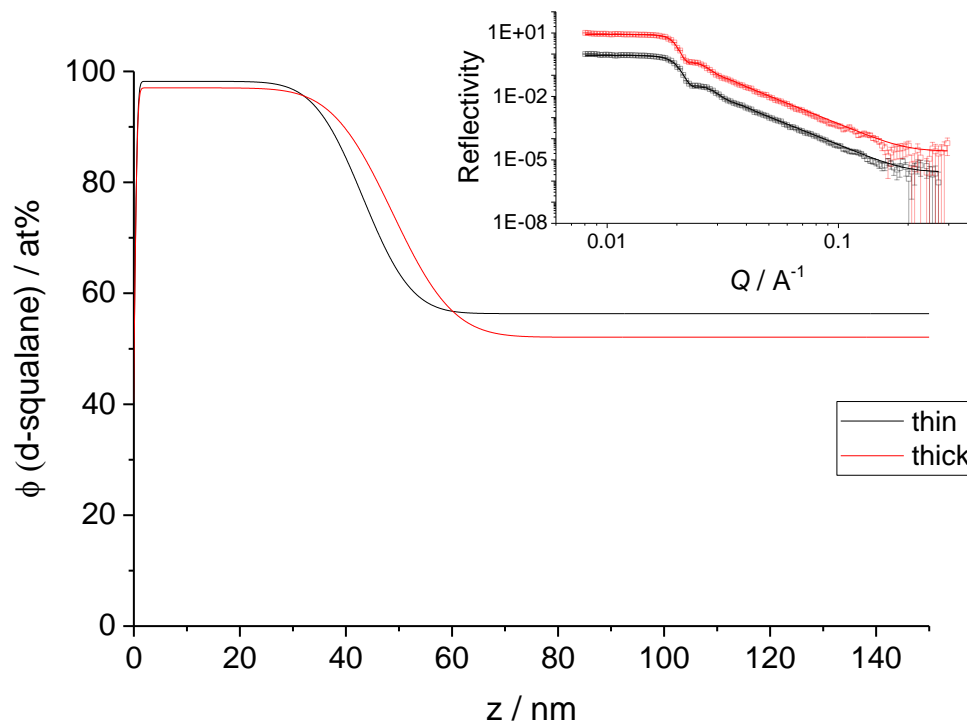


Figure 5-16: 50 % (w.w) dsq in thin fractionated PBcis films of two thicknesses. Inset: NR data measured with SURF and fits. Main figure: Profiles corresponding to the fits in the inset.

Once again, it is shown from Figure 5-16 that the thickness of the wetting layer does not depend on the total thickness of the film. For both films, a ~ 50 nm thick pure wetting layer of dsq is recorded. This thickness is 5x bigger than what was recorded for the samples of dsq in the original PBcis at corresponding concentration and the layer is also more diffuse (Figure 5-11). Hence, it appears that the thickness of the interface with the polymer-rich layer is somehow governed by the molecular weight of the polymer.

5.1.2.4 Effect of time and temperature on the wetting layer formation

A sample containing 50 % (w.w) dsq in PBcis was prepared and measured by NR at RT at several times to investigate its stability. A first measurement was performed (Figure 5-17, black), followed by a second, 16 hours later (Figure 5-17, red) and a third, 23 h later (Figure 5-17, green). It was then decided to cool the sample down to ~ 15 °C (Figure 5-17, dark blue) and subsequently bring it back to 25 °C (Figure 5-17, light blue). From the NR data, it seems that very little modification of the sample occurred after 16 hours. After a day, the concentration in the whole sample seems to have dropped slightly, potentially due to dsq evaporation. Similar results were obtained by Smith *et al.* showing that the diffusion of a nitroplasticiser (50 % (w.w) eutectic

mixture of bis(2,2-dinitropropyl)acetal and bis(2,2-dinitropropyl)formal) to the surface of an annealed polyester-polyurethane (Estane) film at RT is rapid compared to the experimental time and that the rate of plasticiser evaporation from the film is the driver of the plasticiser loss.¹⁰⁸

The cooling step (Figure 5-17, dark blue) increases the thickness and concentration of the surface excess layer. Indeed, as mentioned in 4.1.1.2, this mixture is very close to the phase boundary with a cloud point measured at ~ 20 °C. Hence, there is here phase separation of the dsq. Ultimately, when warming up the sample back to 25 °C (and back in the one-phase regime), the wetting layer that formed at 15 °C is reabsorbed and the concentration profile is again similar to the very initial state but with a slightly thicker excess layer and an increased roughness.

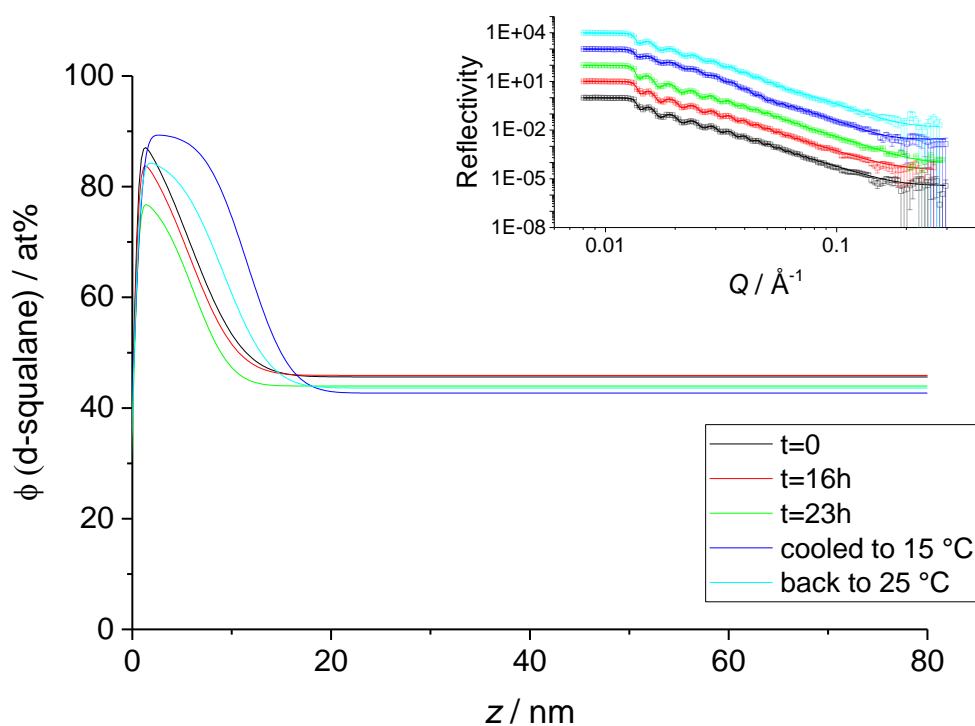


Figure 5-17: 50 % (w.w) dsq in a thin PBcis film at various times and temperatures. Inset: NR data measured with SURF and fits. Main figure: Profiles corresponding to the fits in the inset.

5.1.3 WETTING LAYER ORIENTATION IN PHASE-SEPARATED SYSTEMS

5.1.3.1 Excess directed to the surface

Oligo-dIB 900 g.mol^{-1} was analysed at different concentrations in PI. Similarly to the case of dsq/PB, one can observe some skewing in the proton and deuterium peaks of the ERDA spectra: the deuterium peak (600-800 keV) is skewed to high energy, implying surface enrichment of oligo-dIB 900 and the opposite occurs for the proton peak (400-550 keV). A conversion of the

ERDA data into concentration profiles with a bilayer fit is presented in Figure 5-18. The fits to the experimental data unambiguously show that the oligo-dIB 900 is partially segregated to the film surface. However, it appears unlikely that the surface layer is purely oligo-dIB 900.

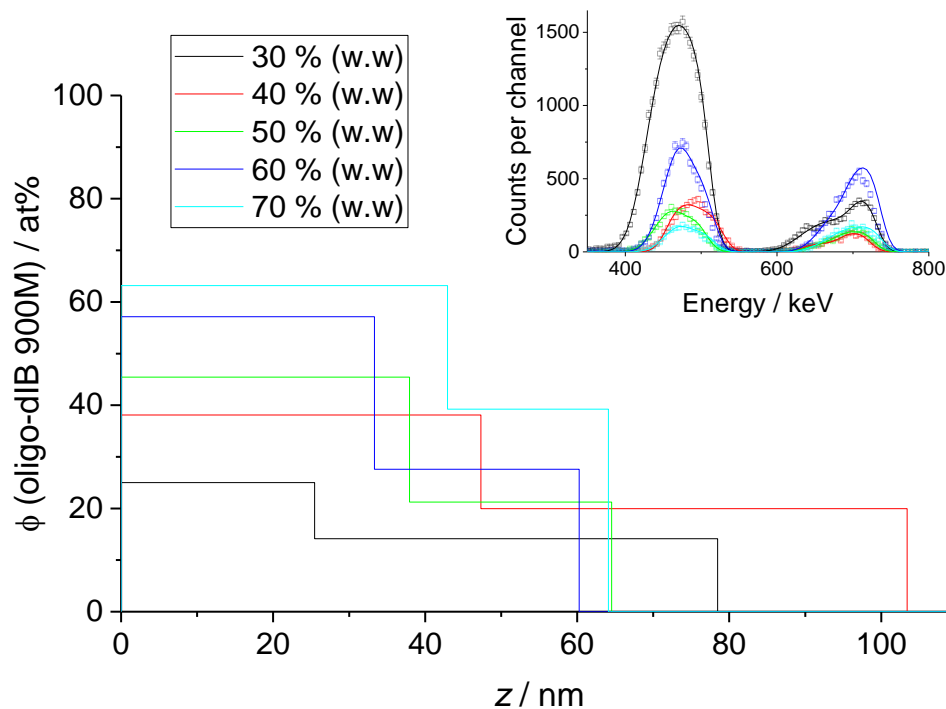


Figure 5-18: Raw ERDA data (inset) of oligo-dIB 900 in PI. The concentration profiles corresponding to the layer fit of the raw data are presented in the main figure.

The oligomer excess at the surface increases with the total amount of oligomer in the film. The bulk concentration increases with the oligomer content as well, which implies that there is no solubility limit within the range of concentration studied. This result agrees with the DSC experiments showing some compatibility of the oligo-dIB 900 in PI around the glass transition temperature of the sample (which corresponds roughly to the ERDA measurement temperature). Values of the total oligomer concentration φ_{tot} and the surface excess z^* are gathered in Table 5-5.

The total oligomer content seems to be underestimated in the layered concentration profiles (absolute error of 12-16 % (w.w) in comparison to the content of the prepared solution, which is well above the expected relative error of 14 %). The oligo-dIB used for this project had a molecular weight of 900 g.mol⁻¹, which is too high to support the hypothesis of a potential evaporation of the oligomer. However, since a hydrogeneous initiator (2,4,4-dimethylpentene / HCl) was used for the synthesis, 17 hydrogen atoms should be found on each of the oligomer

chains, which corresponds to a degree of deuteration of 87.5 at% for a 900 g.mol⁻¹ molecule. This partial deuteration could therefore explain the disparity in φ_{tot} .

Table 5-5: φ_{tot} and z^* calculated for each oligo-dIB 900 content in PI from the concentration profiles in Figure 5-18.

Sample oligo-dIB 900 content / % (w.w)	φ_{tot} / at%	φ_{tot} / % (w.w)	z^* / nm
30	18	18.3	2.8
40	28	28.4	8.6
50	36	36.4	9.2
60	44	44.4	9.9
70	55	55.4	10.3

Knowing the M_n of oligo-dIB 900, one can roughly evaluate the maximum thickness of a 1-molecule thick layer of oligo-dIB 900 at the surface in the all trans conformation: $32 \times 1.38 \times \sin(109.5/2) = 36 \text{ \AA}$ or 3.6 nm. Therefore, a separate wetting layer is implied by a surface excess larger than 3.6 nm, which is the case for all the oligomer contents considered here apart from the 30 % (w.w) sample. However, considering a 11 % relative error on the determination of z^* , a small error on the sample preparation and energy minimisation arguments suggesting that it is quite unlikely for the oligomer chains to be fully stretched, it is likely that phase separation occurs in the 30 % (w.w) sample.

NR was also performed on films containing 30 and 40 % (w.w) of oligo-dIB 900 in PI (Figure 5-19). The fits in the inset correspond very well to the fringes in the raw data. However, the oligomer gradient on the corresponding concentration profiles appears to be larger than what can be accurately characterised by a NR experiment (especially for the 40 % (w.w) sample); reasonably sharp interfaces (< 10 nm) are needed for reflecting the neutron beam. Additionally, the measured surface layer is not pure. It is interesting to note that the raw data features fringes, which indicates that interferences between reflected neutrons are recorded and that the film is still flat or smooth.

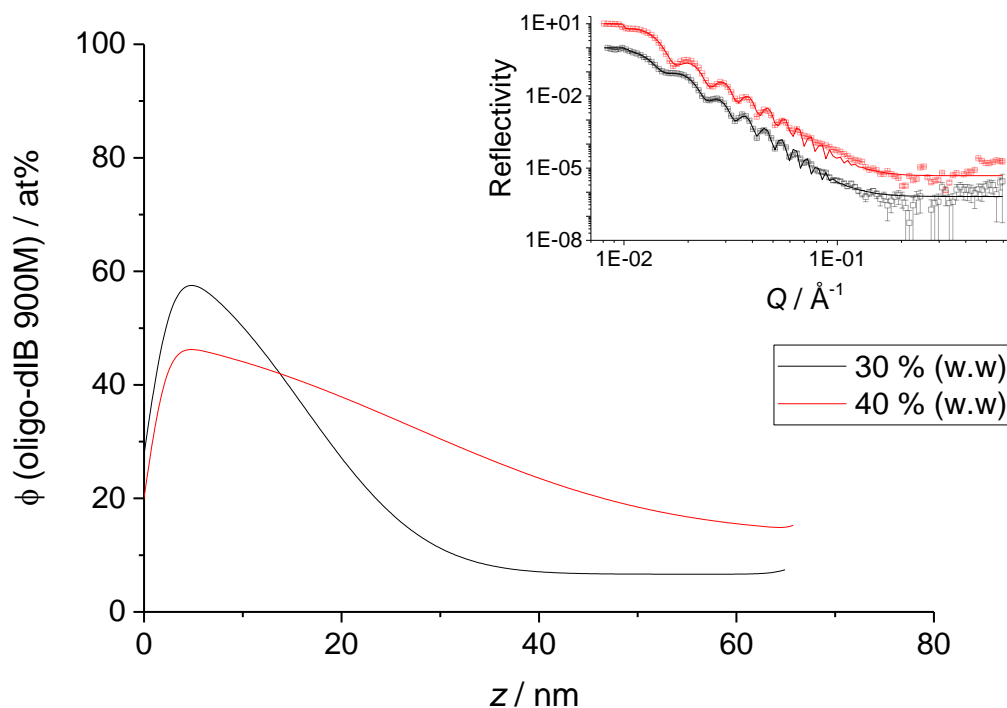


Figure 5-19: 30 and 40 % (w.w) oligo-dIB 900 in thin PI film samples.
 Inset: NR data measured with SURF and fits. Main figure: Profiles corresponding to the fits in the inset.

The comparison of ERDA and NR data suggests that the concentration profiles in Figure 5-19 are not representative of the real oligomer gradient in the film. The low surface concentration and wide gradient suggest that a lateral inhomogeneity is present within the films, and that those films are therefore not well described by a 1D profile. This phenomenon would still lead to the appearance of fringes in the raw NR data, but would imply an incorrect determination of the 1D concentration, as lateral features would give rise to multiple different contributions to the measured specular reflectivity (averaged over a surface corresponding to the footprint of the beam). One can note that the nicely defined measured fringes also show that the sample was stable over the time of the measurement – i.e. about 3 hours. The ERDA data is more reliable since it represents the average number of hydrogen and deuterium atoms at a certain depth, while neutron data may not yield a unique and valid composition profile.¹⁶²

Further NR experiments were performed on oligo-dIB 2200 PI mixtures (Figure 5-20). Typically, from 4.1.2.2, the increase in the oligomer molecular mass leads to a reduced compatibility between the oligomer/polymer pair. Hence, surface segregation is expected to be increased.

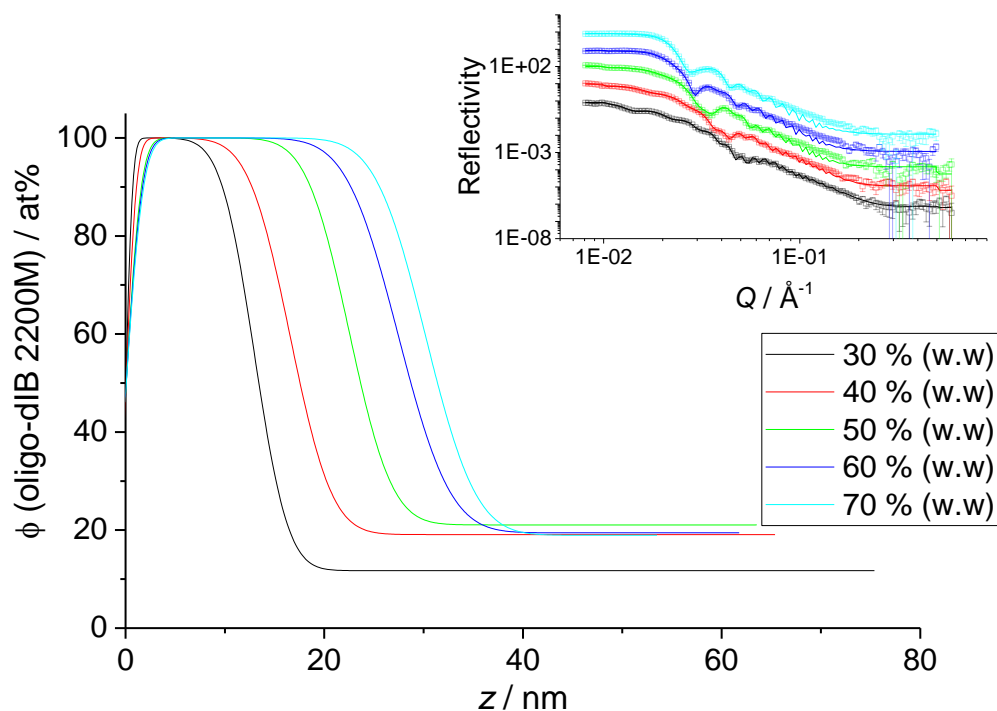


Figure 5-20: oligo-dIB 2200 in thin PI films at various concentrations of oligo-dIB.
 Inset: NR data measured with SURF and fits. Main figure: Profiles corresponding to the fits in the inset.

The NR profiles show a lower compatibility than the ERDA and NR data for oligo-dIB 900, due to the increase in oligomer molecular weight: a large wetting layer is formed at the surface for all concentrations that is possibly almost pure oligomer and a sharp interface between the wetting layer and the bulk is also evidenced, which suggests a strong phase separation. However, because of the approximations on the oligomer's density and structure (which, according to the ERDA experiments, might contain a bit of hydrogen due to the initiator), some uncertainty exists on the s.l.d. chosen for the pure oligomer and the surface layer might contain a small proportion of polymer. It seems that the wetting layer is laterally uniform because the excess layer is almost pure and its roughness is well determined (a few nms), lower than the excess formed for oligo-dIB 900. Its thickness is increasing linearly with the overall migrant content, while the roughness of the interface between the two phases remains constant. A solubility limit around 20 at% oligo-dIB ($2200 \text{ g}\cdot\text{mol}^{-1}$) in the PI film is recorded for samples with a total ratio of oligo-dIB /PI higher 40 % (w.w). The slight depletion in the bulk concentration of the 30 % (w.w) sample (13 instead of 20 at%) might be due to the lower sensitivity of the NR method to measure layers absolute concentrations rather than gradients, or to the low thickness of the sample, as discussed in 5.1.2.2. Therefore, this set of concentration profiles might indicate a phase boundary at around 20 at% oligomer content.

A phase separation at 20 at% at RT agrees with the calculated z^* which suggests that the 5 measured samples are presenting a phase-separated wetting layer (Table 5-6). Indeed, knowing the M_n of oligo-dIB, one can roughly evaluate the maximum thickness of the wetting layer: $78 \times 1.38 \times \sin(109.5/2) = 88 \text{ \AA}$ or 8.8 nm. A separate wetting layer is clearly obtained for all concentrations of oligomer considered.

Table 5-6: φ_{tot} and z^* calculated for each oligo-dIB 2200 content in PI from the concentration profiles in Figure 5-20.

Sample oligo-dIB 2200 content / % (w.w)	φ_{tot} / at%	φ_{tot} / % (w.w)	z^* / nm
30	27	27.4	11.3
40	35	35.4	13.1
50	48	48.5	17.3
60	55	55.5	21.6
70	64	64.4	23.9

Films of PBcis containing several concentrations of oligo-dIB 2200 were spin coated onto silicon blocks and NR measurements were carried out. By fitting the reflectivity versus momentum transfer data, concentration depth profiles were obtained (Figure 5-21), showing a large surface segregation of oligo-dIB at concentrations as low as 10 % (w.w). This signifies a poor compatibility of the components of the film, in agreement with the DSC thermograms that clearly exhibited two distinct T_g s. The surface excess layer contains about 95 at% oligomer and grows in width with total oligomer content in the film. One can note that the thickness of the excess layer is a little bit thicker and more diffuse than in the case of oligo-dIB 2200 in PI (Figure 5-20), which might be due to the large polydispersity of the PBcis.

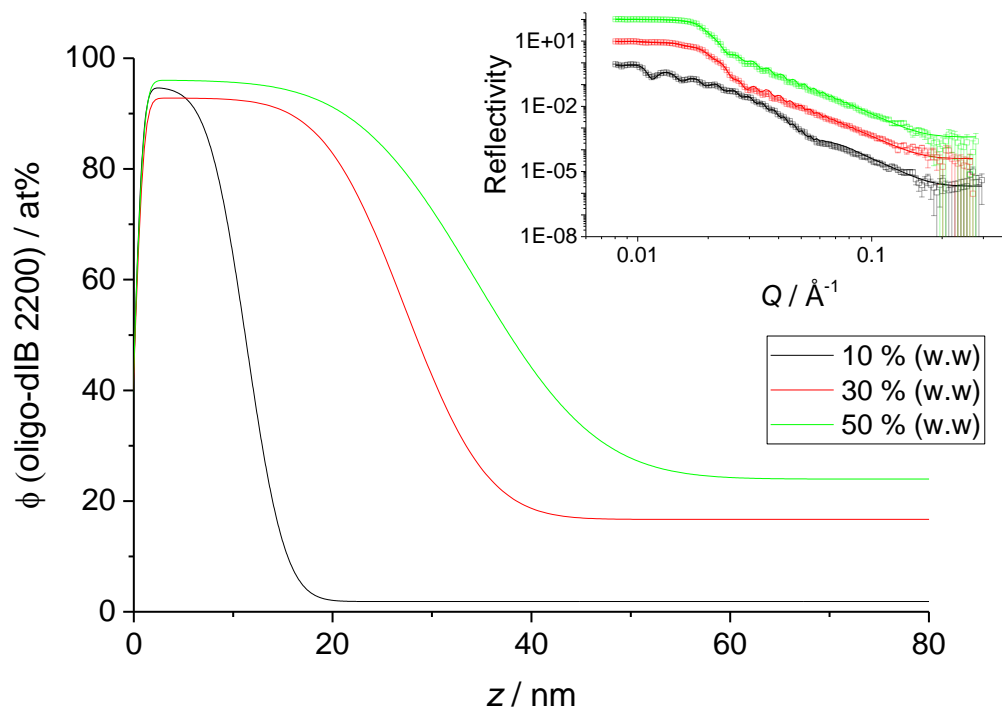


Figure 5-21: oligo-dIB 2200 in thin PBcis films at various concentrations of oligo-dIB. Inset: NR data measured with SURF and fits. Main figure: Profiles corresponding to the fits in the inset.

5.1.3.2 Excess directed to the interface with the substrate

In mixtures of oligo-dS with hPI, the oligomer is found to segregate at the buried interface between the film and the substrate. This system was assessed as highly incompatible by DSC and presents a large surface energy difference, due to the difference in polarisability of the pure components. Figure 5-22 (left) presents the raw ERDA data and the fits for 30 to 70 % (w.w) oligomer content in the matrix. The spectra show that over a broad range of concentrations there is an excess of the D signal at the lower energy range (600- 720 keV) which corresponds to an excess of oligo-dS at the substrate interface. The width of the D and H signals decreases with the migrant content, showing that the total thickness of the film produced decreases. Again, a layer fit has been performed with Datafurnace to obtain the oligomer concentration profiles (Figure 5-22, right). Complementary data for samples from 5 to 20 % (w.w), generated as part of a preliminary work by Mr. Chris James¹⁴⁷ and refitted as part of this work, was added in this figure to show the extended consistency of the results. It was chosen to plot the concentration profiles against a normalised thickness (by the total thickness of the film z_0) for better clarity, since the films spin coated by Mr. James were in general thicker.

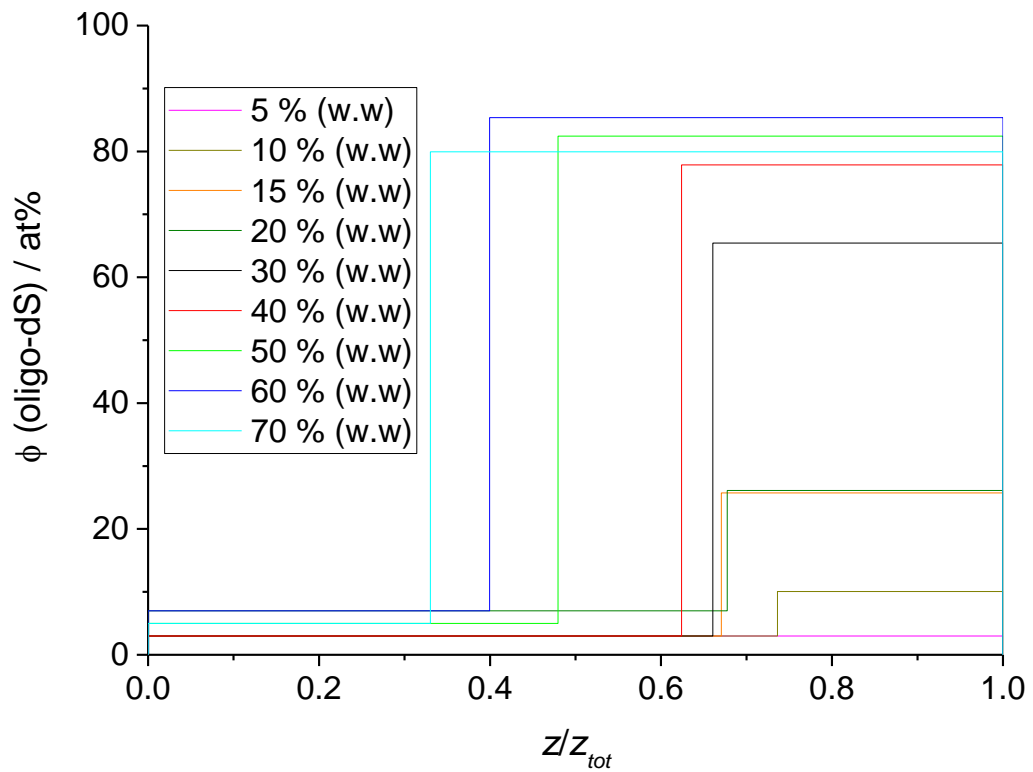
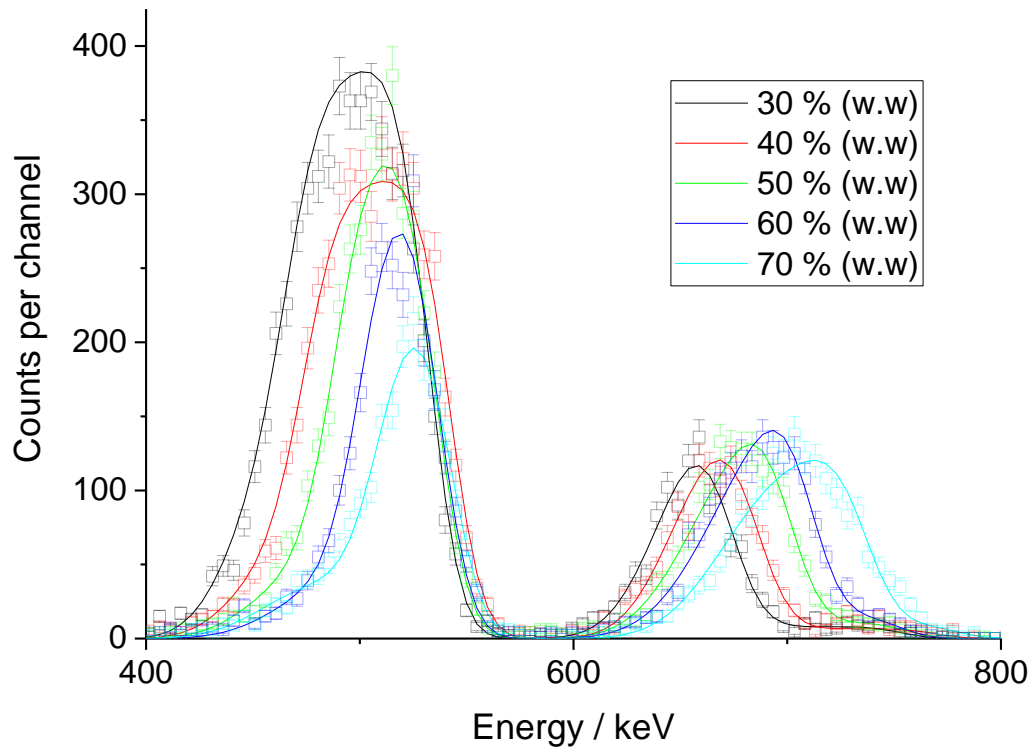


Figure 5-22: Top: Examples of raw ERDA data of oligo-dS in hPI. Bottom: Concentration profiles corresponding to the layer fit of the raw data, with a normalised thickness.

From the layer fit, the concentration of oligo-dS at the surface remains close to zero, and is nearly independent of the overall oligomer concentration, which suggests a high incompatibility between the pair, and agrees with the conclusions of the DSC study. The excess at the buried interface is very large and increases with the oligomer content. Again, values of the total oligomer concentration φ_{tot} and the interface excess z_i^* are gathered in Table 5-7. The values for φ_{tot} are within the experimental error due to the scattering cross-section (about 14 %).

Table 5-7: φ_{tot} and z_i^* calculated for each oligo-dS content from the concentration profiles in Figure 5-22.

Sample oligo-dS content / % (w.w)	φ_{tot} / at%	φ_{tot} / % (w.w)	z_i^* / nm
5	3	4.4	0
10	5	7.3	3.6
15	15	20.9	10.5
20	13	18.3	11.1
30	24	32.1	12.0
40	31	40.2	17.2
50	45	55.1	22.2
60	54	63.8	24.2
70	55	64.7	17.2

Similarly, knowing the M_n of oligo-dS, one can evaluate the maximum thickness of a single molecule thick layer at the surface: $7 \times 1.38 \times \sin(109.5/2) = 8 \text{ \AA}$ or 0.8 nm. A separate wetting layer is clearly obtained for all the oligomer considered in the study.

NR measurements on the same materials led to similar conclusions (Figure 5-23). The oligomer is segregated at the buried interface while the polymer segregates itself at the surface. The fit to the reflectivity data for the 50 % (w.w) sample is relatively poor, especially because the critical edge is not flat. This is suspected to be due to a loss of alignment of the sample. Hence it was decided to exclude this sample from the discussion. Interestingly the shape of the interface does not change much for the 2 other samples (roughness of $\sim 2\text{-}3$ nm), which is consistent with a low degree of miscibility because the interface between the two phases is very sharp (smaller than molecular dimensions). The depth at which the interface is found is then governed by the overall composition and total film thickness as expected from the FH theory (see 1.1.1.3). The profiles

obtained by NR also confirm that these films have very low surface roughness, ~ 1 nm, as evidenced by the sharply resolved interference fringes.

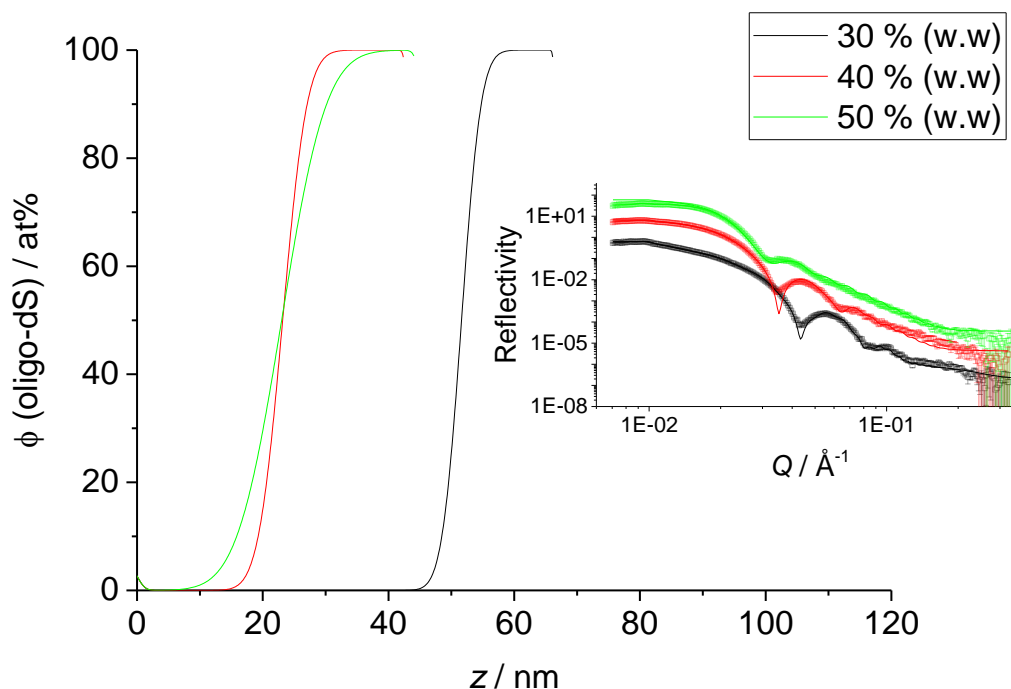


Figure 5-23: oligo-dS in thin hPI films at various concentrations of oligo-dS. Inset: NR data measured with INTER and fits. Main figure: Profiles corresponding to the fits in the inset.

5.1.3.3 Excess directed to both interfaces

The oligo-dIB 900 in PB system was earlier assessed by DSC as incompatible. Thin films of this oligomer/polymer combination are found to exhibit an excess of oligomer at both the exposed air surface and the buried interface with the silicon substrate by ERDA. This behaviour is obvious from the 'double peak' in the deuterium part of the ERDA spectra (600-800 keV in this case) shown in the inset of Figure 5-24 and is confirmed by the depth profiles obtained from fits to these data in the main figure. Again, the horizontal axis is here chosen to be displayed as normalised by the total thickness of each film to ease comparison of the depths profiles.

A three-layer fit was used for 30, 40 and 50 % (w.w) oligo-dIB 900. As the oligomer concentration is increased the excess peaks are less and less resolved because the film thickness decreases and the excess peaks broaden. It is suggested that the excesses at the surface and buried interface overlap in the middle of the film for the sample of 60 to 70 % (w.w), but the resolution of the ERDA experiment does not allow to resolve the two peaks of the D signal or that these samples

exhibit a simple surface excess. Thus, for the 60 and 70 % (w.w) oligomer samples a simple bilayer fit was used.

The excess of oligo-dIB 900 at both interfaces increases with the overall oligomer content while, again, the total thickness of the films decreases. The surface excess is higher than the excess at the interface with the substrate, which seems to plateau at around 35 at% oligomer. The bulk concentration of the films (middle layer) seems to be very low for the 30 and 40 % (w.w) concentrations. The shape of these profiles is reminiscent of the results from Krausch *et al.* for hPEP/dPEP films coated on treated Silica, presented in Figure 1-3.⁵⁷ However, it is surprising to obtain such a result here since the substrate was not treated before spin coating the PB film. It is not obvious why oligo-dIB 900 should be attracted to the silica interface.

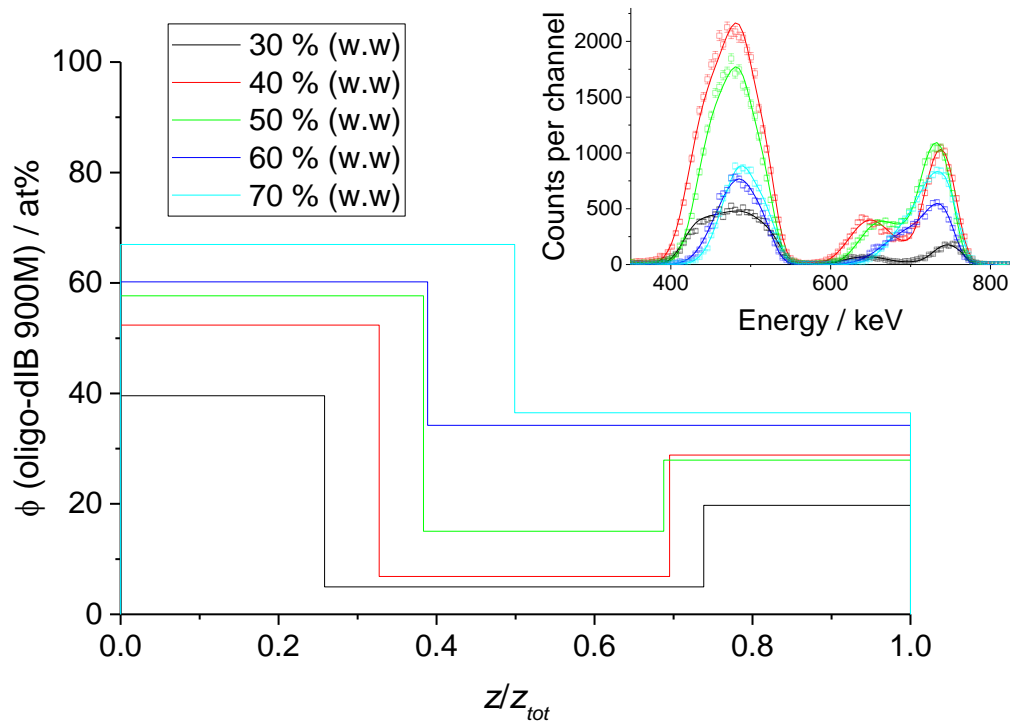


Figure 5-24: Raw ERDA data (inset) of oligo-dIB 900 in PB. The concentration profiles corresponding to the layer fit of the raw data are presented in the main figure.

Because of the rather atypical shape of the profiles, the surface excess z^* was not calculated, but the excess relative to the medium layer for the samples containing 30, 40 and 50 % (w.w) oligomer seems large enough to suggest a wetting layer. Again, it seems that the overall oligomer content is underestimated in those profiles, probably coming from the oligomer synthesis initiator (consistently with what was observed in 5.1.3.1).

Nuclear reaction analysis (NRA) was carried out on spin coated films to validate the ERDA experiments. In NRA, inverse kinematics is observed,¹⁶³ meaning that the high energy channels correspond to deeper elements in the sample. More details on this technique were given in 2.7.1.2. The raw NRA data (Figure 5-25, inset) also showed two peaks at 30 and 40 % (w.w) oligomer suggesting similar results as with ERDA. Concentration profiles (Figure 5-25, main figure) were obtained by simultaneous fitting of NRA data at several measurement angles. More layers were used for these fits, since NRA has a better resolution than ERDA. Again, the total oligomer content is underestimated, which supports the hypothesis that the oligo-dIB 900 is not fully deuterated. However, quantifying deuterium with NRA is more difficult than with ERDA because, using this technique, hydrogen atoms are not detected and the quantification relies only on the accuracy of the beam charge hitting the sample.

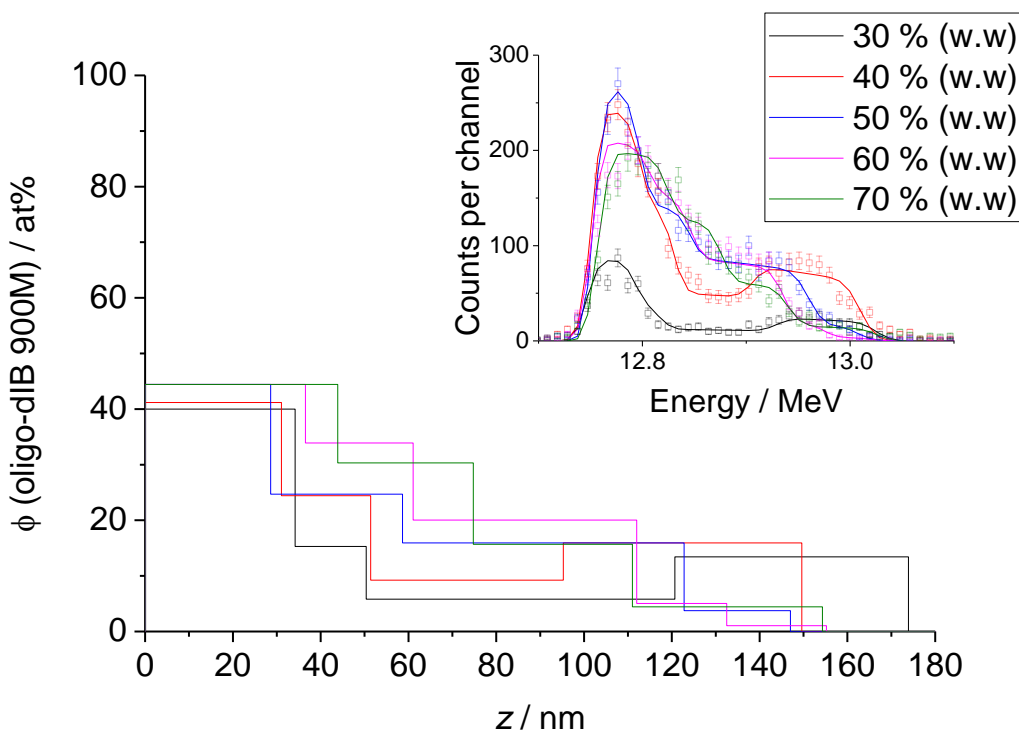


Figure 5-25: Concentration profiles obtained by NRA of 30 to 70 % (w.w) spin coated films of oligo-dIB 900 in PB.

NRA data agrees qualitatively with the ERDA measurements: a partitioning of the oligomer at both interfaces is observed for 30 and 40 % (w.w) oligo-dIB in PB, whereas, at higher concentration, a simple surface excess is recorded. However, even with NRA's higher resolution (5-10 nm vs 15 for ERDA), it was not possible to resolve two peaks in the thinner films with oligomer contents higher than 50 % (w.w). The layer fit performed with DataFurnace led to

solutions that presented no buried interface excess for the high concentrations. One can also notice that the surface is not 100 at% saturated with oligomer, even though this system is rather incompatible.

From the NRA data, analytical fitting was performed on 50, 60 and 70 % (w.w) oligomer samples, using the fitting equation based on the error function $erf(x)$, as expressed in 2.7.2. The results of the analytical fit are compared to those of the layer fit in Figure 5-26 (dashed and solid lines respectively) for samples of 30, 50 and 70 % (w.w). It seems that this equation, corresponding to the description of a simple surface excess, describes well the 70 % (w.w) sample. However, for the 30 and 50 % (w.w) oligomer content, some data points are present in excess at high energies (from 12.9 to 13.0 MeV) which suggests that an excess of oligomer is present at the buried interface with the substrate. This was also observed for the 60 % (w.w) sample (not presented here but available in electronic archive). Therefore, it appears that the double excess is present in the 30, 40, 50 and 60 % (w.w) samples and a single excess is measured in the 70 % (w.w) sample.

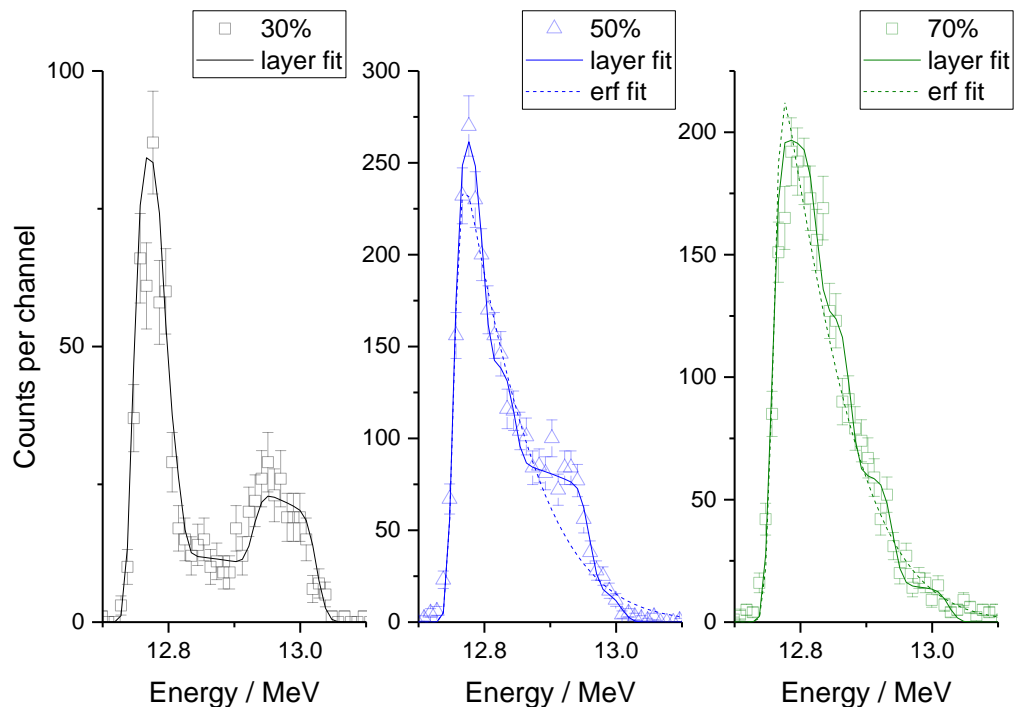


Figure 5-26: NRA data (diamonds), layer fit (solid lines) and functional fit (dashed line) of 30 (left), 50 (middle) and 70 (right) % (w.w) samples of oligo-dIB 900 in PB.

Angle: 80°, charge: 0.7 μC for 30 % (w.w), 3.5 μC for 50 % (w.w) and 2.8 μC for 70 % (w.w).

Because of the atypical concentration profiles observed for the oligo-dIB 900 in PB system and the fact that the surface was not saturated in oligomer, the occurrence of a lateral phase separation phenomenon is again suspected. The measurement of these samples was not performed by specular NR, since the method is not suited to describe such systems (see 5.1.3.1), but it was decided to focus the investigation on the higher molecular weight oligomer, oligo-dIB 2200, because, as shown by DSC in 4.1.2.2, the compatibility between the pair was reduced due to the higher molecular weight of the oligomer.

Again, due to the increased incompatibility, the profiles recorded by NR exhibit a large wetting layer (Figure 5-27). Two alternative fittings were tested, but the three-layer fit for the 30 and 50 % (w.w) were selected as the best option, since with only two layers the overall oligomer content φ_{tot} was incorrectly described (see Table 5-8). Hence, similarly shaped vertical composition profiles were obtained than for the lower molecular weight oligomer (Figure 5-24, Figure 5-25 and Figure 5-26).

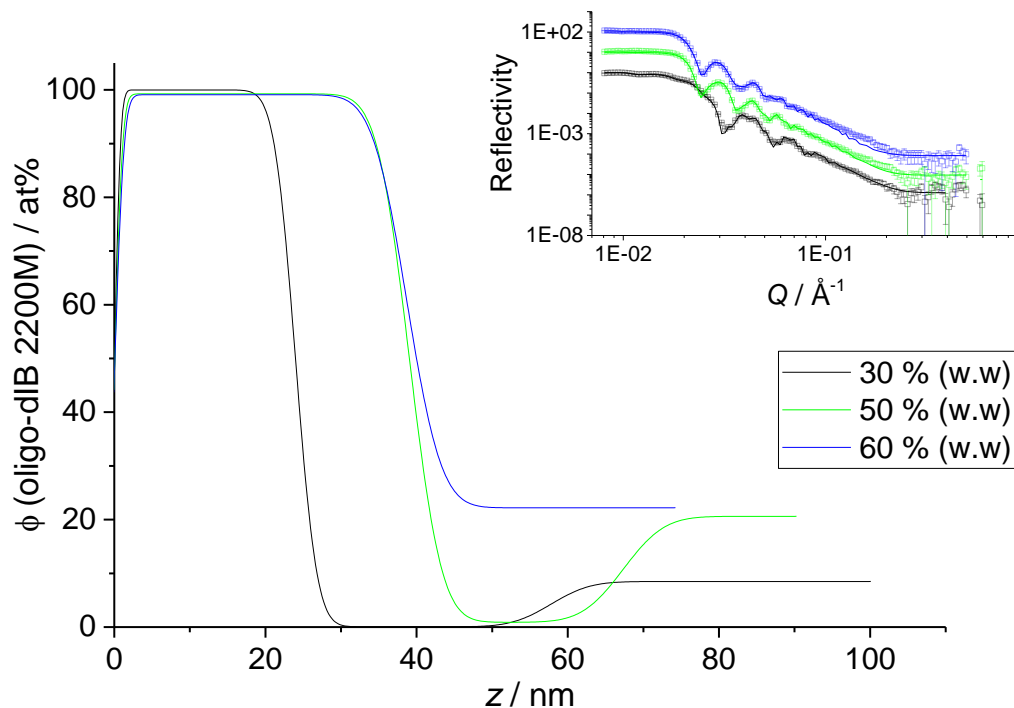


Figure 5-27: oligo-dIB 2200 in thin PB films at various concentrations of oligo-dIB. Inset: NR data measured with SURF and fits. Main figure: Profiles corresponding to the fits in the inset.

Table 5-8: φ_{tot} calculated for each oligo-dIB 2200 content from the concentration profiles in Figure 5-27.

Sample oligo-dIB 2200 content / % (w.w)	φ_{tot} / at% 2-layer fit	φ_{tot} / % (w.w) 2-layer fit	φ_{tot} / at% 3-layer fit	φ_{tot} / % (w.w) 3-layer fit
30	24	25.5	27	28.6
50	70	71.6	48	50.0
60	62	63.8	/	

The results hence suggest that the system exhibits excesses at both surface and interface with the substrate. The surface excess is a pure layer of oligomer of thickness reaching up to 40 nm for the 50 and 60 % (w.w) oligomer samples, which is similar but slightly thicker than the thickness of the wetting layer of oligo-dIB 2200 in PI (about 30-35 nm at these concentrations). It seems that this wetting layer at the surface is uniform, contrary to the impure surface layer formed for oligo-dIB 900. Again, it is important to note that the s.l.d. of the oligomer is not precisely known which implies that the wetting layer might not be completely pure. As in PI, the thickness of the phase-separated wetting layer on PB increases with the overall migrant content, while the roughness of the interface between the two phases is maintained nearly constant (2-3 nm).

The concentration of the surface excess layer is higher than the concentration of the interface excess at the substrate, which reached around 25 at% for the higher oligomer content studied. The middle layer (or bulk layer), is fitted as a pure layer of polymer which suggests a strong incompatibility between the polymer and oligomer. Considering this observation, it seems very unlikely that the layer at the interface with the substrate is a single phase layer, because it would suggest that 3 different compositions of oligomer in polymer would coexist. The Gibbs phase rule implies that this could not persist if pressure and temperature can vary.¹⁶⁴ One can propose that again some lateral phase separation takes place in this buried layer, and/or that the sample is in a metastable state: the oligomer might have been trapped at the interface during sample preparation (spin coating) and cannot diffuse back to the surface over the timescale of the measurement because of a strong incompatibility with the matrix.

5.2 DISCUSSION OF SURFACE PARTITIONING

5.2.1 IMPACT OF SURFACE ENERGY ON SURFACE PARTITIONING

The pendant and sessile drop measurements presented in 5.1.1.1 suggest that the total surface energies of PB, PBcis and squalane are similar, within the range of experimental error (~ 28 - 29 $\text{mN}\cdot\text{m}^{-1}$). This result would imply that for a mixture of squalane with PB or PBcis there is little energetic minimisation of segregating the oligomer or the polymer at the surface – i.e. squalane and PB/PBcis could be indifferently enriched at the surface. Consequently, for such mixtures, the difference in molecular weights would be the main parameter responsible for surface segregation. Alternatively, when considering literature values, the surface energy of squalane (27.8 - 29.4 $\text{mN}\cdot\text{m}^{-1}$ at 20 - 25 °C, with a null or very small polar contribution < 1 $\text{mN}\cdot\text{m}^{-1}$)¹⁵⁷⁻¹⁵⁹ is lower than the surface energy of the two PBs (43.1 - 48.6 $\text{mN}\cdot\text{m}^{-1}$)¹⁷ which would imply an energetic preference for surface enrichment of squalane. Both of these conclusions are in agreement with the depth concentration profiles determined experimentally (Figure 5-10 and Figure 5-11).

Although the total surface energies of PB and PBcis are similar, PBcis exhibits a more polar behaviour than PB, since the derived polar component of its surface energy is bigger (Table 5-1). One can also note that the literature values for polar and dispersive contributions of sq¹⁵⁷⁻¹⁵⁹ match more closely those of PB than those of PBcis. Hence, it is expected that the interfacial tension between sq and PB is lower than between sq and PBcis. This result echoes the bulk polarisability considerations discussed in 4.2.2.4.3, suggesting a higher compatibility of sq with PB than with PBcis.

To complete the discussion and provide a qualitative guide to the order of increasing surface tension, one can briefly consider group contributions. For hydrocarbon polymers, surface energy contributions increase from CH_3 (30 $\text{mN}\cdot\text{m}^{-1}$) to CH_2 (36 $\text{mN}\cdot\text{m}^{-1}$), with higher values up to 45 $\text{mN}\cdot\text{m}^{-1}$ for unsaturated species such as aromatic rings.¹⁷ On this basis, the surface energy of the polymer matrix is expected to increase from hPI to PI to PB and PBcis (PB presenting more 1,2 additions than PBcis). Similarly, the corresponding values for the oligomers would be expected to increase from oligo-dIB to dsq to oligo-dS, but may be significantly shifted due the influence of density, which is sensitive to molecular weight in this range. The observation that dsq is much

more surface active in PB than in PI (Figure 5-4) suggests that the PB matrix has a greater surface energy than PI. This result is consistent with some literature values for the surface energy of PI and PB (31-34 and, again, 43.1-48.6 mN.m⁻¹ respectively).¹⁷

In contrast, for oligo-dS/hPI mixtures, the oligomer is positioned at the interface with the substrate and an enriched hPI layer is exposed at the surface. From the above discussion, one can conclude that such a substrate segregation occurs because oligo-dS presents aromatic groups and is therefore a component with higher surface energy.

The presence of oligo-dIB at the surface of PB and PI films is consistent with the surface energy arguments since this saturated low molecular weight oligomer has a significantly lower surface energy than the polymer matrices. However, it is not expected to see an accumulation of oligo-dIB at the interface with the substrate when blended with PB; on the contrary, it is the polarisable, high surface energy components that usually show the tendency to segregate to buried interfaces of films.¹⁵⁵ Given the higher surface energy of PB than PI, it is not obvious why PB would have more unfavourable interactions with the substrate. The composition profiles seen are in fact more consistent with the oscillating profiles seen for surface-directed spinodal decomposition (Figure 5-28),^{57,68} and may in this case simply arise in PB but not PI because of the timescale of equilibration during spin coating (solvent evaporation within a few seconds) and the very low compatibility of oligo-dIB with PB.^{57, 165} Although beyond the scope of this present work, one can note that the timescale of development of such spinodal interference waves could provide valuable insights into the stability and rate of toughening of adhesive formulations.

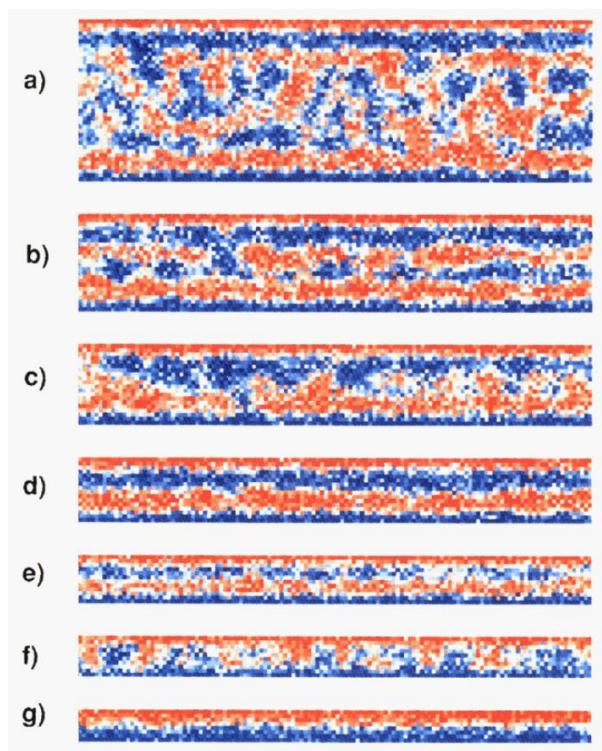


Figure 5-28: Difference between the local concentrations of two components of a binary polymer mixture of surface potentials σ_1 and σ_2 for several film thicknesses: (a) 960 nm, (b) 576 nm, (c) 480 nm, (d) 384 nm, (e) 288 nm, (f) 240 nm and (g) 192 nm. Simulations based on an extended conserved time-dependent Ginzburg-Landau model. Reprinted with permission from Krausch et al., *Macromolecules*, 26 (21), 5566–5571. Copyright 1993 American Chemical Society.

From the vertical concentration profiles obtained for various incompatible systems, it appears that surface energy may direct the wetting layer formation – i.e. which phase is preferentially positioned at the surface. However, surface energy difference alone should not lead to a complete wetting layer of oligomer.⁶³

5.2.2 IMPACT OF FILM THICKNESS ON SURFACE PARTITIONING

5.2.2.1 Impact of film thickness on the wetting layer thickness

The vertical concentration profiles presented in Figure 5-12 and Figure 5-13 show that for 40 and 50 % (w.w) blends of dsq with PBcis, surface excesses of dsq are formed with defined thicknesses that are independent from the total film thickness (respectively 3.3 ± 0.1 and 10.1 ± 0.5 nm). In order to rationalise this result, it is helpful to consider the relationship between the film composition and the phase boundary measured in 4.1.2.1. From the phase diagram of the mixture, it was estimated that the phase separation at 20 °C – i.e. temperature of the NR experiment – occurs at a concentration of dsq above 50 vol%, yielding two phases: one phase of

almost pure dsq and one polymer-rich phase, containing about 50 vol% dsq (these compositions correspond to the measured concentration of the surface and bulk layers of the two thickest 50 % (w.w) films). Hence, it appears that the thickness of the excess is independent from the total film thickness in the one-phase regime but also in the two-phase regime. Another proof of this behaviour in the two-phase regime was observed for the case of the 50 % (w.w) mixtures of dsq with the fractionated PBcis (Figure 5-16), with a characteristic wetting layer thickness of 46 ± 3 nm.

The independence of the total film thickness on the surface excess was expected in the one-phase regime but is surprising in the case of a phase-separated system. In such situations, one might presume that the thickness of the wetting layer would vary proportionally with the thickness of the film, the concentrations of the surface and bulk layer being dictated by the binodal composition of the phase diagram. It is also suggested by the Cahn argument,⁶⁶ that the wetting layer should be of infinite thickness for an infinite system in the case of total wetting – i.e. binary mixture close to its critical point and exposed to a surface. This is however not observed experimentally (see Figure 5-12 and Figure 5-13) and the NR data and fits seem too consistent to indicate experimental or fitting errors. Other experimental studies also show wetting layers that are not infinitely thick.⁶⁵ In these cases the phenomenon is due to density differences between the wetting layer and the bulk phase, the wetting layer exhibiting a higher density. Hence, this is the gravitational energy cost of forming the wetting layer that limits its height to a few hundred of Ångstroms. However, this argument does not apply to the model systems considered in this thesis since the wetting layers of oligomers-rich phase formed on the surface have lower densities than the underlying polymer-rich phase. It is therefore suggested that the thickness of the wetting layer might be dictated by a surface effect that has a characteristic length of tens of nanometres.

The fact that the wetting layer thickness is not dependent on the total film thickness would imply that, in the thickest PBcis samples, some phase-separated regions should be found in the bulk (probably in the form of domains of squalane-rich phase that are not detectable by NR since they are not parallel to the surface and therefore do not reflect the neutron beam). This result would agree with the results from Krausch *et al.*, who investigated the spinodal decomposition of thin polymer films, as a function of film thickness.⁵⁷ In Figure 5-28, one can clearly distinguish a surface effect, with a surface layer of constant characteristic length (~ 20 nm) – which is of the

same order magnitude as the radius of gyration of the PEP chains considered (~ 16 nm from equation (5.1)) – and a bulk effect that they attributed to the interferences between spinodal waves, with, for example in cases (c) and (e) of Figure 5-28 the formation of a large number of droplets. From the simulations,¹²⁴ the thickness of the wetting layer is constant for films that are thicker than $10 \times$ the radius of gyration of the polymer. However, such a phase separation in the bulk contradicts the surface energy minimisation argument – which would ultimately lead to a reduction of the interfacial area between the two phases – and might not be representative of an equilibrium state. One could suggest that for these samples, the spinodal waves initially defined a characteristic wetting layer thickness but became kinetically trapped upon solvent evaporation during the spin coating. Yet, considering the liquid nature of the oligomer (dsq), the amorphous rubbery state of the polymer at 25 °C and the partial solubility of dsq in PBcis, if phase-separated domains are formed in the bulk they should not be kinetically stable and should disappear by Ostwald ripening or coalescence.¹⁶⁶ The reversibility of the surface excess z^* with temperature, shown in 5.1.1.3, also proves the mobility of the molecules in the blend. Coarsening phenomena are not observed over the experiment time scale (3-4 hours), since the reflectivity fringes remain well defined. Hence, if such phase-separated domains exist in the bulk, they are stable over the measurement time. Two explanations can be put forward: the surface energy difference between the two phases is small enough for the domains to be stable in the bulk or the diffusion happens over longer time scales than the measurement time.

Alternatively, it is suggested that although the dsq/PBcis system was measured relatively close to its cloud point, a total wetting is not achieved. Considering the quality of the NR data and the almost pure phase of dsq detected at the surface of the films (Figure 5-12 and Figure 5-13), a partial wetting – consisting of droplets of dsq rich-phase at the surface on top of some exposed areas of PBcis rich-phase – is excluded, because it would lead to a more difficult data analysis (similarly to the case of oligo-dIB 900 in PI (Figure 5-19)). Nonetheless, a possible surface behaviour would consist of a “frustrated total wetting” as described by Bertrand *et al.* in the case of wetting layers of alkanes on flat water surfaces.¹⁶⁷ It consists of an oil film that covers the water layer but also coexists with lenses (droplets) at the surface. In their study the thickness of this “frustrated” wetting layer was of tens of nanometres, which distinguished it from the two other wetting states (partial wetting presenting a thickness of a couple of nms while the thickness becomes infinite for total wetting). Although observed for systems that are quite different from the oligomer/polymer mixtures of interest, such features at the surface would

still enable good NR data acquisition, a high concentration of dsq on the surface and agree with the energy minimisation of the system by the creation of a unique interface. This unusual wetting behaviour would be due to a subtle competition between short-range repulsive and long-range attractive (van der Waals) intermolecular forces.¹⁶⁷

5.2.2.2 Impact of film thickness on interfacial roughness

For thin films, the value of the interfacial roughness between two immiscible polymers is expected to increase with the total film thickness. Sferrazza *et al.* reported that the interfacial width between two incompatible polymers would exhibit a logarithmic dependence with the film thickness, which can persist up to excess layer thicknesses of 100 nm.¹⁶⁸ Alternatively, for a confined interface, Kerle *et al.* proposed that it is proportional to the square root of the total film thickness.¹⁶⁹ The span of roughness measured experimentally for the 50 % (w.w) dsq/PBcis is effectively increasing with the total film thickness (between 45 and ~ 500 nm), from 2.8 to 3.7 nm, and is of the same order of magnitude as literature data.¹⁶⁸ Hence, the behaviour is consistent with what was observed for 2-phase bilayer films.

5.2.2.3 Extremely thin films and bulk depletion

One can suggest that for very thin films (thinner than 10x the size of the excess layer), the thickness of the excess and the width of the interface between surface and bulk compositions might be affected by the total thickness of the film. A low total film thickness may also affect the oligomer bulk concentration due to a low amount of oligomer available in the sample, as observed in the thinnest 50 % (w.w) film (45 nm) where the bulk concentration is depleted from 49 to ~ 39 %. This aspect must be considered when discussing the true thermodynamic equilibrium state of the samples.

5.2.3 IMPACT OF POLYMER MOLECULAR WEIGHT ON SURFACE PARTITIONING

It has been shown in 4.2.2.1 that, considering the large difference in molecular weights between the oligomer and the polymer, the influence of the polymer molecular weight and polydispersity on the compatibility behaviour predicted from FH theory is very limited. However, in 5.2.2.1, it was highlighted that the thickness of the wetting layer for a phase separating system had a characteristic length of the order of tens of nms that is independent from the total film thickness. In 5.1.2.3, it was shown that by increasing the polymer molecular weight (and decreasing its polydispersity) while maintaining all other parameters constant, the thickness of the surface

excess is increased from 10 to 46 nm. Indeed, the fractionation of the PBcis should have almost no effect on polarisability and Hamaker constants. In these conditions, the surface excess also becomes more diffuse (increased width of the interface with the bulk layer from 3.7 nm to ~ 8 nm). Since no squalane molecule could be longer than 2.6 nm (even if one considers a fully stretched succession of 23 C-C bonds), these characteristic lengths cannot depend on the size of the oligomer. This phenomenon seems to be confirmed when comparing the thickness of the wetting layers for oligo-dIB 2200 in PI, PB and PBcis (Figure 5-20, Figure 5-27 and Figure 5-21). This comparison must be done cautiously since the polymers have different structures. However, the length scales involved seem to be of the same order of magnitude as the radius of gyration of the polymers in every case: for example at 30 % (w.w), the wetting layer is 13.0 nm in PI ($M_w = 160 \text{ kg.mol}^{-1}$, PDI = 1.1), 23.9 nm in PB ($M_w = 280 \text{ kg.mol}^{-1}$, PDI = 2.1) and 27.3 nm in PBcis ($M_w = 567 \text{ kg.mol}^{-1}$, PDI = 4.4).

The radius of gyration can be approximated for a Gaussian chain (without taking into account polydispersity) using:^{18, 170, 171}

$$R_g = a \times \sqrt{\frac{N}{6}} \quad (5.1)$$

with a the Kuhn length and N the number of repetitive units of the polymer. The calculated values for the polymers of the study are given in Table 5-9. One must note that the value of N used for the calculation was obtained from M_w and that the values of R_g are also depending on polydispersity.

Table 5-9: R_g values calculated from equation (5.1) and R_h values measured by GPC in THF.

	N	a / nm	Calculated R_g / nm
PI	2353	0.88 ¹⁷²	17.4
PB	5185	0.96 ¹⁷²	28.2
PBcis	10500	0.76 ¹⁷²	31.8
PBcis high M_w	15630	0.76 ¹⁷²	38.8

R_g values for polymers can vary depending on molecular weight and solvent compatibility (for example, between 15 and 150 nm for PBcis).¹⁷³ Following the discussion in 5.2.2.1, the long-range van der Waals forces might be involved in the definition of the wetting layer thickness.

Although no other example was found in literature, it is suggested that the measured wetting layers contain some polymer chains that dictate the thickness and roughness of the surface phase-separated layer. In the case of a polydisperse polymer, it is supposed that the smaller chains would dictate the size of the wetting layer since they should be more soluble in the squalane-rich phase.

5.2.4 IMPACT OF BULK COMPATIBILITY ON SURFACE PARTITIONING

The surface behaviour observed in the oligomer/polymer mixtures is found to be greatly correlated to their bulk compatibility behaviour. The systems studied in the one-phase regime of their phase diagram present either no detectable excess or a simple surface enrichment – i.e. less than a molecule thick layer at the surface. In contrast, incompatible systems exhibit vertical phase separation that can also be combined with lateral features. In a first instance, it is anticipated that the samples are close to kinetic equilibrium, since under ambient conditions, all of the components are well above their T_g s.

5.2.4.1 Surface enrichment in the one-phase regime

Our results show several examples of strong oligomer surface segregation – e.g. dsq in PBcis or PB – but also examples where no oligomer can be detected on the surface – e.g. dsq in PI or oligo-dS in PB. Hence, the disparity in molecular weight, that is a significant factor in oligomer surface segregation, cannot be the dominant factor in all cases. Examples of oligomer surface segregation in polymer films in literature are sparse. Hariharan *et al.*'s classic work^{53, 58} about asymmetric polymer blends showed that (i) disparity in molecular weight could overcome the tendency for deuterated species to segregate to the surface of isotopic blends and (ii) the enrichment of the lower molecular weight component at the surface was only weakly dependent upon the molecular weight of the larger polymer.

The absence of any discernible surface excess for dsq in PI when measured by ERDA is perhaps surprising given the much greater discrepancy in molecular weight for this system (degree of polymerisation ratio of ~ 370) than for the isotopic blends previously reported by Hariharan (ratio < 50).⁵³ Very slightly enriched surface layers were measured by NR (Figure 5-8), from which surface excesses are estimated to be ~ 0.8 and 0.2 nm for the 30 and 40 % (w.w) samples respectively (therefore too small to be detectable by ERDA). These values are of the same order of magnitude as what was calculated in the case of weakly segregating mixtures: for the most

extreme disparity of molecular weight in Hariharan *et al.*'s study (degree of polymerisation ratio of ~ 50) the surface excess z^* is of the order of 0.6-1.1 nm.⁵³ Moreover, the thicknesses of the adsorbed layers for the dsq/PI samples are of the order of 1-5 nm which, while close to the resolution of the NR measurement, is also consistent with the correlation lengths for Hariharan *et al.*'s systems (1.8-5.6 nm).⁵³ Hence, the energy saving coming from adsorbing dsq molecules at the surface of PI is slightly more favourable than the energy reduction which would be obtained by favourable bulk interactions. In other words, the adsorption energy parameter χ_{surf} (defined in equation (1.19')), comprising the difference in adsorption energy of dsq and PI at the surface and the difference in surface tension caused by density gradients,⁵³ is lower than χ .

The dsq/PI model system exhibits an interesting behaviour: the measured surface enrichment decreases with increasing concentration (Figure 5-8). This result, put in parallel with the DSC experiment, proves very good bulk compatibility between the polymer and the oligomer. One can assume that χ_{surf} and χ are very similar for this system and that the surface behaviour depends mainly on oligomer content. However, (i) following FH arguments for UCTS systems, as the oligomer content is increased one should observe less bulk compatibility and (ii) as dsq is expected to have a slightly lower surface energy than PI (27.8-29.4 versus 31-34 mN.m⁻¹ vs respectively), one would expect that the more dsq molecules position themselves at the surface, the more the surface energy will be lowered. Therefore, an increase of oligomer content should yield more dsq surface segregation. Hence, it is still unclear why the experimental data shows the opposite trend. A first hypothesis is that the roughness of the samples increased or that dewetting of the film occurred, which could mask the presence of surface excess. Alternatively, considering the very good compatibility and rather similar surface energies between the components, it is suggested that, for this mixture of high molecular weight disparity, a complex balance exist between the enthalpic and entropic contributions to the surface segregation that might not be reflected by the Flory-Huggins theory, the self-consistent field theory or even the locally correlated lattice theory. The extent of surface segregation depends on the difference in surface energy between the enriched surface composition and what the surface energy could be if the bulk composition was found at the surface. As the concentration of the oligomer in the bulk increases, there is less scope to reduce the surface energy by adsorption and ultimately z^* tends to 0.

Similarly, the concentration profiles showed a homogeneous distribution of oligo-dS in PB when blended at 15 % (w.w). The favourable interactions between oligo-dS and PB, suggested by thermal analysis of the system, could be favourable enough to suppress the adsorption of oligo-dS to the surface and therefore, also in this case, χ_{surf} and χ should be of similar values. On the other hand, the concentration of oligo-dS might not have been sufficient in this sample to create any detectable excess (more than 0.5 nm thick). Indeed, this result is surprising as one would expect the presence of a small excess even for weakly segregating mixtures (comparable to the behaviour for sq/PI) due to the difference in molecular weight between the oligomer and the polymer.

For d-squalane in PB and PBcis, in the miscible part of their phase diagram, a surface excess is recorded: in these slightly more polarisable matrices, the interactions between the migrant and matrix are not favourable enough to prevent surface partitioning – i.e. χ_{surf} is lower than χ in the bulk and the energy of the system is reduced by placing the oligomer at the surface. The surface excess z^* increases with the total oligomer content, which is expected from (i) and (ii) in the discussion above. When in the one-phase regime, the calculated z^* values for this system (Table 5-3) are in the same range as the values obtained by Hariharan *et al.* for weakly segregating mixtures.⁵³ However, the surface excesses are clearly higher than the literature values when going through the phase transition.

5.2.4.2 Phase transition and wetting layer

It is possible to directly juxtapose the surface behaviour of the dsq/PB mixture with its bulk compatibility by comparing the concentration profiles issued from NR measurements and the phase diagram at RT ($\sim 20^\circ\text{C}$). Each concentration profile can be defined, as summarised in Figure 5-29, by:

- the thickness of its excess layer (blue)
- the gradient between the surface and the bulk concentration – i.e. the width of the interface, called in the NR data fitting programme “roughness” (green)
- the concentration of oligomer at the surface φ_1 (black)
- the bulk concentration φ_∞ (red)

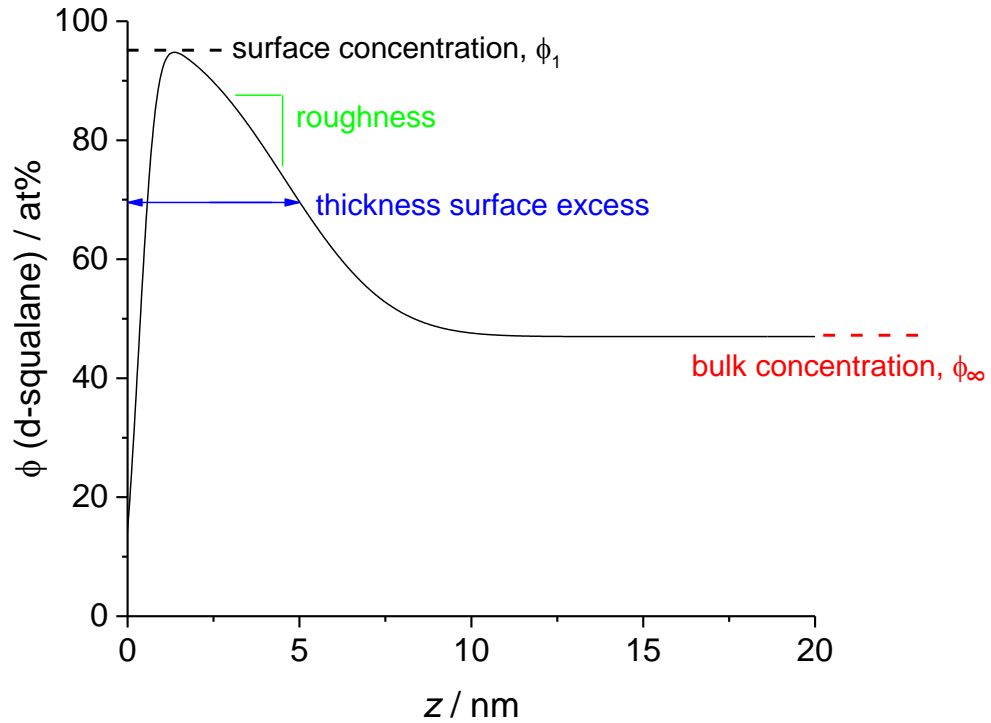


Figure 5-29: Definition of the characteristics of a concentration profile.

Figure 5-30 presents the evolution of these characteristics with the overall dsq content in the sample, as obtained from the concentration profiles in Figure 5-10. On the left axis are presented the surface and bulk concentration in at% (in black and red respectively) and on the right axis the roughness and thickness of the excess layer in Å (in green and blue respectively). The error bars were obtained using the Genetic fit of the Motofit reflectivity package for the software IGOR with Monte Carlo (MC) analysis.

One can note that the error bars on the surface concentration (black) are maximum for the 30 and 40 % (w.w) dsq samples (here converted in 0.32 and 0.43 volume fractions for comparison with the phase diagram in Figure 4-5), simply because the s.l.d. of the film's bulk concentration is getting closer to the s.l.d. of the Si substrate and, as a consequence, the fringes of the reflectometry data are indistinct, making the surface concentration more difficult to determine. The error bars on the bulk concentration shown in the figure were the output of the MC analysis but their reliability might be contested in some cases (see discussion in *Annex 1*).

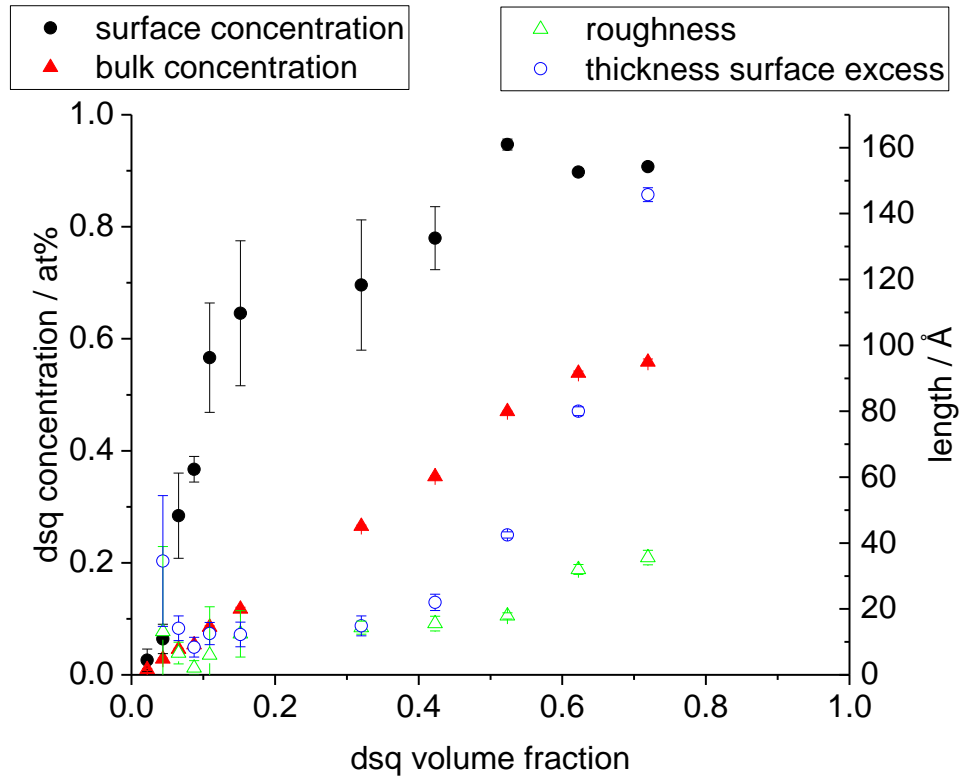


Figure 5-30: Evolution of the concentration profiles characteristics in PB with the dsq volume fraction.

A certain number of conclusions can be drawn from Figure 5-30. Firstly, considering a measurement temperature of 20 °C, one can observe on the sq/PB phase diagram presented in 4.1.2.1, that the phase separation of the mixture happens around 60 vol%. The phases present in the two-phase regime at this temperature are a polymer-rich phase (~ 60 vol% dsq) and a quasi-pure oligomer phase. This is indeed what is observed from the concentration profiles: for concentrations above 60 vol%, the bulk concentration (red) deviates from linearity and plateaus around 55 at% of dsq while the surface concentration (black) is reaching 90 at%. Therefore, the results obtained by NR are in agreement with the phase diagram.

Secondly, the roughness of the surface layer (green) varies from 0.5 to 3.7 nm and is not greatly affected by the dsq content (note that a sensible minimum value for any interface roughness would be 0.5 nm, which would be expected for the root mean square roughness arising from thermal fluctuation and surface tension).¹⁵⁵ Roughness considerations are important in the frame of this project as interface widths can be critical in terms of adhesive mechanical properties. According to the self-consistent field calculation of Helfand *et al.* in the early 70s, the interfacial width w for completely immiscible polymers can be calculated as:¹⁷⁴

$$w = \frac{2a}{\sqrt{6\chi}} \quad (5.2)$$

where a is the Kuhn length and χ is the Flory-Huggins interaction parameter. The interfacial width corresponds in this case to the roughness of the interface between the enriched layer and the bulk. Considering $a = 9.6 \text{ \AA}$ for PB and $a \sim 11 \text{ \AA}$ for squalane (from Kuhn lengths of polymers of similar structures),¹⁷² one can calculate $a_{av} = 10.3 \text{ \AA}$ which corresponds to the average between the Kuhn lengths of squalane and PB molecules. Using $\chi = 0.11$ at $20 \text{ }^\circ\text{C}$, as defined earlier from the Flory-Huggins fit to the phase diagram in 4.2.2.5, one obtains from equation (5.2) an interfacial width $w = 2.5 \text{ nm}$. This value is consistent with, but slightly lower than the roughness measured for the immiscible dsq/PB mixtures: the 60 and 70 % (w.w) samples have a roughness of 3.2 and 3.7 nm respectively. It was however previously established that the experimental interfacial width is generally substantially broader than the mean-field predictions and that the cause of the broadening are thermally excited capillary waves (fluctuations at the interface that are neglected by the theory).¹⁶⁸ Sferrazza *et al.* also reported that the interfacial width is increased for interfaces between immiscible low molecular weight polymers.¹⁷⁵ This result was predicted for polydisperse immiscible polymer interfaces and explained by a higher loss of translational entropy due to confinement for the smaller chains.¹⁷⁶ Hence, for polydisperse systems such as these, the interface is expected to be enriched in small chains.

Lastly, the surface concentration (black) presents an interesting behaviour: it increases very rapidly at low concentration – e.g. for 15 vol% dsq in the sample, the surface is already covered at 70 at% with oligomers – and then more slowly to reach 100 at% surface saturation for 60 vol% dsq in the PB film. The thickness of the surface excess (blue) behaves as a mirror image of the surface concentration: up to a dsq content of 40 vol% it increases slowly, but once the surface is saturated with the oligomer, the wetting layer is formed and the thickness of the surface excess increases more dramatically. Therefore, once the wetting layer is formed, its thickness seems to depend only on the total dsq content in the sample, and not anymore on χ_{surf} and χ .

Plotting the evolution of the thickness of the excess layer with the interfacial width w (or roughness) of the interface is an interesting way to visualise the formation of the wetting layer. In the one-phase regime, the thickness of the surface excess evolves linearly with the roughness of the interface, but as soon as phase separation occurs, the thickness of the excess dramatically

increases while the gradient at the interface is kept almost constant, which leads to a sharp slope increase in Figure 5-31 for dsq contents more than 50 vol%.

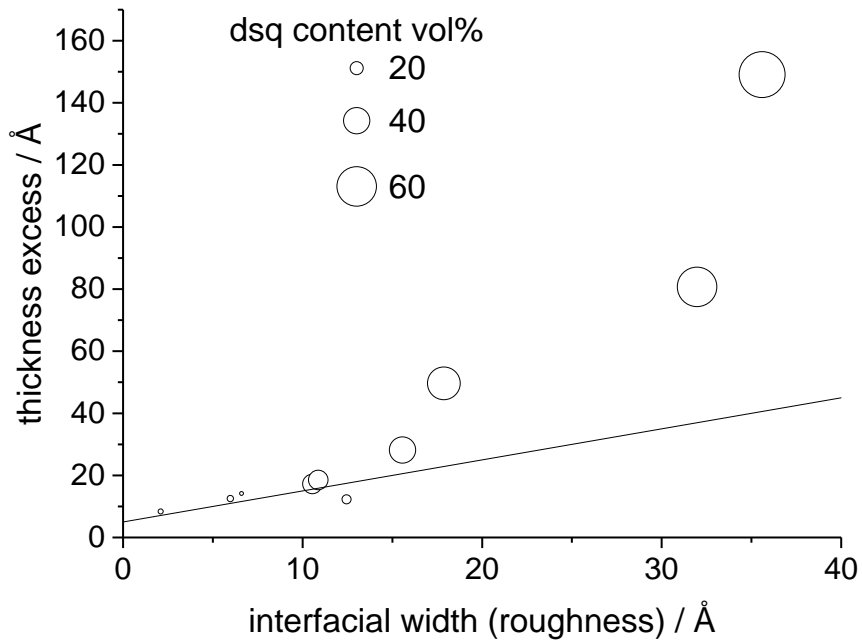


Figure 5-31: Evolution of the thickness of the excess layer with the interfacial width w (roughness). The size of the circles is proportional to the content of *d*-squalane.

A similar data interpretation was developed from the NR measurements on the dsq/PBcis mixtures (Figure 5-11). The same general observations as for the case of dsq in PB can be extracted from Figure 5-32.

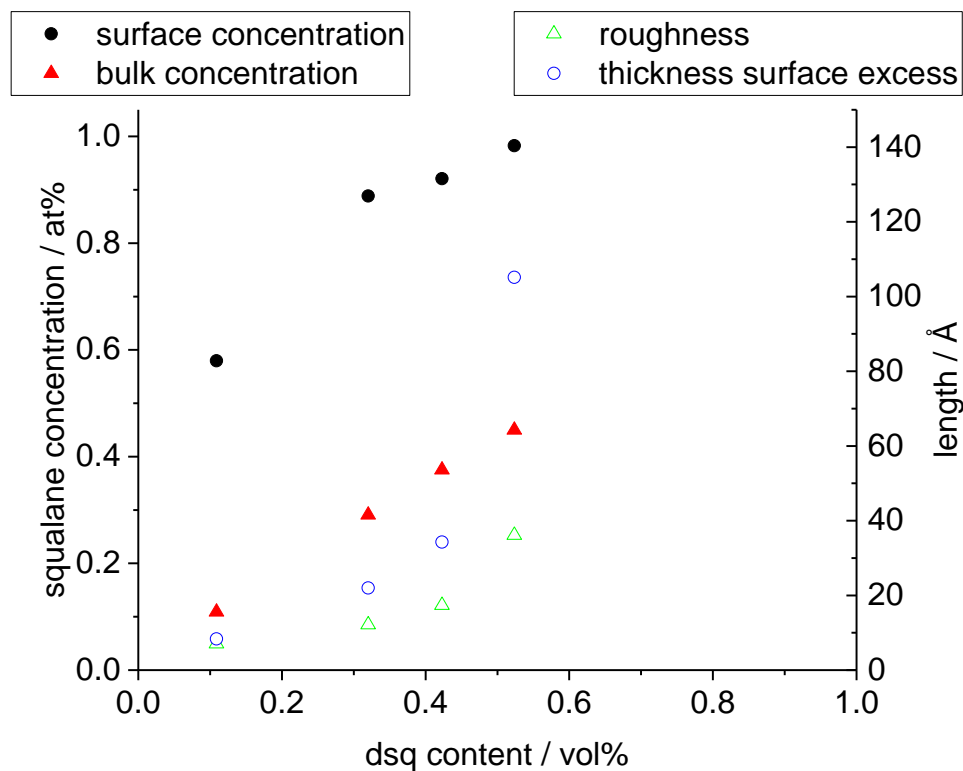


Figure 5-32: Evolution of the concentration profiles characteristics in PBcis with the dsq content.

The formation of the dsq wetting layer occurs slightly earlier than in PB – i.e. around 45 vol% which is in agreement with the suggestion from the phase diagram and is a clear evidence of lower compatibility between the oligomer and PBcis. The deviation from the bulk concentration linearity is not clearly observed in this case as the highest concentration investigated was a 50 % (w.w) sample which is very close to the phase boundary. Again, using equation (5.2) and considering $a_{av} = (11 + 7.6) / 2 = 9.3 \text{ \AA}^{172}$ and $\chi = 0.14$ at 20 °C (as defined from the Flory-Huggins fit to the phase diagram in 4.2.2.5), one obtains an interfacial width $w = 2.0 \text{ nm}$. This value of w is very similar to what has been obtained experimentally for dsq/PBcis, before the wetting layer formation. The calculated w is also slightly lower than for the case of dsq/PB which indicates a higher incompatibility for dsq with PBcis. In both matrices the width of the interface increases from below 2 nm to about 4 nm once the wetting layer is formed. The widening of the interface could signal greater roughness due to the formation of the phase-separated layer on the surface. The step in interfacial width before and after phase separation is not predicted by the Helfand theory since in equation (5.2), w depends mainly on $\sqrt{\chi}$.

From Figure 5-17 it was shown that the 50 % (w.w) sample was stable over time and indeed very close to phase transition since a slight cooling was the driving force for the formation of a wetting layer. Moreover, upon re-heating the sample to room temperature, the original state of the sample was recovered which proves that the equilibrium state was reached and tightly linked to the position on the phase diagram. Hence, the results from Figure 5-32 concur with the phase diagram determined for the dsq/PB mixture, which shows a lower compatibility for dsq in PBcis than in PB at RT.

5.2.4.3 Concentration profiles for incompatible systems

Oligo-dIB was judged by DSC to be more compatible with PI than PB, for the two molecular weights considered. A large surface excess that exceeded what can be accounted for by a single layer was revealed for oligo-dIB 900 in PI (Table 5-5), therefore suggests phase separation. The same oligomer in PB exhibits an excess of oligomer at the surface but also at the buried interface. This double excess was observed by ERDA (Figure 5-24) and confirmed by NRA (Figure 5-26). However, as discussed in 5.2.1, it is not explained by surface energy differences, rather by the formation of a metastable layering resulting from spinodal decomposition waves. Additionally, when oligo-dIB 900 is blended in PI, the particular shape of the vertical concentration profiles obtained by NR (Figure 5-19) suggest that a lateral phenomenon occurs in the film and that no homogeneous wetting layer is formed in this case. It is expected, from the similarity of the two matrices and the shape of the ERDA profiles (low surface concentration), that a similar lateral effect occurs in PB.

For the higher molecular weight oligomers of isobutylene (oligo-dIB 2200), the compatibility with the polymer matrices was reduced as discussed in 4.2.2.2. The concentration profiles obtained by NR are convincing enough – e.g. sharp interfaces – to ensure that no lateral phenomena are exhibited in these films. Moreover, the increase of the wetting layer thickness with oligomer content seems to follow the behaviour expected for a full wetting (Figure 5-20). Larger surface excesses are recorded than for oligo-dIB 900, as expected from the lower compatibility, but the shape of the profiles is generally maintained – i.e. excess at the surface and/or at the interface with the substrate. The concentration of the two phases in equilibrium can be read from the concentration profiles: one oligomer-pure phase and one polymer-rich phase are obtained, as expected from the FH theory.

5.2.5 IMPACT OF TEMPERATURE ON SURFACE PARTITIONING

The effect of temperature on the surface segregation behaviour of the model systems is visible in two aspects, but is mainly related to changes in bulk compatibility.

On one hand, as shown in Figure 5-5 and Figure 5-6, an increase in temperature in a miscible system is decreasing the surface excess of the oligomer – i.e. lower concentration and thickness of the excess layer. As discussed in 4.2.2.5, an elevation of temperature yields in a reduction of χ for these systems. Thus, as the temperature is increased, the difference between χ_{surf} and χ diminishes which results in less oligomer partitioning at the surface. Figure 5-6 also shows that the sample comes back to its initial state after being brought back to room temperature which is a sign of static equilibrium.

On the other hand, the effect of temperature can be more dramatic as it could imply traversing phase boundaries. The phase diagram of the dsq/PB blend showed that the system is compatible at room temperature for concentrations below 60 % (w.w) dsq. As NR measurements are performed at RT, this behaviour should be reflected in the NR-generated concentration profiles. However, as the ERDA end station is cooled down to about -80 °C using liquid nitrogen, the mixture is expected to be in the two-phase regime for concentrations as low as 25 % (w.w) dsq (by extrapolation of the FH fitted phase diagram). Indeed, in Figure 5-9, the bulk concentration seems to be around 20 at%. A big discrepancy was calculated between the z^* from ERDA and from NR. The fit to the experimental ERDA data yields the composition profiles from which z^* (dsq / PB) are calculated to be > 10 nm (Table 5-2). The significance of this value for z^* is that it is an order of magnitude greater than the length of the oligomer molecule; therefore can only be accounted for by a thick wetting layer. The formation of a stable surface excess, with a decay length which can persist to depths of tens of nanometres, is normally associated with a clearly phase-separated system,^{59, 63} or one in which the film is sufficiently thin that the influence of the surfaces on the overall free energy of the system may perturb the phase boundary somewhat.¹⁷⁷ Hence, the discrepancy in z^* between NR and ERDA measurements might be coming from the fact that ERDA measurements were performed at lower temperature, and therefore, lower compatibility.

5.3 CONCLUSIONS ON SURFACE PARTITIONING

The vertical concentration profiles of some binary non-polar oligomer/polymer blends were measured by ERDA, NRA and NR. The extremely rich range of behaviours reported highlighted parameters influencing the shape of the concentration profiles, namely: the surface energy difference between the species and the polymer molecular weight. The extent of segregation is overwhelmingly dependent on the compatibility between the oligomer and the polymer. This in turn depends on molecular weight differences, polarisability and, close to the critical point, on oligomer content and temperature.

It was proven that surface energy differences play a determining role on the “direction” of the oligomer excess. Typically, components of lower surface energy are partitioned at the surface of the blends, while components of higher surface energy are preferentially positioned at the interface with the high energy silica. Here, low surface energy components such as dsq and oligo-dIB tended to segregate to exposed surfaces while unsaturated oligo-dS segregated to the buried interface of hPI films.

The thickness of the polymer film can also alter the shape of the concentration profiles, provided that the film is thin enough to limit the thickness of the excess layer and/or create a concentration depletion in the bulk, by limiting the amount of available oligomer in the sample. This effect has to be kept in mind when discussing equilibrium surface and bulk compositions, especially because the samples studied by NR were relatively thin (70-200 nm). NR is indeed one of the only techniques able to detect a thin enrichment or wetting layer (few nms thick) but is not the best method to measure thicker films (> 200 nm). For films which thickness is greater than $\times 10$ the excess layer, the profile shape is independent from the total film thickness which is an intriguing result, especially in the case of phase-separated mixtures where one would expect an infinite wetting layer at the surface. For incompatible films of such thickness, the size of the wetting layer is then only dependent on the bulk concentration. It is suggested that a “frustrated” total wetting is responsible for this independence. It is also observed that the thickness of the wetting layer varies with the polymer matrix' M_w and is of the same range as its radius of gyration (tens of nms).

In the case of high molecular weight polymer blends, the molecules of lower molecular weight will be preferentially enriched at the surface to minimise the loss in conformational entropy. However, it seems that the tendency of small molecules to segregate to surfaces (or interfaces) of mixtures with larger polymers is insignificant when compared to other factors, notably surface energy differences or the compatibility of the mixed components.

The compatibility of the oligomer/polymer pairs was found to correlate strongly with the extent of surface or interfacial segregation. NR measurements showed that compatible systems – e.g. oligo-dS or dsq in PB – can present a slight surface oligomer enrichment or an even oligomer distribution over the whole sample depth, while incompatible systems – e.g. oligo-dS in hPI or oligo-dIB in PI – exhibit phase separation and segregation of an almost pure oligomer wetting layer at interfaces (with air and/or with substrate). The influence of the difference in polarisability between the oligomer and polymer on compatibility, hypothesised in 4.2.2.4.3, was also confirmed by contact angle measurements. Also, the effect of temperature on concentration profiles of systems close to their critical point is mainly related to changes in compatibility.

The surface enrichment was also discussed in terms of differences between the surface adsorption parameter χ_{surf} and the FH bulk interaction parameter χ . It is proposed that when $\chi > \chi_{surf}$ a surface enrichment of the low energy species be favoured over an even distribution over the thickness of the sample. However, it was also shown that this description is limited and cannot explain the behaviour observed for the dsq/PI mixture, where surface energy differences are low and compatibility is high. For PB and PBCis, a mechanism of wetting layer formation with increasing oligomer content was shown: the surface gets first saturated in oligomer and once saturation is achieved, the wetting layer starts to grow.

Chapter 6: ADHESION

PROPERTIES OF

OLIGOMER/POLYMER MIXTURES

In *Chapter 5*, a rich range of surface excess behaviour was observed for oligomer/polymer thin film mixtures. These results were linked to various compatibilities and surface energies of the model systems which are themselves arising from subtle variations in chemical structure or oligomer molecular weight. In this chapter, attempts to link the compatibility and surface partitioning behaviour with adhesive properties were undertaken, especially in the case of wetting layer formation, which can be the root-cause of poor adhesion performance. Investigations were undertaken to understand the effects of oligomer segregation on the surface and bulk properties of the model systems at the nano and macroscale. Atomic force microscopy and rheology were the main tools used to carry out the experiments but techniques more specific to industrial adhesive characterisation, such as tack tests, were also considered.

6.1 EXPERIMENTAL RESULTS

6.1.1 SURFACE INVESTIGATION OF OLIGOMER/POLYMER MIXTURES

6.1.1.1 Adhesion mapping by atomic force microscopy

6.1.1.1.1 *Oligo-dIB 900 in PI*

The vertical composition profiles obtained by ERDA for the mixtures of oligo-dIB 900 with PI and presented in 5.1.3.1 suggested that the composition of the films might not be homogeneous laterally. This is because the size of the surface excess was large enough to indicate phase separation, but the average composition of each layer was highly mixed and there was a high level of polymer in the oligomer-rich phase. Hence, even though the NR characterisation of the

mixture was carried out, it is not adapted as it is only valid for a 1D description. In order to validate this hypothesis and understand the nature of these lateral inhomogeneities, AFM measurements were performed on a film containing 30 % (w.w) oligomer and prepared by spin coating. The sample did not undergo freezing in liquid nitrogen. The time needed to install the sample on the AFM stage and scan a first image is around 10 minutes. A representative scan of the film's surface, of dimensions $50 \times 50 \mu\text{m}$, was recorded in tapping mode using peak force quantitative nanomechanical mapping (QNM) and is shown in Figure 6-1, where the skin colour code corresponds to the adhesion channel (yellow areas represent parts of higher adhesion). One must note that even when a calibration is performed this type of measurement is only partially quantitative. Hence, the results will be discussed qualitatively in the following sections. A corresponding cross-section is given in Figure 6-2.

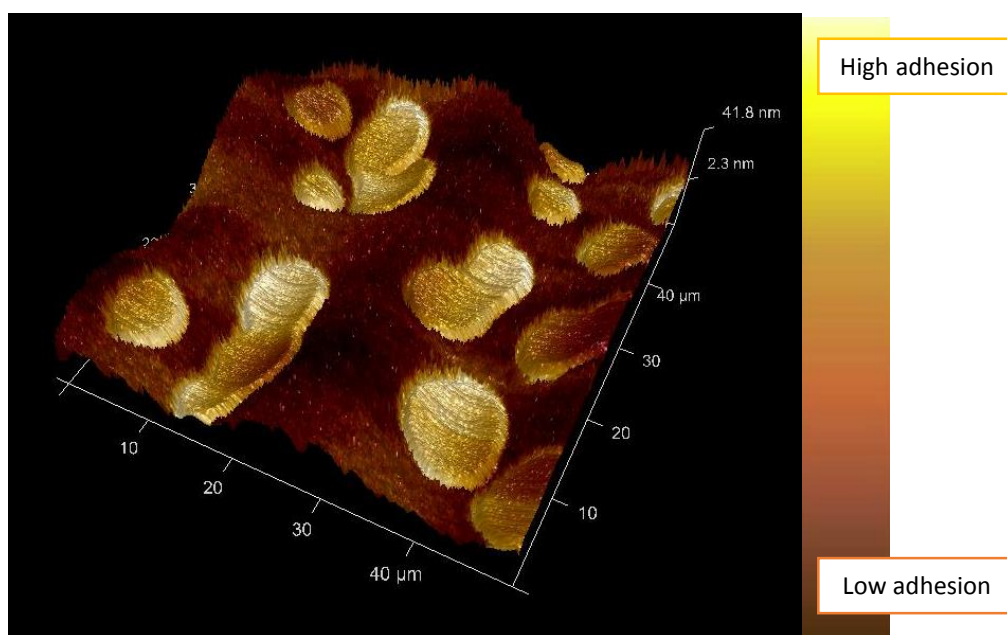


Figure 6-1: 30 % (w.w) oligo-dIB in PI: $50 \times 50 \mu\text{m}$ scan of a spin coated film. Zones of higher adhesion are lighter.

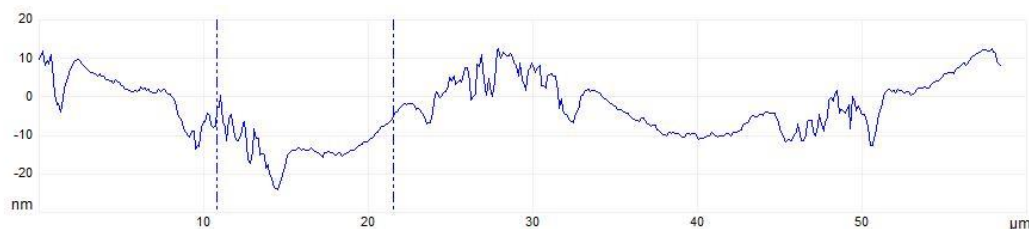


Figure 6-2: Cross sectional plot issued from Figure 6-1.

The AFM scan confirmed the presence of two phases of distinct adhesive properties: large and flat “disks” of higher adhesion are observed (yellow). The domains cover about 30-40 % of the surface, are 5-13 μm in diameter and are higher than the base line by about 5-10 nm. The AFM picture is characteristic of a partial wetting.⁶⁵ Very little evolution of the features was observed over a time scale of about 2.5 hours, as shown in Figure 6-3, which is in agreement with the well-defined reflectivity fringes recorded by NR, suggesting stability of the sample over the time of measurement. The red arrows point out a slight widening of the area at the interface between the islands which might suggest that a slow coarsening occurs.

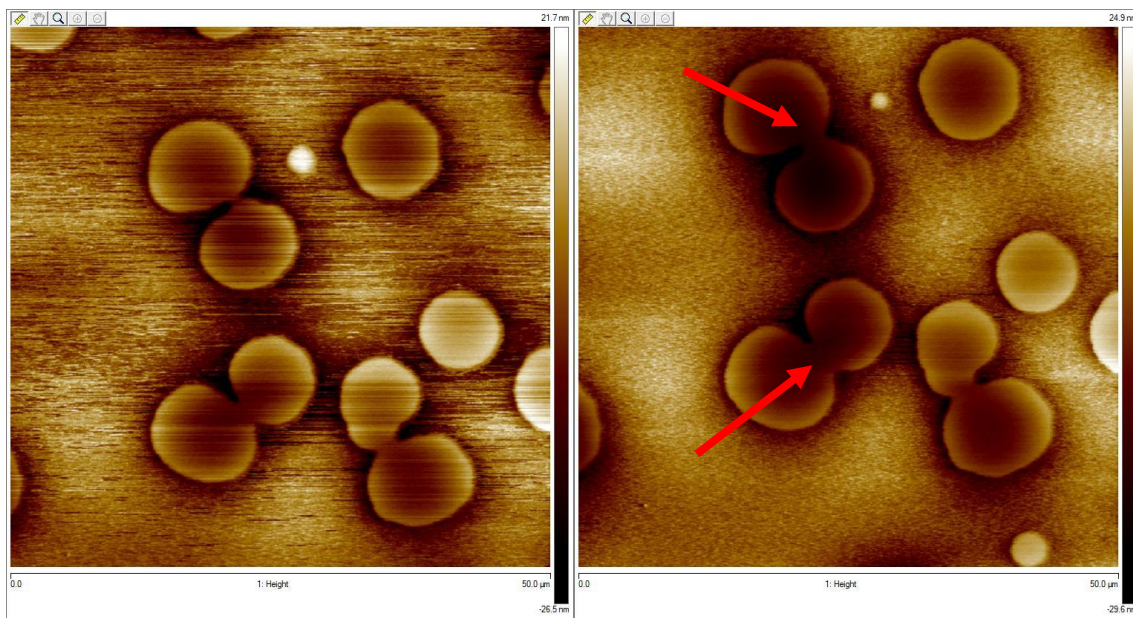


Figure 6-3: Initial $50 \times 50 \mu\text{m}$ 2D images of AFM height scans for a 30 % (w.w) oligo-dIB in PI sample (left) and after 2.5 hours (right).

It was also decided to investigate solution cast films, of larger thickness (few tens of μm , as estimated from the thickness of a $\sim 0.2 \text{ mL}$ of a 2 % (w.w) toluene solution, dried over a $\sim 1 \times 1 \text{ cm}^2$ area). The production of these films implies a slower solvent evaporation. Again, some islands of relatively high adhesion were observed (Figure 6-4 and cross-section in Figure 6-5), but on a different length scale: the features are smaller (about $1 \times 1 \mu\text{m}$ in area) but also taller (higher than the underlying surface of 50-100 nm). One should note that scale of the cross-section can be misleading: the horizontal axis is in μm while the vertical axis is in nm. Hence, if the domains were spherical they could go up to $1 \mu\text{m}$ deep inside the sample.

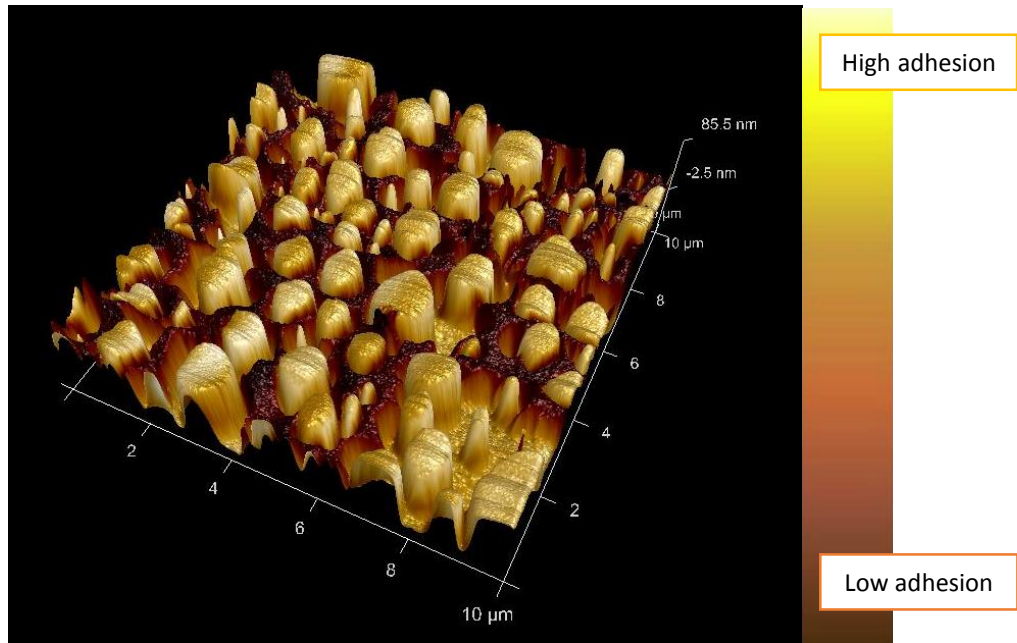


Figure 6-4: 30 % (w.w) oligo-dIB in PI: 10 × 10 μm scan of a solution cast film. Zones of higher adhesion are lighter.

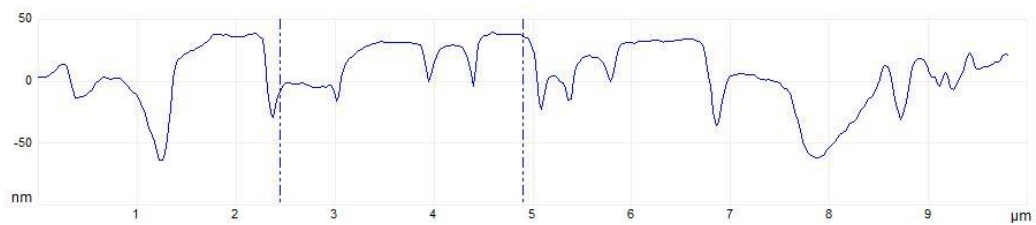


Figure 6-5: Cross sectional plot of a thick film of oligo-dIB in PI.

6.1.1.1.2 Oligo-dIB in PB

The same approach was applied to the oligo-dIB 900/PB mixtures, for which the relatively diffuse profiles obtained by ERDA and NRA, showing surface and interface excess, also suggest that the surface layer is not pure oligomer. The more adhesive zones are represented in yellow on the AFM scans. Samples of 30, 50 and 70 % (w.w) oligomer were investigated (Figure 6-6) and exhibit two distinct phases of different adhesion properties. Corresponding cross sectional plots are displayed in Figure 6-7.

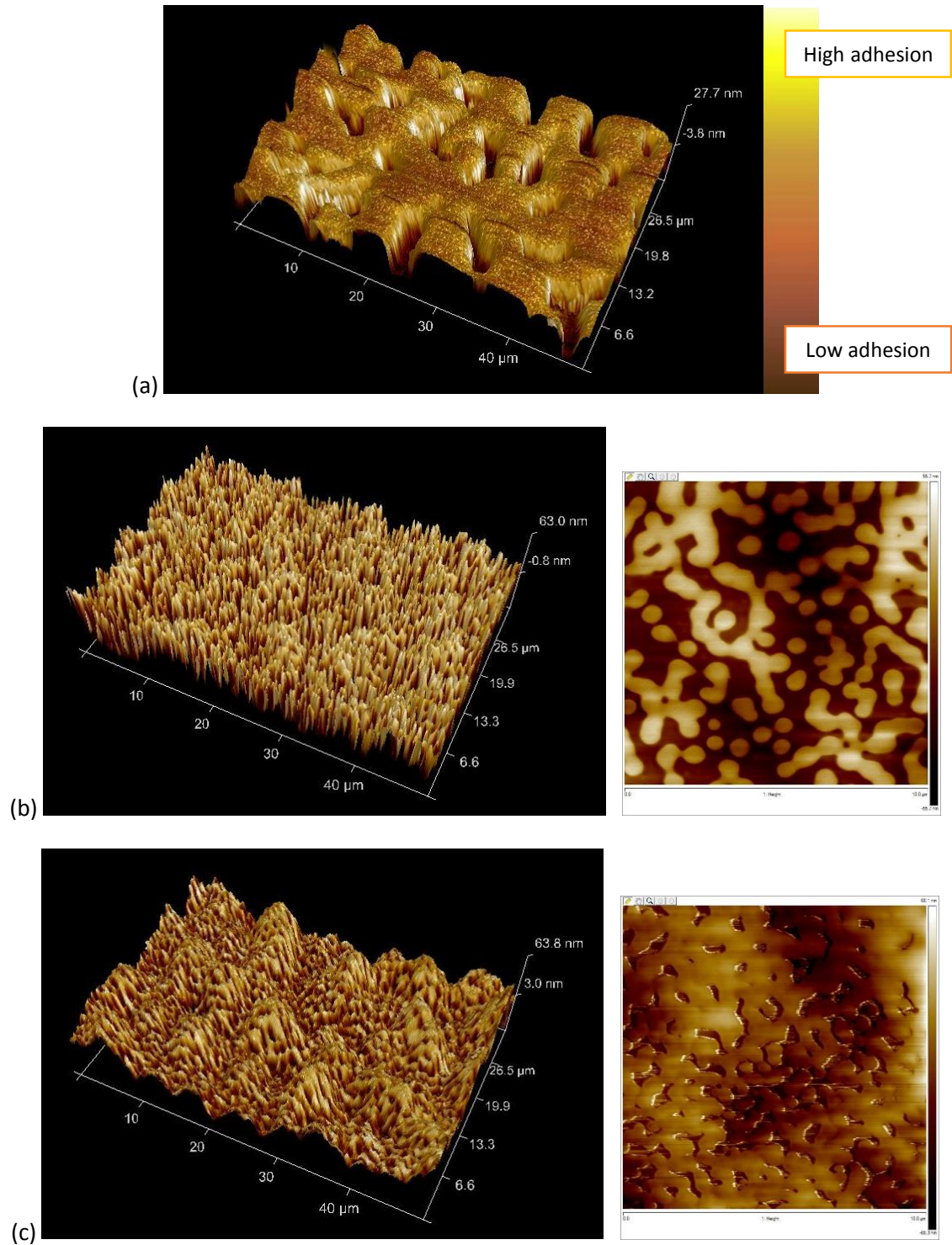


Figure 6-6: $50 \times 30 \mu\text{m}$ scan of (a) 30 (b) 50 and (c) 70 % (w.w) oligo-dIB 900 in PB thin films. Zones of higher adhesion are lighter. On the right side of (b) and (c) are presented $10 \times 10 \mu\text{m}$ 2D images of height scans for the corresponding samples.

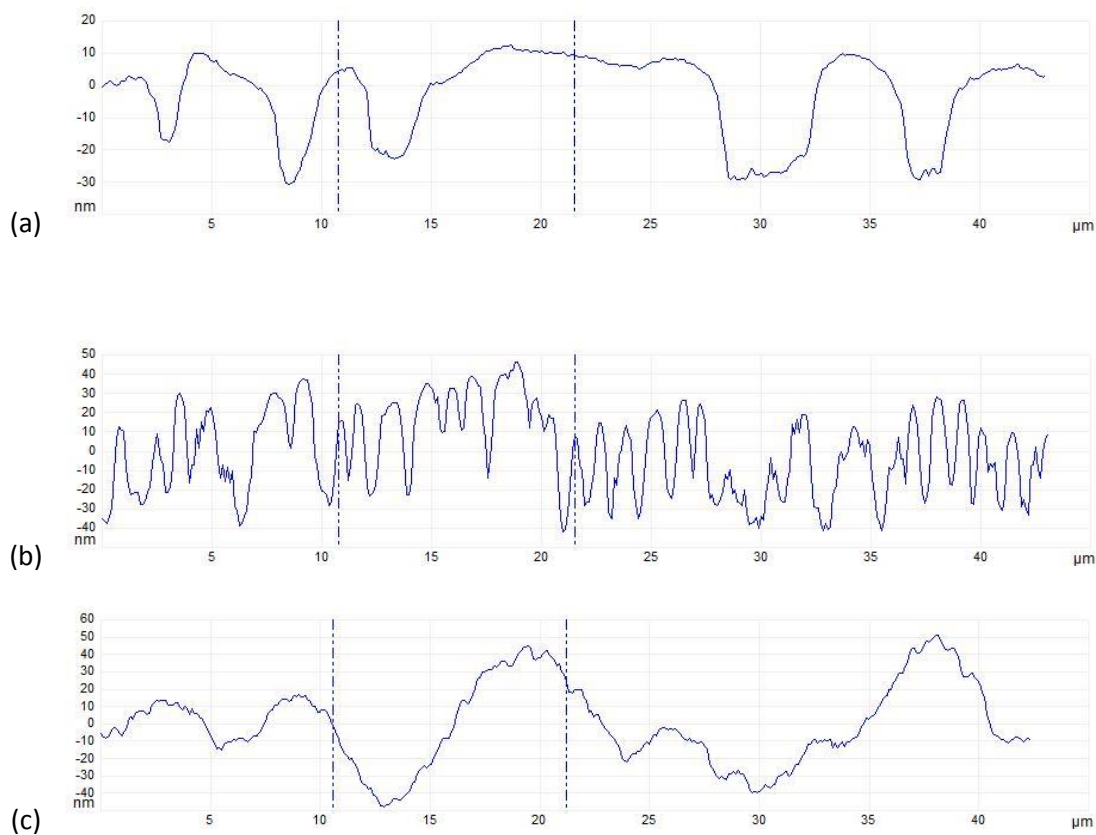


Figure 6-7: Cross sectional plots of (a) 30 (b) 50 (c) and 70 % (w.w) oligo-dIB 900 in PB thin films.

Interestingly, large differences in characteristic length scale between the samples were recorded. The surface features are of larger dimensions at low oligomer contents, while patterns of smaller size are formed for samples of higher oligomer concentrations. Comparing the 30 % (w.w) sample (Figure 6-6, (a)) with the corresponding oligomer concentration in PI (Figure 6-1), it appears that the surface is more covered in the case of PB, suggesting more segregation of the oligomer in the PB matrix than in PI. Again, as shown in Figure 6-8, little evolution of the patterns with time (1.5 hours) was observed, which suggests that a very slow coarsening of the most adhesive domains happens, leading to more surface coverage.

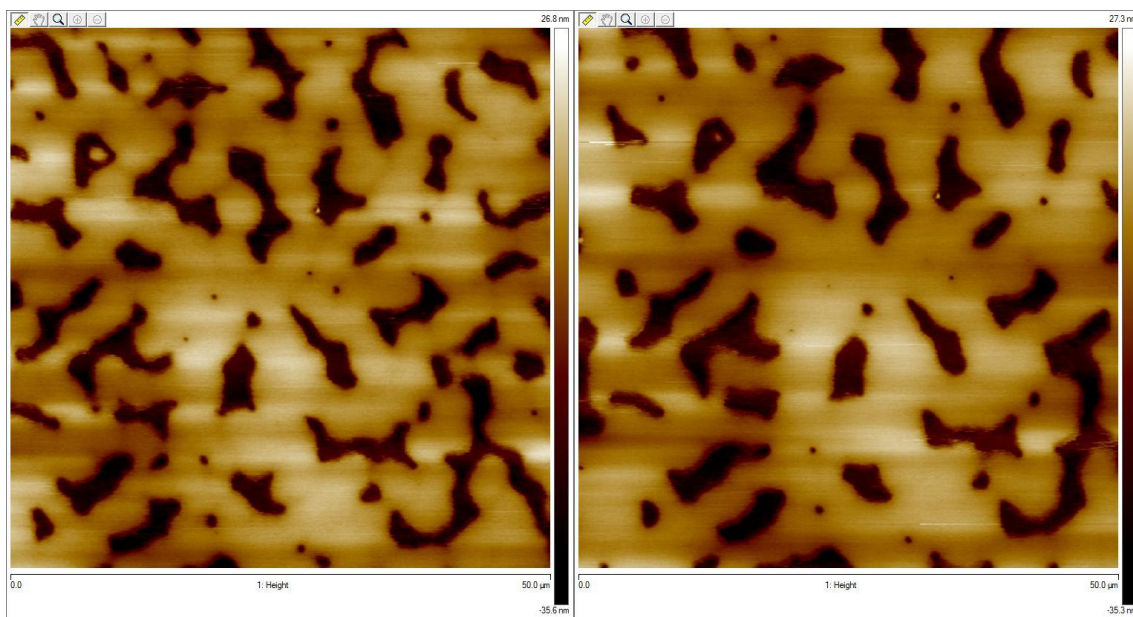


Figure 6-8: Initial $50 \times 50 \mu\text{m}$ 2D images of AFM height scans for a 30 % (w.w) oligo-dIB in PB sample (left) and after 1.5 hours (right).

A comparison with thick films prepared by solution casting was carried out. 3-D image plots of a $10 \times 10 \mu\text{m}$ scan of a 30 % (w.w) oligo-dIB in PB is shown in Figure 6-9. The corresponding cross sectional plot is given in Figure 6-10.

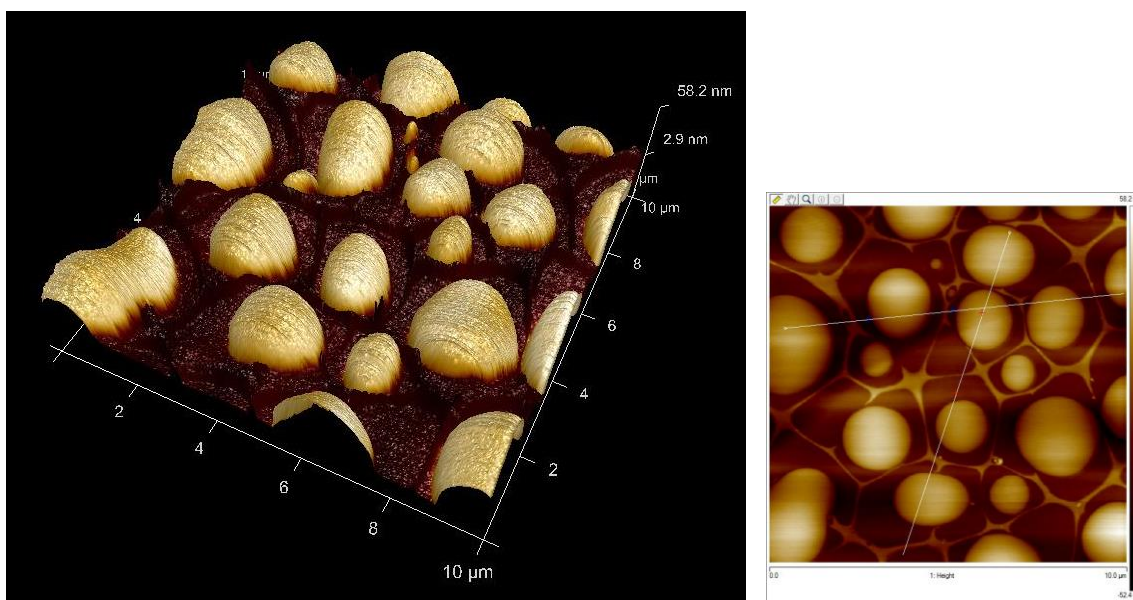


Figure 6-9: $10 \times 10 \mu\text{m}$ scan of a 30 % (w.w) oligo-dIB in PB solution cast film. Zones of higher adhesion are lighter. On the right side is presented the corresponding 2D height image.

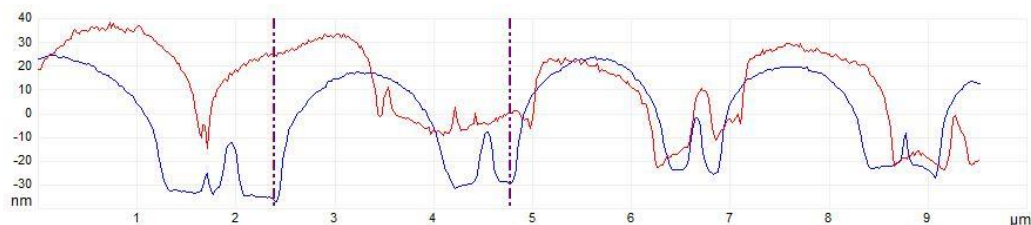


Figure 6-10: Cross sectional plots of a 30 % (w.w) oligo-dIB in PB solution casted film.

In this sample, $\sim 1 \mu\text{m}$ diameter high adhesion hemispheres are formed, that are taller than the surface by approximately 50 nm. It is difficult to determine if the round shape of the domains extend deeper into the sample or if they are sitting on a flat polymer-rich phase. An interesting pattern is observed as some raised “boundaries” of non-adhesive phase are recorded in between the spheres with a rather constant characteristic length scale, as shown on Figure 6-10.

A comparison of the previous images with the corresponding concentration in spin coated films (Figure 6-6, (a)) shows that a smaller pattern characteristic length is again observed in the case of solution cast films. The surface coverage of the most adhesive component appears to be higher in the case of spin coated films as most of the oligomer-rich phase is spread at the surface and not contained into spheres. It is suggested that the difference between the two samples is mainly due to the sample preparation. In the case of a solution cast film, the solvent remains in the sample for several minutes which completely changes the kinetics and thermodynamics of the phase separation process.

6.1.1.2 Macroscopic adhesion via tack tests

Loop tack tests (similar to a 90° peel tests) were performed on sq/PBcis samples of 0, 10, 20, 40 and 60 % (w.w) squalane content as described in the ASTM D6195 test method.¹³⁵ Figure 6-11 gathers the experimental results, presenting the averaged peak force over 3 repetitions as a function of the squalane content. The experimental protocol leads to a large error on the generated data. This is because the test response was really low – as the model formulation tested are not real adhesives. Hence these tests appear to show no significant effect of the presence of a wetting layer on the nominal force required to remove the coated loop from the steel substrate and hence on the adhesion properties. One could however note that for the more concentrated sample (60 % (w.w), which is a concentration at which phase separation occurs) residual wet stains were observed onto the steel plate after removal. This could be interpreted as an interfacial failure due to the presence of a contaminant (i.e. migrated oligomer).

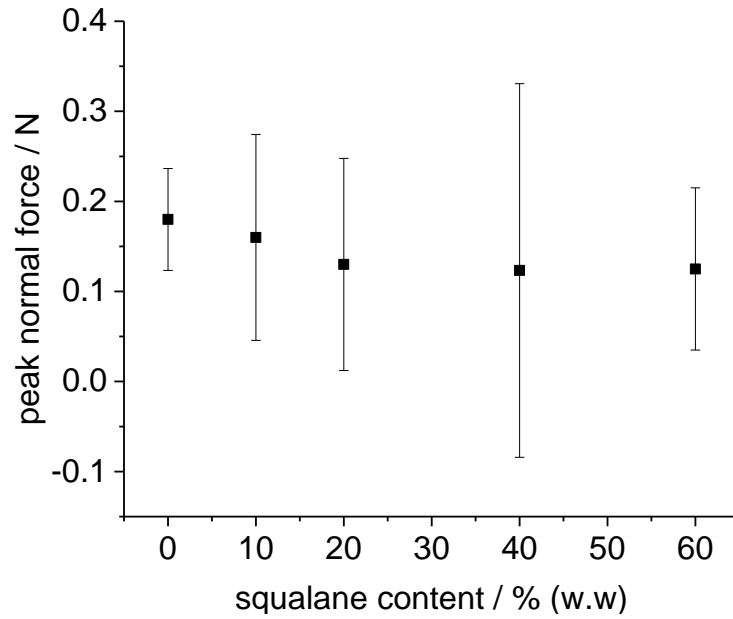


Figure 6-11: Loop tack tests results for sq/PBcis samples of various concentrations.

Tack tests were also performed with a rotational rheometer with a 4 cm diameter parallel plate, according to the method described in 2.11.2. An example of results is given in Figure 6-12, top. Again the results generated present a large error and the data did not resolve any effect of squalane content on the tack properties (Figure 6-12, bottom). No fibril formation was observed which indicates poor tack properties of the model adhesive. Additionally, no trend was measured in terms of normal force peak or maximum displacement. It is suggested that the error is due to the sample preparation (coating and fixation onto the sample stage) and to the low test response, also evidenced in the loop tack test.

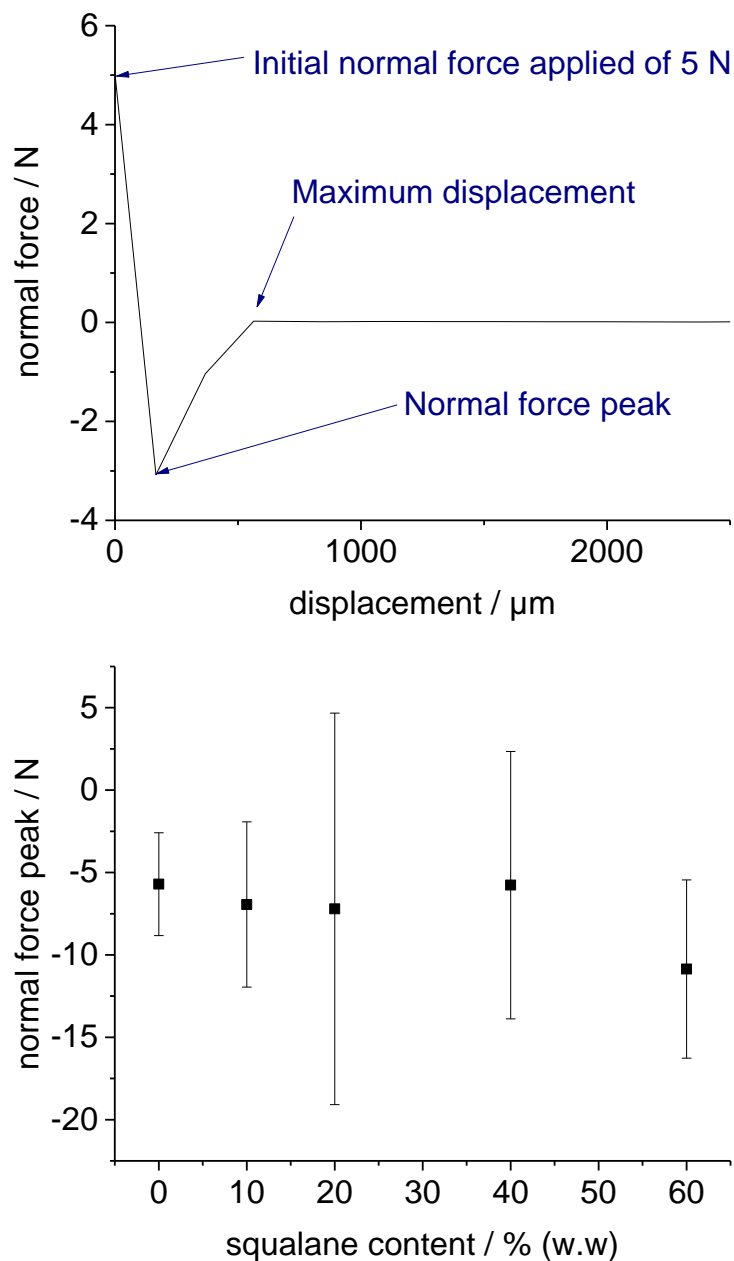


Figure 6-12: Top: Example of a tack test for a 20% (w.w) sq/PBcis sample. Bottom: Tack tests results using the rheometer for sq/PBcis samples of various concentrations.

6.1.2 BULK INVESTIGATION OF OLIGOMER/POLYMER MIXTURES

Because of the large amount of material needed to perform mechanical testing (few grams), the rheological characterisation was limited to two model systems, for which the oligomer (in its hydrogenated form) and the polymer were available in sufficient quantity: squalane in PB and in PBcis. Samples of various sq contents were prepared by solution casting (to obtain a 1 mm thick film) and investigated by oscillatory rheology. The storage and loss moduli (G' and G'')

respectively) of the samples were measured between 10 and 125 °C, in the viscoelastic domain, as a function of angular frequency. The experimental procedure was applied as described in 2.10.1.

For high angular frequencies (equivalent to low temperature), G' is greater than G'' which means that the samples exhibit solid-like properties (rubbery plateau); the chains do not have enough time to relax (disentangle). At lower angular frequencies, corresponding to higher temperatures, G' becomes lower than G'' and the chains can slip by each other in a *reptation* process. Over very long times (very low frequencies), the chains are totally disentangled and are able to flow (terminal region); the samples exhibit a liquid-like behaviour. Generally, for linear monodisperse polymers, G' and G'' present characteristic slopes in the terminal region of 2 and 1 respectively (in log scale).¹³³

The theory of *reptation* was firstly introduced by De Gennes¹⁷⁸ as the thermally activated diffusion of a polymer chain, entangled amongst neighbouring chains. The constraints of diffusion due to the entanglements with other chains are represented by a “*tube*”. The chain can *escape* from this *tube* – i.e. relax the stress carried by the chain segments – when a chain-end becomes free to explore new isotropic configurations. The predicted escape time for reptation scales as M^3 for a linear chain. The length of the rubbery plateau depends on the polymer molecular weight and concentration. The crossover frequency at which the polymer passes from solid to liquid behaviour is an important value as this intersect corresponds to $1/\tau_{max}$, τ_{max} being the longest relaxation time for the polymer molecules to disentangle or the time needed for about 63 % of the stored elastic energy to be converted in dissipation and viscous energy.¹³³

From the oscillatory rheology data obtained at various temperatures, master curves at a reference temperature of 25 °C were automatically built using the tool from the rheometer’s software *TA Instruments TRIOS v4.1.1.33073*. The resulting master curves are presented in Figure 6-13 for samples of squalane contents from 0 to 80 % (w.w) in PB. For each of the samples a crossover point was observed. As the squalane weight ratio is increased in the sample, the rubbery plateau is recorded at lower modulus values and the crossover point shifts towards higher frequencies – i.e. the relaxation time τ_{max} needed for the polymer to disentangle becomes lower: it is reduced from about 6.0 to 0.27 s, as shown in Table 6-1.

One can note that the G' and G'' master curves for the pure PB sample (black) do not present the characteristic slopes at low angular frequencies (of 2 and 1 respectively) for linear monodisperse chains, which makes the crossover point more difficult to determine. A reason for this discrepancy is the high polydispersity of this PB sample (PDI = 2.1) which implies that there is a broad distribution of M_w and a range of different τ_{max} . For the 70 and 80 % (w.w) samples the crossover frequency is unexpectedly reduced. This apparent result is in fact suspected to be related to the failure of the master curve construction itself, as the mixtures are phase-separated for these concentrations. A more detailed discussion is given in 6.2.2.1.

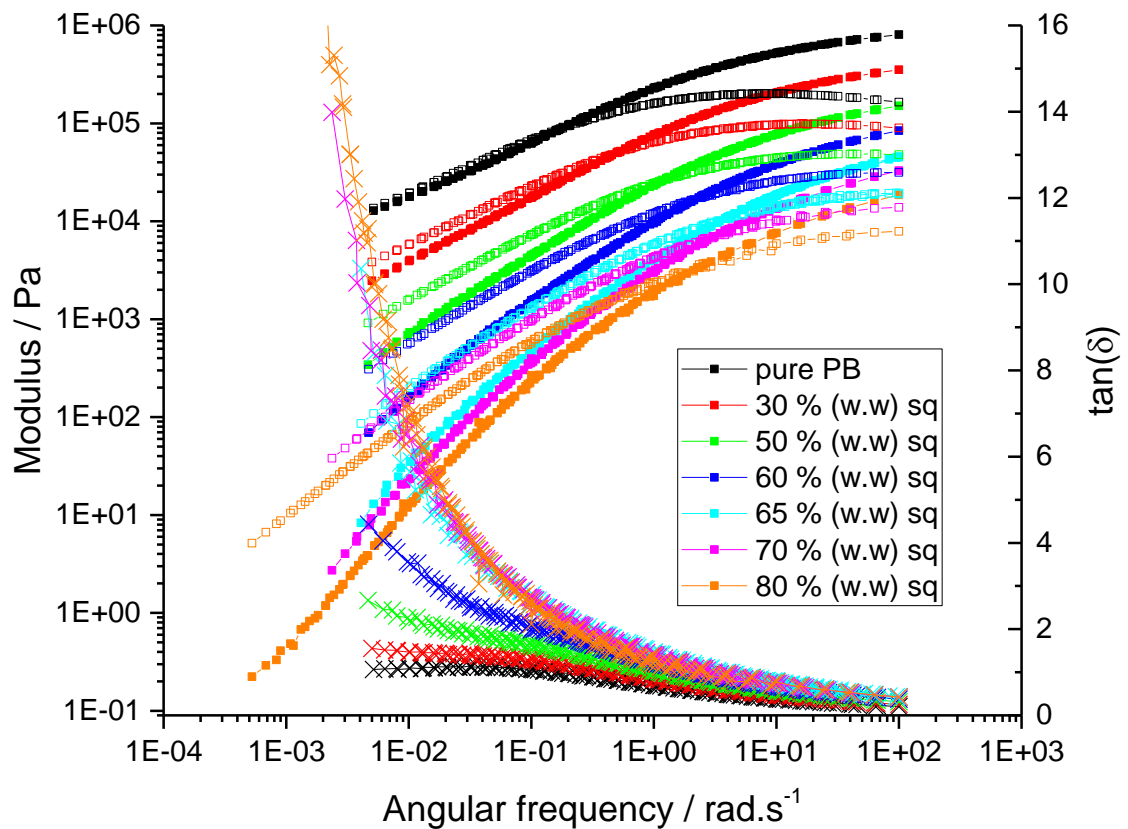


Figure 6-13: Master curves for the sq/PB samples of various sq contents at a reference temperature of 25 °C. Storage modulus G' (plain squares), loss modulus G'' (hollow squares) and $\tan(\delta) = G''/G'$ (crosses) are plotted as a function of angular frequency.

Table 6-1: Evolution of the crossover frequency and relaxation time as a function of the squalane content for the sq/PB mixtures.

Sample sq content / % (w.w)	Crossover frequency / rad.s ⁻¹	τ_{max} / s
0	0.17	5.9
30	0.49	2.0
50	1.16	0.86
60	2.24	0.45
65	3.74	0.27
70	2.99	0.33
80	2.03	0.49

Similarly, master curves were produced for PBcis samples of increasing sq content (Figure 6-14). The storage and loss moduli of the pure PBcis polymer are lower than those of the other PB, presenting a higher percentage of trans-1,4 additions and 1,2 additions. The difference in chain structure induces a lower T_g in the case of PBcis (which are -87.9 °C and -91.5 °C for PB and PBcis respectively, according to the results in 4.1.1.1.2) and hence, a reduction of the moduli, since the reference temperature of the measurement is further away from T_g . Moreover, the crossover point for the pure PBcis sample is not seen in this range of temperature/frequencies: G' remains higher than G'' which is characteristic of a solid rubbery behaviour. This behaviour is explained by the high molecular weight and very high polydispersity of the PBcis (PDI = 4.7). Again, as the quantity of squalane in the sample is increased the moduli are decreased and the crossover points are shifted towards higher frequencies (see Table 6-2): it is measurable in these conditions starting from ~ 30 % (w.w) squalane.

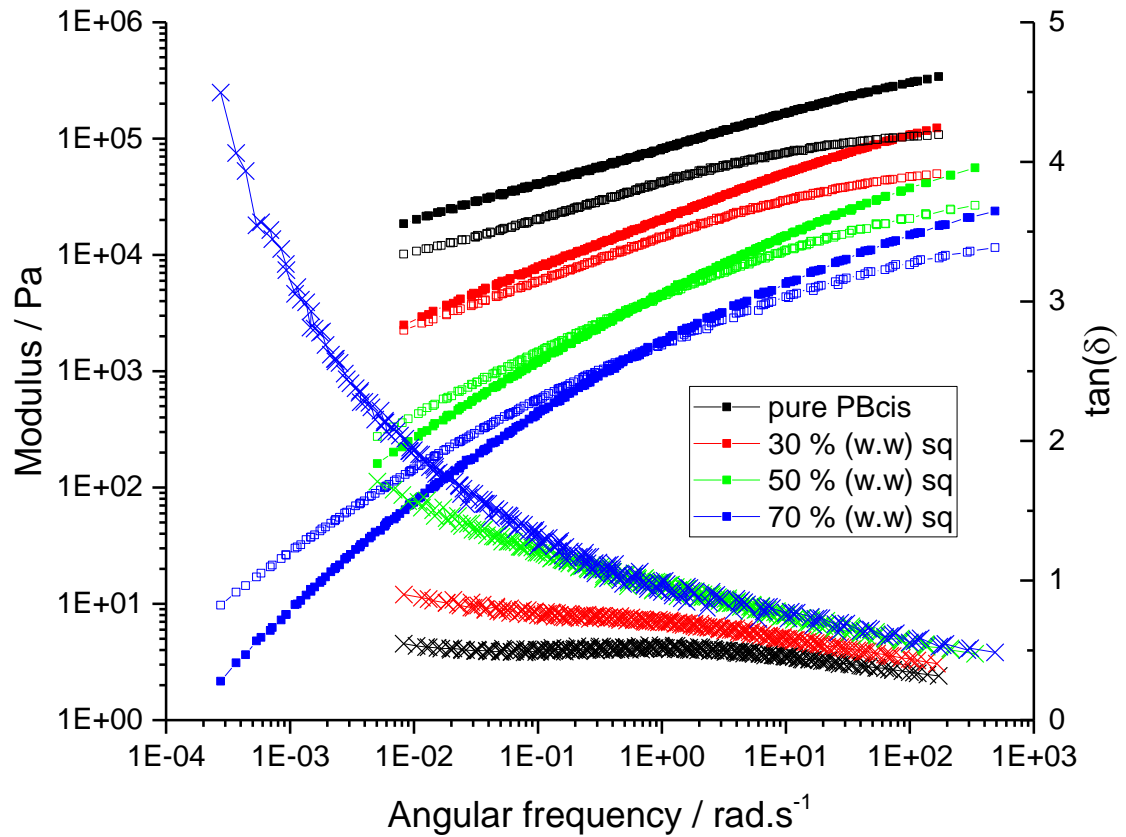


Figure 6-14: Master curves for the sq/PBcis samples of various sq contents at a reference temperature of 25 °C. Storage modulus G' (plain squares), loss modulus G'' (hollow squares) and $\tan(\delta) = G''/G'$ (crosses) are plotted as a function of angular frequency.

Table 6-2: Evolution of the crossover frequency and relaxation time as a function of the squalane content for the sq/PB mixtures.

Sample sq content / % (w.w)	Crossover frequency / rad.s^{-1}	τ_{max} / s.rad^{-1}
0	/	/
30	< 0.01	> 100
50	0.52	1.9
70	0.47	2.1

6.2 DISCUSSION OF ADHESION PROPERTIES

6.2.1 SURFACE ADHESIVE PROPERTIES OF PHASE-SEPARATED SYSTEMS

6.2.1.1 Surface lateral composition of oligomer/polymer films

According to the results of the compatibility study and the predictions from the Flory-Huggins theory, one expects that the blends of oligo-dIB 900 with PI or PB would phase separate into a rich polymer phase and an oligomer pure phase. As illustrated in Figure 6-15, two clearly distinct adhesion forces distributions were indeed evidenced by AFM at the surface of the samples, corresponding to the two expected phases. Although there is no direct chemical characterisation of the domains, the trends in coverage suggest that the tacky adhesive domains correspond to the oligomer-rich phase. At a measurement frequency of 2 kHz ($\sim 12.6 \times 10^3 \text{ rad.s}^{-1}$) the polymers exhibit hard elastic solid behaviours. Oligo-dIB has a shorter τ_{max} since it shows a waxy behaviour at RT. Hence the dynamic contrast enable to differentiate areas of high adhesion on the surface corresponding to oligo-dIB rich domains, and an underlying area of lower adhesion power corresponding to the polymer-rich phase.

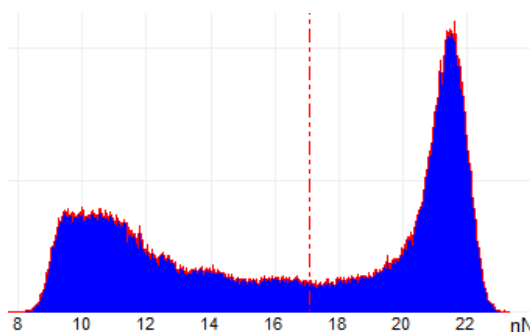


Figure 6-15: Measured adhesion force (in nN) at the surface of the 50 % (w.w) oligo-dIB 900 / PB sample. Histogram built from the AFM scan in Figure 6-6 (b). The y axis is in arbitrary units.

Again, because of such a lateral inhomogeneity in the sample, NR is not an appropriate technique to describe its vertical composition. ERDA is more adapted, as it simply averages the film composition and do not require the beam to be reflected on a flat surface and contributions to the laterally averaged depth profile are simply added.

6.2.1.2 Underlying lateral composition of oligomer/polymer films

The scans recorded by AFM allow visualising only the surface of the sample but do not give information on the underlying composition. The domains observed in the 30 % (w.w) oligo-dIB 900/PI spin coated sample (Figure 6-1) are raised of 5-10 nm with respect to the rest of the film – i.e. about a tenth of the total thickness of the film. In 5.1.3.1, a vertical concentration profile for a sample of similar total thickness was obtained by ERDA: the measured excess (average composition at the surface) was found to spread over the first 25 nm of the film. Hence, this result suggests that the oligomer-rich structure extends well below the surface of the visible features, as sketched on Figure 6-16. This type of partial wetting was also described in literature for the wetting of a binary liquid mixture, in the two-phase regime and far from their critical point.^{65, 66}

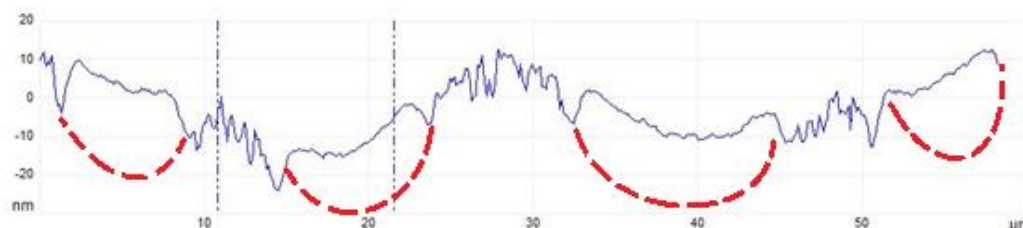


Figure 6-16: Cross sectional plot issued from Figure 6-1. The dotted curves indicate the extent of the oligo-dIB inferred from ERDA. Reproduced from Ref.¹⁴² with permission from The Royal Society of Chemistry.

6.2.1.3 Surface directed phase separation in oligomer/polymer films

Reported surface energies for PI and polyisobutylene are similar (between 31 and 34 mN.m⁻¹ and around 33.6 mN.m⁻¹ respectively).¹⁷ Nonetheless, the surface energy for oligo-dIB is expected to be lowered in respect to polyisobutylene due to density effects for such low molecular weights.¹⁷⁹ The domains observed in the 30 % (w.w) oligo-dIB 900/PI spin coated sample (Figure 6-1) are about 5-13 μm in diameter which far exceeds the total film thickness; this is a feature of lateral phase separation in polymer films of surface active mixtures.¹²⁶ They also appear thicker on their edges and there is no total coverage of the polymer-rich phase by the pure oligomer phase – i.e. no complete wetting (Figure 6-1). Hence, it can be concluded from the AFM scans that the surface energies of the two components do not match, and that the oligomer is preferentially positioned at the surface due to its lower surface energy. A similar conclusion can be drawn from the higher literature values¹⁷ for the surface energy of PB than of PI. Nevertheless, one can note that similar structures than illustrated in Figure 6-16 can form due to the interfacial instability in an originally layered phase-separated film, even for polymers of quite similar

surface energies, when formed by spin coating.^{121, 180, 181} Additionally, at equivalent oligomer content, the AFM scans for PB mixtures showed a higher oligomer surface coverage than in PI (Figure 6-1 vs Figure 6-6 (a)), which is consistent with the bigger surface energy difference between the oligomer and PB and with the results from the two previous chapters evidencing a lower bulk compatibility of the oligomer in PB. One may note that none of the components have a surface tension that is lower than the solvent ($\gamma_{toluene} = 27.76 \pm 0.05$ at 25 °C using the pendant drop method).¹⁸² Hence, the phase separation in the drying film may precede surface segregation in the early stage of the thin film formation. The presence of both phases at the surface is therefore consistent with a small difference in surface energy.

6.2.1.4 Mechanisms of phase separation and evolution of the surface features

The observed features at the surface of the thin polymer films imply that phase separation happened and that the created surface enriched layer was unstable (see 1.2.4). It is hence suggested that the oligomer-rich thin film formed at the surface ruptured and formed the observed patterns in a process called dewetting.

For thin films, dewetting can occur spontaneously by nucleation and growth, due to defects in the film, or from the amplification of thermally excited capillary waves, originating from the surface and interface with the substrate – namely, spinodal dewetting, in analogy to spinodal decomposition.^{57,183,184} In the case of spinodal dewetting, the action of long-range van der Waals forces on the interface between two immiscible polymers introduces a dispersive capillary length l expressed in equation (6.1).¹⁸⁴ The capillary length depends on the thickness of the film d and on the Hamaker constant A , for the interactions between the substrate and the air across the thickness of the bilayer polymer film. This capillary wave length (hence, the square of the film thickness) is dictating the average distance between the surface patterns.¹⁸⁴

$$l = \sqrt{\frac{4\pi\gamma_{12}d^4}{|A|}} \quad (6.1)$$

The Hamaker constant can be calculated from the Lifshitz theory, which is based on the quantum field theory.¹⁸⁵ The refractive index, the zero-frequency dielectric constant and absorption frequencies of the components are needed as input parameters for the calculation. A value of 2×10^{-20} J is reported for PMMA interacting with air across a d-PS film but is recognised as not fully reliable by the authors.¹⁶⁸ Hamaker constants calculated for hydrocarbons and polymers with a

simple group contribution method were about 5×10^{-20} J,¹⁸⁶ which is the same order of magnitude as the reported value for the PMMA/d-PS system. Sensible values for interfacial tension between incompatible homopolymers may be in the range of 1 to 10 mN.m⁻¹.^{187,188} Indeed, for a mixture of two polymers, the interfacial tensions are typically an order of magnitude smaller than the polymer surface tensions.¹⁸⁴ Hence, for a film thickness of about 100 nm, the capillary length should be of the order of 5×10^{-6} to 2×10^{-5} m, namely 5-20 μ m. This order of magnitude corresponds very well to the distance in between the centres of the oligomer-rich islands shown in Figure 6-1 and Figure 6-2. This may suggest that the formation of these patterns is linked to spinodal decomposition. However, for the 50 % (w.w) oligo-dIB 900/PB spin coated sample, the distance in between the features is smaller. Some of the observed patterns are overlapping which suggests that they might have grown from an initial spot and extended by lateral migration on the surface. These features are more characteristic of a nucleation and growth process (hence going through a metastable state) rather than a spinodal decomposition.¹⁸⁹ It is therefore difficult to conclude with certainty on the early-stage process of features formation at the surface of these samples.

Remarkably, given that the film components are at least 75 °C above their respective T_g values at the measurement temperature, the structures appear to be relatively stable, and very little coarsening was observed over 1-2 hours (see Figure 6-3 and Figure 6-8). One can therefore assume that a metastable state was reached after spin coating of the film, but that the real equilibrium state may need several days to be achieved, which might indicate a slow nucleation and growth process. The observation of slowly coarsening domains contradicts the assumption that the films measured by NR were at equilibrium. The assumption was valid in the case of mixtures with dsq, as demonstrated in 5.1.1.3, likely due to the liquid nature of the oligomer. Since oligo-dIB 900 has wax-like behaviour, it is suggested that the diffusion of the oligomer to the surface is slower. Moreover, the observed lateral phase-separated features in Figure 6-1 and Figure 6-6 are 2 orders of magnitude bigger than the film thickness. Hence, when phase separation occurs, equilibration may be slow because it is limited by the lateral diffusion speed. One may note that, in homogeneous films, the timescale of equilibration is expected to be much faster since the vertical diffusion distances are shorter. This result also agrees with the particular profiles obtained for the mixtures of oligo-dIB 2200 and PB, which showed a segregation of oligomer rich-phase at the surface and at the interface with the substrate, whereas it is not expected from surface energy arguments (see 5.2.1) and therefore must come from kinetic

considerations. Similar profile evolutions were reported for dPMMA/SAN thin films, which exhibited surface and interface excess of dPMMA after 120 min annealing time, though after longer annealing times, dPMMA was found in excess at the surface only.⁶⁸

In the case of the solution cast oligo-dIB/PB film (Figure 6-9) some boundaries of polymer-rich phase were observed in between oligomer-rich spheres. Since such a sample structure implies a long drying step, it is proposed that some solvent-rich spheres were rapidly formed at the surface and that they then slowly shrank upon solvent evaporation, leaving behind a meniscus of polymer-rich phase (Figure 6-17, (a)). Alternatively, the spheres could have nucleated and grown slowly, creating opposing lateral concentration gradients at the surface – driving oligomer molecules towards the spheres and polymer molecules away from the spheres – hence, creating raised boundaries in between the nucleating centres (Figure 6-17, (b)).

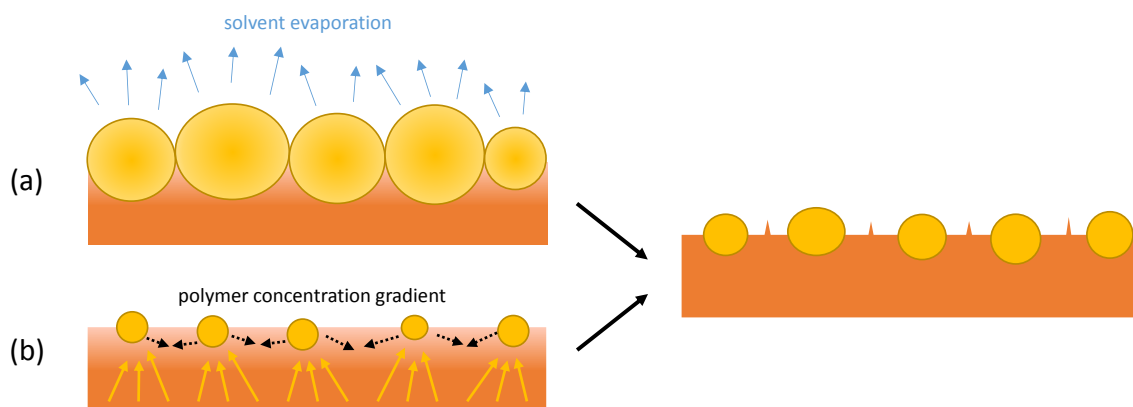


Figure 6-17: Schematic illustrating hypotheses for the formation of boundaries in between the oligomer-rich spheres.

6.2.1.5 Effect of oligomer content on surface topography and adhesion

The difference in surface organisation between samples of different oligomer content was investigated by AFM for oligo-dIB/PB mixtures (Figure 6-6). The average roughness (R_a) and root mean square roughness (R_q) were calculated from the AFM scans (Table 6-3). While a simple increase in surface coverage by the oligomer might have been expected with increasing oligomer content, the AFM images show large differences in surface roughness and characteristic length scale between samples of 30, 50 and 70 % (w.w) oligomer. A maximum roughness was found for the 50 % (w.w) sample, which is coincidentally close to the industrial formulations generally containing about 60 % (w.w) of additives in the polymer matrix. Indeed, positioning a component of lower viscosity at the surface and maximising roughness may increase the mechanical

adhesion to low roughness substrates,¹⁹⁰ although it should be noted that industrial hot-melt adhesives do not use solvents in spreading films.

Table 6-3: Roughness values of films containing varying oligomer content.

oligo-dIB 900 content / % (w.w)	R_a (nm)	R_q (nm)
30	11.7	14.2
50	20.6	23.8
70	14.5	18.1

It was also observed that the features forming at lower concentrations were of larger size than the ones formed at higher concentrations. This phenomenon could imply that the oligomer-rich phase wets the polymer-rich phase to a greater extent at lower oligomer contents. However, a surface energy argument does not make sense here since the surface energy difference between the two phases should be reduced with increasing oligomer concentration. The compositions of the two phases would become more similar. Hence, it would be expected to observe better spreading of the oligomer pure phase at higher oligomer contents. Moreover, upon strong phase separation, the composition of the two phases should not be greatly affected by the sample's overall composition. Therefore, it is suggested that the phenomenon observed is purely kinetic: the segregation of the oligomer follows a slower process in the low concentration sample, enabling the growth of a larger dimension pattern. This process might be controlled by the diffusion of the oligomer within the host matrix and related to the polymer chain's relaxation times. At higher oligomer concentrations, the polymer is plasticised by the oligomer which would allow faster diffusion and the film is generally thinner which would reduce the travel distance and make surface effects more dominant. Hence, nucleation into separate phases may be very rapid upon drying so there are more, smaller domains. Different surface structures attained at the same time would arise from differing viscosity and therefore motility of components. This explanation would also concur with the smaller features observed in the case of the solution cast samples, in which the diffusion of the oligomer would be faster due to the presence of solvent. Also, in solution cast films, the greater thickness diminishes the influence of the surface in directing phase separation. Therefore, less surface stratification is expected which might explain the observation of smaller features.

6.2.2 BULK MECHANICAL PROPERTIES OF OLIGOMER/POLYMER BLENDS

6.2.2.1 Effect of oligomer content on bulk mechanical properties

6.2.2.1.1 Polymer plasticisation

The oscillatory rheology experiments evidenced a plasticisation of the polymer, with increasing squalane content (Figure 6-13 and Figure 6-14). The addition of oligomer in the pure polymer shifts the crossover point to higher frequencies (see Table 6-1) which is a sign of shorter reptation times and hence, a lower number of polymer entanglements. The plasticisation of the polymer should also lead to a T_g shift with increasing oligomer content (as seen by DSC), which would correspond to a shift of the maximum in $\tan(\delta)$. However, this effect was not detected from these experiments because the T_g s of the pure components are far below the range of temperatures at which the measurements were performed (around -95 °C vs 10-125 °C).

From rheological data, it is possible to evaluate the molecular weight in between entanglements, M_e , from the determination of the plateau modulus G'_0 using equation (6.2), where ρ is the density and R is the gas constant.¹³³

$$G'_0 = \frac{\rho(T)RT}{M_e} \quad (6.2)$$

From the range of frequencies accessible experimentally, it was not possible to determine the plateau modulus (Figure 6-13 and Figure 6-14). Hence, it was chosen to estimate this value from the measure of the modulus at the crossover point, G_C , using the Wu method.¹⁹¹ One must note that this method relies on the fact that the ratio of the plateau modulus by the crossover point modulus is relatively insensitive to the molecular weight distribution when the polydispersity is lower than about 3. Hence it should be reliable for PB (PDI=2.1) but is not applicable to the case of PBcis (PDI=4.4). According to Wu, the plateau modulus can be calculated as:

$$G'_0 = G_C \times 10^{\left[0.380 + \frac{2.63 \times \log(M_w/M_n)}{1 + 2.45 \times \log(M_w/M_n)}\right]} \quad (6.3)$$

The values of crossover modulus obtained for mixtures of squalane and PB from the data in Figure 6-13, calculated plateau modulus from equation (6.3) and molecular entanglements from equation (6.2) and using a density of 0.9 g.mol⁻¹ for simplicity are given in Table 6-4. It is clear

that the molecular weight in between entanglements is increased with increasing squalane content which is sign of a decreasing number of entanglements due to plasticisation.

Table 6-4: Crossover point modulus, plateau modulus and molecular entanglements calculated for various amounts of squalane in PB samples from the rheology data in Figure 6-13.

Sample sq content / % (w.w)	G_c / MPa	G'_0 / MPa calculated from (6.3)	M_e / g.mol ⁻¹ calculated from (6.2)
0	87900	627000	3550
30	53700	384000	5810
50	26400	188000	11800
60	17500	125000	17900
65	9960	71100	31400
70	6990	49900	44700
80	3160	22500	98900

6.2.2.1.2 Tack properties of oligomer/polymer blends

To determine which of the measured samples are “tacky”, one can compare the measured values of G' at 25 °C and 1 Hz with the Dahlquist criterion for tack: a material is “tacky” when its elastic modulus at 1 Hz and 25 °C is lower than 0.3 MPa.⁹³ Values reported in literature sometimes range from 0.1 to 0.3 MPa. It is suggested that in such conditions, the contact between the adhesive and a rough substrate be optimum. As the master curves constructions were found unreliable for some cases, the data used for this comparison is the average data measured on the linear viscoelastic range for a 0.01-10 % oscillation strain at 25 °C.

Table 6-5 gathers the values of G' at 25 °C and 1 Hz relative to the measurements of the sq/PB mixtures. One can affirm that the PB samples become “tacky” for contents of squalane of 50 % (w.w) and above. Equivalent data is shown for PBcis in Table 6-6. Samples are assessed as “tacky” according to the Dahlquist criterion for sq contents of 30 % (w.w) and above. In general, the PBcis samples have a lower plateau modulus than the PB ones, due to the structural difference between the host polymers.

As the presence of squalane (molecule of low T_g) has an effect on tackiness of the sample, it is tempting to relate the notion of tackiness for this non crosslinked polymer melt to viscoelastic properties, as suggested by De Gennes.¹⁹² He proposed that the ratio of the high frequency

modulus by the low frequency modulus scales with the overall adhesion energy. For non or loosely crosslinked networks, the modulus at low frequencies (relative to the network) is small while the high frequency modulus (relative to the chain entanglements) is high, hence the adhesion energy is rather big. Practically, this phenomenon is observed when one applies a certain pressure on the materials to bind (low frequency deformation): under pressure, the viscoelastic adhesive formulation flows and fits more closely the substrate roughness, maximising the contact area and therefore the adhesion energy, as discussed in 1.3.1. Such properties are advantageous for rapid adhesion processes on rough surfaces.

Table 6-5: Comparison of the sq/PB data with the Dahlquist criterion for tack.

Sample sq content / % (w.w)	Number of phases at 25 °C	G' at 1 Hz and 25 °C / MPa
0	1	0.4578 ± 0.0056 (2 × std)
30	1	0.1661 ± 0.0019
50	1	0.0575 ± 0.0008
60	1	0.0276 ± 0.0004
65	2	0.0127 ± 0.0002
70	2	0.0083 ± 0.0002
80	2	0.0060 ± 0.0002

Table 6-6: Comparison of the sq/PBcis data with the Dahlquist criterion for tack.

Sample sq content / % (w.w)	Number of phases at 25 °C	G' at 1 Hz and 25 °C / MPa
0	1	0.1803 ± 0.0027
30	1	0.0427 ± 0.0007
50	2	0.0151 ± 0.0002
70	2	0.0064 ± 0.0002

Considering an interface between an adhesive and a substrate, at which no covalent bond is formed, Kinloch *et al.* defined the adhesive failure energy as the product of the work of adhesion and the work of deformation of the adhesive.¹⁹³⁻¹⁹⁵ Similarly, Tse M.F. suggested that the tack (T) of a pressure sensitive adhesive at such an interface can be written as:

$$T = W_A BD \quad (6.4)$$

with W_A the work of adhesion, B a function characteristic of the bonding process and D the viscoelastic loss component characteristic of the debonding process, which is highly dependent on the separation speed (or characteristic debonding frequency) and temperature.¹⁰¹ As discussed in the *Literature Review*, the work of adhesion is dependent on the surface energies of the adhesive and substrate and on the interfacial tension between the two. If the adhesive fulfils the Dahlquist criterion – i.e. optimised contact between the adhesive and the surface –, then B should remain constant for a given adhesion test of defined contact time and pressure. The debonding function D increases with G'' and the dynamic mechanical loss tangent, $\tan(\delta)$. In other words, the tack property of an adhesive fulfilling the Dahlquist criterion is dissipation-limited. Although D is in general considered big in front of W_a , the work of adhesion can still exert a dominant influence upon joint strength, depending on the speed and temperature of deformation.^{193, 194} Also, the work of adhesion is reversible while the work of deformation is irreversible. Hence, to optimise adhesion, it is very important to evaluate the surface tension and dynamic mechanical properties of adhesive formulations.

The capillary number Ca , defined as:

$$Ca = \frac{\mu_L V}{\gamma_L} \quad (6.5)$$

where μ_L is the dynamic viscosity of the liquid, V is the interline velocity, and γ_L is the liquid surface tension, is generally used to compare the relative effect of viscous forces versus surface tension acting across an interface between a liquid and a solid.¹⁹⁶ A capillary number lower than 10^{-5} implies that the flow is dominated by capillary forces and surface tension. Considering the process conditions on production lines – i.e. very high application speed of the adhesive (few m/s) at a temperature of about 125 °C (surface tension lower than 40 mN.m⁻¹ and dynamic viscosity of the order of 1-100 Pa.s – the capillary numbers are relatively high which implies that the viscous forces are dominant, in this case of interest ($Ca > 10$).⁹⁷

As discussed in 1.3.2.1, increasing the tackifier content in industrial formulations enables the polymer's energy dissipation and the formation of fibrils. Indeed, energy dissipation is favoured by shifting $1/\tau_{max}$ to higher rates than encountered in applications and by increasing the T_g to broaden and shift to higher rates the peak in loss modulus G'' . However, as shown in 5.1.2.1, at higher oligomer contents, the sq/PB and sq/PBcis mixtures phase separate and the oligomer is segregated at the surface, forming a pure wetting layer of liquid squalane. Such a layer can be

seen as a contaminant, increasing the risk of interfacial failure, as it introduces an additional interface of poor work of adhesion – i.e. a weak boundary layer. Therefore, although the Dahlquist criterion introduces a measurable definition of tack, it is not a sufficient criterion to evaluate the adhesive performance of a formulation.

6.2.2.2 Validity of the TTS principle used to build the master curves

In order to validate the hypothesis that the automatic master curve construction failed at high concentrations of squalane, a closer look was given to the shift parameters along the horizontal and vertical axis (a_T and b_T respectively). The translation of the data on the vertical axis (modulus) is generally small ($b_T \sim 1$). Along the horizontal axis (frequency), however, the shift is usually more significant. As detailed in 2.10.2, the WLF equation (2.12) can be used to model the evolution of a_T with temperature. The TTS variables a_T and b_T used to build the master curves for PB mixtures at 25 °C, presented in Figure 6-13, are plotted as a function of temperature in Figure 6-18.

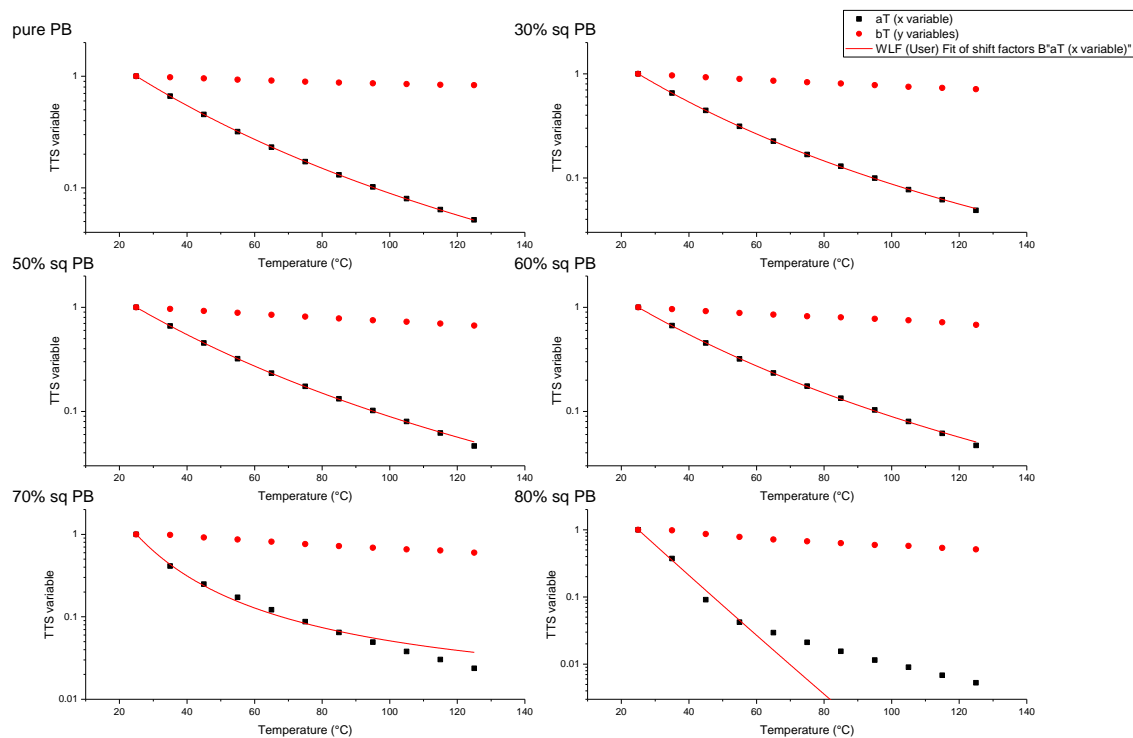


Figure 6-18: Evolution of the shift factors corresponding to the master curves in Figure 6-13.
Red dots: b_T , black dots: a_T , red solid line: fit to a_T using the WLF equation (2.12).

As expected, it is observed that the shift factor along the vertical axis b_T remains close to 1 in all cases. The WLF equation was used to fit the evolution of a_T with temperature. In general, this

equation is applicable for temperatures between T_g and $T_g + 100$ K. Nonetheless, the fits obtained in this case – i.e. for temperatures up to $T_g + 200$ K – are still reasonable enough for samples containing less than 70 % (w.w) of squalane. The fitting parameters A and B of the WLF equation, given in Table 6-7, agree with the non T -dependent suggested values from literature for monodisperse linear polybutadiene chains that are 4.17 and 196.8 K respectively.^{197, 198} For the higher squalane contents (70 and 80 % (w.w) samples) the fitting becomes more difficult to perform and the parameters diverge from the literature values. The approach particularly fails for the 80 % (w.w) sample, for which a large error is obtained on A and B. Correlating this result with the determined cloud point at 25 °C for this system, one can conclude that the TTS principle fails at these concentrations because of phase separation in the sample.

Table 6-7: Fitting parameters of the WLF equation.

Sample sq content / % (w.w)	A	B / K	Adjusted R ²
0	4.14 ± 0.10	221 ± 3	0.99999
30	3.93 ± 0.10	204 ± 3	0.99999
50	4.23 ± 0.22	227 ± 7	0.99996
60	4.30 ± 0.30	232 ± 9	0.99994
65	4.19 ± 0.22	206 ± 7	0.99996
70	2.12 ± 0.30	48 ± 5	0.99806
80	108.60 ± 10000	2386 ± 112781	0.997

Similarly the WLF equation was used to fit the evolution of a_T with temperature for the PBcis polymer matrix (Figure 6-19), corresponding to the master curves in Figure 6-14. The fitting parameters A and B of the WLF equation are given in Table 6-8.

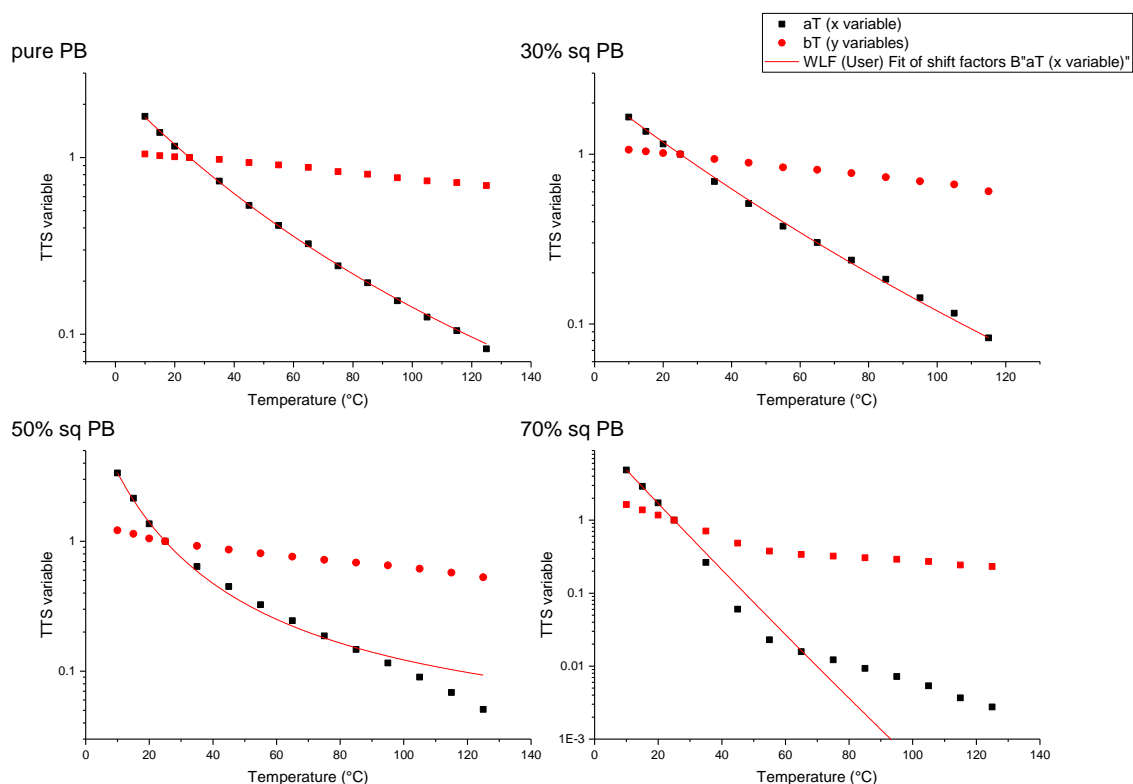


Figure 6-19: Evolution of the shift factors corresponding to the master curves in Figure 6-14. Red dots: b_T , black dots: a_T , red solid line: fit to a_T using the WLF equation (2.12).

Table 6-8: Fitting parameters of the WLF equation.

Sample sq content / % (w.w)	A	B / K	Adjusted R ²
0	3.98 ± 0.34	278 ± 24	0.99943
30	7.44 ± 2.16	530 ± 157	0.99849
50	1.68 ± 0.12	63 ± 4	0.99850
70	91.26 ± 5124	2002 ± 113000	0.99937

For the pure PBcis sample, the parameters agree (B being a bit high) with the suggested values from literature that are 4.17 and 196.8 K respectively.^{197, 198} In another source, A varies between 2.66 and 3.48 and B between 147 K and 168 K, depending on the ratio of cis and trans addition in the chain structure.¹⁹⁹ However, the fitting parameters obtained at higher sq concentrations diverge from the recommended values. Correlating this result with the determined cloud point at 25 °C for this system, one can conclude that the TTS principle fails for the 50 and 70 % (w.w) samples because of phase separation. The 30 % (w.w) sample is not expected to phase separate

in this range of temperature. The deviation from the recommended values is not dramatic in this case and the fit to the data still seems good enough. Hence, the problem for this sample might come from the sample quality itself (thickness inhomogeneity, slip etc).

One can note that this fitting technique agrees with the experimental phase diagrams and could also be used to determine compatibility. Although laborious, this method could be useful for materials which are crystalline or too opaque to measure compatibilities from the cloud point method and at temperatures that are relevant to the industrial application.

6.3 CONCLUSIONS ON ADHESION PROPERTIES

In this chapter, the effects of the oligomer vertical and lateral segregation on adhesion properties were explored. The surface and bulk mechanical properties of binary oligomer/polymer mixtures were investigated by AFM and oscillatory rheology. AFM scans of two systems were performed, for which the very diffuse concentration profiles obtained by ERDA, NRA and NR suggested some lateral inhomogeneity. The scans confirmed lateral phase segregation into a phase of low adhesion and a phase of high adhesion which is a sign of partial wetting. The conclusions from the previous chapters attribute the composition of the two phases to a polymer-rich phase and an oligomer-rich phase, respectively. It is proposed that the observed lateral inhomogeneity in these films come from the disparity in surface energies between the two components of the blend and/or to interfacial instability. From the observed effect of oligomer content on the size of the features and roughness of the surface, it is hypothesised that the lateral segregation at the surface is dominated by kinetic effects. Interestingly, a partial wetting is not suggested from the sharp concentration profiles recorded by NR for the higher molecular weight oligo-dIB and for squalane. Unfortunately it was not possible to use AFM to investigate the dsq/PB blends, because of the highly fluid nature of dsq, but the successful specular NR experiments presented in 5.1.2.1.2 suggest that there is little lateral variation in these samples.

The mechanical bulk properties of the polymer were found to be significantly affected by the presence of oligomer. The oligomer plasticises the chains – i.e. disrupts molecular entanglements – which decreases the elastic modulus at 25 °C and 1 Hz, and therefore increased the tack properties of the blend. As the polymer chains are less entangled, the reptation

relaxation time is also lowered. It is hence observed that the tack properties are linked to viscoelastic properties of the formulation, as suggested by De Gennes.¹⁹² The Dahlquist criterion, still widely used today in industry, is a good indicator for tack but is too simple to take into account all of the complex parameters affecting the tack properties of a formulation.

CONCLUSIONS OF THE THESIS

Hot-melt adhesive formulations are composed of two main ingredients: 40 % of the formulation is the backbone polymer (usually, SBC) and 60 % of the formulation are additives (plasticisers and tackifiers).^{94,88} The large molecular weight disparity between these two components has been postulated to promote surface partitioning of the additives, since positioning chain-ends at the surface decreases the system's conformational entropy. This phenomenon can have dramatic consequences on the adhesion properties. While a modest surface excess of oligomers could be desirable for optimising contact between the adhesive formulation and the substrate, a macroscopically thick oligomer-rich layer would drastically undermine the mechanical strength of bonding – i.e. weak boundary layer – unless it could be reabsorbed into the bulk.

Binary rubbery polymer/oligomer mixtures were selected to mimic these adhesive formulations. It was shown that such binary systems were good model formulations to reasonably mimic the behaviour of middle-block industrial tackifiers that are not compatible with the PS microphase-separated domains, such as Regalite. Several parameters impacting surface segregation and bulk compatibility were identified in the literature and varied in order to evaluate their effect on the depth concentration profiles of the oligomer in a polymer film – i.e. the molecular weight and concentration of the oligomer, the relative polarisabilities of the oligomer/polymer and temperature.

Following arguments from the Flory-Huggins theory, it was suggested that the compatibility of the mixture has very little or no dependency on the molecular weight of the polymer (N_B), because N_B is very large in comparison to the oligomer molecular weight (N_A) – i.e. $N_A/N_B < 10^{-4}$. Additionally, as also expected from the FH theory, DSC and phase diagrams showed that an increase in oligomer molecular weight and concentration yields a lower bulk compatibility. It is also clear that in the two-phase regime, the composition of the phases is generally a polymer-rich phase and an almost pure oligomer phase. Components showing similar polarisability properties, and hence, similar molecular structures, were found more compatible in the bulk. When studying the impact of temperature, it was evident that the mixtures of squalane with the

Conclusions of the thesis

two PBs were of the UCST type, implying that an elevation of temperature increases compatibility and that the FH interaction parameter can be written as $\chi = A + B/T$.

A strong correlation between bulk compatibility and concentration profiles was observed: the mixtures showing less bulk compatibility were found to also exhibit more oligomer surface partitioning. As hypothesised, for mixtures in the one-phase regime, a thin surface enrichment over a distance of a few nms was measured – i.e. order of magnitude of the oligomer molecule. By comparing surface segregation of deuterated squalane in PI and PB, it was shown that there is a critical surface energy difference at which, for a given oligomer molecular weight, surface segregation of the oligomer is exhibited. This surface energy effect was also correlated to differences in polarisability and hence, linked to bulk compatibility. Temperature reversible changes to the surface excess z^* were reported, which gave experimental evidence that the equilibrium state was reached for these compatible samples. For thin films in the two-phase regime, a phase of almost pure oligomer coexisted with a polymer-rich phase, similarly as in the bulk. In most cases, the films were stratified and the phase of lower surface energy was orientated to the surface. When the oligomer-rich phase was found at the surface, the thickness of the surface layer was up to tens of nms, which is well above the maximum length of one oligomer molecule and is sign of the formation of a wetting layer.

Yet, for these less compatible systems, unexpected behaviours were also remarked. In some systems, the thickness of this wetting layer was found to not scale with the total film thickness which contradicts the behaviour expected for total wetting. Hence it was suggested that a “frustrated” total wetting might occur, for which lenses of oligomer-rich phase coexist with the wetting layer. The explanation for these phenomena might be linked to a subtle competition between short-range repulsive and long-range attractive (van der Waals) intermolecular forces.¹⁶⁷ It was also shown that the thickness of the wetting layer was in some cases linked to the polymer molecular weight and that its length scale is of the same order of magnitude as the radius of gyration of the polymer matrix. Additionally, it was observed that the interface between the two phases became wider when the polymer molecular weight was increased. Moreover, it was shown by NR and complemented by AFM that extreme caution must be taken when modelling such two-phase systems as for some mixtures lateral features can form, and hence a 1-D description is not suitable. These features corresponded to a partial wetting of the phase-separated wetting layer onto the polymer-rich phase and appeared to be in a metastable

Conclusions of the thesis

state. Therefore, for these less compatible systems, the compatibility behaviour of the mixture has a much more significant impact on the film composition and surface structure than for compatible systems.

Finally, mechanical characterisation of the samples was performed by rheology. The plasticisation effect of the oligomer on the polymer was evident – i.e. disentanglement of the chains with increasing oligomer content, leading to a decrease of the relaxation time and of the modulus. It was also shown that the Dahlquist criterion, still very widely used in industry is not a sufficient tool to determine the tack performance of a sample. Other parameters must be taken into account such as bulk compatibility, capillary number and viscoelastic properties. For example, tack measurements on the model formulations did not yield conclusive results since the test response was too low, even though the Dahlquist criterion was met. Industrial adhesive experts generally evaluate adhesion performance by fracture characterisation and modelling at the macroscale. This thesis offers significant new insights for understanding adhesion at the nanoscale.

It is imperative for efforts to continue in the modelling aspects of the project in order to build a predictive tool for surface segregation. In the partner theory project, it was shown that applying the SCFT to such oligomer/polymer mixtures could provide insights into the key drivers of surface segregation (trade-offs, trends and orders of magnitude). However, the theory was only in partial agreement with the experimental conclusions in the one-phase regime and did not provide convincing results in the two-phase regime. The lack of descriptive power of the SCFT, especially upon phase separation, probably comes from the fact that it is based on the FH theory which was proven several times to be limited in the case of oligomer/polymer mixtures (see 1.1.2). With the SAFT approach, developed in another parallel project,²⁰ more conclusive results were obtained. It was possible to predict phase diagrams for the sq/PB and sq/PBcis systems that are in partial agreement with the experimental results. The phase diagrams were obtained from fitting Mie potentials parameters to experimental density data for the pure components of the mixture. Moreover, combining SAFT and molecular dynamics, concentration profiles were generated, that are qualitatively representative of the experimental results for sq/PB. More work is needed to establish the validity of SAFT/MD results against the range of materials reported here.

Conclusions of the thesis

To go even further on this thematic, it would be interesting to explore LCST binary blends – i.e. lowered compatibility with increasing temperature – to complete the range of compatibility behaviours observed and provide varied data for the model validation. It would also be important to study the impact of longer times on the lateral phase separation of the phase-separated mixtures and identify the real equilibrium state of such films. Then, the study of SBC-based formulations would be the natural progression. With such systems, it would be possible to study the migration of end-block industrial tackifiers, such as Picco. Mixtures of oligomers with SBC matrices might become difficult to characterise by NR since the glassy domains would be responsible for diffracting the neutron beam and very little reflected beam would be detected. However, SANS could enable the measurement of the size of these domains and therefore directly investigate the effect of the oligomer on the nanostructure of the host polymer. The same principle could be applied to adhesive formulations based on crystalline matrices. Changing the polymer matrix to a more industrially relevant backbone would surely increase the systems' response in terms of tack properties and therefore permit drawing more conclusions on the effect of additives segregation on adhesion properties. Surface segregation of mixtures exhibiting various ranges of surface energies could also be studied, in order to explore the fine balance between surface energy difference and molecular weight ratio in surface segregating systems. This could be achieved by examining the behaviour of various polar oligomers or surfactants of defined structure and hydrophilic-lipophilic balance (HLB) in a reference polymer matrix. At the time of writing, new projects in the field of molecular migration with Durham, Birmingham and Sheffield Universities have been funded by the EPSRC (EP/P007864/1). These suggestions could serve as a foundation for these research projects.

Through this thesis, knowledge on various analytical capabilities was transferred to P&G. These tools have enormous potential for adhesive development and aging characterisation. The results presented here can guide adhesive formulators to effectively and predictively screen adhesive candidates in hygiene products. This work also has potential in other fields, since polymer formulation often implies the mixture of high and low molecular weight components. Controlling the surface segregation of the low molecular weight components could become a tool for time-dependent surface functionalisation of materials which might find applications in drug delivery, tailored surface wettability, antifouling or photonics.

REFERENCES

1. H. Mayama, *Soft Matter*, 2009, **5**, 856-859.
2. K. H. Meyer, *Helvetica Chimica Acta*, 1940, **23**, 1063-1070.
3. M. L. Huggins, *The Journal of Chemical Physics*, 1941, **9**, 440-440.
4. M. L. Huggins, *J Am Chem Soc*, 1942, **64**, 1712-1719.
5. P. J. Flory, *Principles of polymer chemistry*, Cornell University Press, 1953.
6. P. J. Flory, *The Journal of Chemical Physics*, 1942, **10**, 51-61.
7. L. M. Robeson, *Polymer blends: a comprehensive review*, Hanser, 2007.
8. N. P. Balsara, *Physical properties of polymers Handbook*, Springer, New York, second edn., 2007.
9. J. S. Higgins, J. E. G. Lipson and R. P. White, *Philos. Trans. R. Soc. A-Math. Phys. Eng. Sci.*, 2010, **368**, 1009-1025.
10. R. A. L. Jones and R. W. Richards, *Polymers at surfaces and interfaces*, Cambridge University Press, 1999.
11. R. F. Blanks and J. M. Prausnitz, *Industrial & Engineering Chemistry Fundamentals*, 1964, **3**, 1-8.
12. K. H. Dai and E. J. Kramer, *Polymer*, 1994, **35**, 157-161.
13. T. P. Russell, R. P. Hjelm Jr and P. A. Seeger, *Macromolecules*, 1990, **23**, 890-893.
14. P. A. Small, *Journal of Applied Chemistry*, 1953, **3**, 71-80.
15. J. C. Arnold, *Eur Polym J*, 2010, **46**, 1131-1140.
16. R. P. Danner and M. S. High, *Handbook of polymer solution thermodynamics*, Wiley, 2010.
17. J. Brandrup, E. H. Immergut and E. A. Grulke, *Polymer Handbook*, Wiley, 1999.
18. P. G. De Gennes, *Scaling Concepts in Polymer Physics*, Cornell University Press, 1979.
19. A. J. Nedoma, M. L. Robertson, N. S. Wanakule and N. P. Balsara, *Macromolecules*, 2008, **41**, 5773-5779.
20. J. Tasche, PhD thesis (to be published), Durham University, 2017.
21. M. Shibayama, H. J. Yang, R. S. Stein and C. C. Han, *Macromolecules*, 1985, **18**, 2179-2187.
22. J. Dudowicz, M. S. Freed and K. F. Freed, *Macromolecules*, 1991, **24**, 5096-5111.
23. J. D. Londono, A. H. Narten, G. D. Wignall, K. G. Honnell, E. T. Hsieh, T. W. Johnson and F. S. Bates, *Macromolecules*, 1994, **27**, 2864-2871.

References

24. V. S. Minnikanti and L. A. Archer, *Macromolecules*, 2006, **39**, 7718-7728.
25. M. Fujita, M. Kajiyama, A. Takemura, H. Ono, H. Mizumachi and S. Hayashi, *J Appl Polym Sci*, 1997, **64**, 2191-2197.
26. M. Fujita, M. Kajiyama, A. Takemura, H. Ono, H. Mizumachi and S. Hayashi, *J Appl Polym Sci*, 1998, **67**, 221-229.
27. P. G. De Gennes, *Phys Lett A*, 1972, **A 38**, 339-&.
28. I. Teraoka, *Polymer Solutions: An Introduction to Physical Properties*, John Wiley & Sons, 2002.
29. G. Fleer, M. A. C. Stuart, J. M. H. M. Scheutjens, T. Cosgrove and B. Vincent, *Polymers at interfaces*, Springer Netherlands, 1993.
30. T. Kawakatsu, *Statistical physics of polymers: an introduction*, Springer Berlin Heidelberg, 2013.
31. R. A. L. Jones, *Soft condensed matter*, OUP Oxford, 2002.
32. R. Kirchheim, *Macromolecules*, 1992, **25**, 6952-6960.
33. I. C. Sanchez and R. H. Lacombe, *Macromolecules*, 1978, **11**, 1145-1156.
34. J. E. G. Lipson, J. E. Guillet and S. G. Whittington, *Macromolecules*, 1985, **18**, 573-579.
35. J. E. G. Lipson, *Macromolecules*, 1991, **24**, 1334-1340.
36. M. Tambasco, J. E. G. Lipson and J. S. Higgins, *Macromolecules*, 2006, **39**, 4860-4868.
37. J. Baschnagel and K. Binder, *Macromolecules*, 1995, **28**, 6808-6818.
38. J. Kraus, P. Müller-Buschbaum, T. Kuhlmann, D. W. Schubert and M. Stamm, *EPL (Europhysics Letters)*, 2000, **49**, 210.
39. P. G. De Gennes, in *Simple Views on Condensed Matter*, 1988, DOI: doi:10.1142/9789812564849_0043, pp. 405-409.
40. A. Silberberg, *J Colloid Interf Sci*, 1982, **90**, 86-91.
41. I. Bitsanis and G. Hadziioannou, *J Chem Phys*, 1990, **92**, 3827-3847.
42. M. Muller and L. G. MacDowell, *Macromolecules*, 2000, **33**, 3902-3923.
43. W. Zhao, X. Zhao, M. H. Rafailovich, J. Sokolov, R. J. Composto, S. D. Smith, M. Satkowski, T. P. Russell, W. D. Dozier and T. Mansfield, *Macromolecules*, 1993, **26**, 561-562.
44. I. Mitra, X. Y. Lo, S. L. Pesek, B. Makarenko, B. S. Lokitz, D. Uhrig, J. F. Ankner, R. Verduzco and G. E. Stein, *Macromolecules*, 2014, **47**, 5269-5276.
45. S. L. Pesek, Y. H. Lin, H. Z. Mah, W. Kasper, B. Chen, B. J. Rohde, M. L. Robertson, G. E. Stein and R. Verduzco, *Polymer*, 2016, **98**, 495-504.
46. M. P. Weir, D. W. Johnson, S. C. Boothroyd, R. C. Savage, R. L. Thompson, S. R. Parnell, A. J. Parnell, S. M. King, S. E. Rogers, K. S. Coleman and N. Clarke, *Chem Mater*, 2016, **28**, 1698-1704.
47. S. Misra, P. I. D. Fleming and W. L. Mattice, *Journal of Computer-Aided Materials Design*, 1995, **2**, 101-112.

References

48. R. A. L. Jones, L. J. Norton, E. J. Kramer, R. J. Composto, R. S. Stein, T. P. Russell, A. Mansour, A. Karim, G. P. Felcher, M. H. Rafailovich, J. Sokolov, X. Zhao and S. A. Schwarz, *Europhys Lett*, 1990, **12**, 41-46.
49. X. Zhao, W. Zhao, J. Sokolov, M. H. Rafailovich, S. A. Schwarz, B. J. Wilkens, R. A. L. Jones and E. J. Kramer, *Macromolecules*, 1991, **24**, 5991-5996.
50. A. D. Buckingham and H. G. E. Hentschel, *J Polym Sci Pol Phys*, 1980, **18**, 853-861.
51. F. S. Bates, G. D. Wignall and W. C. Koehler, *Phys Rev Lett*, 1985, **55**, 2425-2428.
52. W. W. Graessley, R. Krishnamoorti, N. P. Balsara, L. J. Fetters, D. J. Lohse, D. N. Schulz and J. A. Sissano, *Macromolecules*, 1993, **26**, 1137-1143.
53. A. Hariharan, S. K. Kumar and T. P. Russell, *The Journal of Chemical Physics*, 1993, **98**, 4163-4173.
54. A. Hariharan, S. K. Kumar and T. P. Russell, *Macromolecules*, 1991, **24**, 4909-4917.
55. J. M. H. M. Scheutjens and G. J. Fleer, *The Journal of Physical Chemistry*, 1979, **83**, 1619-1635.
56. I. G. Kokkinos and M. K. Kosmas, *Macromolecules*, 1997, **30**, 577-583.
57. G. Krausch, C. A. Dai, E. J. Kramer, J. F. Marko and F. S. Bates, *Macromolecules*, 1993, **26**, 5566-5571.
58. A. Hariharan, S. K. Kumar and T. P. Russell, *Macromolecules*, 1990, **23**, 3584-3592.
59. L. J. Norton, E. J. Kramer, F. S. Bates, M. D. Gehlsen, R. A. L. Jones, A. Karim, G. P. Felcher and R. Kleb, *Macromolecules*, 1995, **28**, 8621-8628.
60. D. G. Walton and A. M. Mayes, *Phys Rev E*, 1996, **54**, 2811-2815.
61. V. S. Minnikanti and L. A. Archer, *J Chem Phys*, 2005, **123**, 9.
62. R. A. L. Jones, E. J. Kramer, M. H. Rafailovich, J. Sokolov and S. A. Schwarz, *Phys Rev Lett*, 1989, **62**, 280-283.
63. H. Wang, J. F. Douglas, S. K. Satija, R. J. Composto and C. C. Han, *Phys Rev E*, 2003, **67**, 061801.
64. S. Dietrich, *Phase transitions and critical phenomena*, Academic Press, 1988.
65. D. Bonn and D. Ross, *Rep Prog Phys*, 2001, **64**, 1085.
66. J. W. Cahn, *The Journal of Chemical Physics*, 1977, **66**, 3667-3672.
67. I. Schmidt and K. Binder, *Journal De Physique*, 1985, **46**, 1631-1644.
68. H. Wang and R. J. Composto, *The Journal of Chemical Physics*, 2000, **113**, 10386-10397.
69. D. G. Bucknall, J. S. Higgins and S. A. Butler, *Chem Eng Sci*, 2001, **56**, 5473-5483.
70. I. Quijada-Garrido, J. M. Barrales-Rienda and G. Frutos, *Macromolecules*, 1996, **29**, 7164-7176.
71. D. G. Bucknall, J. S. Higgins and S. A. Butler, *J Polym Sci Pol Phys*, 2004, **42**, 3267-3281.
72. D. G. Bucknall, S. A. Butler and J. S. Higgins, *Macromolecules*, 1999, **32**, 5453-5456.

References

73. J. S. Higgins, S. A. Butler and D. G. Bucknall, *Macromol. Symp.*, 2002, **190**, 1-8.
74. R. L. Thompson, S. J. Hardman, L. R. Hutchings, A. P. Narrainen and R. M. Dalgliesh, *Langmuir*, 2009, **25**, 3184-3188.
75. I. Quijada-Garrido, J. M. Barrales-Rienda, J. M. Perena and G. Frutos, *Polymer*, 1997, **38**, 5125-5135.
76. F. Awaja, M. Gilbert, G. Kelly, B. Fox and P. J. Pigram, *Prog Polym Sci*, 2009, **34**, 948-968.
77. K. W. Allen, *The Journal of Adhesion*, 1987, **21**, 261-277.
78. A. J. Kinloch, *J Mater Sci*, 1980, **15**, 2141-2166.
79. J. R. Huntsberger, *J Adhesion*, 1976, **7**, 289-299.
80. J. R. Huntsberger, *Journal of Polymer Science*, 1960, **43**, 581-582.
81. F. S. P. K. J. Hejda, *WDS'10 Proceedings of contributing papers*, 2010, **III**, 25-30.
82. W. A. Zisman, *Ind. Eng. Chem.*, 1963, **55**, 19-+.
83. Y. Kitazaki and T. Hata, *Abstr Pap Am Chem S*, 1971, 4-&.
84. D. K. Owens and R. C. Wendt, *J Appl Polym Sci*, 1969, **13**, 1741-&.
85. R. H. Young and J. M. Tancrede, *Adhesives in manufacturing*, Taylor & Francis, 1983.
86. D. Y. Kwok and A. W. Neumann, *Adv Colloid Interfac*, 1999, **81**, 167-249.
87. D. Y. Kwok and A. W. Neumann, *J Phys Chem B*, 2000, **104**, 741-746.
88. L. F. M. da Silva, A. Öchsner and R. D. Adams, *Handbook of adhesion technology*, Springer, Berlin, 2011.
89. B. V. Derjaguin and I. I. Abrikosova, *Zh Fiz Khim+*, 1958, **32**, 442-453.
90. S. S. Voyutskii and S. S. Voiutskii, *Autohesion and adhesion of high polymers*, Interscience Publishers, New York, 1963.
91. C. Creton, *MRS Bull.*, 2003, **28**, 434-439.
92. L. Leger and C. Creton, *Philos. Trans. R. Soc. A-Math. Phys. Eng. Sci.*, 2008, **366**, 1425-1442.
93. C. A. Dahlquist, *Adhesives Age*, 1959, **2**, 25-29.
94. I. Benedek and M. M. Feldstein, *Handbook of pressure-sensitive adhesives and products: - three volume set*, Taylor & Francis, 2008.
95. C. Creton, E. Papon and M. R. Society, *Materials science of adhesives: how to bond things together*, 2003.
96. D. A. Dillard, *The mechanics of adhesion*, Elsevier, 2002.
97. C. Galán, C. A. Sierra, J. M. G. Fatou and J. A. Delgado, *J Appl Polym Sci*, 1996, **62**, 1263-1275.
98. W. Li, L. Bouzidi and S. S. Narine, *Ind Eng Chem Res*, 2008, **47**, 7524-7532.
99. G. W. Crum, E. T. Nord, A. B. Reighard and S. Z. Tamny, *Journal*, 1976.

References

100. M. Sasaki, K. Fujita, M. Adachi, S. Fujii, Y. Nakamura and Y. Urahama, *Int J Adhes Adhes*, 2008, **28**, 372-381.
101. M. F. Tse, *J Adhes Sci Technol*, 1989, **3**, 551-570.
102. M. Fujita, A. Takemura, H. Ono, M. Kajiyama, S. Hayashi and H. Mizumachi, *J Appl Polym Sci*, 2000, **75**, 1535-1545.
103. M. Fujita, M. Kajiyama, A. Takemura, H. Ono, H. Mizumachi and S. Hayashi, *J Appl Polym Sci*, 1998, **70**, 771-776.
104. M. Fujita, M. Kajiyama, A. Takemura, H. Ono, H. Mizumachi and S. Hayashi, *J Appl Polym Sci*, 1998, **70**, 777-784.
105. H. J. Kim and H. Mizumachi, *J Adhesion*, 1995, **49**, 113-132.
106. B. M. Z. Newby, M. K. Chaudhury and H. R. Brown, *Science*, 1995, **269**, 1407-1409.
107. J. J. Bikerman, *J Adhesion*, 1972, **3**, 333-&.
108. G. S. Smith, C. B. Skidmore, P. M. Howe and J. Majewski, *J Polym Sci Pol Phys*, 2004, **42**, 3258-3266.
109. D. J. Worsfold and S. Bywater, *Can. J. Chem.-Rev. Can. Chim.*, 1964, **42**, 2884-2892.
110. V. Galiatsatos, R. O. Neaffer, S. Sen and B. J. Sherman, ed. J. E. Mark, American Institute of Physics, Woodbury, New York, 1996, ch. 39, pp. 535-543.
111. N. Tripathi, *Int J Thermophys*, 2005, **26**, 693-703.
112. E. Díaz, A. Cazurro, S. Ordóñez, A. Vega and J. Coca, *Brazilian Journal of Chemical Engineering*, 2007, **24**, 293-306.
113. G. Ström, M. Fredriksson and P. Stenius, *J Colloid Interf Sci*, 1987, **119**, 352-361.
114. H. J. Busscher, A. W. J. van Pelt, P. de Boer, H. P. de Jong and J. Arends, *Colloid Surface*, 1984, **9**, 319-331.
115. C. Jie-Rong and T. Wakida, *J Appl Polym Sci*, 1997, **63**, 1733-1739.
116. R. J. Composto, R. M. Walters and J. Genzer, *Materials Science and Engineering: R: Reports*, 2002, **38**, 107-180.
117. R. L. Thompson, in *Polymer Science: A Comprehensive Reference*, ed. K. M. Möller, Elsevier, Amsterdam, 2012, DOI: 10.1016/B978-0-444-53349-4.00051-0, pp. 661-681.
118. C. Jeynes, N. P. Barradas and E. Szilágyi, *Anal Chem*, 2012, **84**, 6061-6069.
119. C. Jeynes, M. J. Bailey, N. J. Bright, M. E. Christopher, G. W. Grime, B. N. Jones, V. V. Palitsin and R. P. Webb, *Nucl Instrum Meth B*, 2012, **271**, 107-118.
120. N. P. Barradas and C. Jeynes, *Nucl Instrum Meth B*, 2008, **266**, 1875-1879.
121. C. D. James, C. Jeynes, N. P. Barradas, L. Clifton, R. M. Dalglish, R. F. Smith, S. W. Sankey, L. R. Hutchings and R. L. Thompson, *Reactive and Functional Polymers*, 2015, **89**, 40-48.
122. C. Jeynes, N. P. Barradas, P. K. Marriott, G. Boudreault, M. Jenkin, E. Wendler and R. P. Webb, *J Phys D Appl Phys*, 2003, **36**, R97-R126.
123. F. Cousin and A. Menelle, *EPJ Web of Conferences*, 2015, **104**, 01005.

References

124. J. Penfold and R. K. Thomas, *Journal of Physics: Condensed Matter*, 1990, **2**, 1369.
125. V. F. Sears, *Neutron News*, 1992, **3**, 26-37.
126. S. J. Hardman, L. R. Hutchings, N. Clarke, S. M. Kimani, L. L. E. Mears, E. F. Smith, J. R. P. Webster and R. L. Thompson, *Langmuir*, 2012, **28**, 5125-5137.
127. O. Arnold, J. C. Bilheux, J. M. Borreguero, A. Buts, S. I. Campbell, L. Chapon, M. Doucet, N. Draper, R. Ferraz Leal, M. A. Gigg, V. E. Lynch, A. Markvardsen, D. J. Mikkelson, R. L. Mikkelson, R. Miller, K. Palmen, P. Parker, G. Passos, T. G. Perring, P. F. Peterson, S. Ren, M. A. Reuter, A. T. Savici, J. W. Taylor, R. J. Taylor, R. Tolchenov, W. Zhou and J. Zikovskiy, *Nuclear Instruments and Methods in Physics Research Section A: Accelerators, Spectrometers, Detectors and Associated Equipment*, 2014, **764**, 156-166.
128. S. Campbell, F. Akeroyd and C. Moreton-Smith, *arXiv preprint cond-mat/0210442*, 2002.
129. A. Nelson, *J Appl Crystallogr*, 2006, **39**, 273-276.
130. D. G. Bucknall, S. A. Butler and J. S. Higgins, in *Scattering from Polymers*, 2000, vol. 739, pp. 57-73.
131. A. Briddick, P. Li, A. Hughes, F. Courchay, A. Martinez and R. L. Thompson, *Langmuir*, 2016, **32**, 864-872.
132. G. Lomboy, S. Sundararajan, K. Wang and S. Subramaniam, *Cement Concrete Res*, 2011, **41**, 1157-1166.
133. G. Couarraze and J.-L. Grossiord, *Initiation à la rhéologie*, Technique et documentation Lavoisier, Paris, 2001.
134. I. Prigogine, A. Bellemans and C. Naar-Colin, *The Journal of Chemical Physics*, 1957, **26**, 710-710.
135. ASTM International, *ASTM D6195-03: Standard test methods for loop tack*, 2011.
136. I. Benedek and M. M. Feldstein, *Technology of pressure-sensitive adhesives and products*, CRC Press, 2008.
137. J. E. Mark, *Physical properties of polymers Handbook*, Springer New York, 2007.
138. W. Patnode and W. J. Scheiber, *J Am Chem Soc*, 1939, **61**, 3449-3451.
139. O. Fandiño, A. S. Pensado, L. Lugo, M. J. P. Comuñas and J. Fernández, *Journal of Chemical & Engineering Data*, 2005, **50**, 939-946.
140. Eastman Chemical, *Technical data sheet: Regalite S1100 hydrocarbon resin*, 2012.
141. Eastman Chemical, *Technical data sheet: Picco 6100 hydrocarbon resin*, 2006.
142. E. F. D. Sabattie, J. Tasche, M. R. Wilson, M. W. A. Skoda, A. Hughes, T. Lindner and R. L. Thompson, *Soft Matter*, 2017, **13**, 3580-3591.
143. T. G. Fox, *Bull Am Phys Soc*, 1956, **1**, 123-135.
144. H. A. Schneider and E. A. Di Marzio, *Polymer*, 1992, **33**, 3453-3461.
145. W. Brostow, R. Chiu, I. M. Kalogeras and A. Vassilikou-Dova, *Mater Lett*, 2008, **62**, 3152-3155.

References

146. T. Hecksher, N. B. Olsen and J. C. Dyre, *The Journal of Chemical Physics*, 2017, **146**, 154504.
147. C. D. James, *Preliminary poof-of-concept project*, Durham University, 2014.
148. R. J. Davey, *L4 M. Sci. Research Project*, Durham University, 2014.
149. G. Wypych, *Handbook of plasticizers*, Elsevier Science, 2017.
150. A. K. Doolittle and R. H. Peterson, *J Am Chem Soc*, 1951, **73**, 2145-2151.
151. Y. Du, Y. Xue and H. L. Frisch, ed. J. E. Mark, American Institute of Physics, Woodbury, New York, 1996, ch. 16, pp. 227-239.
152. C. M. Hansen, *Hansen Solubility Parameters: A User's Handbook, Second Edition*, CRC Press, 2007.
153. J. Krawczyk, S. Croce, T. C. B. McLeish and B. Chakrabarti, *Phys Rev Lett*, 2016, **116**.
154. P. A. V. O'Rourke-Muisener, C. A. Jalbert, C. G. Yuan, J. Baetzold, R. Mason, D. Wong, Y. J. Kim and J. T. Koberstein, *Macromolecules*, 2003, **36**, 2956-2966.
155. L. R. Hutchings, C. J. R. Douglas, C. L. Rhodes, W. D. Carswell, M. W. A. Skoda, J. R. P. Webster and R. L. Thompson, *Langmuir*, 2010, **26**, 15486-15493.
156. Z. Qian, V. S. Minnikanti, B. B. Sauer, G. T. Dee, W. G. Kampert and L. A. Archer, *Journal of Polymer Science Part B: Polymer Physics*, 2009, **47**, 1666-1685.
157. F. L. Riddle and F. M. Fowkes, *J Am Chem Soc*, 1990, **112**, 3259-3264.
158. F. M. Fowkes, F. L. Riddle, W. E. Pastore and A. A. Weber, *Colloid Surface*, 1990, **43**, 367-387.
159. V. Ludviksson and E. N. Lightfoot, *Aiche J*, 1971, **17**, 1166-1173.
160. T. Symes and D. Oldfield, *Treatise on adhesion and adhesives.*, Taylor & Francis, 1991.
161. R. W. Taft, *Progress in physical organic chemistry*, Wiley, 2009.
162. C. R. Brundle, C. A. Evans and S. Wilson, *Encyclopedia of materials characterization: surfaces, interfaces, thin films*, Butterworth-Heinemann, 1992.
163. R. S. Payne, A. S. Clough, P. Murphy and P. J. Mills, *Nucl Instrum Meth B*, 1989, **42**, 130-134.
164. J. W. Gibbs, *The scientific papers of J. Willard Gibbs.*, Dover Publications, New York, 1906.
165. R. A. L. Jones, L. J. Norton, E. J. Kramer, F. S. Bates and P. Wiltzius, *Phys Rev Lett*, 1991, **66**, 1326-1329.
166. F. Leal-Calderon, J. Bibette and V. Schmitt, in *Emulsion Science: Basic Principles*, Springer New York, New York, NY, 2007, DOI: 10.1007/978-0-387-39683-5_6, pp. 143-172.
167. E. Bertrand, D. Bonn, D. Broseta, H. Dobbs, J. Indekeu, J. Meunier, K. Ragil and N. Shahidzadeh, *J Petrol Sci Eng*, 2002, **33**, 217-222.
168. M. Sferrazza, C. Xiao, R. A. L. Jones, D. G. Bucknall, J. Webster and J. Penfold, *Phys Rev Lett*, 1997, **78**, 3693-3696.
169. T. Kerle, J. Klein and K. Binder, *Phys Rev Lett*, 1996, **77**, 1318-1321.

References

170. M. Rubinstein and R. H. Colby, *Polymer physics*, OUP Oxford, 2003.
171. M. Doi and S. F. Edwards, *The theory of polymer dynamics*, Clarendon Press, 1988.
172. S. M. Aharoni, *Macromolecules*, 1983, **16**, 1722-1728.
173. L. J. Fetters, N. Hadjichristidis, J. S. Lindner and J. W. Mays, *Journal of Physical and Chemical Reference Data*, 1994, **23**, 619-640.
174. E. Helfand and Y. Tagami, *Journal of Polymer Science Part B-Polymer Letters*, 1971, **9**, 741-&.
175. M. Sferrazza, C. Xiao, D. G. Bucknall and R. A. L. Jones, *J Phys-Condens Mat*, 2001, **13**, 10269-10277.
176. D. Broseta, G. H. Fredrickson, E. Helfand and L. Leibler, *Macromolecules*, 1990, **23**, 132-139.
177. D. Kawaguchi, M. Ohya, N. Torikai, A. Takano and Y. Matsushita, *Polym. J*, 2007, **39**, 1274-1280.
178. P. G. De Gennes, *The Journal of Chemical Physics*, 1971, **55**, 572-579.
179. S. Wu, *Polymer interface and adhesion*, Marcel Dekker, New York; Basel, 1982.
180. P. Mokarian-Tabari, M. Geoghegan, J. R. Howse, S. Y. Heriot, R. L. Thompson and R. A. L. Jones, *Eur Phys J E*, 2010, **33**, 283-289.
181. S. Y. Heriot and R. A. L. Jones, *Nat Mater*, 2005, **4**, 782-786.
182. H. Kahl, T. Wadewitz and J. Winkelmann, *Journal of Chemical & Engineering Data*, 2003, **48**, 580-586.
183. R. Seemann, S. Herminghaus and K. Jacobs, *Journal of Physics: Condensed Matter*, 2001, **13**, 4925.
184. D. G. Bucknall, *Prog Mater Sci*, 2004, **49**, 713-786.
185. J. N. Israelachvili, in *Intermolecular and Surface Forces (Third Edition)*, Academic Press, Boston, 2011, DOI: <https://doi.org/10.1016/B978-0-12-391927-4.10002-7>, pp. 23-51.
186. J. Vial and A. Carré, *Int J Adhes Adhes*, 1991, **11**, 140-143.
187. P. H. M. Elemans, J. M. H. Janssen and H. E. H. Meijer, *J Rheol*, 1990, **34**, 1311-1325.
188. S. Enders and B. A. Wolf, *Polymer Thermodynamics: Liquid Polymer-Containing Mixtures*, Springer Berlin Heidelberg, 2011.
189. J. Garcia-Ojalvo, A. M. Lacasta, J. M. Sancho and R. Toral, *Europhys Lett*, 1998, **42**, 125-130.
190. A. Zosel, *Colloid Polym Sci*, 1985, **263**, 541-553.
191. S. Wu, *Journal of Polymer Science Part B: Polymer Physics*, 1989, **27**, 723-741.
192. P. G. De Gennes, *Langmuir*, 1996, **12**, 4497-4500.
193. A. N. Gent and A. J. Kinloch, *Journal of Polymer Science Part a-2-Polymer Physics*, 1971, **9**, 659-&.
194. E. H. Andrews and A. J. Kinloch, *Proc. R. Soc. Lond. A-Math. Phys. Sci.*, 1973, **332**, 401-+.

References

195. E. H. Andrews and A. J. Kinloch, *Proc. R. Soc. Lond. A-Math. Phys. Sci.*, 1973, **332**, 385-399.
196. J. E. Seebergh and J. C. Berg, *Chem Eng Sci*, 1992, **47**, 4455-4464.
197. M. Baumgaertel, M. E. Derosa, J. Machado, M. Masse and H. H. Winter, *Rheol Acta*, 1992, **31**, 75-82.
198. J. K. Jackson, M. E. Derosa and H. H. Winter, *Macromolecules*, 1994, **27**, 2426-2431.
199. R. H. Colby, L. J. Fetters and W. W. Graessley, *Macromolecules*, 1987, **20**, 2226-2237.

ANNEX 1: FITTING ERROR ANALYSIS

FITTING ERROR WITH ERDA

In this section the calculation of the error on the ERDA fits is detailed, using as an example the 30 % (w.w) dsq/PB sample. A fitting of the ERDA data using DataFurnace¹²² was performed using the Bayesian inference output, which calculates the standard deviation on the resulting concentration profile. The outcome of the fitting procedure is presented in Figure A1-1 with the red area representing the 95 % confidence interval around the determined concentration profile.

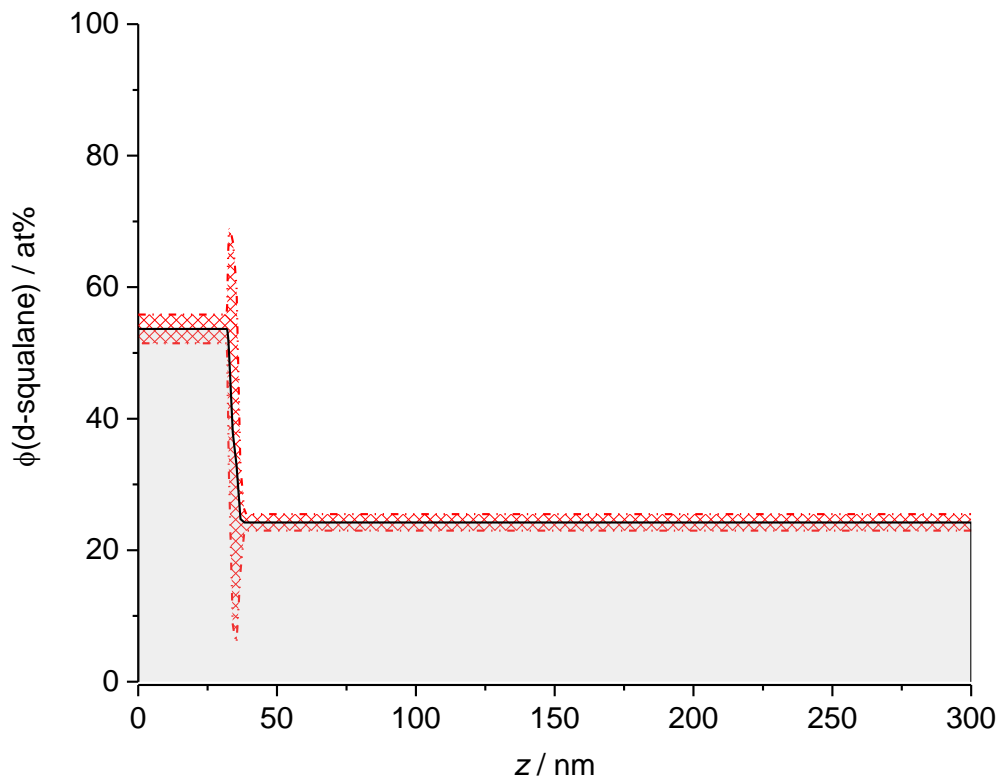


Figure A1-1: Result of the error analysis on the concentration profile of a 30 % (w.w) dsq in PB sample. The ERDA data was fitted using the software DataFurnace. The concentration profile is represented by a black solid line while the red area represents the 95 % confidence interval (twice the standard deviation on each side).

From this type of analysis, one can therefore calculate an error on the surface excess z^* . Since with ERDA one cannot easily make the difference between a thin, highly concentrated layer and

a thicker, less concentrated layer, the relative error on the surface excess was calculated by adding in Gaussian quadrature the relative errors on the surface concentration (4 %), bulk concentration (5 %) and excess layer width (9 %). For this particular sample, the calculation results in a relative error of 11 %. For obtaining the error on the total oligomer concentration φ_{tot} , one would need to add the contribution of the error on the total film thickness, which is unfortunately not an output of the fit. Considering that the order of magnitude of this error should be the same as what is obtained for the error on the thickness of the first layer, one can similarly obtain a relative error of about 14% on φ_{tot} . These relative errors are used in the thesis as an example of fitting errors for the determination of z^* and φ_{tot} by ERDA.

FITTING ERROR WITH NR

In this section is presented the outcome of the Monte Carlo (MC) analysis, performed with the Motofit package and the software IGOR pro,¹²⁹ that enabled the determination of the error bars on the fitted parameters in *Chapter 5*. As an example, the sample containing 40 % (w.w) dsq in the PB matrix is presented.

The s.l.d. and roughness of the fronting, 3rd and backing layer (corresponding to the air, silicon oxide and Silicon layer) as well as the thickness of the silicon oxide layer were fixed to reasonable values and the Genetic fitting was iterated several times to obtain the most accurate values possible for the other parameters. The parameters obtained from the Genetic fit and given in *Annex 3* are the following:

Table A1-1: Fitting parameters related to the initial fit of the 40 % (w.w) dsq/PB sample.

Layer	Thickness / Å	SLD / 10^{-6} Å ⁻²	Roughness / Å
fronting	INF	0	
1	22.011	6.7471	5
2	975.98	2.6576	22.742
3	20	3.45	5
backing	INF	2.07	5

The Genetic + MC Analysis was then performed on the 5 remaining parameters (thickness and s.l.d. of layers 1 and 2 and the roughness between these layers) using 200 iterations. The lower and upper limits were fixed in order to control the extent of the fitting effort. It was observed

Annex 1: Fitting error analysis

that if the limits are too wide, the quality of the fit to the data worsens. The obtained fitting parameters are shown in Table A1-2.

One can note from Table A1-2 that the thickness and s.l.d. of the first layer are very well determined from the Genetic + MC analysis fitting, with an error on the thickness of the order of the measurement's resolution (0.5 nm). The error on the thickness of the 2nd layer is of 4 nm which can be explained by the roughness of the substrate and/or film's surface. The roughness between the two layers is also determined with an accuracy inferior to 1 nm. It seems that the s.l.d. of the second layer (and hence its concentration), named MC_11 in the inset of Figure A1-2 is not very well defined and is actually ranging indifferently from the upper limit to the lower limit used for the fit.

Table A1-2: Results of Monte Carlo fitting of the 40 % (w.w) dsq/PB sample, using a first Genetic fit as a starting point.

	Parameter name	Initial Genetic fitted value	Lower limit	Upper limit	Genetic + MC fitted value	Error on fitted value
Thickness layer 1 / Å	MC_6	22.01	10	40	22.39	± 5.80
s.l.d. layer 1 / 10^{-6}Å^{-2}	MC_7	6.75	6	6.8	6.62	± 0.13
Thickness layer 2 / Å	MC_10	975.98	900	1050	974.27	± 42.89
s.l.d. layer 2 / 10^{-6}Å^{-2}	MC_11	2.66	2.3	3.2	2.677	± 0.27
Roughness between layer 1 and 2 / Å	MC_13	22.74	10	50	15.00	± 8.13

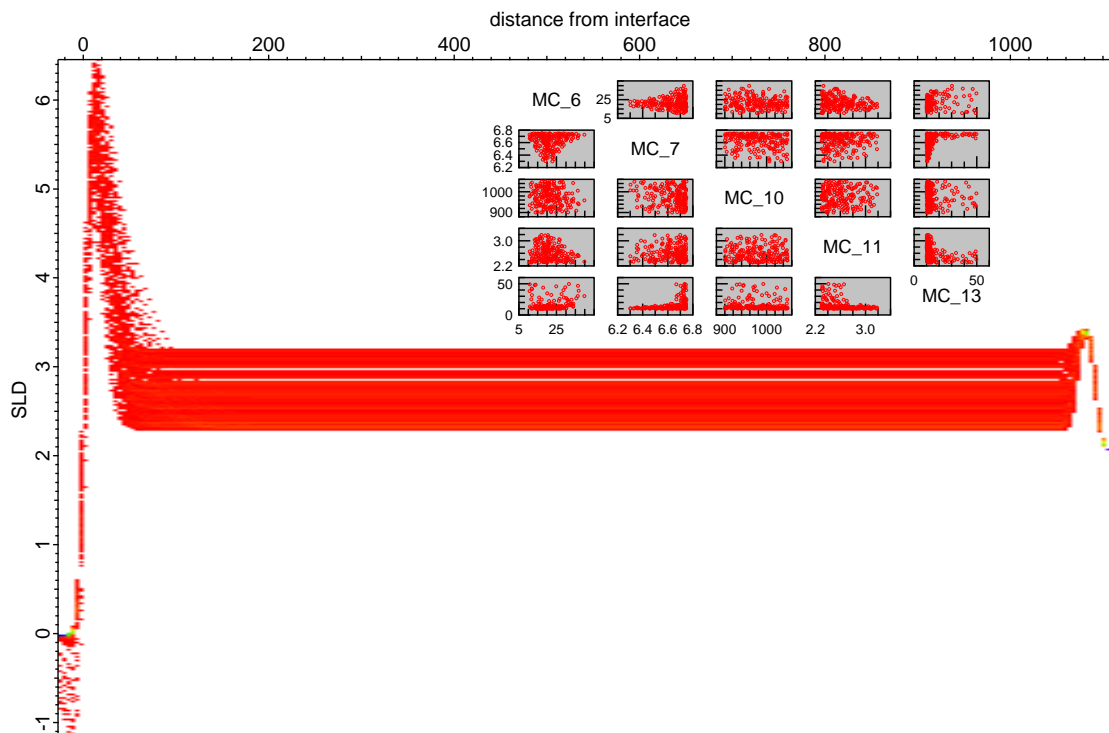


Figure A1-2: Top: Plot of the MC fitting iterations corresponding to the results in Table A1-2.

Unfortunately, widening these limits did not improve the convergence of the iterations, but it did worsen the quality of the fit to the NR data (Figure A1-3, bottom). Hence, it appears that the Genetic + MC analysis struggles to determine the concentration of the 2nd layer and that the error on this layer might be unreliable. This problem is not encountered with a simple Genetic fit: a good repeatability of the results was generally obtained with a good correlation between the area under the curve of the concentration profiles obtained and the total oligomer amount in the sample. The fitting using Genetic + MC analysis remains quite subjective for obtaining the error on this parameter since it involves assessing manually the quality of the fit to the raw data.

Annex 1: Fitting error analysis

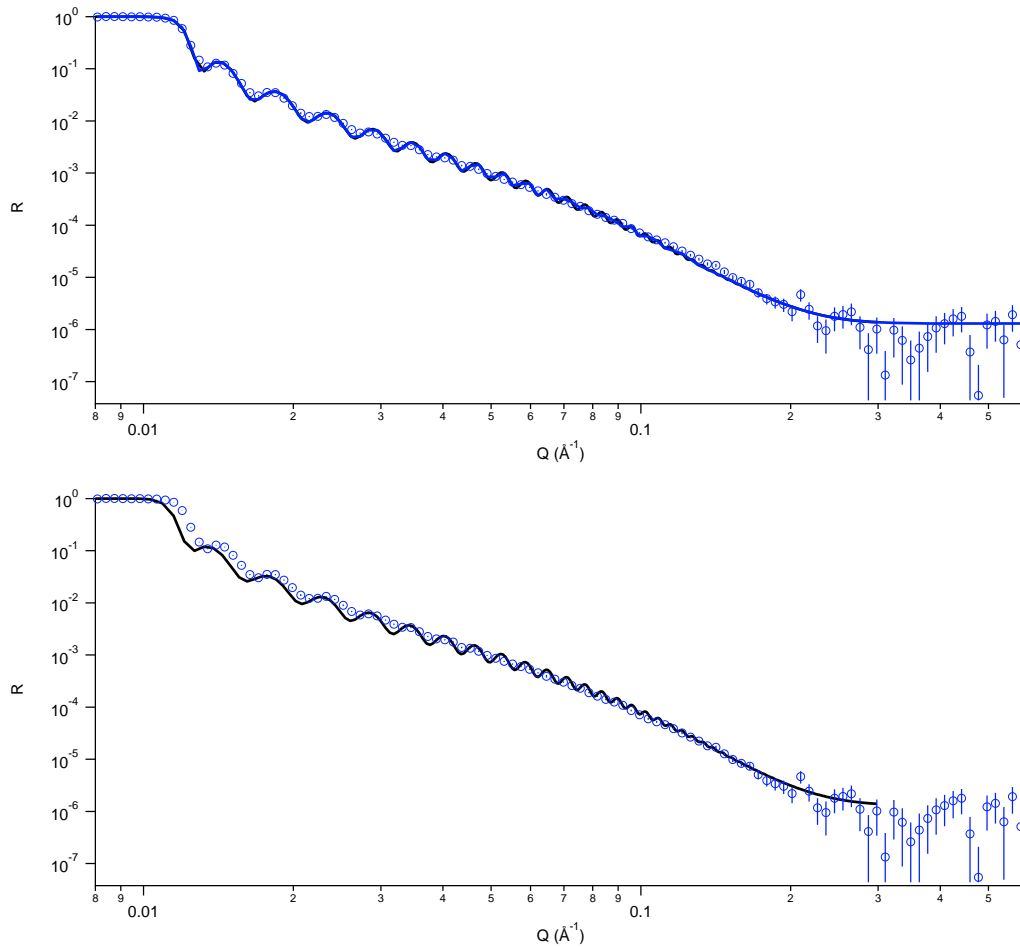


Figure A1-3: Fit to the raw NR data corresponding to (top) the fitted parameters reported in Table A1-2 and plotted in Figure A1-2 and (bottom) the result when the limits for the s.l.d. of the 2nd layer are wider.

From this error analysis, fitting errors on z^* and φ_{tot} can be estimated. As it is difficult to obtain an error on the second layer concentration (even when all other parameters are kept constant), the same error than for the 1st layer was chosen ($\pm 0.127 \times 10^{-6} \text{ \AA}^{-2}$, which corresponds to an error of 1.6 at% for the dsq/PB system) and confirmed by manually changing the value of the parameter and assessing its effect on the quality of the fit. The error on z^* and φ_{tot} arising from roughness is zero since the shape of the profile is symmetric. Hence, it was chosen to calculate the relative error on z^* by adding in Gaussian quadrature the relative errors on the concentration of the first and second layer (2 and 5 % respectively) and on the thickness of the first layer (26 %). For the calculation of the relative error on φ_{tot} , the error on the thickness of the second layer is also included (4 %). Hence, one obtains relative errors of 26 % and 27 % on z^* and φ_{tot} respectively. These errors seem very large for NR and it is suspected that there are

Annex 1: Fitting error analysis

overestimated with this fitting method. Moreover, the quality of the fits obtained in Figure A1-3 is not convincing enough to support the reliability of these calculated errors.

Alternatively, a statistical fit was performed using the Levenberg-Marquardt method, also available in the motofit package of the IGOR pro software.¹²⁹ The results of this fit are very close to those of the initial Genetic fit. They are presented in Table A1-3.

Table A1-3: Results of Levenberg-Marquardt fitting of the 40 % (w.w) dsq/PB sample.

	Levenberg-Marquardt fitted value	Error on fitted value	Relative error
Thickness layer 1 / Å	18.67	± 1.24	6.64 %
s.l.d. layer 1 / 10^{-6}Å^{-2}	6.99	± 0.05	0.72 %
Thickness layer 2 / Å	980.67	± 1.95	0.20 %
s.l.d. layer 2 / 10^{-6}Å^{-2}	2.65	± 0.00	0.00 %
Roughness between layer 1 and 2 / Å	26.23	± 1.67	6.37 %

Similarly, adding the relative errors in Gaussian quadrature leads to a calculated relative error on z^* and φ_{tot} of 6 %. This value is closer to what is expected for NR data. It was decided to use these relative errors as an example of fitting errors for the determination of z^* and φ_{tot} by NR throughout the thesis.

ANNEX 2: IBA FITTING PARAMETERS

In this annex are reported a few example of the parameters used in DataFurnace to fit the IBA data, shown in the thesis. The complete fitting details for the other datasets can be found in the archive folder of DOI number [10.15128/r11544bp095](https://doi.org/10.15128/r11544bp095).

NDF v9.6a 30Oct13 rev 17Jan14 run 25/02/2015 12:09:44 Filename: dsq01.res
Richard Thompson (1.7MV 5SDH NEC Tandem), Dept.Chemistry, University of Durham
Any public outcome using these results must cite
N.P. Barradas, C. Jeynes, NIMB 266 (2008) 1875.
Used ZBL stopping powers. Should cite SRIM The Stopping and Range of Ions in Matter, J.F. Ziegler, J.P. Biersack and M.D. Ziegler (2008)

ERDA

30 % (w.w) dsq in PB

Batch dsqPB.spc structure dsqPB.str. The data switches were:

- Isotopic distribution was used.
- Data was not smoothed.
- Roughness model 1. Forced fast Gaussian model
- x2 is normalised and not standard

File: dsqPB3066.ASC: 2048 ch, 512 are read, 2 cols: 2nd is used. Geometry file dsq66.geo
Compressed to 2048 channels, no pileup correction
Autolayer option was used.
Detector FWHM 0.18000E+02 keV, Chu stragging Gauss.
ERDA: 1516.0 keV 4He on 2H ROI= 90+ 9: 180
IBM geometry: angle of incidence = -66.00, scattering angle = 30.00, exit angle = 84.00
E =0.44556E+01 ch +0.19372E+01 keV, Charge =0.35700E+01 puC, Omega =0.14300E+01 msr
Andersen screening
LLD channel 101 for pileup calculation
Foil with 1 layers:
thick:0.465E+05 1e15at/cm2, comp: C 45.5 H 36.4 O 18.2
Non-Rutherford cross section for 2H created: file xd0101.dat
"Resonance" resolution convolution done on 2H
All stopping powers are ZBL2000
Partial chisquared 0.1350E+03

File: dsqPB3066.ASC: 2048 ch, 512 are read, 2 cols: 2nd is used. Geometry file hsq66.geo

Annex 2: IBA fitting parameters

Compressed to 2048 channels, no pileup correction
Autolayer option was used.
Detector FWHM 0.18000E+02 keV, Chu straggling Gauss.
ERDA: 1516.0 keV 4He on 1H ROI= 60+ 10: 120
IBM geometry: angle of incidence = -66.00, scattering angle = 30.00, exit angle = 84.00
E =0.44688E+01 ch +/- .11296E+02 keV, Charge =0.33252E+01 puC, Omega =0.14300E+01 msr
Andersen screening
LLD channel 101 for pileup calculation
Foil with 1 layers:
thick:0.465E+05 1e15at/cm2, comp: C 45.5 H 36.4 O 18.2
Non-Rutherford cross section for 1H created: file xh0102.dat
"Resonance" resolution convolution done on 1H
All stopping powers are ZBL2000
Partial chisquared 0.9431E+01

Custom local search optimisation, from ndf.prf and NDF.TCN
Fine constraints on fit imposed with file NDFPRF.ORD
Logical elements present in calculation:

Molecule 1: c41h610.16476
has fixed stoichiometry:
C : 40.000000 at.%
1H : 60.000004 at.%
Density (1e22at/cm3):10.16476

Molecule 2: c302h629.249093
has fixed stoichiometry:
C : 32.608696 at.%
2H : 67.391304 at.%
Density (1e22at/cm3): 9.24909

Element 3: si4.977
Density (1e22at/cm3): 4.97700

The fit assigned 3 layers. The composition was:

density (1e22at/cm3): 10.16476 9.24909 4.97700
Layer t (1e15at/cm2) t (nm) r(1e22at/cm3) c41h610. c302h629 si4.977 roughnes
1 310.000 32.087 9.661 45.0000 55.0000 0.0000 0.150000E+01
2 2689.961 269.894 9.967 78.3752 21.6248 0.0000 0.458243E+01
3 631085.000 126800.273 4.977 0.0000 0.0000 100.0000 0.100000E+00
Total amount (1e15at/cm2): .2248E+04 .7522E+03 .6311E+06
Not considering last layer: .2248E+04 .7522E+03 .0000E+00

Layer t (1e15at/cm2) t (nm) r(1e22at/cm3) C 1H 2H Si
1 310.000 32.087 9.661 35.9348 27.0000 37.0652 0.0000
2 2689.961 269.894 9.967 38.4016 47.0251 14.5733 0.0000
3 631085.000 126800.273 4.977 0.0000 0.0000 0.0000 100.0000
Total amount (1e15at/cm2): .1144E+04 .1349E+04 .5069E+03 .6311E+06
Not considering last layer: .1144E+04 .1349E+04 .5069E+03 .0000E+00

Annex 2: IBA fitting parameters

30 % (w.w) oligo d-IB in PB

Batch dIBPB.spc structure dIBPB.str. The data switches were:

Isotopic distribution was used.

Data was not smoothed.

Roughness model 1. Forced fast Gaussian model

x2 is normalised and not standard

File: dIBPB3066.ASC: 2048 ch, 512 are read, 2 cols: 2nd is used. Geometry file dIB66.geo

Compressed to 2048 channels, no pileup correction

Autolayer option was used.

Detector FWHM 0.18000E+02 keV, Chu stragglng Gauss.

ERDA: 1516.0 keV 4He on 2H ROI= 100+ 8: 160

IBM geometry: angle of incidence = -66.00, scattering angle = 29.00, exit angle = 85.00

E =0.48515E+01 ch +0.52913E+02 keV, Charge =0.14927E+01 puC, Omega =0.14300E+01 msr

Andersen screening

LLD channel 141 for pileup calculation

Foil with 1 layers:

thick:0.465E+05 1e15at/cm2, comp: C 45.5 H 36.4 O 18.2

Non-Rutherford cross section for 2H created: file xd0401.dat

"Resonance" resolution convolution done on 2H

All stopping powers are ZBL2000

Partial chisquared 0.1332E+01

File: dIBPB3066.ASC: 2048 ch, 512 are read, 2 cols: 2nd is used. Geometry file hIB66.geo

Compressed to 2048 channels, no pileup correction

Autolayer option was used.

Detector FWHM 0.18000E+02 keV, Chu stragglng Gauss.

ERDA: 1516.0 keV 4He on 1H ROI= 20+ 8: 105

IBM geometry: angle of incidence = -66.00, scattering angle = 29.00, exit angle = 85.00

E =0.48541E+01 ch +0.44199E+02 keV, Charge =0.13500E+01 puC, Omega =0.14300E+01 msr

Andersen screening

LLD channel 141 for pileup calculation

Foil with 1 layers:

thick:0.465E+05 1e15at/cm2, comp: C 45.5 H 36.4 O 18.2

Non-Rutherford cross section for 1H created: file xh0402.dat

"Resonance" resolution convolution done on 1H

All stopping powers are ZBL2000

Partial chisquared 0.4107E+01

Custom local search optimisation, from dIB04.prf and NDF.TCN

Fine constraints on fit imposed with file NDFPRF.ORD

Error from data.

Logical elements present in calculation:

Molecule 1: c41h610.16476

has fixed stoichiometry:

C : 40.000000 at.%

1H : 60.000004 at.%

Density (1e22at/cm3):10.16476

Molecule 2: c321h92h569.35

has fixed stoichiometry:

Annex 2: IBA fitting parameters

C : 32.989689 at.%
1H : 9.278350 at.%
2H : 57.731956 at.%
Density (1e22at/cm3): 9.35000

Element 3: si4.977
Density (1e22at/cm3): 4.97700

The fit assigned 4 layers. The composition was:

density (1e22at/cm3): 10.16476 9.35000 4.97700
Layer t (1e15at/cm2) t (nm) r(1e22at/cm3) c41h610. c321h92h si4.977 roughnes
1 400.000 40.655 9.839 60.0000 40.0000 0.0000 0.000000E+00
2 580.592 57.347 10.124 95.0209 4.9791 0.0000 0.000000E+00
3 561.615 55.938 10.040 84.6837 15.3163 0.0000 0.000000E+00
4 7721.959 1551.529 4.977 0.0000 0.0000 100.0000 0.140625E-01
Total amount (1e15at/cm2): .1267E+04 .2749E+03 .7722E+04
Not considering last layer: .1267E+04 .2749E+03 .0000E+00

Layer t (1e15at/cm2) t (nm) r(1e22at/cm3) C 1H 2H Si
1 400.000 40.655 9.839 37.1959 39.7113 23.0928 0.0000
2 580.592 57.347 10.124 39.6510 57.4745 2.8745 0.0000
3 561.615 55.938 10.040 38.9263 52.2313 8.8424 0.0000
4 7721.959 1551.529 4.977 0.0000 0.0000 0.0000 100.0000
Total amount (1e15at/cm2): .5976E+03 .7859E+03 .1587E+03 .7722E+04
Not considering last layer: .5976E+03 .7859E+03 .1587E+03 .0000E+00

Signal areas (in counts) - Data, with the calculated partial spectra from other elements and background subtracted

Geometry C 1H 2H Si
1 .0000E+00 .0000E+00 .0000E+00 .0000E+00
2 .0000E+00 .0000E+00 .0000E+00 .0000E+00

Signal areas (in counts) - same as before, but background not subtracted

Geometry C 1H 2H Si
1 .0000E+00 .0000E+00 .0000E+00 .0000E+00
2 .0000E+00 .0000E+00 .0000E+00 .0000E+00

40 % (w.w) oligo d-S in hPI

Batch dShPI.spc structure dShPI.str. The data switches were:

- Isotopic distribution was used.
- Data was not smoothed.
- Roughness model 1. Forced fast Gaussian model
- x2 is normalised and not standard

File: dS4063.ASC: 2048 ch, 512 are read, 2 cols: 2nd is used. Geometry file dS63.geo

Compressed to 2048 channels, no pileup correction

Autolayer option was used.

Detector FWHM 0.18000E+02 keV, Chu stragglng Gauss.

ERDA: 1516.0 keV 4He on 2H ROI= 100+ 10: 150

IBM geometry: angle of incidence = -63.00, scattering angle = 29.00, exit angle = 88.00

E =0.48823E+01 ch +0.44567E+02 keV, Charge =0.15138E+01 puC, Omega =0.14300E+01 msr

Annex 2: IBA fitting parameters

Andersen screening

Foil with 1 layers:

thick:0.465E+05 1e15at/cm2, comp: C 45.5 H 36.4 O 18.2

Non-Rutherford cross section for 2H created: file xd0201.dat

"Resonance" resolution convolution done on 2H

All stopping powers are ZBL2000

Partial chisquared 0.1368E+01

File: dS4063.ASC: 2048 ch, 512 are read, 2 cols: 2nd is used. Geometry file hS63.geo

Compressed to 2048 channels, no pileup correction

Autolayer option was used.

Detector FWHM 0.18000E+02 keV, Chu straggling Gauss.

ERDA: 1516.0 keV 4He on 1H ROI= 20+ 10: 105

IBM geometry: angle of incidence = -63.00, scattering angle = 29.00, exit angle = 88.00

E =0.48550E+01 ch +0.38020E+02 keV, Charge =0.14797E+01 puC, Omega =0.14300E+01 msr

Andersen screening

Foil with 1 layers:

thick:0.465E+05 1e15at/cm2, comp: C 45.5 H 36.4 O 18.2

Non-Rutherford cross section for 1H created: file xh0202.dat

"Resonance" resolution convolution done on 1H

All stopping powers are ZBL2000

Partial chisquared 0.2716E+01

File: dS4063b.ASC: 2048 ch, 512 are read, 2 cols: 2nd is used. Geometry file dS63.geo

Compressed to 2048 channels, no pileup correction

Autolayer option was used.

Detector FWHM 0.18000E+02 keV, Chu straggling Gauss.

ERDA: 1516.0 keV 4He on 2H ROI= 100+ 10: 150

IBM geometry: angle of incidence = -63.00, scattering angle = 29.00, exit angle = 88.00

E =0.48821E+01 ch +0.44678E+02 keV, Charge =0.14640E+01 puC, Omega =0.14300E+01 msr

Andersen screening

Foil with 1 layers:

thick:0.465E+05 1e15at/cm2, comp: C 45.5 H 36.4 O 18.2

Non-Rutherford cross section for 2H created: file xd0203.dat

"Resonance" resolution convolution done on 2H

All stopping powers are ZBL2000

Partial chisquared 0.1439E+01

File: dS4063b.ASC: 2048 ch, 512 are read, 2 cols: 2nd is used. Geometry file hS63.geo

Compressed to 2048 channels, no pileup correction

Autolayer option was used.

Detector FWHM 0.18000E+02 keV, Chu straggling Gauss.

ERDA: 1516.0 keV 4He on 1H ROI= 20+ 10: 105

IBM geometry: angle of incidence = -63.00, scattering angle = 29.00, exit angle = 88.00

E =0.48529E+01 ch +0.38859E+02 keV, Charge =0.14748E+01 puC, Omega =0.14300E+01 msr

Andersen screening

Foil with 1 layers:

thick:0.465E+05 1e15at/cm2, comp: C 45.5 H 36.4 O 18.2

Non-Rutherford cross section for 1H created: file xh0204.dat

"Resonance" resolution convolution done on 1H

All stopping powers are ZBL2000

Partial chisquared 0.3100E+01

Annex 2: IBA fitting parameters

File: dS4063c.ASC: 2048 ch, 512 are read, 2 cols: 2nd is used. Geometry file dS63.geo
Compressed to 2048 channels, no pileup correction
Autolayer option was used.
Detector FWHM 0.18000E+02 keV, Chu straggling Gauss.
ERDA: 1516.0 keV 4He on 2H ROI= 100+ 10: 150
IBM geometry: angle of incidence = -63.00, scattering angle = 29.00, exit angle = 88.00
E =0.48825E+01 ch +0.44133E+02 keV, Charge =0.14979E+01 puC, Omega =0.14300E+01 msr
Andersen screening
Foil with 1 layers:
thick:0.465E+05 1e15at/cm2, comp: C 45.5 H 36.4 O 18.2
Non-Rutherford cross section for 2H created: file xd0205.dat
"Resonance" resolution convolution done on 2H
All stopping powers are ZBL2000
Partial chisquared 0.1707E+01

File: dS4063c.ASC: 2048 ch, 512 are read, 2 cols: 2nd is used. Geometry file hS63.geo
Compressed to 2048 channels, no pileup correction
Autolayer option was used.
Detector FWHM 0.18000E+02 keV, Chu straggling Gauss.
ERDA: 1516.0 keV 4He on 1H ROI= 20+ 10: 105
IBM geometry: angle of incidence = -63.00, scattering angle = 29.00, exit angle = 88.00
E =0.48530E+01 ch +0.38395E+02 keV, Charge =0.14687E+01 puC, Omega =0.14300E+01 msr
Andersen screening
Foil with 1 layers:
thick:0.465E+05 1e15at/cm2, comp: C 45.5 H 36.4 O 18.2
Non-Rutherford cross section for 1H created: file xh0206.dat
"Resonance" resolution convolution done on 1H
All stopping powers are ZBL2000
Partial chisquared 0.2804E+01

Custom local search optimisation, from dSh02.prf and NDF.TCN
Fine constraints on fit imposed with file NDFPRF.ORD
Logical elements present in calculation:

Molecule 1: c82h87.728896
has fixed stoichiometry:
C : 50.000000 at.%
2H : 50.000000 at.%
Density (1e22at/cm3): 7.72890

Molecule 2: c51h1013.52374
has fixed stoichiometry:
C : 33.333336 at.%
1H : 66.666672 at.%
Density (1e22at/cm3):13.52374

Element 3: si
Density (1e22at/cm3): 4.97700
The fit assigned 3 layers. The composition was:

density (1e22at/cm3): 7.72890 13.52374 4.97700

Annex 2: IBA fitting parameters

```
Layer t (1e15at/cm2) t (nm) r(1e22at/cm3) c82h87.7 c51h1013 si roughnes
1 510.000 38.203 13.350 3.0000 97.0000 0.0000 0.255000E+01
2 207.464 23.022 9.012 77.8625 22.1375 0.0000 0.854519E+02
3 25000.000 5023.106 4.977 0.0000 0.0000 100.0000 0.100000E+00
Total amount (1e15at/cm2): .1768E+03 .5406E+03 .2500E+05
Not considering last layer: .1768E+03 .5406E+03 .0000E+00
```

```
Layer t (1e15at/cm2) t (nm) r(1e22at/cm3) C 2H 1H Si
1 510.000 38.203 13.350 33.8333 1.5000 64.6667 0.0000
2 207.464 23.022 9.012 46.3104 38.9313 14.7583 0.0000
3 25000.000 5023.106 4.977 0.0000 0.0000 0.0000 100.0000
Total amount (1e15at/cm2): .2686E+03 .8842E+02 .3604E+03 .2500E+05
Not considering last layer: .2686E+03 .8842E+02 .3604E+03 .0000E+00
```

NRA

50 % (w.w) oligo d-IB in PB

Batch dIBPBnra.spc structure dIBPB.str. The data switches were:

Isotopic distribution was used.

Data was not smoothed.

x2 is normalised and not standard

File: dIBPB5080.ASC: 2048 ch, 512 are read, 2 cols: 2nd is used. Geometry file dIB80.geo

Compressed to 2048 channels, no pileup correction

Autolayer option was used.

Detector FWHM 0.17000E+02 keV, Chu stragglng Gauss.

NRA: 2H (3He 700.0 keV,1H)4He Q= 18351 keV Detect:1H ROI= 1290+ 6:1340

Cornell geometry: angle of incidence = 80.00, scattering angle = 170.00, exit angle = 80.15

E =0.97000E+01 ch +0.62258E+02 keV, Charge =0.32200E+01 puC, Omega =0.20000E+01 msr

Andersen screening

Non-Rutherford cross section for 2H created: file xn0301.dat

"Resonance" resolution convolution done on 2H

All stopping powers are ZBL2000

Partial chisquared 0.4471E+02

File: dIBPB5083.ASC: 2048 ch, 512 are read, 2 cols: 2nd is used. Geometry file dIB83.geo

Compressed to 2048 channels, no pileup correction

Autolayer option was used.

Detector FWHM 0.17000E+02 keV, Chu stragglng Gauss.

NRA: 2H (3He 700.0 keV,1H)4He Q= 18351 keV Detect:1H ROI= 1290+ 6:1350

Cornell geometry: angle of incidence = 83.00, scattering angle = 170.00, exit angle = 83.11

E =0.97000E+01 ch +0.53555E+02 keV, Charge =0.22680E+01 puC, Omega =0.20000E+01 msr

Andersen screening

LLD channel 166 for pileup calculation

Non-Rutherford cross section for 2H created: file xn0302.dat

"Resonance" resolution convolution done on 2H

All stopping powers are ZBL2000

Partial chisquared 0.1728E+02

Annex 2: IBA fitting parameters

Custom local search optimisation, from dIB03.prf and NDF.TCN

Logical elements present in calculation:

Molecule 1: c41h610.16476
has fixed stoichiometry:
C : 40.000000 at.%
1H : 60.000004 at.%
Density (1e22at/cm3):10.16476

Molecule 2: c42h8
has fixed stoichiometry:
C : 33.333336 at.%
2H : 66.666672 at.%
Density (1e22at/cm3): 6.63533

The fit assigned 5 layers. The composition was:

Equation for molecule c42h8 in file erf.txt
.5+.5*erf((a0-t)/a1)+a2+a2*erf((t-a3)/a4)
a 0=-.23218E+02
a 1=0.10015E+03
a 2=0.36183E-01
a 3=0.84836E+02
a 4=0.21000E+02

Matrix composition:

	density (1e22at/cm3):	10.16476	6.63533		
Layer	t (1e15at/cm2)	t (nm)	r(1e22at/cm3)	c41h610.	c42h8
1	1475.656	145.174	9.881	91.9497	8.0503
2	384.068	37.784	10.165	100.0000	0.0000
3	807.473	79.438	10.165	100.0000	0.0000
4	255.288	25.115	10.165	100.0000	0.0000
5	231306.000	22755.678	10.165	100.0000	0.0000
Total amount (1e15at/cm2):			.2341E+06	.1188E+03	
Not considering last layer:			.2804E+04	.1188E+03	

Layer	t (1e15at/cm2)	t (nm)	r(1e22at/cm3)	C	1H	C	2H
1	1475.656	145.174	9.881	36.7799	55.1699	2.6834	5.3668
2	384.068	37.784	10.165	40.0000	60.0000	0.0000	0.0000
3	807.473	79.438	10.165	40.0000	60.0000	0.0000	0.0000
4	255.288	25.115	10.165	40.0000	60.0000	0.0000	0.0000
5	231306.000	22755.678	10.165	40.0000	60.0000	0.0000	0.0000
Total amount (1e15at/cm2):			.9364E+05	.1405E+06	.3960E+02	.7920E+02	
Not considering last layer:			.1121E+04	.1682E+04	.3960E+02	.7920E+02	

ANNEX 3: NR FITTING PARAMETERS

Squalane and d-PS

Squalane in contact with dPS – 25 °C (through Si) / $\chi^2 = 29.9151$

Layer	Thickness / Å	SLD / 10^{-6}Å^{-2}	Roughness / Å
fronting	INF	2.07	
1	20	3.45	10
2	616.91	6.1916	10
backing	INF	-0.37	12.542

Squalane in contact with dPS – 35 °C (through Si) / $\chi^2 = 109.967$

Layer	Thickness / Å	SLD / 10^{-6}Å^{-2}	Roughness / Å
fronting	INF	2.07	
1	20	3.45	5
2	615.89	6.2076	5
backing	INF	-0.37	13.072

Squalane in contact with dPS – 45 °C (through Si) / $\chi^2 = 33.6603$

Layer	Thickness / Å	SLD / 10^{-6}Å^{-2}	Roughness / Å
fronting	INF	2.07	
1	20	3.45	5
2	615.16	6.3887	5
backing	INF	-0.37	11.859

Squalane in contact with dPS – 55 °C (through Si) / $\chi^2 = 44.2185$

Layer	Thickness / Å	SLD / 10^{-6}Å^{-2}	Roughness / Å
fronting	INF	2.07	
1	20	3.45	5
2	618.78	6.2622	5
backing	INF	-0.37	11.752

Squalane in contact with dPS – 65 °C (through Si) / $\chi^2 = 37.4756$

Layer	Thickness / Å	SLD / 10^{-6}Å^{-2}	Roughness / Å
fronting	INF	2.07	
1	20	3.45	5
2	627.5	6.0203	5
backing	INF	-0.37	10.767

Squalane in contact with dPS – initial RT (through Si) / $\chi^2 = 2.75881$

Layer	Thickness / Å	SLD / 10^{-6}Å^{-2}	Roughness / Å
fronting	INF	2.07	
1	44.98	3.7283	9.9142
2	710.16	6.1703	5.0352
3	1094.4	-0.3747	7.5109
backing	INF	0	5

Annex 3: NR fitting parameters

Squalane in contact with dPS – 120 °C (through Si) / $\chi^2 = 2.05289$

Layer	Thickness / Å	SLD / 10^{-6}Å^{-2}	Roughness / Å
fronting	INF	2.07	
1	49.079	3.4426	9.8
2	774.71	5.6421	5.0016
3	1129.2	-0.34	13.502
backing	INF	0	5

Squalane in contact with dPS – final RT (through Si) / $\chi^2 = 3.05262$

Layer	Thickness / Å	SLD / 10^{-6}Å^{-2}	Roughness / Å
fronting	INF	2.07	
1	44.996	3.6476	9
2	738.64	5.9088	5.004
3	900.28	-0.37	12.903
backing	INF	0	5

Picco and d-PS

Picco in contact with dPS – 80 °C (through Si) / $\chi^2 = 17.7428$

Layer	Thickness / Å	SLD / 10^{-6}Å^{-2}	Roughness / Å
fronting	INF	2.07	
1	20	3.45	5
2	1075.4	5.2251	10
backing	INF	0.2	11.24

Picco in contact with dPS – 90 °C (through Si) / $\chi^2 = 14.9936$

Layer	Thickness / Å	SLD / 10^{-6}Å^{-2}	Roughness / Å
fronting	INF	2.07	
1	20	3.45	5
2	1092.9	5.1763	10
backing	INF	0.2	12.677

Picco in contact with dPS – 100 °C (through Si) / $\chi^2 = 8.71126$

Layer	Thickness / Å	SLD / 10^{-6}Å^{-2}	Roughness / Å
fronting	INF	2.07	
1	20	3.45	5
2	1092.5	5.0741	10
backing	INF	0.2	19.778

Picco in contact with dPS – 110 °C (through Si) / $\chi^2 = 10.3625$

Layer	Thickness / Å	SLD / 10^{-6}Å^{-2}	Roughness / Å
fronting	INF	2.07	
1	20	3.45	5
2	1094	5.0335	10
backing	INF	0.2	5.1969

Picco in contact with dPS – 120 °C (through Si) / $\chi^2 = 10.3625$

Layer	Thickness / Å	SLD / 10^{-6}Å^{-2}	Roughness / Å
fronting	INF	2.07	
1	20	3.45	5
2	1114	5.2731	10
backing	INF	0.2	5.0783

Annex 3: NR fitting parameters

Picco in contact with DPS – 25 °C (through Si) / $\chi^2 = 8.8232$

Layer	Thickness / Å	SLD / 10^{-6}Å^{-2}	Roughness / Å
fronting	INF	2.07	
1	20	3.45	5
2	1068.1	5.2881	10
backing	INF	0.2	5.089

Regalite and d-PS

Regalite in contact with DPS – 80 °C (through Si) / $\chi^2 = 5.22964$

Layer	Thickness / Å	SLD / 10^{-6}Å^{-2}	Roughness / Å
fronting	INF	2.07	
1	20	3.45	5
2	36.944	-0.35	10
3	1042.8	6.162	49.644
backing	INF	-0.35	13.817

Regalite in contact with DPS – 90 °C (through Si) / $\chi^2 = 10.0333$

Layer	Thickness / Å	SLD / 10^{-6}Å^{-2}	Roughness / Å
fronting	INF	2.07	
1	20	3.45	5
2	59.705	0.42116	10
3	1043.6	6.0498	52.743
backing	INF	-0.35	15.477

Regalite in contact with DPS – 100 °C (through Si) / $\chi^2 = 9.65$

Layer	Thickness / Å	SLD / 10^{-6}Å^{-2}	Roughness / Å
fronting	INF	2.07	
1	20	3.45	5
2	86.923	0.6907	10
3	1080.7	5.9788	74.781
backing	INF	-0.35	14.907

Regalite in contact with DPS – 110 °C (through Si) / $\chi^2 = 9.34163$

Layer	Thickness / Å	SLD / 10^{-6}Å^{-2}	Roughness / Å
fronting	INF	2.07	
1	20	3.45	5
2	99.85	1.1068	10
3	1215.4	5.426	84.015
backing	INF	-0.35	16.704

Regalite in contact with DPS – 120 °C (through Si) / $\chi^2 = 3.98666$

Layer	Thickness / Å	SLD / 10^{-6}Å^{-2}	Roughness / Å
fronting	INF	2.07	
1	20	3.45	5
2	95.714	1.7936	10
3	1267.3	4.9954	44.807
backing	INF	-0.35	19.24

Regalite in contact with DPS – 25 °C (through Si) / $\chi^2 = 6.97213$

Layer	Thickness / Å	SLD / 10^{-6}Å^{-2}	Roughness / Å
fronting	INF	2.07	
1	20	3.45	5
2	15.85	1.3018	10
3	1196.9	5.2134	23.603
backing	INF	-0.35	14.118

oligo-dS in PB

15 % (w.w) oligo-dS in PB / $\chi^2 = 5.68771$

Layer	Thickness / Å	SLD / 10^{-6}Å^{-2}	Roughness / Å
fronting	INF	0	
1	1717.3	1.0804	12.273
2	18.425	3.1082	10
backing	INF	2.07	5

dsq in PI

30 % (w.w) dsq in PI / $\chi^2 = 32.9362$

Layer	Thickness / Å	SLD / 10^{-6}Å^{-2}	Roughness / Å
fronting	INF	0	
1	47.988	0.58923	1.2179
2	920.01	0.47624	28.921
3	5.3945	3.7456	5
backing	INF	2.07	5

40 % (w.w) dsq in PI / $\chi^2 = 14.4179$

Layer	Thickness / Å	SLD / 10^{-6}Å^{-2}	Roughness / Å
fronting	INF	0	
1	0.70711	4.9115	4.2055
2	643.36	2.7218	18.577
3	15.048	3.1536	5
backing	INF	2.07	5

60 % (w.w) dsq in PI (through Si) / $\chi^2 = 7.55867$

Layer	Thickness / Å	SLD / 10^{-6}Å^{-2}	Roughness / Å
fronting	INF	2.07	
1	10.422	3.1105	5
2	53.105	2.3805	5
3	532.66	4.045	51.015
4	89.484	3.2502	46.529
backing	INF	0	5

70 % (w.w) dsq in PI (through Si) / $\chi^2 = 9.40922$

Layer	Thickness / Å	SLD / 10^{-6}Å^{-2}	Roughness / Å
fronting	INF	2.07	
1	10.269	3.1355	5
2	139.3	2.1305	5
3	500.03	4.3387	86.054
4	89.602	3.4919	43.674
backing	INF	0	7

dsq in PB

2 % (w.w) dsq in PB / $\chi^2 = 1.51824$

Layer	Thickness / Å	SLD / 10^{-6}Å^{-2}	Roughness / Å
fronting	INF	0	
1	47.988	0.58923	1.2179
2	920.01	0.47624	28.921
3	5.3945	3.7456	5
backing	INF	2.07	5

Annex 3: NR fitting parameters

4 % (w.w) dsq in PB / $\chi^2 = 3.94458$

Layer	Thickness / Å	SLD / 10^{-6}Å^{-2}	Roughness / Å
fronting	INF	0	
1	34.557	0.82473	1.0625
2	911.65	0.59577	13.126
3	10	3.5	5
backing	INF	2.07	5

6 % (w.w) dsq in PB / $\chi^2 = 3.31722$

Layer	Thickness / Å	SLD / 10^{-6}Å^{-2}	Roughness / Å
fronting	INF	0	
1	10.799	2.4979	0.49912
2	891.77	0.70535	8.261
3	12.504	3.3497	5
backing	INF	2.07	5

8 % (w.w) dsq in PB / $\chi^2 = 7.79577$

Layer	Thickness / Å	SLD / 10^{-6}Å^{-2}	Roughness / Å
fronting	INF	0	
1	9.0803	3.0304	0.51754
2	1181.4	0.75619	5.4636
3	15.662	3.5081	5
backing	INF	2.07	5

10 % (w.w) dsq in PB / $\chi^2 = 3.80512$

Layer	Thickness / Å	SLD / 10^{-6}Å^{-2}	Roughness / Å
fronting	INF	0	
1	12.225	4.4315	0.55219
2	1044.8	0.95574	9.0896
3	0.69709	3.5438	5
backing	INF	2.07	5

14 % (w.w) dsq in PB / $\chi^2 = 12.5522$

Layer	Thickness / Å	SLD / 10^{-6}Å^{-2}	Roughness / Å
fronting	INF	0	
1	12.252	5.2709	0.1815
2	1096.3	1.1607	12.449
3	5.3594	3.1064	5
backing	INF	2.07	5

30 % (w.w) dsq in PB / $\chi^2 = 10.0655$

Layer	Thickness / Å	SLD / 10^{-6}Å^{-2}	Roughness / Å
fronting	INF	0	
1	14.875	6.6502	5
2	1473.3	2.0961	14.318
3	20	3.45	5
backing	INF	2.07	5

40 % (w.w) dsq in PB – 25 °C / $\chi^2 = 17.6316$

Layer	Thickness / Å	SLD / 10^{-6}Å^{-2}	Roughness / Å
fronting	INF	0	
1	22.011	6.7471	5
2	975.98	2.6576	22.742
3	20	3.45	5
backing	INF	2.07	5

Annex 3: NR fitting parameters

40 % (w.w) dsq in PB – 35 °C / $\chi^2 = 10.0407$

Layer	Thickness / Å	SLD / 10^{-6}Å^{-2}	Roughness / Å
fronting	INF	0	
1	18.443	6.5371	5
2	988.88	2.6539	23.433
3	20	3.45	5
backing	INF	2.07	5

40 % (w.w) dsq in PB – 55 °C / $\chi^2 = 9.27933$

Layer	Thickness / Å	SLD / 10^{-6}Å^{-2}	Roughness / Å
fronting	INF	0	
1	13.628	6.5582	5
2	1026.2	2.6786	22.755
3	20	3.45	5
backing	INF	2.07	5

50 % (w.w) dsq in PB (125 nm – INTER) / $\chi^2 = 3.27729$

Layer	Thickness / Å	SLD / 10^{-6}Å^{-2}	Roughness / Å
fronting	INF	0	
1	42.461	6.7498	4
2	1224.4	3.393	23.81
3	20	3.45	5
backing	INF	2.07	5

50 % (w.w) dsq in PB (200 nm – SURF) / $\chi^2 = 13.6939$

Layer	Thickness / Å	SLD / 10^{-6}Å^{-2}	Roughness / Å
fronting	INF	0	
1	96.211	6.2537	5
2	1776.1	3.986	39.248
3	20	3.45	5
backing	INF	2.07	5

50 % (w.w) dsq in PB (375 nm – SURF) 25 °C / $\chi^2 = 5.23332$

Layer	Thickness / Å	SLD / 10^{-6}Å^{-2}	Roughness / Å
fronting	INF	0	
1	61.831	6.5138	5
2	3250	3.8088	41.396
3	20	3.45	5
backing	INF	2.07	5

50 % (w.w) dsq in PB (375 nm – SURF) 35 °C / $\chi^2 = 6.2301$

Layer	Thickness / Å	SLD / 10^{-6}Å^{-2}	Roughness / Å
fronting	INF	0	
1	51.945	6.2284	5
2	3200	3.7038	35.068
3	20	3.45	5
backing	INF	2.07	5

50 % (w.w) dsq in PB (375 nm – SURF) 45 °C / $\chi^2 = 10.1112$

Layer	Thickness / Å	SLD / 10^{-6}Å^{-2}	Roughness / Å
fronting	INF	0	
1	39.01	6.0952	5
2	3250	3.6735	38.525
3	20	3.45	5
backing	INF	2.07	5

Annex 3: NR fitting parameters

50 % (w.w) dsq in PB (375 nm – SURF) cooled to 25 °C / $\chi^2 = 6.36147$

Layer	Thickness / Å	SLD / 10^{-6}Å^{-2}	Roughness / Å
fronting	INF	0	
1	59.172	6.5353	5
2	3257.1	3.7305	40.256
3	20	3.45	5
backing	INF	2.07	5

50 % (w.w) dsq in PB (thick – SURF) / $\chi^2 = 1.3473$

Layer	Thickness / Å	SLD / 10^{-6}Å^{-2}	Roughness / Å
fronting	INF	0	
1	32.322	6.1948	5
2	9999.2	3.081	24.598
3	20	3.45	5
backing	INF	2.07	5

60 % (w.w) dsq in PB (through Si) / $\chi^2 = 8.25554$

Layer	Thickness / Å	SLD / 10^{-6}Å^{-2}	Roughness / Å
fronting	INF	2.07	
1	20	3.45	5
2	752.42	3.8284	5
3	80.003	6.1714	33.485
backing	INF	0	5

70 % (w.w) dsq in PB (through Si) / $\chi^2 = 14.7682$

Layer	Thickness / Å	SLD / 10^{-6}Å^{-2}	Roughness / Å
fronting	INF	2.07	
1	20	3.45	5
2	75.394	2.8785	5
3	555.99	3.9591	107.21
4	145.73	6.1606	39.204
backing	INF	0	5

dsq in PBcis

10 % (w.w) dsq in PBcis / $\chi^2 = 9.88499$

Layer	Thickness / Å	SLD / 10^{-6}Å^{-2}	Roughness / Å
fronting	INF	0	
1	8.336	6.5378	4
2	9158	1.0994	7.0502
3	20	3.45	5
backing	INF	2.07	5

30 % (w.w) dsq in PBcis / $\chi^2 = 1.41152$

Layer	Thickness / Å	SLD / 10^{-6}Å^{-2}	Roughness / Å
fronting	INF	0	
1	21.992	6.7499	4
2	7434.2	2.2514	12.168
3	20	3.45	5
backing	INF	2.07	5

Annex 3: NR fitting parameters

40 % (w.w) dsq in PBcis – thick / $\chi^2 = 2.91056$

Layer	Thickness / Å	SLD / 10^{-6}Å^{-2}	Roughness / Å
fronting	INF	0	
1	34.291	6.7496	4
2	9237.6	2.8581	17.361
3	10	3.45	5
backing	INF	2.07	5

40 % (w.w) dsq in PBcis – 146 nm / $\chi^2 = 3.78764$

Layer	Thickness / Å	SLD / 10^{-6}Å^{-2}	Roughness / Å
fronting	INF	0	
1	32.798	6.7498	4
2	1354.5	2.7853	18.583
3	20	3.45	5
backing	INF	2.07	5

50 % (w.w) dsq in PBcis –thick / $\chi^2 = 2.24161$

Layer	Thickness / Å	SLD / 10^{-6}Å^{-2}	Roughness / Å
fronting	INF	0	
1	103.1	6.7457	4
2	14096	3.4466	37.377
3	20	3.45	5
backing	INF	2.07	5

50 % (w.w) dsq in PBcis – 143 nm / $\chi^2 = 3.85913$

Layer	Thickness / Å	SLD / 10^{-6}Å^{-2}	Roughness / Å
fronting	INF	0	
1	105.16	6.6749	5
2	1343.3	3.2631	36.132
3	20	3.45	5
backing	INF	2.07	5

50 % (w.w) dsq in PBcis – 45 nm / $\chi^2 = 12.3041$

Layer	Thickness / Å	SLD / 10^{-6}Å^{-2}	Roughness / Å
fronting	INF	0	
1	94.594	6.5162	4
2	370.35	2.901	28.446
3	20	3.45	5
backing	INF	2.07	5

50 % (w.w) dsq in PBcis – t=0 / $\chi^2 = 6.63612$

Layer	Thickness / Å	SLD / 10^{-6}Å^{-2}	Roughness / Å
fronting	INF	0	
1	56.863	6.44	5
2	1003.5	3.3057	42.774
3	20	3.45	5.0176
backing	INF	2.07	5

50 % (w.w) dsq in PBcis – t=16h / $\chi^2 = 8.63317$

Layer	Thickness / Å	SLD / 10^{-6}Å^{-2}	Roughness / Å
fronting	INF	0	
1	56.508	6.1094	5
2	1005.1	3.3233	38.387
3	20	3.45	8.6128
backing	INF	2.07	5

Annex 3: NR fitting parameters

50 % (w.w) dsq in PBcis – t=23h / $\chi^2 = 6.63612$

Layer	Thickness / Å	SLD / $10^{-6} \cdot \text{Å}^{-2}$	Roughness / Å
fronting	INF	0	
1	60.58	5.4284	5
2	1003.7	3.2012	30.171
3	20	3.45	6.1804
backing	INF	2.07	5

50 % (w.w) dsq in PBcis – cooled down to 15 °C / $\chi^2 = 8.63317$

Layer	Thickness / Å	SLD / $10^{-6} \cdot \text{Å}^{-2}$	Roughness / Å
fronting	INF	0	
1	115.66	6.0882	7.938
2	910.23	3.1206	33.603
3	20	3.45	5.0022
backing	INF	2.07	5

50 % (w.w) dsq in PBcis – warmed up to 25 °C / $\chi^2 = 8.63317$

Layer	Thickness / Å	SLD / $10^{-6} \cdot \text{Å}^{-2}$	Roughness / Å
fronting	INF	0	
1	91.453	5.8242	6.1558
2	944.3	3.1787	37.018
3	20	3.45	6.1371
backing	INF	2.07	5

50 % (w.w) dsq in fractionated PBcis – thin / $\chi^2 = 3.92469$

Layer	Thickness / Å	SLD / $10^{-6} \cdot \text{Å}^{-2}$	Roughness / Å
fronting	INF	0	
1	432	6.6362	5
2	2810	3.9841	72.737
3	20	3.45	10
backing	INF	2.07	5

50 % (w.w) dsq in fractionated PBcis – thick / $\chi^2 = 4.9913$

Layer	Thickness / Å	SLD / $10^{-6} \cdot \text{Å}^{-2}$	Roughness / Å
fronting	INF	0	
1	487.58	6.5619	5
2	2739	3.7151	90.368
3	20	3.45	5
backing	INF	2.07	5

oligo-dIB 900 in PI

30 % (w.w) oligo-dIB 900 in PI / $\chi^2 = 7.87725$

Layer	Thickness / Å	SLD / $10^{-6} \cdot \text{Å}^{-2}$	Roughness / Å
fronting	INF	0	
1	161.49	4.0806	22.334
2	562.88	0.64933	97.377
3	23.243	3.2362	35.61
backing	INF	2.07	5

40 % (w.w) oligo-dIB 900 in PI / $\chi^2 = 19.352$

Layer	Thickness / Å	SLD / $10^{-6} \cdot \text{Å}^{-2}$	Roughness / Å
fronting	INF	0	
1	272.98	3.2471	18.361
2	423.42	1.0503	201.12
3	12.705	3.2656	18.309
backing	INF	2.07	5

oligo-dIB 2200 in PI

30 % (w.w) oligo-dIB 2200 in PI / $\chi^2 = 19.136$

Layer	Thickness / Å	SLD / $10^{-6} \cdot \text{Å}^{-2}$	Roughness / Å
fronting	INF	0	
1	129.74	6.57	5.5725
2	642.95	1.0034	26.674
3	15.004	3.111	5
backing	INF	2.07	5

40 % (w.w) oligo-dIB 2200 in PI / $\chi^2 = 14.3747$

Layer	Thickness / Å	SLD / $10^{-6} \cdot \text{Å}^{-2}$	Roughness / Å
fronting	INF	0	
1	165.69	6.57	8.4736
2	510.09	1.4677	33.2
3	15.018	3.1029	5
backing	INF	2.07	5

50 % (w.w) oligo-dIB 2200 in PI / $\chi^2 = 21.0983$

Layer	Thickness / Å	SLD / $10^{-6} \cdot \text{Å}^{-2}$	Roughness / Å
fronting	INF	0	
1	225.05	6.57	12.241
2	428.56	1.5919	34
3	15.13	3.14	5
backing	INF	2.07	5

60 % (w.w) oligo-dIB 2200 in PI / $\chi^2 = 35.8487$

Layer	Thickness / Å	SLD / $10^{-6} \cdot \text{Å}^{-2}$	Roughness / Å
fronting	INF	0	
1	274.53	6.57	13.159
2	361.98	1.4896	41.368
3	15.011	3.106	5
backing	INF	2.07	5

70 % (w.w) oligo-dIB 2200 in PI / $\chi^2 = 47.4642$

Layer	Thickness / Å	SLD / $10^{-6} \cdot \text{Å}^{-2}$	Roughness / Å
fronting	INF	0	
1	302.15	6.57	14.002
2	251.91	1.4581	40.018
3	15.064	3.1279	5
backing	INF	2.07	5

oligo-dIB 2200 in PBcis

10 % (w.w) oligo-dIB 2200 in PBcis / $\chi^2 = 21.2705$

Layer	Thickness / Å	SLD / $10^{-6} \cdot \text{Å}^{-2}$	Roughness / Å
fronting	INF	0	
1	112.51	5.9746	7.28
2	1411.3	0.52991	29.23
3	20	3.45	9.9429
backing	INF	2.07	5

Annex 3: NR fitting parameters

30 % (w.w) oligo-dIB 2200 in PBcis / $\chi^2 = 8.3548$

Layer	Thickness / Å	SLD / 10^{-6}Å^{-2}	Roughness / Å
fronting	INF	0	
1	273.19	6.1279	7.9754
2	1039.9	1.4433	65.405
3	20	3.45	9.9312
backing	INF	2.07	5

50 % (w.w) oligo-dIB 2200 in PBcis / $\chi^2 = 13.4707$

Layer	Thickness / Å	SLD / 10^{-6}Å^{-2}	Roughness / Å
fronting	INF	0	
1	345.76	6.3401	7.9754
2	804.26	1.8866	97.208
3	20	3.45	9.9312
backing	INF	2.07	5

oligo-dS in hPI

30 % (w.w) oligo-dS in hPI / $\chi^2 = 4.36978$

Layer	Thickness / Å	SLD / 10^{-6}Å^{-2}	Roughness / Å
fronting	INF	0	
1	516.19	-0.32	10
2	150.71	5.72	24.492
3	24.254	3.1003	3
backing	INF	2.07	5

40 % (w.w) oligo-dS in hPI / $\chi^2 = 6.25247$

Layer	Thickness / Å	SLD / 10^{-6}Å^{-2}	Roughness / Å
fronting	INF	0	
1	231.63	-0.32	10
2	201.42	5.72	30.458
3	16.656	3.1254	5
backing	INF	2.07	5

50 % (w.w) oligo-dS in hPI / $\chi^2 = 26.9715$

Layer	Thickness / Å	SLD / 10^{-6}Å^{-2}	Roughness / Å
fronting	INF	0	
1	118.71	-0.32	10
2	220.81	5.72	61.068
3	15.501	3.451	5
backing	INF	2.07	5

oligo-dIB 2200 in PB

30 % (w.w) oligo-dIB 2200 in PB / $\chi^2 = 58.1473$

Layer	Thickness / Å	SLD / 10^{-6}Å^{-2}	Roughness / Å
fronting	INF	0	
1	238.91	6.56	7.0503
2	331.29	0.42149	22.584
3	449.8	1.0152	36.851
4	16.947	3.1298	5
backing	INF	2.07	5

Annex 3: NR fitting parameters

50 % (w.w) oligo-dIB 2200 in PB / $\chi^2 = 44.071$

Layer	Thickness / Å	SLD / 10^{-6}Å^{-2}	Roughness / Å
fronting	INF	0	
1	390.38	6.5145	8.3426
2	282.89	0.47047	33.549
3	244.85	1.6826	42.92
4	15.408	3.1976	5
backing	INF	2.07	5

60 % (w.w) oligo-dIB 2200 in PB / $\chi^2 = 53.4508$

Layer	Thickness / Å	SLD / 10^{-6}Å^{-2}	Roughness / Å
fronting	INF	0	
1	387.12	6.5045	9.8702
2	370.63	1.78	36.113
3	15.326	3.1506	5
backing	INF	2.07	5